SYNTHESIS AND CHARACTERIZATION OF FLUORENE-TYPE AND
HYDROGENATED AMORPHOUS CARBON THIN FILMS
IN RF AND DC GLOW DISCHARGES

A THESIS SUBMITTED TO
THE GRADUATE SCHOOL OF NATURAL AND APPLIED SCIENCES
OF
MIDDLE EAST TECHNICAL UNIVERSITY

BY

DOĞAN MANSUROĞLU

IN PARTIAL FULFILLMENT OF THE REQUIREMENTS
FOR
THE DEGREE OF DOCTOR OF PHILOSOPHY
IN
PHYSICS

SEPTEMBER 2015

Approval of the thesis:

SYNTHESIS AND CHARACTERIZATION OF FLUORENE-TYPE AND HYDROGENATED AMORPHOUS CARBON THIN FILMS IN RF AND DC GLOW DISCHARGES

submitted by **DOĞAN MANSUROĞLU** in partial fulfillment of the requirements for the degree of **Doctor of Philosophy in Physics Department, Middle East Technical University** by,

Prof. Dr. Gülbin Dural Ünver
Dean, Graduate School of **Natural and Applied Sciences** _____

Prof. Dr. Mehmet Zeyrek
Head of Department, **Physics** _____

Prof. Dr. Sinan Bilikmen _____
Supervisor, **Physics Dept., METU**

Examining Committee Members:

Assoc. Prof. Dr. Nurdan D. Sankır
Mater. Sci. and Nanotech. Eng. Dept., TOBB _____

Prof. Dr. Sinan Bilikmen
Physics Dept., METU _____

Assoc. Prof. Dr. Hakan Altan
Physics Dept., METU _____

Assoc. Prof. Dr. Kadir Gökşen
Physics Dept., Duzce University _____

Asst. Prof. Dr. Kemal Efe Eseller
Physics Dept., Atılım University _____

Date: _____*18.09.2015*_____

I hereby declare that all information in this document has been obtained and presented in accordance with academic rules and ethical conduct. I also declare that, as required by these rules and conduct, I have fully cited and referenced all material and results that are not original to this work.

Name, Last name : DOĞAN, MANSUROĞLU

Signature :

ABSTRACT

SYNTHESIS AND CHARACTERIZATION OF FLUORENE-TYPE AND HYDROGENATED AMORPHOUS CARBON THIN FILMS IN RF AND DC GLOW DISCHARGES

Mansuroğlu, Doğan

Ph.D., Department of Physics

Supervisor   : Prof. Dr. Sinan Bilikmen

September 2015, 195 pages

Fluorene ($C_{13}H_{10}$)-type and hydrogenated amorphous carbon (a-C:H) thin films were synthesized under a capacitively coupled single radio frequency (RF) and a direct current (DC) plasma systems. In the first system, the RF plasma reactor, circular parallel plate electrodes were used; the upper electrode was connected to 13.56 MHz RF power while the lower electrode was grounded. To control the positive ion bombardment, a negative bias voltage was applied between the holder of the substrate and the wall of the chamber. For the second system, the DC plasma reactor, consisted of three cylindrical electrodes and two quartz tubes. In both systems, the thin films were deposited on glass discs and silicon wafers. The fluorene-type thin films were produced in the RF plasma reactor under the biphenyl ($C_{12}H_{10}$)/methane (CH_4) and biphenyl/ethylene (C_2H_4) mixtures, and the methane plasma was used to produce the a-C:H films. In the DC plasma reactor, the vaporization of the powder monomer (fluorene) was used. To improve the electrical and optical properties of the thin films, the generated films were doped by Iodine (I_2) and annealed under variable temperatures. The thin films were applied to a

crystalline silicon (c-Si) solar cell and an increase around 5 % was observed in the efficiency of the solar cell.

The chemical structures and physical properties of the thin films were examined under such plasma parameters as the plasma power, gas flow rate, negative bias voltage, deposition time, and plasma pressure. Diagnostics of the system was done using a double Langmuir probe. To characterize the chemical structural properties of thin films Fourier Transform Infrared (FTIR) and X-ray Photoelectron (XPS) Spectroscopy were used, and the changes in the plasma chemistry during the deposition were measured by Residual Gas Analysis (RGA) Mass Spectrometer and Optical Emission Spectroscopy (OES). According to results, applying negative bias voltage could be considered an effective way in controlling the reactions in plasma depositions, and an increase in the quality of generated films when the plasma power and gas flow rate increased as well as the deposition time was generally observed. Moreover, the morphology of the films was analyzed by X-ray diffraction (XRD) and the nanotopographic properties of the surfaces were examined using an Atomic Force Microscope (AFM) and Scanning Electron Microscope (SEM). The surfaces of fluorene-type thin films had remarkable nanostructured characteristics generated by various negative bias voltages, and the rough surfaces made them useful for photovoltaic applications. Furthermore, the optical properties of the films were examined with UV-visible Spectroscopy and the thickness was measured with an ellipsometer and Dektak Profilometer. From the results, it could be suggested that the structures of thin films produced by plasma polymerization technique were different than the ones produced by the conventional techniques. Additionally, the different chains order were observed in the film structure with respect to independent plasma parameters and the conductivity of the films was improved by controlling of the plasma parameters and iodine doping. Finally, for the determination of hydrophobic behavior of the thin films, the contact angle measurement method was used.

Keywords: Plasma Polymerization, Thin Film, Radio Frequency (RF) and Direct Current (DC) Plasma Discharges, Fluorene, Biphenyl, Methane, Ethylene, Hydrogenated Amorphous Carbon (a-C:H).

ÖZ

FLUOREN-TİPİ VE HİDROJENLENMİŞ AMORF KARBON İNCE FİLMLERİN RF VE DC ELEKTRİKSEL BOŞALMALARI ALTINDA SENTEZLENMESİ VE KARAKTERİZASYONU

Mansuroğlu, Doğan

Doktora, Fizik Bölümü

Tez Yöneticisi   : Prof. Dr. Sinan Bilikmen

Eylül 2015, 195 sayfa

Fluoren ($C_{13}H_{10}$)-tipi ve hidrojenlenmiş amorf karbon (a-C:H) ince filmleri tek kapasitör destekli (bağlı) radyo frekans (RF) ve doğru akım (DC) plasma sistemleri kullanılarak sentezlenmiştir. İlk sistem olan RF plazma reaktörü birbirine paralel alt ve üst iki dairesel eletrottan oluşmaktadır. Üst elektrot 13.56 MHz' lik RF güç kaynağına, alt elektrot ise toprağa bağlanmıştır. Alt taş yüzeyine pozitif iyon akısını (bombardımanını) yönlendirmek için, alt taş tutucu ile vakum odacığının duvarı arasına negatif voltaj uygulanmıştır. İkinci sistem olan DC plazma reaktörü üç silindirik eletrot ile iki quartz tüpünden oluşmaktadır. İnce film üretimi iki sistemde de cam alt taş ve silikon pul üzerinde gerçekleştirilmiştir. Fluoren-tipi ince filmler RF plazma reaktörü içerisinde bifenil ($C_{12}H_{10}$)/metan (CH_4) ve bifenil /etilen (C_2H_4) plazmaları kullanılarak, hidrojenlenmiş amorf karbon (a-C:H) filmleri ise metan plazması kullanılarak üretilmiştir. DC plazma reaktöründe ise ince film üretmek için fluorene monomeri kullanılmıştır. Üretilen ince filmlerin elektrik ve optik özelliklerini iyileştirmek için İyodin katkılaması yapılmış ve farklı sıcaklıklar altında tavlanmıştır. Ayrıca bu ince filmler kristal silikon (c-Si) güneş hücreleri

üzerine kaplanmış ve güneş hücrelerinin verimliliğini % 5 civarında arttırdığı gözlemlenmiştir.

Bu çalışmada, ince filmlerin kimyasal yapıları ve fiziksel özellikleri plazma gücü, gaz akış hızı, uygulanan negatif voltaj değeri, kaplama süresi, ve plazma basıncı gibi farklı plazma parametreleri altında analiz edilmiştir. Plazma diyagnostik özellikleri çift Langmuir sondası ile ölçülmüştür. İnce filmlerin kimyasal bağ yapı özelliklerinin karakterizasyonu için Fourier Dönüşümlü Kızılötesi (FTIR) ve X-ışını Fotoelektron (XPS) Spektroskopileri kullanılmış ve ince film üretimi sırasında oluşan plazmadaki kimyasal değişiklikler Artan (Residual) Gaz Analiz (RGA) Kütle Spektrometresi ve Optik Yayılım Spektroskopisi (OES) kullanılarak analiz edilmiştir. Elde edilen sonuçlara göre, ince film üretimi sırasında negatif voltaj uygulamanın oluşan reaksiyonların kontrol edilmesinde etkili bir yöntem olduğu ortaya çıkmış, plazma gücü ve gaz akış hızının yanı sıra kaplama süresi arttırıldığında üretilen filmlerin kalitesinde genellikle bir artış olduğu tespit edilmiştir. Ayrıca, filmlerin yüzey morfolojisi X-ışın Kırınım (XRD) Spektroskopisi ile ölçülmüş, yüzeyin topografik özelliklerinin analizi için ise Atomik Kuvvet Mikroskobu (AFM) ve Taramalı Elektron Mikroskobu (SEM) kullanılmıştır. Fluoren-tipi ince filmlerin yüzeylerinin farklı negatif voltajlar ile oluşturulmuş olağanüstü nanoyapısal özelliklere sahip oldukları ve yüzeyler üzerinde oluşan piklerin bu filmleri fotovoltaik uygulamalar için uyumlu hale getirdiği gözlemlenmiştir. Bunlara ek olarak, filmlerin optik özelliklerini belirlemek için Morötesi (UV)-görünür bölge Spektroskopisi kullanılmış, filmlerin kalınlığı elipsometre ve Dektak Profilometre ile ölçülmüştür. Sonuçlara göre, plazma polimerizasyon yöntemi ile üretilmiş ince filmlerin yapılarının geleneksel yöntemlerle üretilen filmlerden daha farklı olduğu gözlemlenmiştir. Ayrıca, film yapısının içerisindeki zincir bağların (chains) bağımsız plazma parametrelerine göre farklı sıralamalarda oldukları tespit edilmiş ve ince filmlerin iletkenliği plazma parametrelerinin kontrol edilmesi ve İyodin katkılaması yapılarak iyileştirilmiştir. Son olarak, üretilen ince fimlerin hidrofobik özelliğini ölçmek için kontak açı (contact angle) ölçüm yöntemi kullanılmıştır.

Anahtar Kelimeler: Plazma Polimerizasyon, İnce Film, Radyo Frekans (RF) ve Doğru Akım (DC) Elektriksel Boşalmaları, Fluoren, Bifenil, Metan, Etilen, Hidrojenlenmiş Amorf Karbon (a-C:H).

To my family

ACKNOWLEDGEMENTS

I would like to express my endless gratitude to my parents, Makbule and Ahmet, and my brother Necim, and my sisters, Nil and Ebru for their love, support and motivation during the whole period of my study.

TABLE OF CONTENTS

LIST OF TABLES

TABLES

LIST OF FIGURES

FIGURES

CHAPTER 1

INTRODUCTION

Plasma technology has been investigated and used in the gas phase deposition of materials for at least half a century. Although the discharge was used to produce some oily polymer-like products in the early nineteenth century, researchers started to pay attention to the technique of plasma polymerization after the beginning of the 1960s [1]. Plasma processes play an important role in many areas of technology such as device fabrication. The studies in this area offer solutions to drawbacks in structural design and sustainable growth, and also increase the interest to smaller dimensions. Plasma technology provides the environmental compatibility, high productivity and quality, and flexibility, required for a variety of diverse areas including electronics, optics, tool-making, and textile industries. Moreover, this technology has recently become more visible in the area of biomaterials, biosensing, and biomedical applications, due to its promising impact to improve, by multi-step processing, the adhesion, stability, sterility, and functionality within a single process [2].

When a plasma reactor contains an organic gas, a polymer-like product deposits on the substrate surface as well as the walls of the reactor. This product, which is referred to as the *plasma polymer film*, is different than the polymer film produced via conventional methods, even though the same monomer is used by both of the polymerization techniques. The conventional (wet processing) methods have limitations on the control of deposition and the level of reproducibility. Since the films are not obtained with the desired thinness and homogeneity, the conventional methods are not preferred for use in the microsensor and microelectronics technologies which require polymers as an interface. The plasma polymerization, therefore, is an alternative technique being more advantageous for semiconductor technologies compared to the conventional processes. The ability to cover any shape and size over is one of the most significant properties of plasma-deposited films.

1

Additionally, plasma polymer thin films offer a variety of features including solvent- and pinhole-free, chemical and mechanical stability, flat surface structure, and thin thickness (<1μm) [3]. A wide range of monomers can be used by the plasma polymerization technique to obtain materials with virtually no limitation. Thus, this technique has a remarkable potential to develop new materials for technological utilization in different areas.

Among polymers, π-conjugated polymers such as polyfluorene, polythiophene, polyaniline, and their derivatives have been widely studied due to their potential applications as active layers in organic electronic and chemical sensor devices [4–6]. Fluorene and its derivatives have attracted appreciable attention in π-conjugated polymers due to their excellent physical and chemical properties [7–11]. Their stable and highly blue light-emitting properties make them suitable for organic light emitting diodes [12–16]. Additionally, they are very attractive materials with good charge mobility [17] and offer the possibility of construction of ultrathin layers [18] for photovoltaic applications [19,20]. Furthermore, the flexible behavior of backbone structure of the fluorene makes it possible to obtain almost the entire visible colors range with high efficiency for devices with fluorene derivatives [21–23].

Another promising materials produced by the plasma deposition are amorphous hydrogenated carbon (a-C:H) films due to their extraordinary physical and chemical properties such as high density and strength, thermal stability, chemical inertness for both acids and alkalis, effective infrared (IR) transparency and high electrical resistivity [24–31]. Recent studies have demonstrated that the anti-reflective properties of infrared (IR) optical elements and solar cells could be enhanced by coating the surface with the a-C:H film that has also contributed to the protection for magnetic storage disks and tool materials [29–36]. It has been shown that the a-C:H film has improved the performance of electronic devices [35,37] due to the property of having a wide band gap. Moreover, it has been used for flat-panel displays as a cathode emitter, and for biomedical applications [29–32,38–43].

This thesis focuses on the fabrication and characterization of the fluorene-type and the amorphous hydrogenated carbon (a-C:H) thin films by the plasma polymerization technique. Two different plasma systems are used for the deposition:

the single capacitively coupled radio frequency (RF) plasma system and the double discharge system. The chemical structures of the films are analyzed by the RGA, FTIR, XPS, and OES spectrometers. The optical characterization is carried out with the UV-vis spectroscopy and the ellipsometer and Dektak Profilometer are used for thickness measurements. The surface morphology is explored by AFM, SEM, and XRD analysis. The thesis outline is organized as follows:

The second chapter contains a brief history of the plasma polymerization. The principles of plasma polymerization method are also explained and compared to the other deposition techniques such as wet processing (conventional) and dry processing.

In the third chapter, the single capacitively coupled RF plasma system that is manufactured in our lab is introduced in detail and its diagnostics studied with a double Lagmuir probe under Ar an N_2 plasmas are illustrated.

The fourth chapter includes the synthesis of the fluorene thin film by a double discharge system which occurs from the combination of a low pressure DC glow discharge and a high current pulsed discharge. The solid monomer of the fluorene is used in the deposition. The optical and chemical properties of the film are characterized and the surface morphology is discussed. This chapter is published in Plasma Chemistry and Plasma Processing by title of "Polyfluorene Thin Films Synthesized by a Novel Plasma Polymerization Method", 2012, 32, 35-44.

In the fifth chapter, the fluorene-type thin film is produced by a single capacitively coupled RF plasma system under the biphenyl/methane and biphenyl/ethylene plasmas. This work is done at the Center for Plasma-Aided Manufacturing (CPAM), University of Wisconsin-Madison, USA. The synthesis of the thin film is carried out by applying a negative bias voltage and the influence of the negative voltage on the chemical structure of the film during the deposition is investigated. Additionally, the optical properties of the film are analyzed by the iodine doping method and the nanotopographic features on the surface are illustrated with respect to the different plasma parameters. The first part of this chapter is published in Plasma Processes and Polymers by title of "Synthesis of Fluorene-Type Thin Film Under

Biphenyl/Methane Plasma Environment", 2015, doi: 10.1002/ppap.201400136 and license number is 3720740752252.

The sixth chapter focuses on the amorphous hydrogenated carbon (a-C:H) thin film synthesized by the single capacitively coupled RF system under the methane plasma. The characterization of the physical and chemical properties of the film is analyzed by the different experimental sets. Additionally, the transmission of the deposited films and the property of the surface wettability are explored. Moreover, the crystalline silicon (c-Si) solar cell is coated by the a-C:H film. The efficiency of the coated solar cell shows significant differences relative to the uncoated solar cell and these differences are studied with various deposition features. This chapter is published in Plasma Science and Technology by title of "Optical Characterization of Amorphous Hydrogenated Carbon (a-C:H) Thin Film Prepared by Single RF Plasma Method", 2015, 17, 6, 488-495.

The seventh chapter examines the annealing effect on the fluorene-type thin film, which is produced by the single capacitively coupled RF system under the biphenyl/methane plasma. The chemical structures and the crystallinity of the film are investigated before and after the annealing. The wettability of the film surface and the nanotopography are also characterized after the annealing. Furthermore, the film produced is used to coat the c-Si solar cell and the influence of the coating on the cell efficiency is discussed.

Finally, the eighth chapter summarizes this thesis and includes a discussion on the future work.

1.1 References

[1]   N. Inagaki, Plasma Surface Modification and Plasma Polymerization, Technomic Publishing, Pennsylvania, USA, 1996.

[2]   W. Knoll, R.C. Advincula, Functional Polymer Films Volume 1: Preparation and Patterning, Wiley-VCH Verlag GmbH, 2011.

[3]   A. Hiratsuka, I. Karube, Electroanalysis 12 (2000) 695.

[4]   B.S. Ong, Y. Wu, Y. Li, P. Liu, H. Pan, Chem. A Eur. J. 14 (2008) 4766.

[5]   J.T. Mabeck, G.G. Malliaras, Anal. Bioanal. Chem. 384 (2006) 343.

[6]   V. Saxena, B.D. Malhotra, Curr. Appl. Phys. 3 (2003) 293.

[7]   A.C. Grimsdale, K. Müllen, Adv. Polym. Sci. 199 (2006) 1.

[8]   J. Pei, W.-L. Yu, W. Huang, A.J. Heeger, Chem. Commun. (2000) 1631.

[9]   W. Yu, J. Pei, Y. Cao, A.J. Heeger, R. Columbia, A. August, Chem. Commun. (1999) 1837.

[10]   Q. Pei, Y. Yang, J. Am. Chem. Soc. 118 (1996) 7416.

[11]   N.S. Cho, J.-H. Park, S.-K. Lee, J. Lee, H.-K. Shim, M.-J. Park, D.-H. Hwang, B.-J. Jung, Macromolecules 39 (2006) 177.

[12]   M. Bernius, M. Inbasekaran, E. Woo, W. Wu, L. Wujkowski, Thin Solid Films 363 (2000) 55.

[13]   M. Inbasekaran, E. Woo, W. Wu, M. Bernius, L. Wujkowski, Synth. Met. 111-112 (2000) 397.

[14]   H. Cho, D. Kim, Y. Kim, Adv. Mater. 9 (1997) 326.

[15]   B.U. Scherf, E.J.W. List, Adv. Mater. 14 (2002) 477.

[16]   M. Kreyenschmidt, G. Klaerner, T. Fuhrer, J. Ashenhurst, S. Karg, W.D. Chen, V.Y. Lee, J.C. Scott, R.D. Miller, Macromolecules 31 (1998) 1099.

[17]   A. Babel, S.A. Jenekhe, Macromolecules 36 (2003) 7759.

[18]   D. Neher, Macromol. Rapid Commun. 22 (2001) 1365.

[19]   E. Bundgaard, F. Krebs, Sol. Energy Mater. Sol. Cells 91 (2007) 954.

[20]   F. Zhang, K. Jespersen, C. Bjostrom, M. Svensson, M. Andersson, V. Sundstrom, Adv. Funct. Mater. 16 (2006) 667.

[21]   M. Leclerc, J. Polym. Sci. Part A Polym. Chem. 39 (2001) 2867.

[22] B.S. Beauprø, M. Leclerc, Adv. Funct. Mater. 12 (2002) 192.

[23] N.S. Cho, D.-H. Hwang, J.-I. Lee, B.-J. Jung, H.-K. Shim, Macromolecules 35 (2002) 1224.

[24] J. Angus, P. Koidl, S. Domitz, in:, J. Mort, F. Jansen (Eds.), Plasma Depos. Thin Film., CRC Press, Boca Raton, FL, 1986, p. 89.

[25] D. Green, D. McKenzie, P. Lukins, Mater. Sci. Forum 52-53 (1990) 103.

[26] H. Tsai, Mater. Sci. Forum 52-53 (1990) 71.

[27] J. Robertson, Mater. Sci. Eng. R Reports 37 (2002) 129.

[28] J. Robertson, Surf. Coatings Technol. 50 (1992) 185.

[29] M. Geis, M. Tamor, Encyclopedia of Applied Physics, VCH, New York, 1993.

[30] H.T. Kim, S.H. Sohn, Vacuum 86 (2012) 2148.

[31] H. Vora, J. Appl. Phys. 52 (1981) 6151.

[32] G. Dearnaley, J.H. Arps, Surf. Coatings Technol. 200 (2005) 2518.

[33] C. Casiraghi, A.C. Ferrari, R. Ohr, D. Chu, J. Robertson, Diam. Relat. Mater. 13 (2004) 1416.

[34] C. Casiraghi, A.C. Ferrari, J. Robertson, R. Ohr, M. V Gradowski, D. Schneider, H. Hilgers, Diam. Relat. Mater. 13 (2004) 1480.

[35] B.N. Jariwala, C. V. Ciobanu, S. Agarwal, J. Appl. Phys. 106 (2009) 073305.

[36] J. Robertson, Thin Solid Films 383 (2001) 81.

[37] G.A.J. Amaratunga, Science 297 (2002) 1657.

[38] R.J. Narayan, Mater. Sci. Eng. C 25 (2005) 405.

[39] S.E. Rodil, R. Olivares, H. Arzate, S. Muhl, Diam. Relat. Mater. 12 (2003) 931.

[40] S.R.P. Silva, R.D. Forrest, D.A. Munindradasa, G.A.J. Amaratunga, 7 (1998) 645.

[41] J. Xu, X. Huang, W. Li, L. Wang, X. Huang, K. Chen, J. Xu, I.H. Wilson, Appl. Phys. Lett. 79 (2001) 141.

[42] J. Robertson, Thin Solid Films 296 (1997) 61.

[43] M.W. Geis, N.N. Efremow, K.E. Krohn, J.C. Twichell, T.M. Lyszczarz, 393 (1998) 431.

CHAPTER 2

PLASMA POLYMERIZATION

2.1 History of Plasma Polymerization

The term plasma polymer was first used during the second half of the nineteenth century [1,2]. Many studies on plasma polymerization were done in the 1930s [3–6], and this subject became even more attractive in the 1950s [7,8]. König and Helwig [9] deposited hydrocarbon plasma polymers from benzene vapors using parallel Al plate electrodes in a glass bell-jar. Brokes and König [10] produced plasma polymer films using benzene and methane. In this study, a hard plasma polymer film was obtained by increasing voltage, which increased the bombardment of energetic ions. The process of plasma polymer was explained in detail by Heisen [7], and this first period of plasma polymer was reviewed by Pagnia [11].

Although plasma polymers were recognized in the early 19th century, people began to pay more attention to this subject after Goodman's [12] development of the dielectric property of the plasma polymers in the 1960s made these thin films appear more useful for the microelectronics industry. This study also demonstrated that the generated plasma polymers had a crosslinked structure. After Goodman's study, several monomers, including organics and metalorganics, were synthesized using Al electrodes and Bradley and Hammes [13] measured their electrical properties. Moreover, the newly discovered properties of plasma polymers—including chemical and thermal stability, as well as pinhole-free and solvent-free thin films—continued to be developed by Mollenstedt and Speidel [14], Stuart [15,16], Bashara and Doty [17], Bradley [18,19], Williams and Hayes [20], Gregor [21] and Hirai and Nakada [22]. Several studies investigated the ionic and radical mechanisms of plasma polymer films [20,23–29]. Kobayashi et al. [28,29] demonstrated that the activation of monomers generally occurs in a larger concentration near the cathode as compared to the anode, so the chemical reactions occur in the negative glow region. The details of the plasma polymerization process were reviewed by Mearns [30],

Gregor [31], and Hogarth and Igbal [32]. Koenig and Maissel investigated the effect of applying rf voltage during the deposition through a sputtering process and found that rf discharge provides a remarkable positive potential between the two dark regions [33]. The positive ion bombardment to substrates was investigated by Coburn and Kay [34]; ion bombardment improved the film's quality, stoichiometry, and topography by increasing the concentration of the deposition. Duval and Theoret [35] deposited benzene under a capacitively coupled rf plasma system and studied chemical reactions occurring during plasma deposition under various parameters. They demonstrated that molecular ionization depends on the pressure and power of the discharge, and that increasing the energy of the bombarding species led to an increase in the crosslinking. Tibbitt et al. [36] proposed a model for the kinetics of plasma polymerization which indicated a process consisting of five steps: initiation, adsorption, propagation in the gas phase (homogenous reaction), propagation at the surface of the substrate (heterogeneous reaction), and termination. Although this model is important for analysis, it is not sufficient for fully understanding plasma polymerization. Yasuda [37] introduced a new aspect of basic reactions during plasma polymerization. He suggested that the level of rf power and the deposition location are very important in determining the chemical features of polymer films, and also that chain reactions of the deposited polymer films are different than deposition under conventional methods. While the chains of deposited polymers are predicted by the structure of the monomer in the conventional polymerization processes, the structure of the films deposited in plasma polymerization is not predictable due to the fragmentation and rearrangement of monomers during the deposition. This feature of plasma polymerization is referred to as atomic polymerization, and this concept is now generally accepted by researchers defining characteristics of the plasma polymerization method.

The properties of plasma polymer films were widely examined for several applications, including the electrical and optical applications, biomedical applications, etc., [38–51]. Recent publications note that plasma polymers were used as barriers or protective materials in the automotive industry [52–56]. Studies of plasma polymerized films synthesized for sensor devices and optical coatings were reviewed by Hiratsuka and Martinu [57,58]. Organic and inorganic hybrid polymer thin films were deposited by plasma deposition and their electrical, optical, and

mechanical properties were investigated [59–65]. Plasma polymer thin films produced for biomedical applications were extensively reviewed by several investigators [66–70]. The chemical mechanism of plasma polymerization has been reviewed by Friedrich [71] and the most recent applications in plasma polymerization have been discussed by Ren [72], Kylian [73], and Jiang[74].

2.2 Plasma

2.2.1 Plasma State

William Crooks [75] exposed gases to an electric field at low pressure for the first time, verifying that gases under an electric field in a vacuum chamber exhibit characteristics of a new state of matter. Tonks and Langmuir called this new state 'plasma' in 1929. Plasma can be defined as a collection of ionized gas occurring from equal numbers of charged (positive and negative) particles, the unionized neutral particles, and electromagnetic emission [76]. The majority of the universe is in the plasma state, and more than 99% of the visible universe is considered plasma.

In the laboratory, plasma has been created by generating electrical discharges between two metal electrodes under pressure between 10^{-1} and 1 torr. When voltage is applied to electrodes inside a vacuum, negatively charged electrons and positively charged ions gain random velocities, beginning to move in opposite directions according to the direction of the applied electric field. This reaction then creates an emission in the vacuum area. Moreover, the plasma behaves as electrically conductive due to ionization [50,77–80].

2.2.2 Energy, Velocity, and Temperature in Plasma

The kinetic energy of a particle is $\vec{E} = \frac{1}{2}mv^2$ where m is the mass of the particle and v is the velocity of the particle. The average energy E_{av} is defined for a system of N particles with different kinetic energies which is given as

$$E_{\text{av}} = \frac{1}{2N}\sum_{i=1}^{N} m_i v_i^2 \qquad (2.1)$$

If a gas is in thermal equilibrium, the average energy per particle is defined as $E = 3k_B T/2$, where $k_B = 1.38 \times 10^{-23}$ JK^{-1} is Boltzmann's constant, and T is the absolute temperature. Plasma species with random velocities—such as electrons, ions, and radicals—are defined by a Maxwellian (or Maxwell – Boltzmann)

distribution function, assuming the system is at thermal equilibrium at temperature T. The Maxwell distribution can be defined in a one-dimensional system by $f(v) = Ae^{-\frac{mv^2}{k_BT}}$, where $A = N\sqrt{\frac{m}{2\pi k_BT}}$. The velocity distribution of particles is defined as

$$\frac{dN}{N} = 4\pi v^2 \left(\frac{m}{2\pi k_BT}\right)^{3/2} exp\left(-\frac{mv^2}{2k_BT}\right) dv = f(v)dv \qquad (2.2)$$

where N is the total number of particles and m is the mass of each particle. The equation (2.2) gives the number of particles per unit volume with velocity in the range v to dv. There are two average values for velocities: linearly averaged velocity and root-mean square velocity.

$$\bar{v} = \int_0^\infty vf(v)dv = \sqrt{\frac{8k_BT}{\pi m}}$$

$$\bar{v}_r = \sqrt{\bar{v^2}} = \left[\int_0^\infty v^2 f(v)dv\right]^{1/2} = \sqrt{\frac{3k_BT}{m}} \qquad (2.3)$$

The measurement of the average energy is often employed in terms of electrons volts (eV). For example, the average energy $E = 3k_BT/2$ per particle for a gas at 1 K refers to 2.07 x 10^{-23} J. Since the sufficient energy to accelerate a charge through a potential difference of 1 V is equal to 1.602 x 10^{-19} J, the energy is defined in term of electron volt. The temperature of a gas in thermal equilibrium is also defined as electron volt. Therefore, the energy corresponding to k_BT is expressed as the temperature of plasma. The 1 eV refers to 11600 K, and the average energy is 0.75 eV in three dimensions. The temperature that is needed to ionize the material and generate the plasma changes in the range from ~4000 K (for celsium) to ~20000 K (for helium) [81].

Due to the different kinetic energies of the species, the temperature is described by the electron temperature T_e, ion temperature T_i, and gas temperature T_g. The energy ε of the system is defined by the total of the translation energy ε_{trans}, rotation energy ε_{rot}, vibration energy ε_{vib}, and electronic state energy ε_{elect}. In this case, to determine the plasma's energy, it should be engaged with many gas particle temperatures such as the rotational temperature T_r, the vibrational temperature T_v, and the electronic temperature T_{elect}. In contrast to a gas molecule, an electron

should be described only by the electron temperature T_e since it lacks an internal structure [77]. Since the plasma have several temperatures which are different than each of them, it is not possible to obtain a thermal equilibrium between the particles in a plasma. However, the electron temperature T_e or the ion temperature T_i indicate their own thermal equilibriums due to the electrons and the ions have separate Maxwellian distributions. Moreover, in plasma discharges, electrons obtain their energy from the electric field more easily than neutral particles and ions. Due to the energy exchange with the other atoms and the walls of the vacuum chamber, ions and neutrals have a fast thermal equilibrium [76]. The thermal equilibrium is only acceptable in of itself, so characterization of the plasma by Maxwellian distribution is possible by working with the temperatures of electrons and ions separately [50,77,80].

2.2.3 Plasma Density and Debye Length

Although plasma is made from electrons, ions and excited molecules, determining the density of plasma requires focusing on electrons and ions since they are charged particles. The density of ions is defined by $n_{i1}, n_{i2}, n_{i3}, \dots$ due to different kind of ions, and the density of electrons is described by n_e.

$$n_e = n_{i1} + n_{i2} + n_{i3} + \cdots = n \qquad (2.4)$$

For plasma in electrically neutral and equilibrium states, n is defined as the plasma density. In the equilibrium state of the plasma, if a test particle (negatively charged) placed into the plasma, a cloud of ions is generated around the test particle. At this point, the cloud of ions becomes surrounded by electrons and a cloud of electrons forms around the positively charged object (Figure 2.1). A sheath of plasma can be introduced by cloud of ions and electrons. The bulk of the plasma inside of this cloud only has an electric field and the outside of the sheath shows electrical neutrality. The thickness of the sheath is called Debye length and this circumstance is defined as the Debye shielding [50,77,78,80,82].

$$\lambda_D = \sqrt{\frac{\epsilon_0 k_B T_e}{n e^2}} \qquad (2.5)$$

λ_D is the Debye length or Debye shielding length, n is the plasma density, e is the electron's charge, and ϵ_0 permittivity of free space. The range of Debye length can be observed for different types of plasma in Figure 2.2.
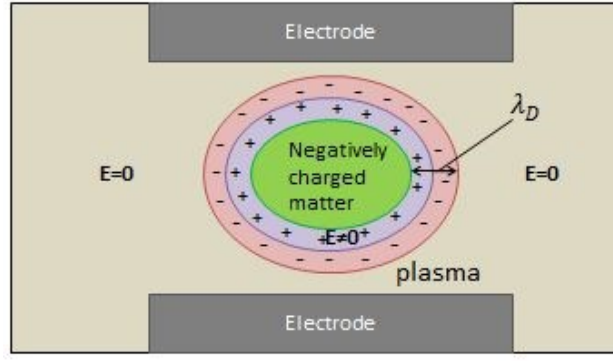
Figure 2.1 The Debye shielding and Debye length

2.2.4 Plasma Oscillation and Plasma Frequency

In plasma, there is a large collision rate between electron-electron pairs, ion-ion pairs, and electron-ion pairs. Therefore, plasma's equilibrium can be broken at any time, and this causes constant fluctuations in plasma. Charged particles begin to oscillate due to Coulomb forces. If a particle such as an electron has a density larger than the uniform point, it will return to its original position through Coulomb force, and then—due to its inertia—it is inclined to return to its equilibrium position and therefore will move by Coulomb force in the opposite direction. This plasma oscillation occurs frequently, and is defined with the plasma frequency ω_p that is given by:

$$\omega_p = \sqrt{\frac{ne^2}{\epsilon_0 m}} \tag{2.6}$$

The plasma frequency is given for typical laboratory plasma by $\omega_p = 1885$ MHz with $n = 10^{15}$ m^{-3}, for the microwave plasma by $\omega_p = 5642$ MHz with $n = 10^4$ m^{-3}, and for the ionosphere $\omega_p = 18.9$ MHz with $n = 10^{11}$ m^{-3}. Plasma oscillations include both electrons and ions, and are called plasma-electron oscillations and plasma-ion oscillations respectively. Since the mass of an electron is smaller than the mass of an ion, the frequency of plasma-electron oscillation is generally high. Fluctuations for density distribution are dependent on the Debye length, and the length of the oscillation generally parallels the range of the Debye length [77,78,80,82].

2.3 Nonthermal and Thermal Plasma

Electron energy $k_B T_e$ and electron density n_e play an important role in the characterization of plasma. Figure 2.2 illustrates electron densities and electron temperatures across many types of plasma. Thin films are generally produced at low pressures, around 10^{-3}-10 torr. In this kind of plasma, average electron energies and electron densities average 1-10 eV and 10^{16} m^{-3} respectively. Plasmas can be classified in two groups based on their local thermal equilibrium: nonthermal (cold) plasma and thermal plasma [77,78,80,82].
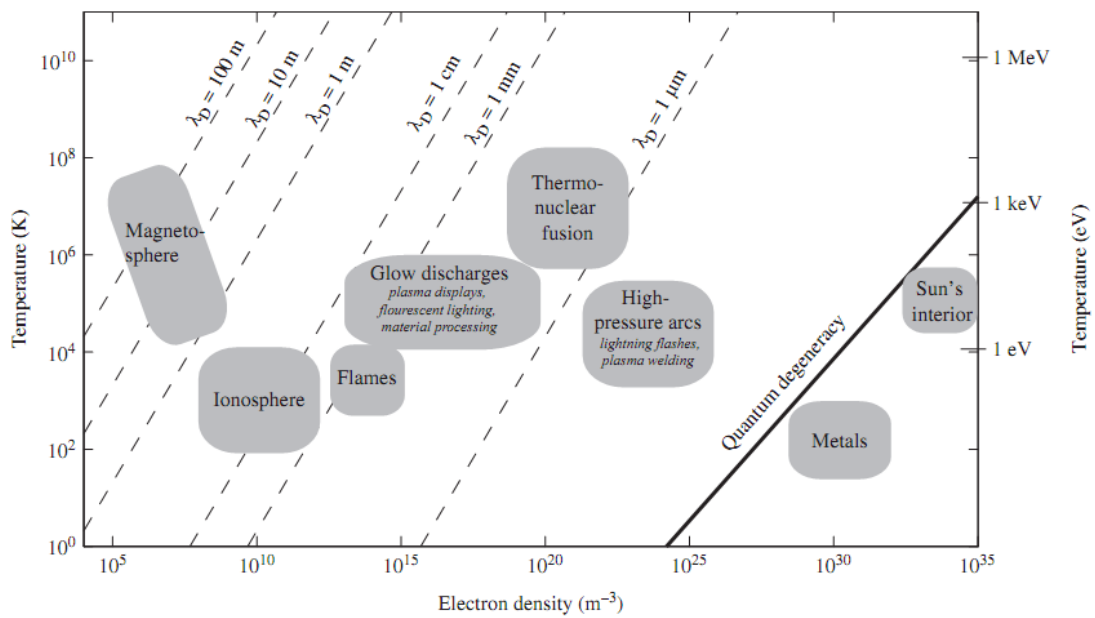
Figure 2.2 The classification of plasma phenomena in nature and in technological applications with respect to temperature, electron density, and Debye length [81]

When plasma is produced by a direct current (DC) glow discharge, a high frequency (HF) at low pressure, or a microwave (MW) discharge at low pressure, ionization will be in the order of 10^{-4}. This causes gas to contain more neutral particles than excited particles. In this case, a difference in thermal equilibrium manifests between the temperature of electrons and the temperature of gas. This plasma is referred to as nonequilibrium plasma. The electron temperature is higher than the gas temperature. Due to the low temperature of gas particles, collisions between electrons and gas particles occur infrequently. Plasma like this, in a state of thermal nonequilibrium, is referred to as nonthermal plasma.

15

$$T_e > T_{elect} > T_v \geq T_r > T_g \qquad (2.7)$$

Additionally, in nonthermal plasma, average electron energy is larger than that of atoms and ions. Plasma in a state of thermal nonequilibrium includes glow discharge, corona discharge and low pressure radio frequency discharge [76–78,80]. The thin film production is engaged in the nonthermal plasma where the energy distribution is usually defined by Maxwellian distribution instead of the Druyvesteyn distribution (which assumes that effects of inelastic collisions can be neglected, the velocity of the electrons does not affect the cross section of elastic collisions, and the mean-free path of electrons is like a function of electron energy) or the Maxwellian-Boltzmann distribution (in which the system is at thermal equilibrium, particle densities are homogenous, and there are no external forces) [50,77].

If the current is increased while generating a glow discharge, the voltage of the discharge decreases and the current density of the discharge increases. In this way, the transition from a plasma state to an arc discharge can be observed. Since the temperature of the cathode is high in arc discharges, an emission of thermal electrons will be generated from the cathode. In arc discharges, the energy distribution of electrons and gas particles will be almost identical to the energy distribution in the plasma. Therefore, collisions between electrons and gas molecules occur frequently, and the plasma reaches thermal equilibrium [76–78,80].

$$T_e \simeq T_g \qquad (2.8)$$

Thermal plasma, or hot plasma, is obtained through the presence of gas molecules at high temperatures in the plasma. High intensity arcs, plasma torches and high density discharges are examples of thermal plasma.

2.4 Collisions in Plasma

When electrons gain energy from electric fields in plasma, they collide with gas molecules. These collisions generate excitation and ionization of the gas molecules.

2.4.1 Elastic and Inelastic Collisions

Elastic collisions are defined as collisions without any change in internal energy, and inelastic collisions are defined as collisions with an exchange of internal energy

between particles. Inelastic collisions in plasma have a significant role in materials processing. As a result of these collisions, many species, such as an excited atom or molecule, radicals, a fragmented molecule, ionized particles, the generation of a negative ion, and radiation, occur in plasma [76,77,79]. In these collisions, the energy transfer coefficient is determined by the ratio of the transferred energy E_t to the initial kinetic energy E_i.

$$\frac{E_t}{E_i} = \frac{4mMCos^2\theta}{(m+M)^2}$$
(2.9)

where m and M are masses of colliding particles, and θ is the angle of collision.

2.4.2 Mean-Free Path and Reaction Cross Section

The mean-free path is the statistical average of the free path between the point of collision and the point of next collision.

$$\lambda = \frac{\bar{v}}{v_c}$$
(2.10)

where v_c is the collision frequency and the number of collisions per second is defined as $v_c = n_g \pi r_1^2 \bar{v}$. n_g is the density of a gas particle, $\bar{v}$ is the mean velocity of a particle, and r_1 is the radius of the particle.

$$\lambda_g = \frac{1}{\sqrt{2}\pi n d^2}, (d = 2r_1), \quad \lambda_g = \frac{kT}{\sqrt{2}\pi p d^2}, (p = nkT)$$
(2.11)

The cross section can be calculated from the change in intensity of the particle beam occurring in scattering while the particle passes through the target particles.

$$I(x) = I_0 e^{-\sigma n_2 x}$$
(2.12)

where I_0 is the intensity of an incident particle beam, n_2 is the density, and $I(x)$ is the intensity after diffusing through a distance x. For various kinds of inelastic collisions, the reaction cross sections that must be determined include the excitation cross section, the dissociation cross section, and the ionization cross section [77,82].

2.5 Excitation and Ionization

2.5.1 Internal Energy

Excitation indicates the transition of an atom or molecule's internal energy from a ground state to a higher state through an increase in translational energy. While excitation is described as a higher energy level for an atom, it is more accurately

understood as a change in the vibrational or rotational state of a molecule. Due to the short lifespan of a molecule's excited state, excited atoms continue to de-excite in a short time to a lower energy states, emitting light as they do so. Therefore, excited atoms are not involved in collisions and do not provide additional reactions in plasma unless they are metastable. In other words, atoms in a metastable state—the energy state in which optical transition is forbidden or the probability of transition is very small—lead to excitation and ionization of atoms and molecules in a plasma phase. Ionization is the reanimation of electrons from an atom or molecule by acquired energy, and the minimum required energy for ionization is known as the ionization energy [50,76,77]. Since electrons formed with ionization are again accelerated in an electric field and obtain ions from other atoms or molecules, ionization has a significant role in sustaining plasma. Ionization energy is defined in units of eV that are referred to as the ionization potential. Ionization potentials for molecules are listed in Table 2.1.

Table 2.1 The list of the first ionization potentials of molecules

Molecule	First ionization potential (eV)	Molecule	First ionization potential (eV)
H_2	15.42	CO_2	13.76
N_2	15.57	NO_2	9.78
O_2	12.06	N_2O	12.94
F_2	15.70	NH_3	10.19
Cl_2	11.48	CH_4	12.70
CO	14.01	C_2H_2	11.39
NO	9.25	C_2H_4	10.45
H_2O	12.61	C_2H_6	11.52

2.5.2 Excitation and Ionization Processes

The processes of excitation and ionization for an atom or a molecule are described by the following reactions:

    (1) Excitation and ionization by an electron collision

    (2) Excitation and ionization by an ion collision

    (3) Excitation and ionization by a neutral particle collision

    (4) Excitation and ionization by radiation (photo-excitation and -ionization)

(1) Excitation and Ionization by an Electron Collision

Electrons have a more significant effect on excitation and ionization. When the internal energy of collision is higher than the excitation energy, an atom can be shifted into the excited state by an electron. A positive ion is generally obtained by removing electrons from atoms or molecules. A negative ion is created through the attachment of electrons to atoms or molecules. When a neutral particle collides with an electron, ionization creates an electron, which contributes to further ionization by producing ions. Moreover, if an electron has the required energy, it is capable of removing an electron from a metastable atom and generating an ion with one extra electron [76–79].

(1) Excitation

$A + e \rightarrow A^* + e$ (electron impact excitation)

$AB + e \rightarrow AB^* + e$

(2) Dissociation
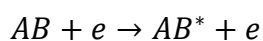
$AB + e \rightarrow A + B + e$ (electron impact dissociation)

(3) Direct ionization

$A + e \rightarrow A^+ + 2e$ (electron impact ionization)

$AB + e \rightarrow AB^+ + 2e$ (normal ionization)
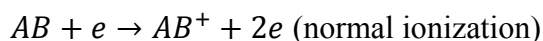
(4) Cumulative ionization

$A^* + e \rightarrow A^+ + 2e$ (electron metastable ionization)

$AB^* + e \rightarrow A^+ + B + 2e$
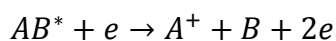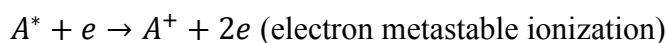
(5) Dissociative ionization

$AB + e \rightarrow A^+ + B + 2e$
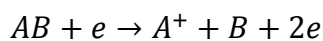
During excitation and ionization of an atom, the electronic excitation cross section determines the singlet-triplet and singlet-singlet transition according to the threshold energy value by increasing energy with electron impact. The ionization cross section and ionization potential also increase with an increase in electron energy. Voltage reaches its maximum value and then decreases slowly.

If excitation and ionization occur in a molecule, the rotational and vibrational excitation cross section increases linearly with increasing electron energy due to electron impact. For example, a H_2 molecule (a diatomic molecule) can be

dissociated through collision with an electron carrying an energy of more than 8.8 eV. In dissociation, two H atoms are produced. The energy of each atom will be equal to half of the difference between the electron impact dissociation energy and the thermal dissociation energy. The ion of a molecule is produced when the amount of the given energy is larger than the ionization potential. Since the energy levels of vibration and rotation change during ionization, the process of a molecule's ionization is more complicated than the process of an atom's ionization. Independent from the generated ions, total ionization cross sections can be found only through the total number of ions. Dissociation and ionization will continue if higher energy continues to be given to a molecule, and the dissociative ionization cross section will reach its maximum value, usually close to the value of the electron energy.

(2), (3) Excitation and Ionization by Collisions of Energetic Ions or Neutral Particles

It is also possible to obtain ions through collisions of neutral atoms and molecules. Neutral atoms and molecules are not affected by an electric field in cold plasma, and ions do not have sufficient kinetic energy to directly generate the ionization of other molecules directly. Therefore, the ionization of atoms or molecules is only possible through collisions with excited metastable particles with high internal energy [77–79].

(a) Thermal Ionization

Thermal ionization is produced through thermal movement of particles. This process is usually observed in arc plasmas or burning flames.

(b) Penning Ionization

Penning ionization results from collisions between metastable particles at excited states and neutral particles, but only when ionization energy is less than excitation energy. An excited atom or molecule generally results from a collision with an electron or the absorption of a phonon.

$$A + B^* \rightarrow A^+ + e + B \text{ (metastable neutral ionization)}$$

where B^* is the excited atom or molecule. Penning ionization is more common in the longer mean-free path or at pressures lower than 10 mtorr.

(c) Ionization by Collisions Among Excited Particles

This ionization is obtained by collisions of excited molecules and is more notable at lower electron temperatures.

$$A^* + B^* \rightarrow A^+ + e + B$$
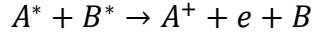
(4) *Photo-Excitation and Photo-Ionization*

If a gas is exposed to radiation through a light source, the gas molecule will become excited or ionized.

2.6 Recombination

2.6.1 Recombination Processes

According to the rule of conservation, charged particles will attempt to neutralize in the gas phase, combining a positive ion with an electron or a negative ion. This phenomena is called recombination, and it can be divided into two types: ion-electron and ion-ion recombination [77,79]. The recombination coefficient α can be expressed as

$$\frac{dn}{dt} = \frac{dn_+}{dt} = \frac{dn_-}{dt} = -\alpha n_+ n_- \tag{2.13}$$

where n_+ and n_- are the densities of positive and negative charges respectively.

2.6.2 Ion-Electron Recombination

The recombination processes between positive ion and electrons include:

(1) Radiative recombination

$$A^+ + e \rightarrow A^* + h\nu$$
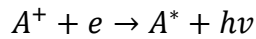
(2) Dielectronic recombination

$$A^+ + e \rightarrow A^{**}$$

$$A^{**} \rightarrow A^* + h\nu$$

$$A^{**} + B \rightarrow A^* + B^*$$
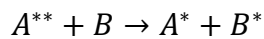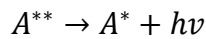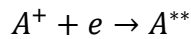
(3) Dissociative recombination

$$AB^+ + e \rightarrow A^* + B^*$$
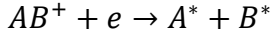
(4) Three-body recombination

$$A^+ + e + e \rightarrow A + e$$

$$A^+ + e + B \rightarrow A + B$$
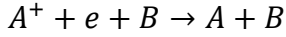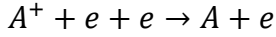
where A^* is the singly excited atom and A^{**} is the doubly excited atom.

In the process of combining electrons with ions (1), excited neutral atoms or molecules are generated, usually with photon radiation energy of $h\nu$. The recombination coefficient α is between 10^{-10} and 10^{-13} cm^3/s.

In the second process (2), a doubly excited atom is produced by combining an electron with a positive ion. Here, one electron bound to the ion jumps to a higher level by the excitation energy. Then, this doubly excited atom transfers to a singly excited atom by losing part of its energy. This energy can be referred to as the emission energy of a photon or as the exchanging energy of inelastic collision with another particle. The coefficient α is very small, lower than 10^{-12} cm^3/s.

In the third process (3), a molecular ion recombines with an electron. The molecular ion is first produced by an excited molecule, and then this molecule dissociates into excited atoms. The electron temperature is low and the coefficient α is large as 10^{-6}-10^{-8} cm^3/s.

In the fourth process (4), the third body can be an electron or an atom or a molecule. When the electron temperature and density are low, the coefficient α increases.

2.6.3 Ion-Ion Recombination

This recombination is generated between the combination of a positive ion and a negative ion. This process is common when negative ions are generated through electron attachment, such as O_2, Cl_2, and SO_2 [77–79].

(1) Radiative recombination

$$A^+ + B^- \rightarrow AB + h\nu$$
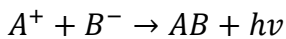
In radiative recombination, a positive ion combines with a negative ion, producing a neutral molecule by releasing a photon. The recombination coefficient is very small, about 10^{-14} cm^3/s.

(2) Mutual neutralization

$$A^+ + B^- \rightarrow A^* + B^*$$
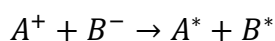
In this process, excited atoms or molecules are produced by the recombination of a positive ion and a negative ion. The coefficient is in the range of 10^{-8}-10^{-7} cm^3/s at room temperature.

(3) Three-body recombination

$$A^+ + B^- + M \rightarrow AB + M$$
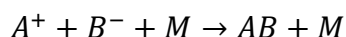
The recombination coefficient changes between 10^{-7} and 10^{-6} cm^3/s at room temperature.

2.7 Ion-Molecule Reactions and Reactions Concerned with Negative Ions

2.7.1 Attachment and Detachment

When a neutral gas molecule captures an electron, a negative ion is produced.. This process is called attachment. The inverse process, when a negative ion releases an electron, is called detachment. Attachment processes can be classified in the following steps [77–79]:

(1) Radiative attachment

$$A + e \rightarrow A^- + hv$$
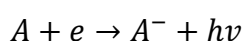
(2) Three-body attachment

$$A + e + M \rightarrow A^- + M$$
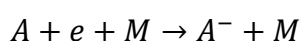
(3) Collisional attachment

$$AB + e \rightarrow AB^{-*} \rightarrow AB^-$$

(4) Dissociative attachment

$$AB + e \rightarrow AB^{-*} \rightarrow A + B^-$$
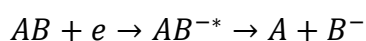
(5) Dielectronic attachment

$$A + e \rightarrow A^{-**} \rightarrow A^- + hv$$
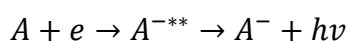
(6) Electron transfer

$$A + B \rightarrow A^+ + B^-$$
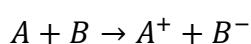
(7) Ion pair production

$$A + B + e \rightarrow A^+ + B^- + e$$
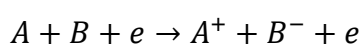
The processes of detachment are as follows:

(1) Associative detachment

$$A^- + B \rightarrow AB + e$$
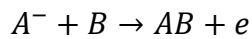
(2) Photo-detachment

$$A^- + hv \rightarrow A + e$$
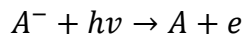
(3) Collisional detachment

$$AB^- + M \rightarrow AB + e + M$$

$$A^- + e \rightarrow A + 2e$$

$$A^- + B^* \rightarrow A + B + e$$

$$A^+ + B^- \rightarrow A^+ + B + e$$

$$A^- + B^- \rightarrow A + B^- + e$$
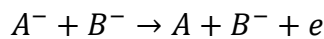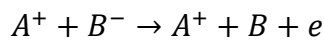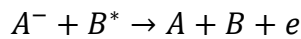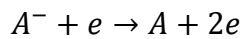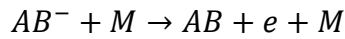
(4) Dissociative photo-detachment

$$AB^- + hv \rightarrow A + B + e$$
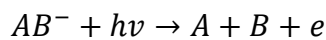
The possibility of forming a negative ion is proportional to the electron affinity.

2.7.2 Ion-Molecule Reaction

This reaction is defined as an ion reacting with a neutral atom or a molecule. Although there are combinations and charge transferring, the system becomes electrically neutral [71]. The ion-molecular reaction can be classified in the following steps:

(1) Charge transfer

$$A^+ + B \rightarrow A + B^+$$

(2) Clustering

$$A^+ + B + M \rightarrow AB^+ + M$$
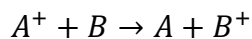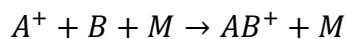
(3) Ion-atom interchange

$$A^+ + BC \rightarrow AB^+ + C$$

(4) Switching

$$AB^+ + C \rightarrow A + BC^+$$
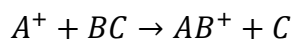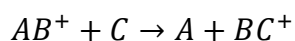
(5) Photodissociation

$$AB^+ + hv \rightarrow A^+ + B$$
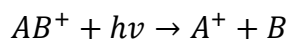
2.8 Method of Plasma Polymerization

As mentioned above in section 2.2, an electric field is formed by applying power to the electrodes, and electron transfer begins to generate plasma discharge. As a result of inelastic collisions between electrons and atoms or molecules, and according to the law of the conservation of momentum, the electrons transfer all their energy to the atoms or molecules and this leads to ionization. Then, the secondary electrons are generated in the cathode through the bombardment of positive ions. If an organic compound or a monomer is included in the plasma reactor, this compound or monomer will be activated by the energy from inelastic collisions and then will fragment into to small molecules. Since small fragments are generally prone to be generated in a larger compound, activated small molecules begin to recombine when they gain sufficient energy from reactions in the plasma. All of these interactions cause plasma diffusion on the substrate and the polymer thin film is deposited on the surface of the substrate as well as on the wall of the reactor. During deposition, recombination can also be observed on the surface, and irradiation continues until the polymerization process is complete. The generation of plasma polymer is simply diagramed in Figure 2.3.

$$A\text{-}B\text{-}C\text{-}D\text{-}E\text{-}F \xrightarrow{\text{Plasma}} \left[A\text{-}B\text{-}C\text{-}D\text{-}E\text{-}F \right]^* \xrightarrow{\text{Fragmentation}}$$

Starting molecule   Activation by plasma

$$\left\{ \begin{array}{ccc} A\cdot & \cdot E\text{-}F & \cdot D\cdot \\ \cdot C\cdot & A\text{-}B\cdot & \cdot F \\ \cdot E\cdot & \cdot B\cdot & \cdot C\text{-}D\cdot \end{array} \right\} \xrightarrow{\text{Rearrangement}} A\text{-}D\text{-}B\text{-}E\text{-}C\text{-}D\text{-}B\text{-}E\text{-}F$$

Fragments in Plasma State   Plasma polymer
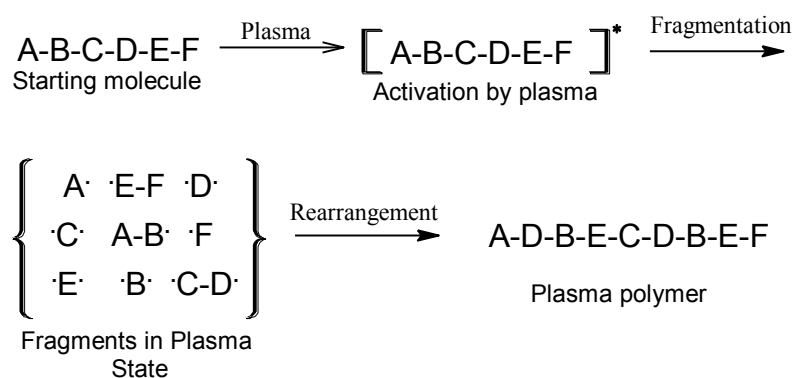
Figure 2.3 The diagram of reaction steps in the plasma polymerization

As the diagram suggests, after the original molecule is fragmented into atoms and these activated fragments are recombined into larger molecules, plasma polymer is formed through different chains from the original molecule. Therefore, it is not possible to predict the chemical structure of the formed polymer from the structure of the starting molecule.

According to D`Agostino [83], plasma polymerization can be divided into two types of reactions: plasma-induced polymerization and plasma-state polymerization. Plasma-induced polymerization is radical polymerization, which means reactions are generated by the radical species at the ends of the polymer chains and that the polymerized molecules have unsaturated carbon-carbon bonds. This polymerization is also referred to as conventional free-radical-induced polymerization. Free radical reactions generally become dominant in the formation of decompound products of plasma deposition. Plasma-state polymerization, the main process of plasma polymerization, is a type of ionic polymerization controlled by the presence of electrons and other energetic species. The radicals and ions in the polymerization generate polymer chains different than the polymer chains generated in conventional polymerizations. Therefore, the plasma polymerization is chemically different from conventional polymerizations, even if the same monomer is used in both processes [50,57,84].
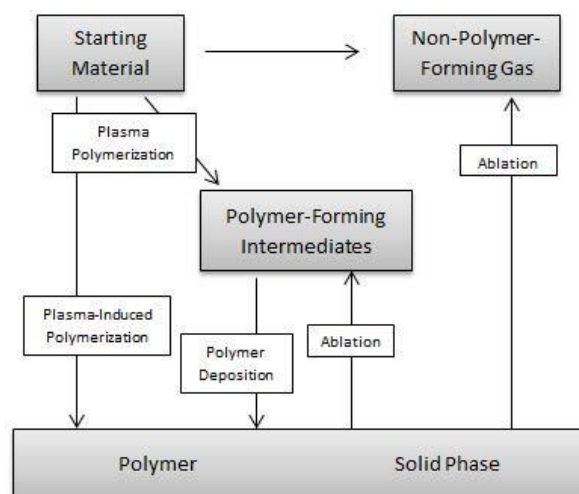
Figure 2.4 The pattern of the plasma polymerization process

Reactions occurring in plasma polymerization can outlined in five steps, as shown in Figure 2.4: (i) ionization and fragmentation of the starting material [85], (ii) diffusion of the reactive species on the surface, (iii) interaction and/or deposition at the surface, (iv) ablation and desorption [86], and (v) the generation of a new monomer [87–90].

26

Since reactions in plasma are highly complex and no equilibrium exists in plasma, it is difficult to predict the products that will result from reactions. To better understand reactions, plasma chemistry is interpreted in three main ways: plasma chemistry, chemical reactions coming from the deposited materials, and reactions of surface modification. Plasma chemistry is controlled by plasma species such as electrons, ions, radicals, etc. From these species, the radicals and the ions (especially the ions) have a crucial impact on the formation of chemical reactions and the structure of the deposited plasma polymer. The chemical reactions of plasma deposition was illustrated by Friedrich [71] in a diagram, including energy distribution in collisions and radiation occurring during polymerization (Figure 2.5).
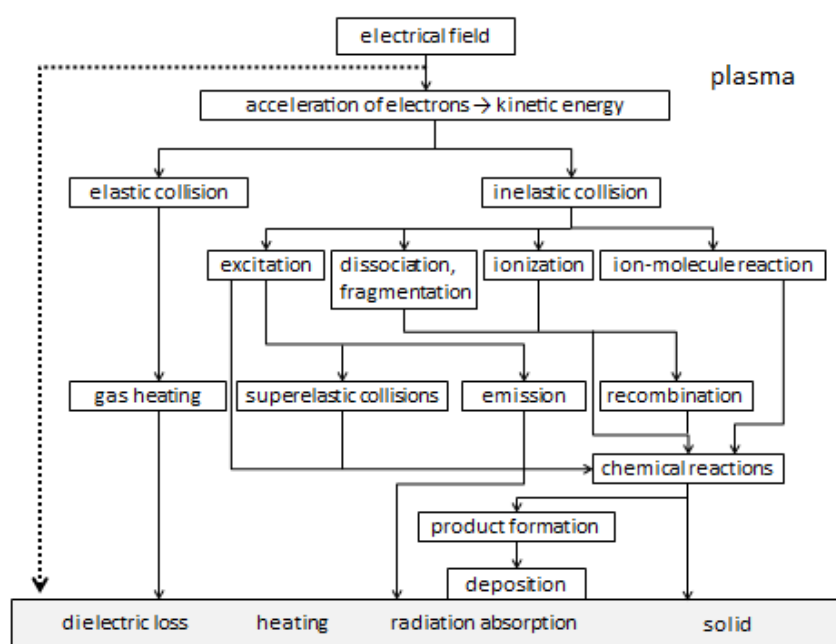
Figure 2.5 The energy distribution to collision and radiation processes during the plasma polymerization [71]

The physical and chemical properties of plasma polymer films, as well as the deposition rate, depend on parameters such as rate of gas flow, power and frequency, pressure, substrate temperature and position, and reactor type. Increasing the rate of gas flow while keeping other parameters constant leads to an increase in the deposition rate by feeding the plasma with fresh gas until it reaches the balance point, a term for the maximum deposition rate. If the flow rate continues to increase,

the deposition rate will decrease. This is because the duration, which is necessary for the flowing gas to sufficiently stay in the reactions, decreases and this reduces the number of activated species reaching the substrate [42]. In addition, the comparatively unsaturated bonds of flowing gas lead to an increase in the deposition rate [37,91,92]. Since the densities of energetic ions and electrons are controlled by the applied power, increasing the power leads to an increase in these densities and thus also increases the deposition rate [42] when other parameters are held constant. Although the deposition rate first increases with a raise in power, this increase is not continuous and the power does not affect the deposition rate at higher values. The pressure of the plasma reactor affects the residence time of the feed gas, the average electron energy, and the mean free path of the polymerization. All of these parameters increase with raised pressure. Therefore, it might be assumed that it would be more effective to work at high pressures to easily obtain plasma polymerization. However, increasing the pressure also causes an increase in the inhomogeneity of film distribution during polymerization. Therefore, deposition pressure should be kept at a point which produces a greater rate of homogeneity and meets the requirements of long residence time, low free path, and sufficient electron energy, keeping other plasma parameters constant [42,44,57,71,84]. The substrate temperature decreases the deposition rate by increasing the temperature [91,92]. In addition, the design of plasma reactors has an important role in chemistry since the distribution of plasma species changes with different geometries and fabrication materials.

While a polymer occurs in the conventional process from a repetition of covalently bonded units, a polymer in the plasma polymerization process arises from infinitely distinctive units connected by covalent chemical bonds. Repetitions in the plasma polymer are determined by functional groups placed randomly through the structure and covalently connected with hydrocarbon chains of different lengths. The conditions in the process and fragmentation of the monomer impact the structure and compound. During plasma polymerization, as a result of the fragmentation of molecules and recombination of the fragments, the emerging polymers exhibit cross-linking structures. The intensity of the functional groups is inversely proportional to the density of the cross-linking structures. In other words, the repetition of the functional groups decreases as the density of the cross-link increases in direct

proportion to the fragmentation of the monomer. Thus, the abundance of cross-links in the polymer network can be used to characterize the structure of the plasma polymer. Moreover, this high degree of crosslinking generally make plasma polymer films insoluble in organic solvents [84].

Radicals play a significant role in the initiation and control of polymerization. Radicals can be formed in a gas phase and at the surface of the substrate. Radical reactions can be classified into four steps: initiation, propagation, termination, and re-initiation. These steps are schematically represented below, where X is the monomer or polymer segment, R_n is a radical of n unit, and S is a surface site. The formed plasma polymer segments, referred to as X_{n+m} and S-X_{n+m}, are reactivated during polymerization, providing a new initiation of polymerization. The re-initiation of the polymerization is the main cause of the highly branched and highly cross-linked structure of plasma-polymerized compounds.

Initiation:
$$C_2H_2 + H\cdot + X \rightarrow R_n^{\cdot} + X$$
$$(S - X) + e \rightarrow (S - R_n^{\cdot}) + H\cdot$$

Propagation:
$$R_n^{\cdot} + C_2H_4 \rightarrow R_{n+1}^{\cdot}$$
$$(S - R_n^{\cdot}) + C_2H_2 \rightarrow (S - R_{n+1}^{\cdot})$$

Termination:
$$R_n^{\cdot} + R_m^{\cdot} \rightarrow X_{n+m}$$
$$(S - R_n^{\cdot}) + R_m^{\cdot} \rightarrow (S - X_{n+m})$$
$$(S - R_n^{\cdot}) + (S - R_m^{\cdot}) \rightarrow (S - X_{n+m}) + S$$

Re-initiation:
$$X_n + e \rightarrow R_n^{\cdot} + H\cdot + e$$
$$X_{n+m} + e \rightarrow R_n^{\cdot} + R_m^{\cdot} + e$$
$$(S - X_n) + e \rightarrow (S - R_n^{\cdot}) + H\cdot + e$$

In the process, if radicals are formed by an opening of a double or a triple bond, it causes the pressure of a plasma reactor to decrease during polymerization because there is no change in the total number of molecules when hydrogen is not produced. However, if the radicals are produced as a result of hydrogen detachment, the

pressure does not change since equilibrium is maintained between loss of an organic compound and hydrogen production. Moreover, when the cleavage of a C-C bond becomes a cyclic compound, this contributes to polymerization and decreases the pressure, unlike what happens with a noncyclic compound [50,83].

The products produced by this process exhibit different chemical structures and physical properties than those produced by conventional processes. While the structure of conventional polymer is characterized by chains with a regularly repeated unit, the structure of plasma polymer is not. Instead, it exhibits a structure with irregular crosslinking chains in three dimensions. Plasma polymer thin films generally have thermal and chemical stability, mechanical toughness, and indissolubility. The most noteworthy feature of plasma polymerization is the chance to produce a polymer thin film from almost any organic vapor [57]. In other words, a wide range of monomers can be used in plasma polymerization, and there is virtually no limitation in the deposition of these materials. In plasma deposition, a coating with a thicknesses of tens of nanometers of material can be obtained in only one or two depositions [93], making it more suitable for samples of membranes, semiconductors, metals, textiles or polymers [71]. This makes plasma deposition more economical and efficient. Besides being used for a wide range of samples, plasma polymer thin films have been used in areas including protective coatings for industry, electrical applications, optical applications, and biomedical applications [45,84,94,95]. Surfaces of plasma polymer films generally exhibit hydrophobic properties [83]. As compared to conventional methods, understanding the reaction mechanism of the plasma polymerization method in the radical and ionic sense is complicated. In plasma polymerization, the chemical structure of the generated polymer is never predicted from the structure of the starting molecule due to the high degree of fragmentation and rearrangement in the plasma. Activation and fragmentation of the starting molecule is controlled by the plasma conditions and the nature of the molecule. Therefore, the plasma polymer is obtained with different chemical compositions at different conditions, including power, monomer flow rate, and pressure [57,68,96–101]. The plasma polymerization technique has remarkable potential for the improvement of materials and opens the door to the development of new materials in almost all technologies.

2.9 Comparison to the Plasma Polymerization Method to Other Methods of Producing Polymer Thin Films

The production of polymeric thin films employs two main methods: the wet processing (conventional) method and the dry processing method. In the wetting processes, materials are used in liquid form and then a coating is obtained from a solvent in solid form through evaporation, spinning, painting, curing, electroplating, chemical reduction deposition, baking, or cooling, etc. Evaporation is a process in which a substance in a liquid state transitions into a vapor or gaseous state. In this process, atoms or molecules in the liquid state transfer to the vapor state as they accumulate sufficient energy under a high temperature. The atoms or molecules in the vapor state diffuse onto the surface of the substrate and are coated. Conventional brush painting and dip coating require immersing an object in a liquid under controlled conditions, such as exposure time and temperature. In the process of spin coating, a solution is put onto a sample and then the sample is rotated at a high speed. The fluid is spread across the surface of the sample by the rotation and thickness can be controlled by rotation time. Spin coating is widely used to obtain a uniform thin film on flat samples with thicknesses below 10 nm. Another chemical process used for coating is the hydrophilic method, also known as the Langmuir Blodgett method. To obtain thin films, a sample is first immersed in water, a low-chain fatty acid is spread on the water's surface, and then the sample is withdrawn through the compressed layer of fatty acid. Electroplating is the deposition on the cathode obtained from metallic ions emerging from the electrolyte. Electrodeless plating does not require external voltage or a source for a current. Instead, the chemical reduction of a material is used. Displacement plating involves a deposition created by the electronegativity difference between the ions and the surface. Here, ions are placed in a solution and this solution is then spread on the surface. In chemical reduction deposition, thin films are generated by inserting substrates into chemical solutions [102–104].

Dry processing methods include physical vapor deposition (PVD), ion plating, chemical vapor deposition (CVD), plasma enhanced chemical vapor deposition (PECVD), and plasma polymerization. Physical vapor deposition (PVD) processes are also known as atomistic deposition processes. In these processes, vaporized solid or liquid materials are sent through a vacuum or plasma environment and begin to

diffuse on the substrate. The range in thickness of deposited films with PVD processes varies from a few nanometers to thousands of nanometers. This process can also be used to obtain coatings with multiple layers, depth, and graded configurations. The substrates can be deposited in a wide range of shapes, ranging from flat shapes to different geometries. PVD processes include vacuum evaporation or deposition, sputter deposition, arc vapor deposition, and ion plating. The materials are thermally vaporized in the vacuum deposition and vaporization is very high in comparison to other processes. Non-thermal vaporization is generated by physical sputtering in sputtering deposition. With the ion bombardment of a target by an ion gun, deposition is formed on the substrate. In arc vapor deposition, a high current of low voltage is used to vaporize materials from a cathodic or anodic electrode. Ion plating is also known as ion-assisted deposition (IAD), ion vapor deposition (IVD), or ion beam-assisted deposition (IBAD). Bombardment of energetic particles (generally ions) is used to improve the features of deposited films. Vaporization can be obtained through evaporation, sputtering, or a chemical vapor. Chemical vapor deposition (CVD) is the deposition of solid materials through the decomposition of a chemical vapor of a thermally generated precursor species. Deposition generally arises from the reaction of volatile products and precursor species. When plasma is used for the decomposition of the precursor species, the process is called plasma-enhanced chemical vapor deposition (PECVD) or plasma-assisted chemical vapor deposition (PACVD). An rf generator is used to produce the plasma, providing deposition at lower temperatures in comparison with thermal CVD process. This deposition is commonly used in the semiconductor industry [77,80,105–108]. In the recent years, several studies have focused on deposition technology generated under atmospheric pressure [109]. This deposition process is called atmospheric pressure plasma enhanced (or assisted) chemical vapor deposition. As opposed to the vacuum systems, there is no need to use complex plasma chambers with costly combinations such as a pump, valve, etc. Control of the plasma parameters in this process is far simpler than in the other processes.

It is possible to use a PECVD process to deposit polymer films by using an organic or inorganic monomer like a precursor vapor. This process is known as plasma polymerization, which is explained in detail in section 2.8. This novel method improves the performance and properties of thin film structures, producing

characteristics not attainable by conventional methods. Polymer films deposited by plasma polymerization become crosslinked and exhibit several remarkable properties including desirable surface coating and very low porosity. This method can be used to obtain an excellent insulating film. As compared to conventional methods, there are several advantages to the plasma polymerization process. This process is more economical and efficient with a wide range of monomers. It is possible to select any starting feed gas, which allows for a selection between different types of functional groups. In conventional polymerization, gases have to belong to a similar functional group. Plasma polymerized films generally have high coherence and adherence, and they can be coated onto almost any type of substrate, including metal, glass, conventional polymer, wafers, etc. Unlike the conventional processes, no solvents are used in plasma deposition. The plasma process makes it possible to easily obtain polymer thin films with thicknesses ranging from 10 nm to 1 μm. Pinhole-free thin films can also be produced, and with a good control of plasma parameters, ultrathin films can be obtained through the plasma polymerization process. Plasma polymerization techniques have remarkable potential to supply the necessary materials for almost all technologies [47,57,58,68,71,84,96–101].

2.10 References

[1]   M.P. v Wilde, Berichte Dtsch. Chem. Ges. 7 (1874) 352.

[2]   A. Thenard, C.R. Hebd, Seances Acad. Sci. 78 (1874) 219.

[3]   O. Eisenhut, R. Conrad, Z. Elektrochem. 36 (1930) 654.

[4]   W.B. Harkins, Trans. Faraday Soc. 30 (1934) 221.

[5]   W.B. Harkins, J.M. Lackson, J. Chem. Phys. 1 (1933) 37.

[6]   R. Conrad, Trans. Faraday Soc. 30 (1934) 215.

[7]   A. Heisen, Analen Der Phys. 2 (1958) 23.

[8]   H. Schmellenmeier, Exp. Tech. Phys. 1 (1953) 49.

[9]   H. König, G. Helwig, Z. Phys. 129 (1951) 491.

[10]   A. Brockes, H. König, Z. Phys. 152 (1958) 75.

[11]   H. Pagnia, Prog. Colloid Polym. Sci. 78 (1988) 143.

[12]   J. Goodman, J. Polym. Sci. 44 (1960) 551.

[13]   A.P. Bradley, J.P. Hammes, J. Electrochem. Soc. 110 (1963) 15.

[14]   G. Mollenstedt, R. Speidel, Z. Angew. Phys. 13 (1961) 231.

[15]   M. Stuart, Proc. Inst. Electr. Eng. 112 (1965) 1614.

[16]   M. Stuart, Nature 199 (1963) 59.

[17]   N.M. Bashara, C.T. Doty, J. Appl. Phys. 35 (1964) 3498.

[18]   A.P. Bradley, Ind. Eng. Chem. Prod. Res. Dev. 9 (1970) 101.

[19]   A.P. Bradley, Trans. Faraday Soc. 61 (1965) 773.

[20]   T. Williams, M.W. Hayes, Nature 209 (1966) 769.

[21]   L. V Gregor, Thin Solid Films 2 (1968) 235.

[22]   T. Hirai, O. Nakada, Jpn. J. Appl. Phys. 7 (1968) 112.

[23]   I. Haller, D. White, J. Phys. Chem. 67 (1963) 1748.

[24]   A.R. Westwood, Eur. Polym. J. 7 (1971) 363.

[25]   L.F. Thompson, K.G. Mayhan, D. Chemistry, J. Appl. Polym. Sci. 16 (1972) 2291.

[26]   A.R. Denaro, P.A. Dwens, A. Crawshaw, Eur. Polym. J. 4 (1968) 93.

[27]   A.R. Denaro, P.A. Dwens, A. Crawshaw, Eur. Polym. J. 5 (1969) 471.

[28]   H. Kobayashi, A.T. Bell, M. Shen, J. Appl. Polym. Sci. 17 (1973) 885.

[29] H. Kobayashi, A.T. Bell, M. Shen, Macromolecules 7 (1974) 277.

[30] A.M. Mearns, Thin Solid Films 3 (1969) 201.

[31] L. V Gregor, IBM J. 12 (1968) 140.

[32] C. Hogarth, T. Igbal, Phys. Status Solidi A 65 (1981) 11.

[33] H.R. Koenig, L.I. Maissel, IBM J. Res. Dev. 14 (1970) 168.

[34] J. Coburn, E. Kay, J. Appl. Phys. 43 (1972) 4965.

[35] M. Duval, A. Théorêt, J. Appl. Polym. Sci. 17 (1973) 527.

[36] J.M. Tibbitt, R. Jensen, A.T. Bell, M. Shen, Macromol. Res. 10 (1977) 647.

[37] H. Yasuda, J. Polym. Sci. Macromol. Rev. 16 (1981) 199.

[38] H. Yasuda, in:, J. V Vossen, W. Kern (Eds.), Thin Film Process., Academic Press, New York, 1978, p. 361.

[39] M. Shen, T. Bell, ACS Symp. 108 (1979) 1.

[40] A.T. Bell, in:, V. S, M. Venugopalan (Eds.), Curr. Chem. Vol. 94, Plasma Chem., Springer-Verlag, Berlin, Heidelberg, New York, 1980, p. 43.

[41] H. Yasuda, M. Gazicky, Plasma Chem. Plasma Process. 3 (1983) 279.

[42] H. Biederman, Vacuum 37 (1987) 367.

[43] Y. Osada, H. Biederman, Adv. Polym. Sci. 95 (1990) 57.

[44] N. Morosoff, in:, R. D'Agostino (Ed.), Plasma Depos. Treat. Etch. Polym., Academic Press, Boston, 1990, pp. 1–93.

[45] F.F. Shi, J. Macromol. Sci. Part C Polym. 36 (1996) 795.

[46] P. Favia, R. D'Agostino, Surf. Coatings Technol. 98 (1998) 1102.

[47] H. Biederman, D. Slavínská, Surf. Coatings Technol. 125 (2000) 371.

[48] E.E. Johnston, B.D. Ratner, J. Electron. Spectrosc. Relat. Phenom. 81 (1996) 303.

[49] H. Yasuda, Plasma Polymerization, Academic Press, Orlando, 1985.

[50] N. Inagaki, Plasma Surface Modification and Plasma Polymerization, Technomic Publishing, Pennsylvania, USA, 1996.

[51] H. Biederman, Y. Osada, Plasma Polymerization Processes, Elsevier, Amsterdam, 1992.

[52] H. Yasuda, J. Memb. Sci. 18 (1984) 273.

[53] N. Inagaki, N. Kobayashi, M. Matsushima, J. Memb. Sci. 38 (1988) 85.

[54] L. Agres, Y. Segui, R. Delsol, P. Raynaud, J. Appl. Polym. Sci. 61 (1996) 2015.

[55] F. Fracassi, R. d'Agostino, P. Favia, M. van Sambeck, Plasma Sources Sci. Technol. 2 (1993) 106.

[56] H. Grunwald, M. Jung, R. Kukla, R. Adam, J. Krempel-Hesse, in:, K.L. Mittal (Ed.), VSP, Utrecht, 1998.

[57] A. Hiratsuka, I. Karube, Electroanalysis 12 (2000) 695.

[58] L. Martinu, D. Poitras, J. Vac. Sci. Technol. A 18 (2000) 2619.

[59] I.-S. Bae, S.-H. Cho, S.-B. Lee, Y. Kim, J.-H. Boo, Surf. Coatings Technol. 193 (2005) 142.

[60] I.-S. Bae, S.-J. Cho, W.S. Choi, H.J. Cho, B. Hong, H.-D. Jeong, J.-H. Boo, Prog. Org. Coatings 61 (2008) 245.

[61] S. Cho, I. Bae, J. Boo, J. Korean Phys. Soc. 53 (2008) 1634.

[62] C. Sang-Jin, B. In-Seob, B. Jin-Hyo, L. Sungwoo, J. Donggeun, J. Korean Phys. Soc. 55 (2009) 1780.

[63] S.-J. Cho, I.-S. Bae, Y.S. Park, B. Hong, W. Park, S.C. Park, J.-H. Boo, Surf. Coatings Technol. 202 (2008) 5654.

[64] I.-S. Bae, S.-J. Cho, S.-H. Jeong, H.J. Cho, B. Hong, J.-H. Boo, Plasma Process. Polym. 4 (2007) S812.

[65] I.S. Bae, S.J. Cho, W.S. Choi, B.Y. Hong, Y.J. Kim, Y.M. Kim, J.H. Boo, Thin Solid Films 516 (2008) 3577.

[66] R. Förch, A.N. Chifen, A. Bousquet, H.L. Khor, M. Jungblut, L.Q. Chu, Z. Zhang, I. Osey-Mensah, E.K. Sinner, W. Knoll, Chem. Vap. Depos. 13 (2007) 280.

[67] K. Vasilev, S.S. Griesser, H.J. Griesser, Plasma Process. Polym. 8 (2011) 1010.

[68] K.S. Siow, L. Britcher, S. Kumar, H.J. Griesser, Plasma Process. Polym. 3 (2006) 392.

[69] K.S. Siow, S. Kumar, H.J. Griesser, Plasma Process. Polym. 12 (2015) 8.

[70] T. Jacobs, R. Morent, N. De Geyter, P. Dubruel, C. Leys, Plasma Chem. Plasma Process. 32 (2012) 1039.

[71] J. Friedrich, Plasma Process. Polym. 8 (2011) 783.

[72] J. Ren, M. Yao, W. Yang, Y. Li, J. Gao, Cent. Eur. J. Chem. 12 (2014) 1213.

[73] O. Kylián, a. Choukourov, H. Biederman, Thin Solid Films 548 (2013) 1.

[74] Z. Jiang, Z.-J. Jiang, J. Memb. Sci. 456 (2014) 85.

[75] W. Crookes, Philos. Trans. R. Soc. London 170 (1879) 641.

[76] K.S. Sree Harsha, Principles of Vapor Deposition of Thin Films, Elsevier Science, 2006.

[77] M. Konuma, Plasma Techniques for Film Deposition, Alpha Science, Harrow, UK, 2005.

[78] A. Fridman, L.A. Kennedy, Plasma Physics and Engineering, CRC Press, Boca Raton, FL, 2010.

[79] M.A. Lieberman, A.J. Lichtenberg, Principles of Plasma Discharges and Materials Processing, 2nd Editio, John Wiley & Sons, Inc., New Jersey, USA, 2005.

[80] A. Grill, Cold Plasma in Materials Fabrications, IEEE Press, New York, 1993.

[81] U.S. Inan, M. Golkowski, Principles of Plasma Physics for Engineers and Scientists, Cambridge University Press, Cambridge, UK, 2011.

[82] M. Keidar, I.I. Beilis, Plasma Engineering Applications from Aerospace to Bio- and Nanotechnology, Academic Press, 2013.

[83] R. D'agostino, Plasma Deposition, Treatment, and Etching of Polymers, Academic Press, Inc., 1990.

[84] F.F. Shi, Surf. Coatings Technol. 82 (1996) 1.

[85] H. Yasuda, Q.S. Yu, Plasma Chem. Plasma Process. 24 (2004) 325.

[86] H. Yasuda, T. Yasuda, J. Polym. Sci. Part A Polym. Chem. 38 (2000) 943.

[87] W. Knoll, R.C. Advincula, Functional Polymer Films Volume 1: Preparation and Patterning, Wiley-VCH Verlag GmbH, 2011.

[88] D. Hegemann, U. Schütz, A. Fischer, Surf. Coatings Technol. 200 (2005) 458.

[89] D. Hegemann, M.M. Hossain, E. Körner, D.J. Balazs, Plasma Process. Polym. 4 (2007) 229.

[90] E. Stoffels, W.W. Stoffels, G.M.W. Kroesen, Plasma Sources Sci. Technol. 10 (2001) 311.

[91] R. d'Agostino, F. Cramarossa, F. Fracassi, E. De Simoni, L. Sabbatini, P.G. Zambonin, G. Colaprico, Thin Solid Films 143 (1986) 163.

[92] R. d'Agostino, F. Cramarossa, F. Illuzi, J. Appl. Phys. 61 (1987) 2754.

[93] J. Zhang, W. van Ooij, P. France, S. Datta, A. Radomyselskiy, H.Q. Xie, Thin Solid Films 390 (2001) 123.

[94] S. Morita, S. Hattori, in:, R. d'Agostino (Ed.), Plasma Depos. Treat. Etch. Polym., Academic Press, 1990.

[95] Y. Kagami, T. Yamauchi, Y. Osada, J. Appl. Phys. 68 (1990) 610.

[96] J. Carpentier, G. Grundmeier, Surf. Coatings Technol. 192 (2005) 189.

[97] N.K. Dutta, N.D. Tran, N.R. Choudhury, J. Polym. Sci. Part B Polym. Phys. 43 (2005) 1392.

[98] G. Grundmeier, P. Thiemann, J. Carpentier, N. Shirtcliffe, M. Stratmann, Thin Solid Films 446 (2004) 61.

[99] J. Zhang, X.F. Feng, H.K. Xie, Y.C. Shi, T.S. Pu, Y. Guo, Thin Solid Films 435 (2003) 108.

[100] J. Cho, F.S. Denes, Chem. Mater. 18 (2006) 2989.

[101] C. Oehr, Nucl. Instruments Methods Phys. Res. B 208 (2003) 40.

[102] P.M. Martin, Hanbook of Deposition Technologies for Films and Coatings, Elsevier, 2010.

[103] R. Glang, L.I. Maissel, Handbook of Thin Film Technology, McGraw-Hill Companies, 1995.

[104] R.F. Bunshah, Handbook of Deposition Technologies for Films and Coatings: Science, Technology and Applications, Noyes Publications, 1994.

[105] H. Biederman, Plasma Polymer Films, Imperial College Press, London, 2004.

[106] S.M. Rossnagel, J.J. Cuomo, W.D. Westwood, Handbook of Plasma Processing Technology, Noyes Publications, New York, 1990.

[107] D.M. Mattox, Handbook of Physical Vapor Deposition (PVD) Processing, Second Edi, Elsevier, 2010.

[108] H. Usui, in:, Funct. Polym. Film. Vol. 1 Prep. Patterning, Wiley-VCH Verlag GmbH, 2011, p. 287.

[109] D. Merche, N. Vandencasteele, F. Reniers, Thin Solid Films 520 (2012) 4219.

CHAPTER 3

PLASMA DIAGNOSTICS

3.1 Direct Current (DC) Plasma Discharge

3.1.1 Glow Discharges

If the required voltage is applied to an electrode gap including a gas, breakdown will take place in the gap and the gas will function as a conductor. The first state between the electrodes after the breakdown is known as the gas or glow discharge. Glow discharge is a continuous discharge from electrons, coming from cathode. The secondary electron generation occurs as a result of the ions' effect on the surfaces [1,2].

3.1.2 DC Breakdown

When a dc power supply with voltage V_{ps} is applied between two electrodes, which are connected with a ballast resistor R, the voltage of the discharge will be $V=V_{ps}$ since the neutral gas will have a larger resistance than R. If even one free electron is generated near the cathode, it will accelerate through the electric field to the anode. Ionization then begins as a result of the increase in the energy of an electron within the electric field.

3.1.3 DC Glow Discharge

The dc glow discharge is composed of several distinct layers, as shown in Figure 3.1.
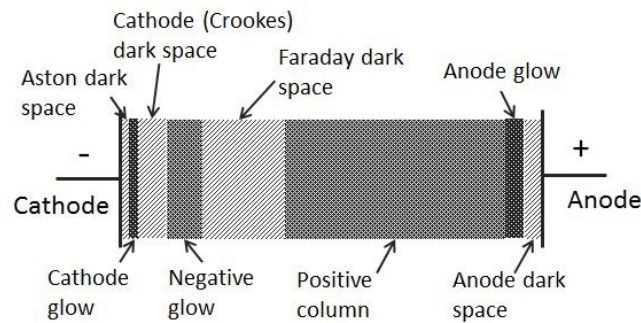
Figure 3.1 Characteristics of a dc glow discharge

The dark layer near the cathode is known as the Aston dark space, where electrons with low energy (not sufficient for excitation) emerge from the cathode. The cathode glow layer is located beyond the Aston dark space. Electrons gain the required energy from the electric field in this layer. Electrons are accelerated through the next region, known as the cathode (Crookes) dark space, and ionization occurs. Ionization can occur directly or occur when energy transfers to free electrons. As a result, low-level radiation occurs and electron density significantly increases. Due to the slow motion of the ions, a high electric current is generated. The applied voltage produces a linear drop in the cathode region and the ions accelerate along the cathode. Secondary electrons are then formed by ion bombardment of the cathode. This secondary electron generation depends on the material, contamination of the surface, and the energy of ions [1]. The electron energy and ionization decrease at the end of the cathode dark space by a decrease of the electric field. This causes stronger radiation. The zone with the highest luminosity is known as negative glow space. The negative glow is also known as the plasma region with a small electric field because in the plasma the densities of electrons and ions are nearly equal. The secondary electrons produced at the cathode region are accelerated through the negative glow region, providing the required energy to the plasma. Thus, discharge will be generated by the anode in this region. The electrons continue to decrease their energy in the negative glow. Therefore, luminosity begins to decrease and the transition to the next space, the Faraday dark space, begins. Plasma density also decreases in this space and the electric field again increases. Then, the large zone known as the positive column begins and an emission of light is observed in this region. However, the luminosity is not brighter than the negative glow. The

42

electrons balance with the local electric field and provide the main energy input. Emission and diffusion onto the walls leads to a loss of energy. A thin layer following the positive column is known as the anode glow region. The electric field increases in this region by repelling ions and removing electrons by the anode. The current flowing through the plasma is constant throughout this region. Therefore, the electron current at the anode must be equal to the ion current at the cathode. The final layer adjacent to anode is known as the anode dark space. The electron density begins to decrease in this region [1,2].

The dc discharge seems simpler than the rf discharge because of time independence. However, since dc discharge requires a continuous current to provide power, this cause a complication. In comparison, the rf discharge has no complication in the rf sheath [3].

3.2 Radio Frequency (RF) Plasma Discharge

3.2.1 RF Breakdown

In the rf breakdown, electrons are exposed to the oscillating electric field, and this oscillation causes electrons to heat up through collisions with neutrals. The electrons, which reach sufficient energy, drive the ionization. It is clear that rf breakdown is simpler than dc breakdown.

3.2.2 RF Glow Discharge

Radio frequency (rf) glow discharge is one of the most widely used discharges. In rf discharge, secondary electrons are generated through a collision of energetic ions with an electrode. The accelerated electrons in the sheath then lead to ionization, similar to a dc discharge. Additionally, as a positive column of dc discharge, the electric fields provide the main source of energy for the electrons by oscillation in the discharge. Although rf glow discharge has similar properties to dc glow discharge, and although ions and electrons in both of the sheaths are accelerated by the electric field, these same kinds of behavior only appear at low frequencies in rf glow discharge. Furthermore, the ions in the rf discharge follow time averaged fields instead of instantaneous electric field at high frequencies. Here, a self-bias occurs and this causes a time-averaged negative voltage. Thus, the ions are accelerated by the potential difference between the time-average plasma potential

and the time-average bias potential. Moreover, unlike the dc discharge, the oscillating sheath electric field accelerates electrons in the rf glow discharge. In the rf system, the rf current and voltage are directly applied to an electrode through a coupling capacitor and a high voltage capacitive sheath occurs between the electrode and the bulk plasma. Since the electrons have greater mobility than the ions, the electron current will be much more substantial than the ion current. Therefore, the resistance for an ion current will be more effective than for an electron current [1]. In the rf discharge, stochastic or collisonless heating occurs in the sheath while the rf currents drive ohmic heating in the bulk [3]. To obtain an effective power transfer, a matching network between the source and the discharge is required to control the discharge.

Since most of the power in dc glow discharge is consumed by the acceleration of ions into the sheath, rf glow discharge is more attractive for processes requiring ion bombardment such as sputtering and ion plating. An rf discharge can be applied to both electrically conductive and non-conductive materials, whereas dc discharge can be applied only to conductive samples. Another difference between the discharges is their density and energy distribution. Ionization occurring in rf discharge is more efficient than that occurring in the dc discharge, and higher ionization makes rf discharge the preferred glow discharge in the microelectronics industry [4].

3.3 Probes

To determine plasma parameters such as electron and ion densities, electron temperature, and potentials, many types of electron probes are used. These include single, double, triple, and emissive probes [5–10]. A small metal electrode or probe is inserted into the plasma, and the plasma properties are then measured from a graph of current-voltage characteristics obtained by applying different voltage values to the metal probe. While single probes can be used in plasma discharges with at least one electrode, double or triple probes can be used for discharges without electrodes. Emissive probes are generally used in plasma discharges sensitive to sudden changes in the probe current that occur when thermionic emissive electrons heat the probe.

Materials used for probes should have a high melting point and resistance to the bombardment of charged particles. Therefore, probes are produced from metals

such as Pt, W, Mo, or stainless steel. The metal probe is inserted inside an insulator tube, allowing a piece measuring only 5-10 mm to be placed in the plasma. A space between the metal probe and the insulator tube prevents sputtering deposition of probe materials on the insulator surface, which would lead to a leak in the current. This space also prevents the probe from changing the distinct surface area [10].

In spite of its simple construction and measurements procedures, theoretical analysis of the probe is immensely complex work. This complication originates from the interactions of particles inside plasma discharges. Working at a low-pressure region less than 0.1 Torr means that the mean free paths of charged particles are longer than the Debye length and the probe size therefore provides a simplicity for the complexity. Another solution involves using a smaller probe with a length less than the length of the mean free paths of particles for higher pressures. However, the mechanical stability and manufacturing difficulty of the probe presents a constraint in size, and the size of the probe is between several tens and hundreds of micrometers.

3.3.1 Langmuir Single Probe

The determination of plasma parameters (such as electron temperature, plasma density, and electron energy distribution function) from the I-V characteristics of a single probe was widely practiced after Irvin Langmuir's work. This probe is therefore called a single Langmuir probe [11,12]. Although the cylindrical probe has been frequently used, there are other options including planar and spherical probes [10]. In the circuit of a single probe, as shown in Figure 3.2, there is always a connection with a grounded reference electrode, one of the electrodes of the main discharge. A variable potential is applied to the circuit and the current is measured. By recording the change in the current according to variable potential coming from external DC power supply, the current of the probe is presented as a function of probe potential.
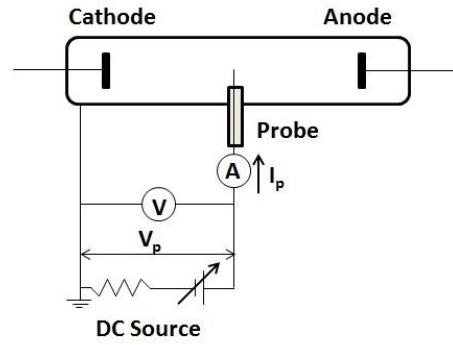
Figure 3.2 The single probe circuit (I_p: probe current, V_p: probe voltage)

The graph of the probe is illustrated in four regions as shown in Figure 3.3 [5,10]. In Region II, which is called the ion-current saturation region, ions are accelerated and collected by the probe while electrons negatively biased against plasma are repelled from the probe surface. Region III can be defined as the retarding-field region, the electron-current inflow region, or the transition region. This region is located in the area between the floating potential V_f and the plasma potential V_s. In this region, the probe potential is less than the plasma potential V_s, so the probe engages the ions itself. Electrons with a larger thermal energy than probe potential can be also be attracted to the probe by overcoming the electrostatic repulsion. At that point, the probe potential exceeds the plasma potential in Region IV. This region is referred to as the electron-current saturation region. The electrons begin to reach the probe and the ions are repelled. In Region I, applying an enormous negative potential to the probe causes discharge between the anode and the probe. When the net current of the probe is zero, the floating potential V_f is described by the plasma potential. The plasma potential V_s can be determined by the extrapolation of curves at Region III and IV. The crossing point of the extrapolation gives the plasma potential.
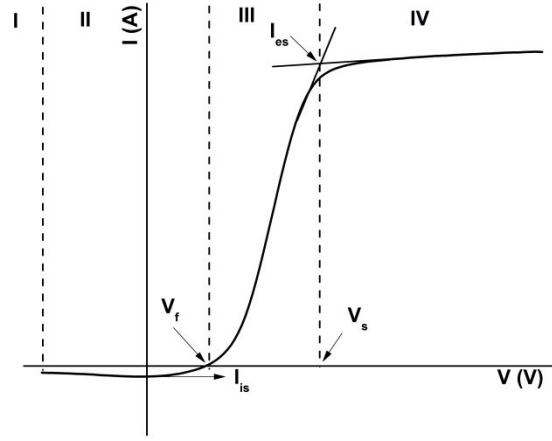
Figure 3.3 The I-V curve of a single probe

During probe analysis, characterization depends on several assumptions. First, the plasma is collisionless and electron energy distribution is Maxwellian. Second, the electron temperature is much higher than the ion temperature and ions are independently charged when ion and electron densities become equal. In the third region, or transition region, where both electrons and ions are collect at the probe, the electron current is very large compared to the ion current. Therefore, to find the probe current, the electron energy distribution function $f(\varepsilon)$ is taken as:

$$I = \frac{1}{4} N_e A e \int_{eV}^{\infty} \sqrt{\frac{2\varepsilon}{m}} f(\varepsilon) \left(1 - \frac{eV}{\varepsilon}\right) d\varepsilon \qquad (3.1)$$

Where N_e is the electron density, A is the area of the probe, e and m are the electron`s charge and mass, respectively, V is the probe potential, which is $V = V_s - V_p$. If the energy distribution function is written as a Maxwellian distribution and solving the integral, the probe current becomes as

$$I = \frac{1}{4} N_e A e \sqrt{\frac{8kT_e}{\pi m}} \exp(\frac{-e(V_s - V_p)}{kT_e}) \qquad (3.2)$$

A slope of the logarithm of the probe current lnI_p gives the inverse of the average electron temperature e/kT_e. The saturation electron current $i_{e,sat}$ and ion current $i_{i,sat}$ are defined as

$$I_{es} = N_e s e \sqrt{\frac{kT_e}{2\pi m}}, \quad I_{is} = N_i s e \sqrt{\frac{kT_e}{2\pi M}} \qquad (3.3)$$

47

where M is the mass of an ion, m is the mass of an electron, s the surface area of the probe, and e is the charge of electron.

In the single probe, characteristics were obtained from the measurement of the electron saturation current. Due to the connection with the reference electrode, the probe tends contribute to the plasma discharge and this causes a collection of large currents. Thus, the single probe is exposed to plasma fluctuations during the characterization. Moreover, it is very difficult to determine the exact return path of the current [13]. However, it is possible to eliminate these drawbacks by using a probe such as the double probe.

3.3.2 Double Langmuir Probe

The double probe consists of two Langmuir probes, and it was originally developed by Johnson and Malter [14]. In the double probe, voltage is applied between two probes, unlike the single probe where it is applied between the electrode and plasma chamber. The change in the current between the two separated probes is measured, and through characterization of the I-V curve parameters like ion density, n_i, and electron temperature, T_e can be measured [15,16].
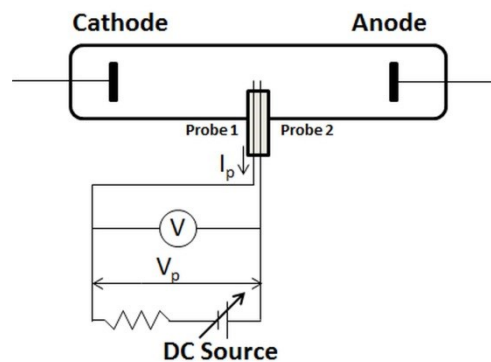
Figure 3.4 The double probe circuit

The double probe gives a symmetrical curve of current-voltage, and while the upper part of the curve provides measurements from the first probe, the lower part provides measurements from the second probe [10]. In the double probe, first probe has a current I_1 and the second has a current I_2. According to Kirchoff's current law:

48

$$\Sigma I = I_1 + I_2 = 0 \tag{3.4}$$

Using definition of the I₁ and I₂,

$$I_1 = I_{1is}\left[1 - exp\left(\frac{eV_1}{kT_e}\right)\right]$$

$$I_2 = I_{2is}\left[1 - exp\left(\frac{eV_2}{kT_e}\right)\right] \tag{3.5}$$

Since $I_{1is} = I_{2is} = I_{is}$ and $I = I_1 = -I_2$

$$I = I_{1is}\left[1 - exp\left(\frac{eV_1}{kT_e}\right)\right] = I_{2is}\left[1 - exp\left(\frac{eV_2}{kT_e}\right)\right] \tag{3.6}$$

From the definition of $tanh x = \frac{e^{2x}-1}{e^{2x}+1}$, the double probe characterization is defined by

$$I(V) = I_{is}tanh\left(\frac{eV_d}{2kT_e}\right) \tag{3.7}$$

where V is the applied voltage between the probes, k_B is the Boltzmann constant, T_e is the electron temperature, I_{is} is the ion saturation current, and V_d is the potential difference between voltages of probes V_1 and V_2. The electron temperature can be found from the first derivation of the probe current at the origin [17–21].

$$\left(\frac{dI}{dV_d}\right)_{V_d=0} = \frac{eI_{is}}{2kT_e} \tag{3.8}$$

The I$_{is}$ is given by the following equation:

$$I_{is} \approx 0.61eN_iA\sqrt{\frac{kT_e}{M}} \tag{3.9}$$

where M is the mass of ion, e is the electron charge, A is the probe area, and N_i is the ion density.
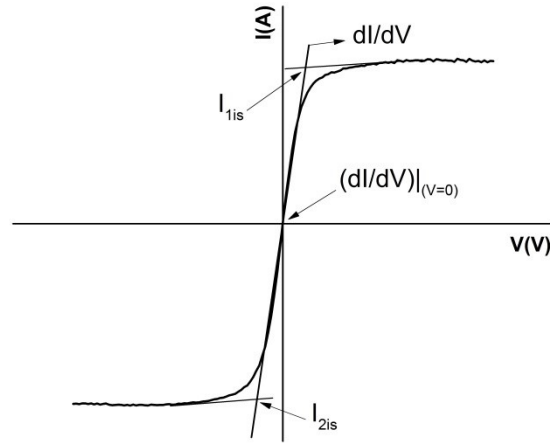
Figure 3.5 The I-V curve of a double probe

The double Langmuir probe has been studied by several investigators [13,22–28]. Double Langmuir probes have several advantages over single Langmuir probes, including smaller probe currents, less dependence on plasma potential fluctuations, and an ability to measure in electrodeless discharges [28–32]. The circuit of a double probe does not include a ground connection with the plasma as in the single probe, thus the floating potential is free. According to Chen [5], the total current collected by the double probe is less than the ion saturation and Castro [33] showed that the ion saturation was 20 times less than the electron saturation used in characterization of the single probe. Therefore, it can be suggested that the effects of the plasma to the measurements are minimized by analysis of the double probe. One disadvantage is the impossibility of determining the electron energy distribution function from the symmetrical double probe. However, this problem can be easily solved by using an asymmetric double probe [34].

3.4 Radio Frequency Plasma System

The radio frequency plasma system, shown in Figure 3.6, consists of two parallel cylindrical stainless steel electrodes placed on top of each other inside the chamber. The upper one has rf power with 13.56 MHz frequency (capacitively coupled) and the lower one is connected to the ground. This plasma reactor was designed for this study and was manufactured in the Plasma Laboratory in the Physics Department of Middle East Technical University. Diagnostic properties were explored under N_2 and Ar plasma with the independent plasma parameters of rf power (25 – 250 W)

and pressure (0.1 – 1 torr). The distance between the electrodes was changeable and measurements were recorded at distances of 3 and 4 cm. After the pressure dropped below 10^{-2} torr with the use of a mechanical vacuum pump, generally with a base pressure of 5.0×10^{-3} torr, the gas flow was activated. Then, the rf power supply was activated as the desired pressure was achieved. This system used a double Langmuir probe (purchased from Impedans Ltd, Dublin) made from tungsten wire 0.4 mm in diameter. Probes with the same areas were isolated with a ceramic jacket, and only a length of 10 mm was inserted into the plasma. All the measurements were controlled by ALP system software.
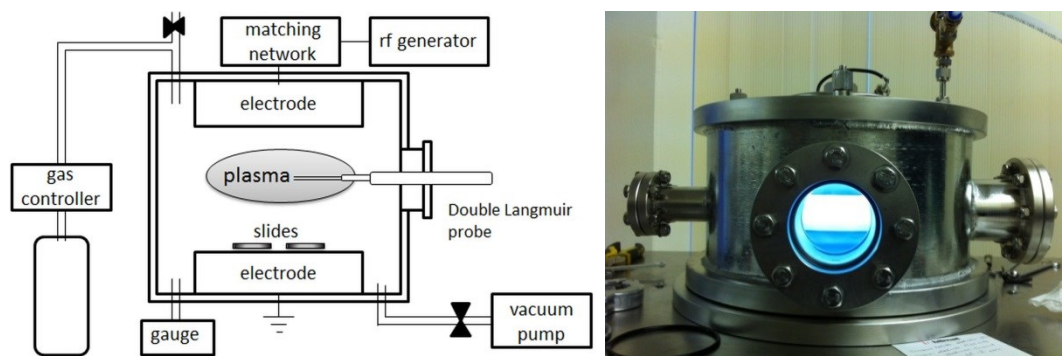
Figure 3.6 The radio frequency plasma system

3.5 Results and Discussion

The diagnostics of N_2 and Ar plasma were characterized by the double Langmuir probe. The parameters of the ion density N_i and the electron temperature kT_e were measured. The results recorded for N_2 plasma are listed in Table 3.1. From Figure 3.7, it is clear the electron temperature kT_e exhibited an increase as the power increased. This increase could be explained by the increase in the kinetic energy of the electrons at sufficient mean free path and the probability of collisions for electrons. The amount of ionization and recombination inside the plasma played an important role in determining the ion density. The increase in power led to ionization with large probabilities, thus the ion density N_i increased with increasing power. Additionally, the ion saturation current showed an increase with the power. As the pressure increased, recombination in plasma increased and led to a decrease in free electrons. Since high pressure decreased the mean free path, the ions moved

closer to electrons under high pressure. Therefore, electron (collisional) heating was dominant in the plasma at high pressure whereas collisionless stochastic heating was dominant at low pressure [35,36]. Furthermore, since there were not enough free electrons with sufficient energy glowing from the electrode, producing plasma with low power values was difficult at a high pressure [37]. The results demonstrate that electron temperature kT_e and ion density N_i were inversely proportional to pressure. All results agreed with previous studies in the literature [19,20,36,38–41].
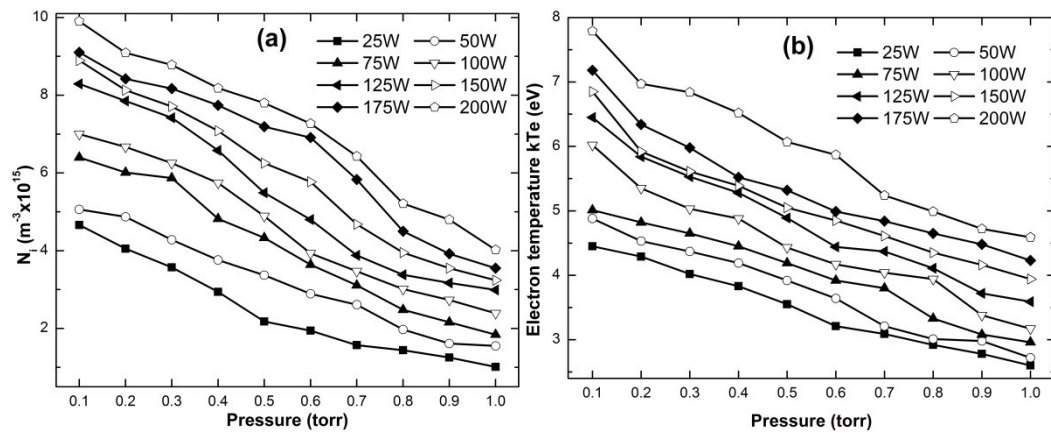
Figure 3.7 The plots of N_i (a) and electron temperature kT_e (b) with respect of pressure and power for N_2 plasma for 3 cm electrode distance
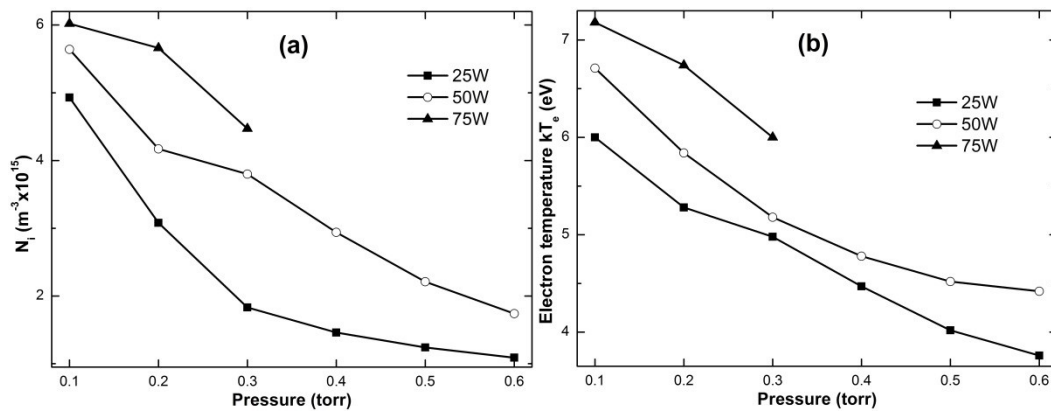
Figure 3.8 The plots of N_i (a) and electron temperature kT_e (b) with respect of pressure and power for N_2 plasma for 4 cm electrode distance

Table 3.1 The double probe results of N_2 plasma for 3 cm electrode distance

P	p	kT_e	N_i	p	kT_e	N_i	p	kT_e	N_i	p	kT_e	N_i
25		4.45	4.66		4.29	4.05		4.02	3.57		3.83	2.94
50		4.88	5.06		4.53	4.87		4.37	4.28		4.19	3.76
75		5.01	6.4		4.82	6.01		4.65	5.87		4.45	4.82
100		6.02	7		5.35	6.67		5.03	6.25		4.88	5.74
125	0.1	6.45	8.29	0.2	5.84	7.85	0.3	5.53	7.42	0.4	5.28	6.58
150		6.85	8.89		5.92	8.13		5.61	7.71		5.39	7.08
175		7.18	9.1		6.34	8.42		5.98	8.17		5.52	7.74
200		7.79	9.9		6.97	9.09		6.84	8.78		6.52	8.18
25		3.55	2.18		3.21	1.94		3.09	1.57		2.92	1.44
50		3.92	3.37		3.64	2.89		3.21	2.61		3.01	1.97
75		4.19	4.33		3.92	3.64		3.8	3.11		3.33	2.48
100		4.43	4.89		4.19	3.93		4.04	3.47		3.94	3.01
125	0.5	4.89	5.49	0.6	4.43	4.8	0.7	4.37	3.88	0.8	4.11	3.38
150		5.05	6.25		4.89	5.77		4.61	4.68		4.35	3.95
175		5.32	7.19		4.99	6.91		4.84	5.83		4.65	4.5
200		6.07	7.8		5.87	7.27		5.24	6.43		4.99	5.21
25		2.78	1.25		2.6	1.01						
50		2.98	1.61		2.72	1.55						
75		3.08	2.16		2.96	1.84						
100		3.38	2.73		3.17	2.39						
125	0.9	3.72	3.17	1	3.59	2.99						
150		4.16	3.55		3.94	3.24						
175		4.48	3.92		4.23	3.55						
200		4.72	4.8		4.59	4.02						

P=power (W), p=pressure (torr), kT_e= electron temperature (eV), and N_i=ion density (m^{-3} x10^{15})

When the distance between electrodes was increased from 3 cm to 4 cm, the plasma parameters showed similar changes (Figure 3.8). However, the values of the parameters decreased as the anode-cathode separation increased. This is caused by the higher plasma energy density between electrodes with a smaller electrode gap.

The results recorded for Ar plasma are listed on Table 3.2 and compared with the results of N_2 plasma in Figure 3.9. Comparing the results of electron temperature and ion density for Ar and N_2 plasmas, both parameters increased with an increase in power, which might be due to the directly proportional relationship between the current density and the applied power. Since the mass of the Ar atoms was heavier than the N_2 molecule, the rate of recombination was higher in Ar plasma and the high recombination limited the production of atoms. Therefore, both the ion density and the electron temperature of N_2 plasma were higher than that of Ar plasma [21,41].

Table 3.2 The double probe results of Ar and N_2 plasma

		Ar gas		N_2 gas	
P	p	kT_e	N_i	kT_e	N_i
50		3.89	4.77	4.53	4.87
75		4.02	5.84	4.82	6.01
100	0.2	4.55	6.46	5.35	6.67
150		5.09	7.6	5.92	8.13
200		5.61	8.55	6.97	9.09
250		6.32	9.08	7.23	9.45

P=power (W), p=pressure (torr), kT_e= electron temperature (eV), and N_i=ion density (m^{-3} x10^{15})
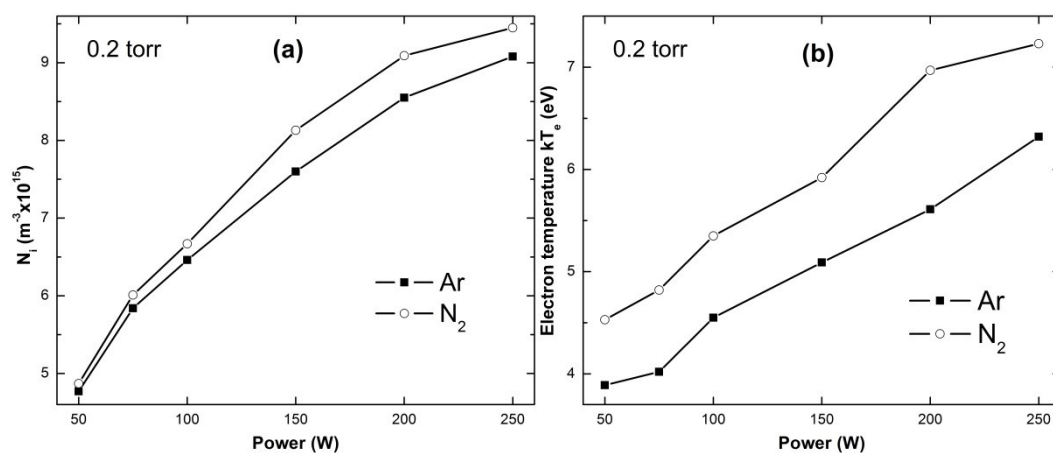
Figure 3.9 The plots of N_i (a) and electron temperature kT_e (b) with respect to power for Ar and N_2 plasma

3.6 Conclusion

N_2 and Ar plasmas were obtained under the capacitively coupled single radio frequency system with 13.56 MHz power supply. All plasma diagnostics were measured using the double Langmuir probe. Increasing the applied rf power resulted in an increase in both the electron temperature and ion density. However, increasing the pressure led to a decrease in both of these features. An increase in the electrode gap led to a decrease in the electron temperature and ion density due to lower plasma energy density between the electrodes.

3.7 References

[1]   S.M. Rossnagel, J.J. Cuomo, W.D. Westwood, Handbook of Plasma Processing Technology, Noyes Publications, New York, 1990.

[2]   A. Fridman, L.A. Kennedy, Plasma Physics and Engineering, CRC Press, Boca Raton, FL, 2010.

[3]   M.A. Lieberman, A.J. Lichtenberg, Principles of Plasma Discharges and Materials Processing, 2nd Editio, John Wiley & Sons, Inc., New Jersey, USA, 2005.

[4]   M.R. Winchester, R. Payling, Spectrochim. Acta Part B At. Spectrosc. 59 (2004) 607.

[5]   F.F. Chen, in:, R.H. Huddlestone, S.L. Leonard (Eds.), Academic Press, Boston, 1965, p. 113.

[6]   H. Amemiya, Y. Sakamoto, Shinku 28 (1985) 177.

[7]   B.E. Cherrington, Plasma Chem. Plasma Process. 2 (1982) 113.

[8]   R.M. Clements, J. Vac. Sci. Technol. 15 (1978) 193.

[9]   M.J. Druyvesteyn, Z Phys. 64 (1930) 787.

[10]   M. Konuma, Film Deposition by Plasma Techniques, Springer-Verlag, Berlin, Heidelberg, 1992.

[11]   I. Langmuir, H. Mott-Smith, Gen. Electr. Rev. 26 (1923) 731.

[12]   H. Mott-Smith, I. Langmuir, Phys. Rev. 28 (1926) 727.

[13]   P.D. Pedrow, L.M. Burrage, J.L. Shohet, IEEE Trans. Power Appar. Syst. PAS-100 (1981) 2740.

[14]   E. Johnson, L. Malter, Phys. Rev. 80 (1950) 58.

[15] A. Brockhaus, C. Borchardt, J. Engemann, Plasma Sources Sci. Technol. 3 (1994) 539.

[16] M. Schiller, W. Kulisch, Surf. Coatings Technol. 98 (1998) 1590.

[17] W. Kim, M. Lee, C. Chung, J. Korean Phys. Soc. 49 (2006) 1687.

[18] S.-J. Oh, S.-J. Oh, C.-W. Chung, Rev. Sci. Instrum. 81 (2010) 093501.

[19] M. Naz, A. Ghaffar, Prog. Electromagn. Res. 115 (2011) 207.

[20] M. Naz, A. Ghaffar, Prog. Electromagn. Res. 114 (2011) 113.

[21] W. Tao, H.K. Yasuda, Plasma Chem. Plasma Process. 22 (2002) 297.

[22] W. McColl, C. Brooks, M.L. Brake, J. Vac. Sci. Technol. A 11 (1993) 1152.

[23] C. Liu, J. Wang, K. Yu, B. Eliasson, Q. Xia, B. Xue, Y. Zhang, J. Electrostat. 54 (2002) 149.

[24] M. Mozetic, Mater. Tehnol. 45 (2011) 457.

[25] J. Wild, P. Kudrna, M. Tichý, V. Nevrlý, M. Střižík, P. Bitala, B. Filipi, Z. Zelinger, Contrib. to Plasma Phys. 52 (2012) 692.

[26] B. Beal, L. Johnson, D. Brown, J. Blakely, D. Bromaghim, Rev. Sci. Instrum. 83 (2012) 073506.

[27] K.T.A.L. Burm, Eur. Phys. J. Appl. Phys. 58 (2012) 30802.

[28] T. Welzel, T. Dunger, H. Kupfer, F. Richter, J. Appl. Phys. 96 (2004) 6994.

[29] B. Annaratone, G. Counsell, H. Kawano, J. Allent, Plasma Sources Sci. Technol. 1 (1992) 232.

[30] H. Amemiya, Jpn. J. Appl. Phys. 27 (1988) 2423.

[31] I.H. Hutchinson, Principles of Plasma Diagnostics, 2nd Editio, Cambridge University Press, Cambridge, 2002.

[32]   L. Schott, Electrical Probes in Plasma Diagnostics, AIP, Woodbury, 1995.

[33]   R. Castro, G. Cirino, P. Verdonck, H.S. Maciel, M. Massi, M.B. Pisani, R.D. Mansano, Contrib. to Plasma Phys. 39 (1999) 235.

[34]   J. Husárik, M. Širý, M. Kando, Jpn. J. Appl. Phys. 47 (2008) 7334.

[35]   H. Park, S.J. You, W. Choe, Phys. Plasmas 17 (2010) 103501.

[36]   E. Abdel-Fattah, M. Bazavan, H. Sugai, J. Appl. Phys. 110 (2011) 113303.

[37]   Y. Sung, H.B. Lim, R.S. Houk, J. Anal. At. Spectrom. 17 (2002) 565.

[38]   E. Abdel-Fattah, M. Bazavan, H. Sugai, Phys. Plasmas 19 (2012) 113503.

[39]   M. Chen, T. Yang, 37 (1999) 325.

[40]   A. Sarkissian, A. Bourque-Viens, R. Paynter, R. Saint-Jacques, B. Stansfield, Surf. Coatings Technol. 98 (1998) 1336.

[41]   T.H. Chung, J.M. Park, M.A. Song, S.H. Bae, in:, 19th Int. Symp. Plasma Chem., Bochum, Germany, 2009, p. 247.

CHAPTER 4

SYNTHESIS AND CHARACTERIZATION OF FLUORENE THIN FILM UNDER LOW PRESSURE DC GLOW DISCHARGE AND HIGH CURRENT PULSED DISCHARGE

4.1 Introduction

π-Conjugated polymers (CPs), such as polyfluorene , polythiophene, polyaniline, and their derivatives have been widely studied due to their potential applications as active layers in organic electronic and chemical sensor devices [1–3]. Besides their intrinsic conductivity, the advantages of CPs are the diversity of structures and tunability of properties offered through the molecular design. Among these polymers, fluorene and its derivatives have emerged as the dominant class of polymers for light-emitting diodes [4–6] and photovoltaic cells [7,8] applications due to their easy processability, high luminescence efficiency and electronic-semiconducting properties.

Since the way of producing the organic thin films have a strong influence on the morphology and molecular structures, the chemical and physical properties of the synthesized species has to be well characterized. The methods of producing polymeric thin films could be classified as; wet processing (conventional) method, such as chemical, electrochemical, spreading, and dry processing method, such as physical vapor deposition and plasma polymerization. The polyfluorenes produced by conventional methods are extensively studied and well characterized [9–11]. The disadvantages of this method are the poor spatially controlled deposition and the nonhomogeneous films with thickness > 1 μm [12]. As a dry processing method, the plasma polymerization is a solvent-free, room temperature process and can be used to deposit onto almost any substrate homogeneously with thicknesses ranging from tens of angstroms to micrometers. In contrast to the conventional methods, it is difficult to predict the exact chemical structure of a surface deposited via plasma polymerization technique, because of the reactive species (e.g. radicals, ions, and

electrons) present in the plasma. Hence, the monomer, the gas phase composition, reactor pressure, plasma power and the geometry of the reactor strongly affect the molecular structure and properties of the plasma polymer [13].

Here, we present the synthesis of fluorene thin films by superposing simultaneously a continuous and pulsed discharge and the characterization of these samples. To the best of our knowledge, fluorene thin films have been synthesized for the first time by the plasma polymerization technique. The aims are to study the molecular structure and the morphology of the polymerized fluorene thin films and to investigate the influence of the iodine doping on the grown samples. The molecular structure of the samples was investigated by Fourier transform infrared (FTIR), UV–visible (UV–vis), and X-ray photoelectron spectrometer (XPS); and the morphology was studied by X-ray diffractometer (XRD) and scanning electron microscope (SEM).

4.2 Double Discharge System

The double discharge system is a double discharge pulsed electron beam generator which consists of a low pressure dc glow discharge and a high current pulsed discharge. By applying a high voltage pulse to the electrodes during the dc glow discharge, a filamentary pulsed discharged is generated through the generator. The details of the double plasma system are given in [14–16]. A part of the system, shown in Figure 4.1, consists of three cylindrical hollow electrodes $K_{1,2}$, A_1, A_2 and two quartz tubes with 100 mm length and 30 mm internal diameter in between them. The glass substrates are placed at two different regions at the reactor given in Figure 4.1. A high pulsed voltage with a 5 Hz repetition rate was applied to $K_{1,2}$ and A_2, while an ordinary low-pressure glow discharge was operating between the hollow cathode, $K_{1,2}$ and A_1. A filamentary pulsed discharge with 2 mm diameter forms along the symmetrical axis of the tube at specific values of current and pressure [14]. Higher plasma density and energy is established inside the $K_{1,2}$ electrode where the hollow cathode effect (HCE) is observed [17,18]. The HCE provides vaporization of the powder monomer in argon gas environment without any processes.
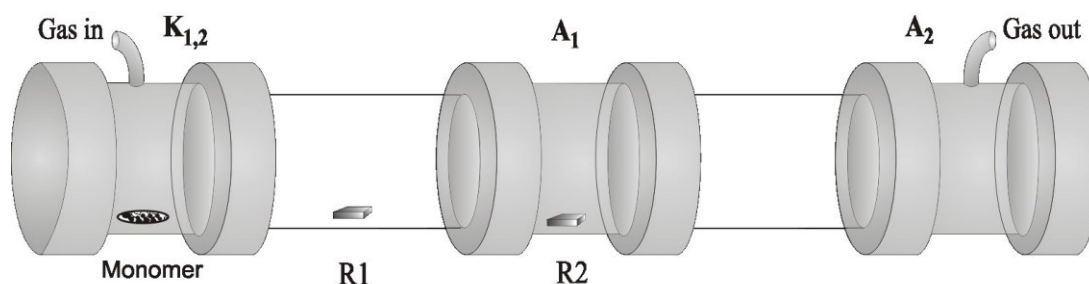
Figure 4.1 The locations of the fluorene monomer and the substrates at the experimental set-up

A solution, heated for an hour at 350 ºC, made from H_2SO_4 (100 mL) and $K_2Cr_2O_7$ (5 g) was prepared for the cleaning of the glassware and the quartz glass substrates. The substrates were submerged in the solution for 30 min, and then rinsed with water, and acetone. After that the samples were dried at room temperature. The fluorene monomer ($C_{13}H_{10}$) (Alfa Aesar, A Johnson Matthey Company) was used as purchased. It was in powder form and replaced inside the hollow $K_{1,2}$ cathode. The thin films were produced at fixed 2 kV DC and 19 kV pulsed voltages, with a 5 Hz repetition rate for a 20 min deposition time. The operating pressure was 0.5 mbar. The analyzed samples thickness was in the order of 500 ± 10 nm.

For the structural analysis of the deposited films a Bruker IFS 66/s FTIR spectrophotometer with 4 cm^{-1} spectral resolution and the noise less than 10^{-5} AU in a minute for peak to peak were used. The spectra of the fluorene monomer were measured by Perkin Elmer ATR-FTIR Spectrum One. The absorption measurements of the thin films were carried out by the UV-visible spectroscopy (Analytikjena Specord S600 spectrometer). The XPS analysis was recorded by a Specs EA 200 system; the measurement performed by using 279 W Mg K_α X-ray source and SPECS EA-200 Energy analyzer in a vacuum of 1×10^{-7} Pa equipped with a hemispherical electron analyzer operated with a focusing lens at a spot size of 250 μm and at a take-off angle of 90°. The morphology of the thin films was analyzed with Rigaku Miniflex standard X-ray diffractometer (the excitation source Cu K_α, λ = 1.54 A˚) and also with FEI Quanta 400F SEM system.

4.3 Results and Discussion

4.3.1 Fourier Transform Infrared Spectroscopy

The FTIR spectra of the deposited polymer thin films for two different regions (R1 and R2) were measured in the range of 4000-400 cm^{-1} and the results were shown in Figure 4.2 and the peak assignment of these spectra was presented in Table 4.1. The fluorene monomer spectra were also plotted in the same figure. The chemical structures of the plasma polymer thin films have different features than the ones produced under the conventional processes, explained in detail in Chapter 2. One of these features is that the bands of the FTIR spectra of the plasma polymerized thin films become much broader than the conventional ones due to the existence of cross-linked and branched structures [13]. The other feature is the fast and easy reacting of the plasma polymer films with the open atmosphere. Although the monomer structure does not include oxygen atoms and no any oxygen gas flowing to the reactor, if the thin films is exposed to the open atmosphere, the oxygen bands can be easily observed in the structures of the thin films as a result of their reactions with the radicals present in the atmospheric gases and water vapor [13,19,20]. Since the high energy coming from the plasma transfers to the monomer during the plasma polymerization, high levels of monomer fragmentation occur and the bands of the fragmentation are observed in the FTIR spectra.

From the FTIR results, it could be clearly seen that the bands of the deposited thin films were really much broader than that of the monomer, as shown in Figure 4.2. The oxygen existed for both of structures of the thin films deposited in two different regions. This existence was exhibited with the presence of the bands (a) and (e); the band (a) refers to the stretching vibrations of OH group, and the strong band (e) refers to C=O stretching vibration. Here also it was observed that the weak band (i) corresponding to C-O strech and/or aromatic, in-plane CH deformation.

The band (b) observed at 3040 cm^{-1} corresponds to the aromatic C-H stretching which is coming from the aromatic structure of fluorene [21]. The bands (f) and (g) which were appeared between 1600 and 1450 cm^{-1} refer to the C=C stretching of aromatic rings and the C=C bond, respectively [22]. The in-plane CH deformation and the out-of-plane CH deformation were observed in the band (j) from 900 to 745 cm^{-1}. The band (n) seen at 670 cm^{-1} corresponds to the C=C out-of-plane ring

bending vibration [23]. The sequential weak bands were appeared in the region between 2000 – 1700 cm^{-1} as well as the overtone bands seen from 900 to 670 cm^{-1}. These bands showed the presence of substitution at the aromatic ring. Therefore, it could be suggested that the substitution pattern occurred in the film formation because of the fragmented compounds during the plasma polymerization. The bands observed at 2000 – 1700 cm^{-1} and 900 – 670 cm^{-1} reveal that a combination of mono-, and disubstitution pattern present at the structure, so that the aromatic ring at the thin film structure could be a monosubstituted or disubstituted [22].

The bands (c) and (d) representing the presence of the methylene (CH_2) group, which is expected from the fluorene structure, correspond to the asymmetric and symmetric stretching mode of aliphatic C-H, respectively, and the in-plane of C-H bending of CH_2 was observed at the band (h).
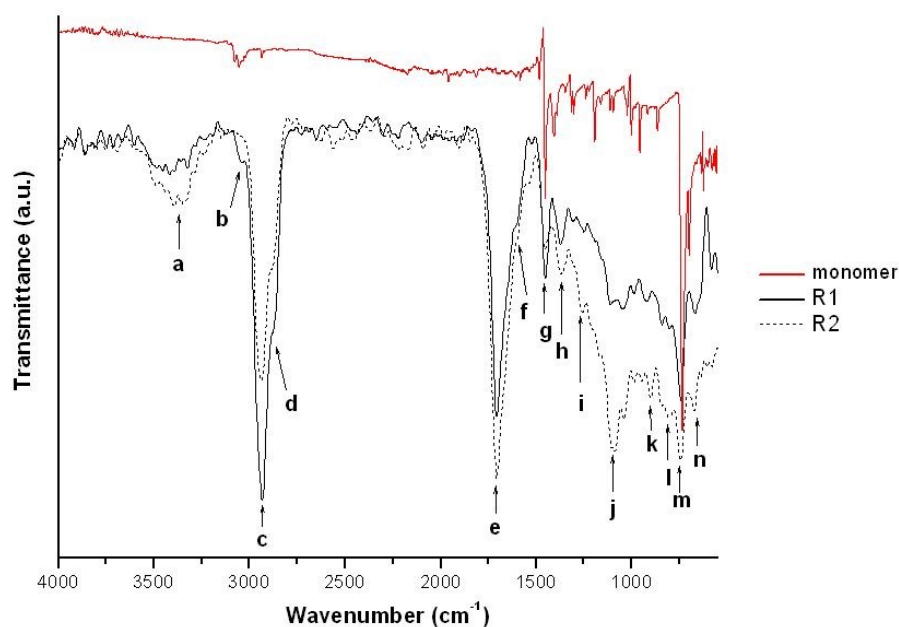
Figure 4.2 FTIR spectra of the fluorene monomer and the plasma polymerized fluorene thin films

Table 4.1 The peak assignments of Figure 4.2

Band	Wavenumber(cm^{-1})	Structure
a	3370	O-H stretching
b	3040	aromatic C-H stretching
c, d	2932, 2875	C–H stretching of aliphatic CH_2 group
e	1706	C=O stretching
f, g	1620, 1451	C=C, ring stretching vibration
h	1372	in-plane C-H bending of CH_2
i	1260	C-O strech and/or aromatic, in-plane CH deformation
j	1095	aromatic, in-plane CH deformation
k, l, m	901, 804, 745	aromatic, out-of-plane C-H bending
n	670	C=C out-of-plane ring deformation

4.3.2 UV-visible Spectroscopy

The UV-vis spectra of the fluorene thin films and the monomer were recorded in the region between 200 and 600 nm, as shown in Figure 4.3. It was observed that the fluorene thin films represented resemble structures with similar configuration. The electronically π - π^* transition of the fluorene are obtained at the bands around 206, 260, 290, and 300 nm [24,25]. There was a shifting observed in the absorption edges of the deposited thin films to the higher wavelengths which can be due to the extension of the conjugation length, represented in Figure 4.3. Also, the maximum absorption wavelengths (λ_{max}) shifted a few nanometers: 260 to 265 nm and 300 to 305 nm.
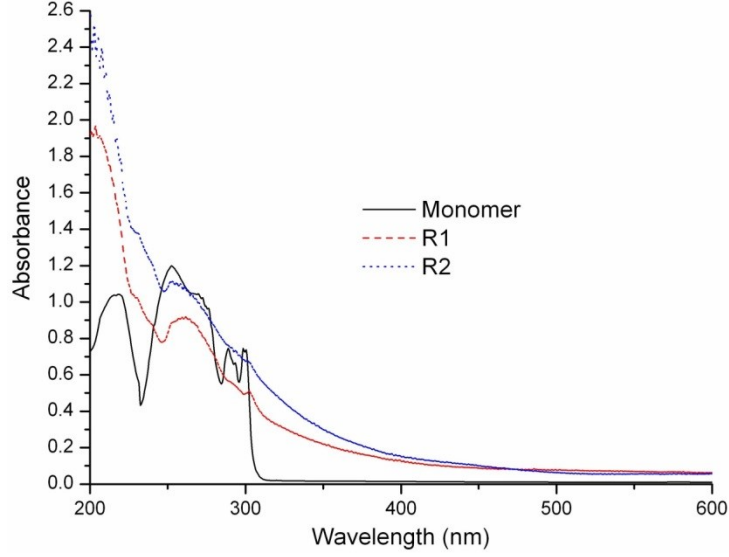
Figure 4.3 The UV-vis spectra of the fluorene monomer and the produced thin films

The UV-vis spectra can be used to calculate the fundamental energy band gap from the absorption edge. It can be investigated from Tauc relation [26]

$$(\alpha h v) = A(h v - E_g)^n, \tag{4.1}$$

where α is the absorption coefficient, $h v$ is the photon energy, A is an energy-independent constant, E_g is the optical energy band gap, and n is a constant which determines the type of optical transitions. For direct allowed and forbidden transition n is 1/2 and 3/2, respectively. For indirect allowed and forbidden transition n is 2 and 3, respectively. For all the samples, the value of n is investigated from the slope of the curve of $ln(\alpha h v)$ vs $ln(h v - E_g)$. The value of n is found at around 0.50 ± 0.03. It is revealed that since the density of state function can be approximated to 1/2 here, the samples have direct optical band gap. Hence, the E_g can be obtained now by plotting $(\alpha h v)^2$ vs $h v$ and extrapolating the linear portion of the plot to $(\alpha h v)^2 = 0$ as shown in Figure 4.4. As a result, the E_g value of the monomer, the R1 and R2 samples are 3.9, 3.68 and 3.57 eV, respectively. The reproducibility of the samples of both regions was very high in that for ten different experiments at constant parameters, the E_g values changed in between ± 0.05 eV.
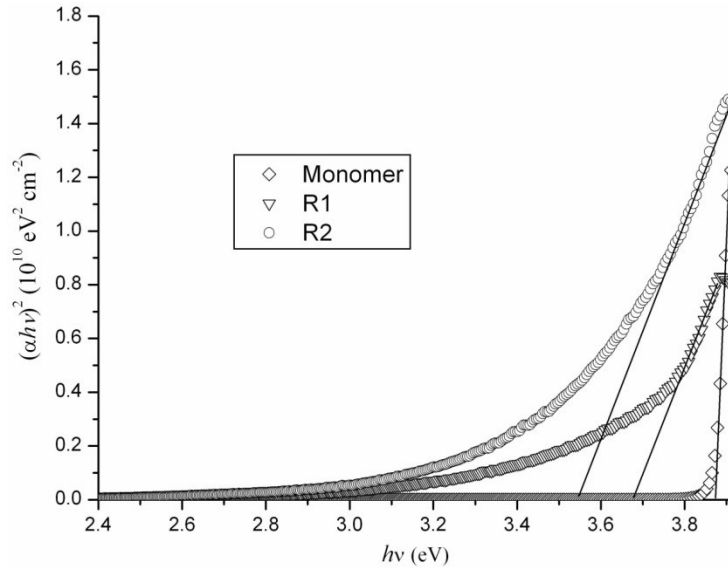
Figure 4.4 The dependencies of $(\alpha h\nu)^2$ on photon energy of the monomer, R1 and R2 samples

The iodine doping method [27,28] was used to improve the electrical conductivity of the deposited thin films. In this method, the iodine increases the hole density of the films by absorbing on the surface of polymer films and additional band level occurs in the structure as result of the attraction with the electrons from the orbitals [29,30]. The plasma polymerized fluorene thin films was subjected to iodine vapor for different time periods: 1, 20, and 28 hours. The normalized UV-vis spectra of the deposited and iodine doped fluorene thin films of R1 and R2 regions are given in Figure 4.5 (a) and (b), respectively. The undoped spectra are labeled as (A) and the doped one for 1, 20, and 28 hours are labeled as (B), (C), and (D), respectively. After the iodine doping, the light absorption wavelength shifted to higher wavelength for the spectra of both regions because of the addition of charge carriers to the structure and a new absorption band existed around 380 nm. This band corresponded to the fluorene structure which is a weak band prior to subjecting to iodine doping [31]. The E_g of thin films calculated from Tauc relation decreased with respect to increasing the doping time as shown at Figure 4.5 (c) and (d) for R1 and R2, respectively. The E_g values of this decrease are given in Table 4.2.
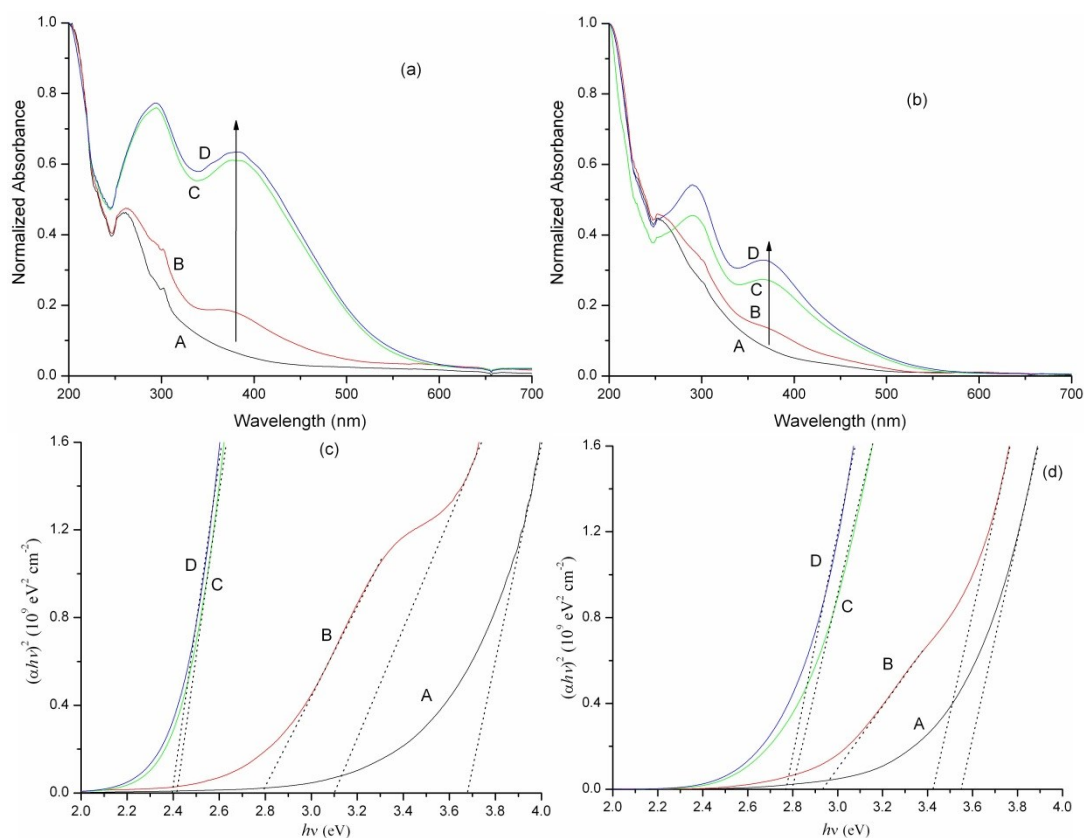
Figure 4.5 The normalized UV-vis spectra of iodine doped fluorene thin films for (a) region R1 and (b) region R2; and the $(\alpha h v)^2$ versus photon energy plot of (c) R1 and (d) R2 samples where the undoped samples labeled as (A), the doped one for 1 hour (B), 20 hours (C), and 28 hours (D)

Table 4.2 The E_g values of iodine doped fluorene samples

Doping time (hour)	R1 (eV)	R2 (eV)
0 (undoped)	3.68	3.57
1	2.79	2.93
20	2.42	2.79
28	2.39	2.76

4.3.3 X-ray Photoelectron Spectroscopy

X-ray photoelectron spectroscopy (XPS) has been known as one of the most useful analysis tools for investigating the atomic composition, the chemical state of the elements and their chemical environments. Survey spectra were acquired from 0 to

1100 eV with a step size of 0.5 eV. The XPS survey spectrum of the fluorene thin films is given in Figure 4.6 where the spectra reflects the carbon (from core level C 1s), and oxygen (O 1s) composition on the surface of the thin films. The observation of O, fairly low concentration from that of the C (given in Figure 4.6), is consistent with the FTIR results. At the inset of Figure 4.6, the enlarged C 1s and O 1s peaks demonstrate that the binding energies shift to a lower value at R2 region. It indicates that the conjugation length is higher at the R2 sample which is in agreement with UV-vis result where the E_g value is lower than that of the R1 sample [32,33].
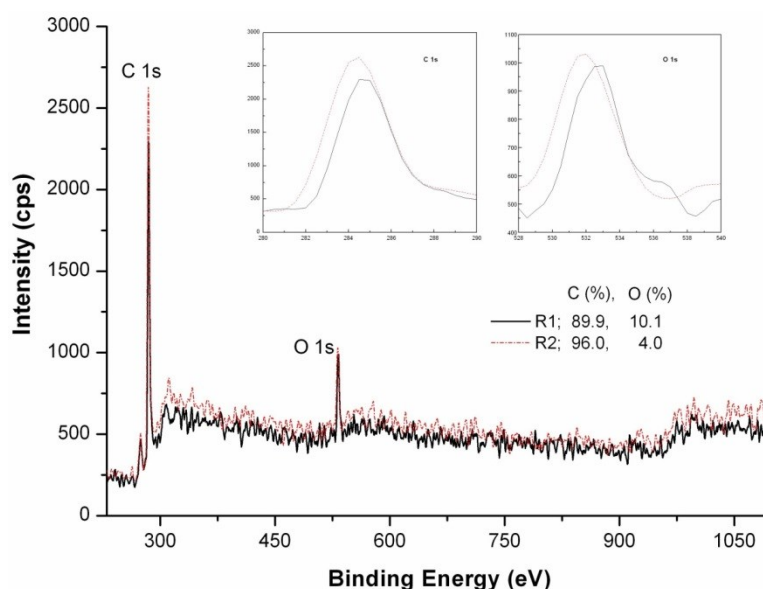
Figure 4.6 XPS surveys for fluorene thin films. Inset shows the enlarged C 1s and O 1s peaks
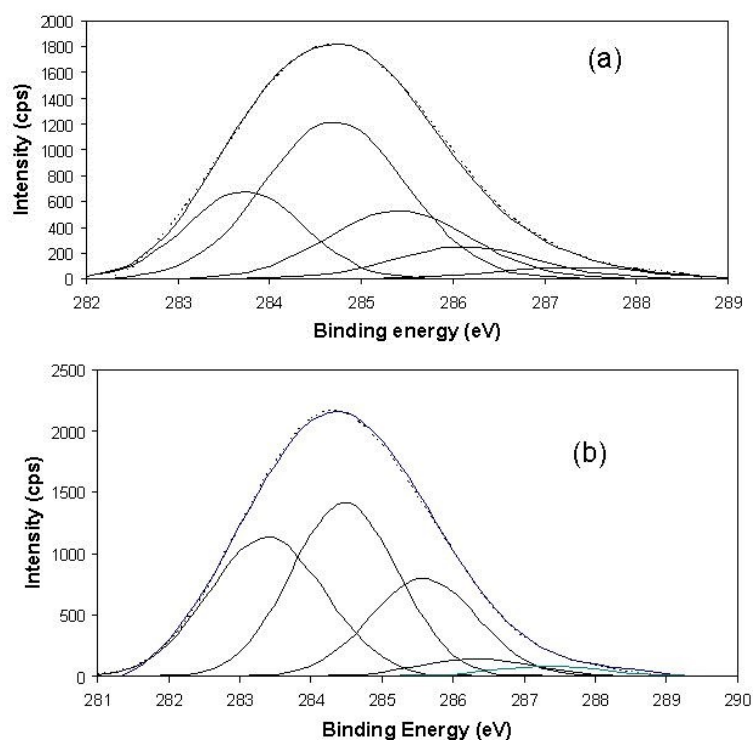
Figure 4.7 Deconvolution of C 1s core level of (a) R1 and (b) R2 region; ─ original spectrum and deconvoluted peaks, ---------- sum of deconvoluted peaks

To identify the presence and the contributions of the different bonds to the overall spectrum, the peak fit of the C 1s core level for the two regions is deconvoluted (see Figure 4.7). In the peak fits, Gaussian to Lorentzian ratio (*G/L*) of individual peaks were kept equal and taken as 1.0 for the plasma polymers [34]. The full width at half maximum (FWHM) of the peaks were 1.8 eV except the FWHM of 283.6 eV peak's at at R1 and R2 was taken as 1.5 and 1.9 eV, respectively [19]. The assigned binding energies (BE) of the peaks having the same value (± 0.1 eV) for the two regions is taken with respect to the database of the polymeric compounds [33]. The results of the peak fitting are given in Table 4.3. Theoretically, the ratio of the peak of 284.7 eV to 283.6 eV one at the benzene ring of polyfluorene is 2:1. However, the synthesized thin films in both regions violate this ratio and the relative area of $-CH_2$ is higher than the expected theoretical one. These results are in agreement with the FTIR spectra in that substitution of the fluorene exists at the structure of the thin films.

69

Table 4.3 Peak assignments and areas of C 1s component of plasma polymerized fluorene thin films

BE (eV)	Group	Relative Area (%)	
		R1	R2
283.6	C | C – C =	21.2	33.6
284.7	H | C – C =	46.0	38.4
285.4	-CH$_2$	20.1	21.6
286.3	C-O (OH, C-O-C)	9.3	4.2
287.6	C = O	3.4	2.4

4.3.4 X-ray Diffraction

The morphology of a conjugated polymer synthesized by conventional techniques can vary from completely amorphous to some fractional crystallinity. Besides of this issue, due to the fragmentation occurred during plasma polymerization process, it is expected that the crystallinity to decrease with respect to that of the conventional one. The spectra given in Figure 8 were recorded at room temperature, under a scan step rate of 0.2˚ per 12 s in the scattering angle range (2θ) from 0˚ to 80˚. Since the peak observed at 2θ, 22.9 is too broad and the ratio of the half-height width to diffraction angle (Δ2θ/2θ) is greater than 0.35, the fluorene thin films are mostly amorphous [35]. The semi-conducting amorphous solids, where no long-range order exists, only direct optical transitions are meaningful which is in agreement with the results revealed from the UV-vis spectra.
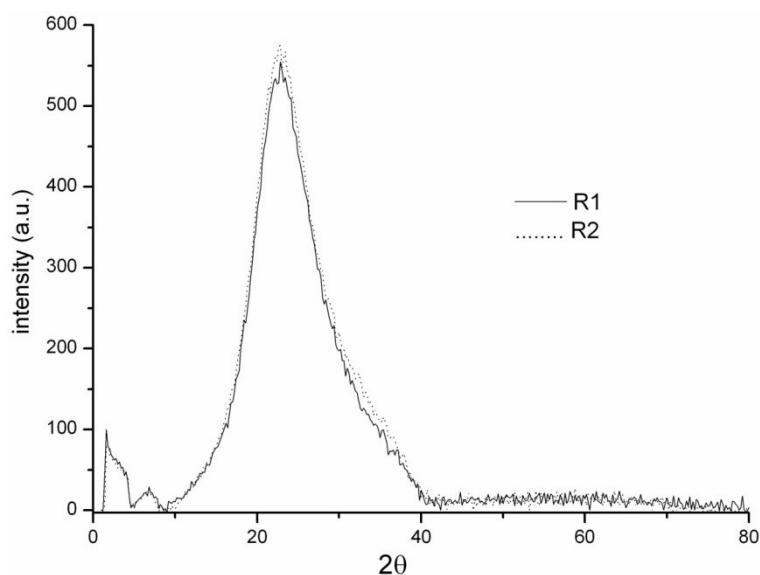
Figure 4.8 X-ray diffraction spectra of the fluorene thin films

4.3.5 Scanning Electron Microscope

The morphology of the fluorene thin films was also investigated by SEM system (Figure 4.9). There are significant differences in morphology among the two films, in that a smoother surface is obtained at R1 and they have granular structures with decreasing size towards region R2. And, the shape of the grains changes from spheroid to an irregular one at R2. It can be described as when the temperature of the plasma is high enough the hollow cathode effect is observed close to R1 region, any irregular features of the gas phase-borne nano assemblies often disappear as a result of coagulation and spheroidization effects [36]. The agglomeration of nano sized particulates which leads to an irragular surface at R2 is an indication of a gas phase dominated plasma polymerization.
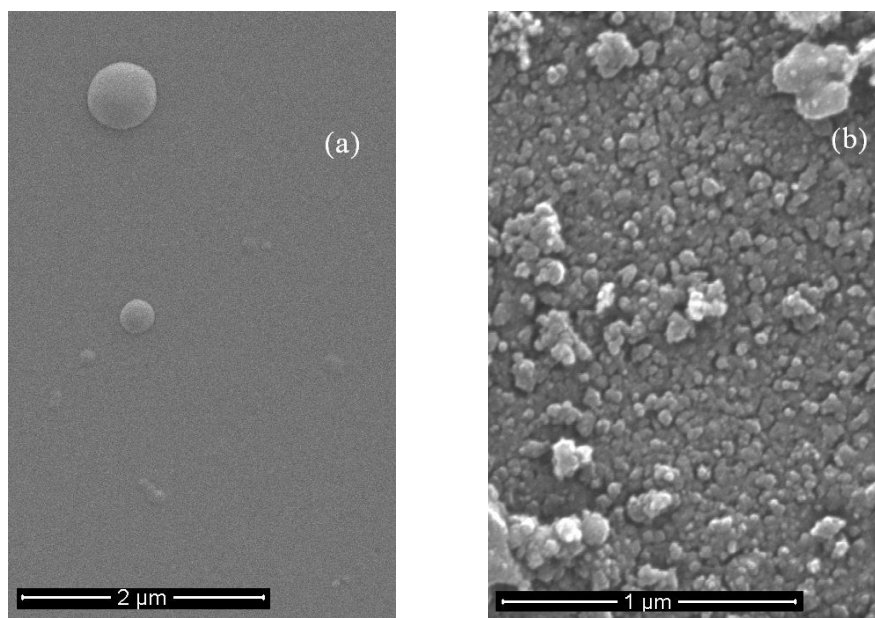
Figure 4.9 SEM images of the plasma polymerized fluorene thin films at (a) R1 and (b) R2

4.4 Conclusion

We presented the characterizations of the plasma polymerized fluorene thin films synthesized by double discharges system on silicon wafer and glass substrates at different locations in the reactor. The FTIR, the UV-visible and XPS spectra reflect the fluorene structure and the substitution pattern formation at the produced thin films. The XRD and UV-vis results revealed that the produced samples are amorphous and the optical energy band gap values of the deposited and iodine doped samples would have potential applications at semiconductor devices. And, it is essential to study the optimum doping time where it is necessary.

4.5 References

[1]   B.S. Ong, Y. Wu, Y. Li, P. Liu, H. Pan, Chem. A Eur. J. 14 (2008) 4766.

[2]   J.T. Mabeck, G.G. Malliaras, Anal. Bioanal. Chem. 384 (2006) 343.

[3]   V. Saxena, B.D. Malhotra, Curr. Appl. Phys. 3 (2003) 293.

[4]   M.T. Bernius, M. Inbasekaran, J. O'Brien, W. Wu, Adv. Mater. 12 (2000) 1737.

[5]   Q. Zhao, S.-J. Liu, W. Huang, Macromol. Chem. Phys. 210 (2009) 1580.

[6]   S. Chen, H.-H. Lu, C.-W. Huang, Adv. Polym. Sci. 212 (2008) 49.

[7]   E. Bundgaard, F. Krebs, Sol. Energy Mater. Sol. Cells 91 (2007) 954.

[8]   F. Zhang, K. Jespersen, C. Bjostrom, M. Svensson, M. Andersson, V. Sundstrom, Adv. Funct. Mater. 16 (2006) 667.

[9]   M. Fukuda, K. Sawada, K. Yoshlno, J. Polym. Sci. Part A Polym. Chem. 31 (1993) 2465.

[10]   M. Leclerc, J. Polym. Sci. Part A Polym. Chem. 39 (2001) 2867.

[11]   R. Abbel, A.P.H.J. Achenning, E.W. Meijer, J. Polym. Sci. Part A Polym. Chem. 47 (2009) 4215.

[12]   A. Hiratsuka, I. Karube, Electroanalysis 12 (2000) 695.

[13]   H. Biederman, Plasma Polymer Films, Imperial College Press, London, 2004.

[14]   H. Goktas, M. Udrea, G. Oke, A. Alacakir, A. Demir, J. Loureiro, J. Phys. D. Appl. Phys. 38 (2005) 2793.

[15]   H. Goktas, E. Kacar, A. Demir, Spectrosc. Lett. 41 (2008) 189.

[16]   H. Goktas, F.G. Ince, Plasma Process. Polym. 6 (2009) 126.

[17]   G. Schaefer, K.H. Schoenbach, in:, M.A. Gundersen, G. Schaefer (Eds.), Phys. Appl. Pseudosparks NATO ASI Ser. B, Springer US, New York, 1990, pp. 55–76.

[18]   V.I. Kolobov, L.D. Tsendin, Plasma Sources Sci. Technol. 4 (1995) 551.

[19]   M.S. Silverstein, I. Visoly-Fisher, Polymer (Guildf). 43 (2002) 11.

[20] H. Goktas, F.G. Ince, A. Iscan, I. Yildiz, M. Kurt, I. Kaya, Synth. Met. 159 (2009) 2001.

[21] J.B. Lambert, H.F. Shurvel, D.A. Lightner, R.G. Cooks, Organic Structural Spectroscopy, Prencite-Hall, New Jersey, USA, 1998.

[22] D. Pavia, G. Lampman, G. Kriz, J. Vyvan, Introduction to Spectroscopy, 4th ed., Brooks Cole, Fort Worth, 2001.

[23] B.H. Stuart, Infrared Spectroscopy: Fundamentals and Applications, John Wiley & Sons, Ltd, New York, 2004.

[24] H. Kenzo, Handbook of Ultraviolet and Visible Absorption Spectra of Organic Compounds, Plenum Press Data Division, New York, 1967.

[25] J.W. Robinson, Practical Handbook of Spectroscopy, CRC Press, Boca Raton, FL, 1991.

[26] J. Pankove, Optical Processes in Semiconductors, Prencite-Hall, Englewood Cliffs, NJ, 1971.

[27] J.L. Yagüe, S. Borrós, Plasma Process. Polym. 9 (2012) 485.

[28] B. Paosawatyanyong, P. Kamphiranon, W. Bannarakkul, Y. Srithana-anant, W. Bhanthumnavin, Surf. Coatings Technol. 204 (2010) 3053.

[29] J. John, S. Sivaraman, S. Jayalekshmy, M.R. Anantharaman, J. Phys. Chem. Solids 71 (2010) 935.

[30] P. Coppo, R. Schroeder, M. Grell, M.L. Turner, Synth. Met. 143 (2004) 203.

[31] A. Bilici, İ. Kaya, M. Yıldırım, Eur. Polym. J. 47 (2011) 1005.

[32] R.M. France, R.D. Short, Langmuir 14 (1998) 4827.

[33] G. Beamson, D. Briggs, High-Resolution XPS of Organic Polymers: The Scienta ESCA 300 Database, John Wiley & Sons, Ltd, Chichester, West Sussex, England, 1992.

[34]   S.N. Jampala, M. Sarmadi, S. Manolache, F.S. Denes, J. Appl. Polym. Sci. 107 (2008) 1686.

[35]   Y.-S. Gal, S.-H. Jin, H.-S. Lee, S.Y. Kim, Macromol. Res. 13 (2005) 491.

[36]   K.K. Ostrikov, S. Xu, Plasma-Aided Nanofabrication From Plasma Sources to Nanoassembly, Wiley-VCH, Weinheim, Germany, 2007.

CHAPTER 5

SYNTHESIS AND CHARACTERIZATION OF FLUORENE-TYPE THIN FILM UNDER BIPHENYL/ METHANE AND BIPHENYL/ ETHYLENE RF PLASMA ENVIRONMENT

5.1 Introduction

Fluorene and its derivatives have attracted appreciable attention in π-conjugated organic materials due to their excellent physical and chemical properties [1–5]. Their stable and highly blue light-emitting property makes them suitable for organic light emitting diodes (OLEDs) [6–10]. They are very attractive materials with good charge mobility [11] and facility of construction ultrathin layers [12] for photovoltaic applications [13,14]. The flexible behavior of backbone structure of the fluorene makes it possible to obtain almost the entire visible colors range with high efficiency for devices with fluorene derivatives [15–17]. In the deposition methods, producing thin films via plasma is a very influential way to improve the chemical and physical properties of the films with the various plasma species, such as electrons, ions, and radicals, etc [18–24]. The properties of the generated film depend on the kinetic energy of the ions [25,26]. Therefore the positive ion bombardment plays a significant role in determining the film quality, stoichiometry, topography, re-emission coefficient, and deposition rate [27–32]. The surface of the substrate can be bombarded with the positive ions by applying a negative bias voltage between the substrate holder and the grounded reactor. Thus, ions exchange higher energy with atoms on the surface, which causes an increase in the average energy of these atoms [26]. The fluency of the ions provides an easier electrical controllability of chemical pathway. In our study, the biphenyl, which is accepted a possible source of aromatic rings [23,33,34], was separately combined with methane and ethylene to produce the fluorene-type thin films from the plasma of these mixtures, and they were investigated by AFM, UV-visible spectroscopy,

ellipsometry, XRD and conductivity after doping with iodine. Plasma environment was characterized for chemical composition by residual gas analysis (RGA).

5.2 Experimental Details
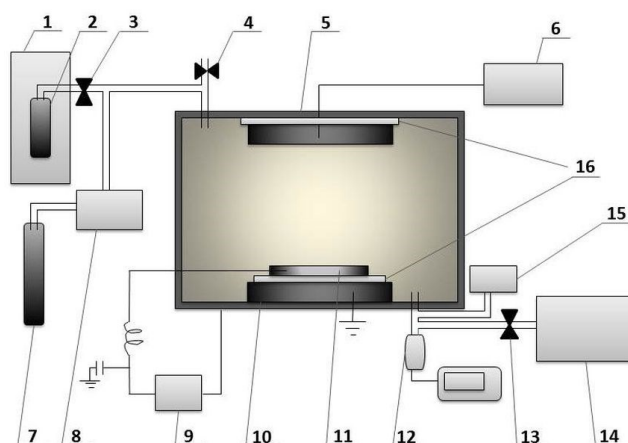
Figure 5.1 Scheme of plasma reactor: 1, heater; 2, container of biphenyl; 3, shut-off valve of biphenyl; 4, purge valve; 5, upper electrode; 6, 13.56 MHz RF power generator with matching network; 7, CH_4 or C_2H_4 gas cylinder; 8, mass flow controller; 9, negative DC power supply; 10, bottom electrode (grounded); 11, holder for samples; 12, Baratron type capacitance manometer; 13, valve; 14, mechanical vacuum pump; 15, RGA mass spectrometer; 16, insulator

The system is a stainless-steel vacuum chamber with two parallel electrodes; upper one isolated connected to 13.56 MHz rf power and the chamber is grounded (Figure 5.1). The substrates are placed on a holder with negative bias voltage. Solid biphenyl (purchased from Sigma-Aldrich Company, Milwaukee WI), melting at 69°C, was introduced into heated reservoir and degased down to base pressure of the installation before heating the device. When the biphenyl became volatile enough (reservoir thermostated at 130°C), vapors were mixed with methane or ethylene and introduced in the chamber; the total pressure was controlled at 200 mTorr with a MKS butterfly valve. Plasma discharge was activated and the negative potential, between the holder and chamber, was applied simultaneously. The deposition time was 20 minutes for each sample.

Plasma experiments have been conducted using a design of experiments (20 experiments set, Design-Expert 8 software) with independent parameters: RF power

(70 - 250 W), CH_4 or C_2H_4 flow rate (0 – 7 sccm) and negative bias voltage (-120 – 0 V). The volatile compounds from vacuum environment were recorded at the exhaust of the chamber by residual gas analysis (RGA) mass spectrometer using a Spectra Products, MKS (Wilmington, MA) instrument with a 200 amu Vac-Check analyzer and 1E-09 scanning range. The nanostructual and nanomechanical properties of the surface of the deposited films were investigated by Atomic Force Microscope (AFM) (Pico Scan, Molecular Imaging Inc. Tempe, AZ) in contact mode with silicon nitride nanoprobe for scanning area of 6×6 μm^2. The thickness of the thin films was measured through ellipsometry using an VASE Instruments (J.A. Woollam Co., Inc.). The transmittance spectra were recorded by UV-visible spectroscopy, ASEQ Instruments, LR1 compact spectrometer; with a range of 200-1200nm; resolution <5nm, and with DT-MINI-2 Deuterium Tungsten Halogen Lamp (Ocean Optics). The thin films were doped by Iodine (I_2) for different time periods inside a vacuum desiccator, and the changes after doping were investigated by UV-visible spectroscopy. Structural orderings of the thin films were studied by a Rigaku Miniflex standard X-ray diffractometer (Cu K_α, λ = 1.54 A˚).

5.3 Results and Discussion

5.3.1 Fabrication Under Biphenyl/ Methane RF Plasma Environment

5.3.1.1 RGA Mass Spectrometer

In plasma, both of the excited biphenyl and methane start to dissociate their fragments after transferring sufficient energy from the inelastic collisions. The molecule of methane, since it has one carbon atom in its structure, behaves more active inside the plasma. In addition, methane consumes more energy during the fragmentation and formation of a bigger molecule structure. Reaction 5.1 shows the primary fragmentation of the methane and some stable molecules generated from reactions of the methane with methylene radicals [35]. In the methane discharge at low pressure, the amount of ·CH_3 is observed at much higher level than ·CH_2 [36].

$$CH_4 + e^- \nearrow CH_3^{\cdot} + H^{\cdot} + e^-$$
$$\searrow CH_2^{\cdot} + H_2 + e^-$$

methane

$$CH_2^{\cdot} + CH_4 \longrightarrow H_3C\!-\!CH_3$$

ethane

$$H_3C\!-\!CH_3 + e^- \longrightarrow H_2C\!=\!CH_2 + H_2 + e^-$$

ethylene
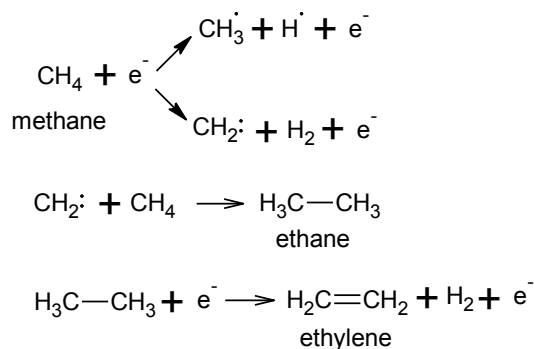
(Reaction 5.1)

The molecule of biphenyl is an aromatic hydrocarbon consisting of two benzene rings connected by a C-C bond. The aromatic hydrocarbons are more stable and usually need high energies for aromatic ring cleavage. Since π-electrons are delocalized and easier to move than a σ-electron, in the aromatic compounds the ionization generally takes place in the π-electron system [37]. When the biphenyl is exposed to plasma discharge, the first break is expected at the C-C bond between two benzene rings and then, when the fragmentation starts for a ring, two carbon atoms are simultaneously separated [38] and dissociations of H-atoms from benzene rings follow this division.
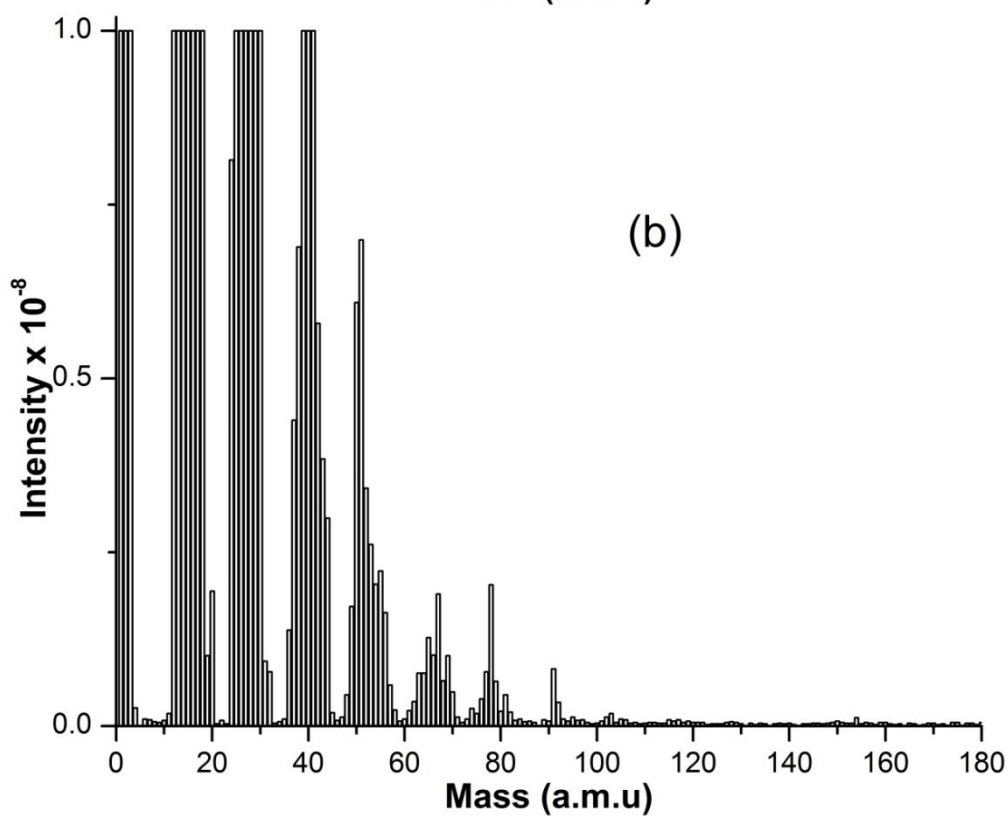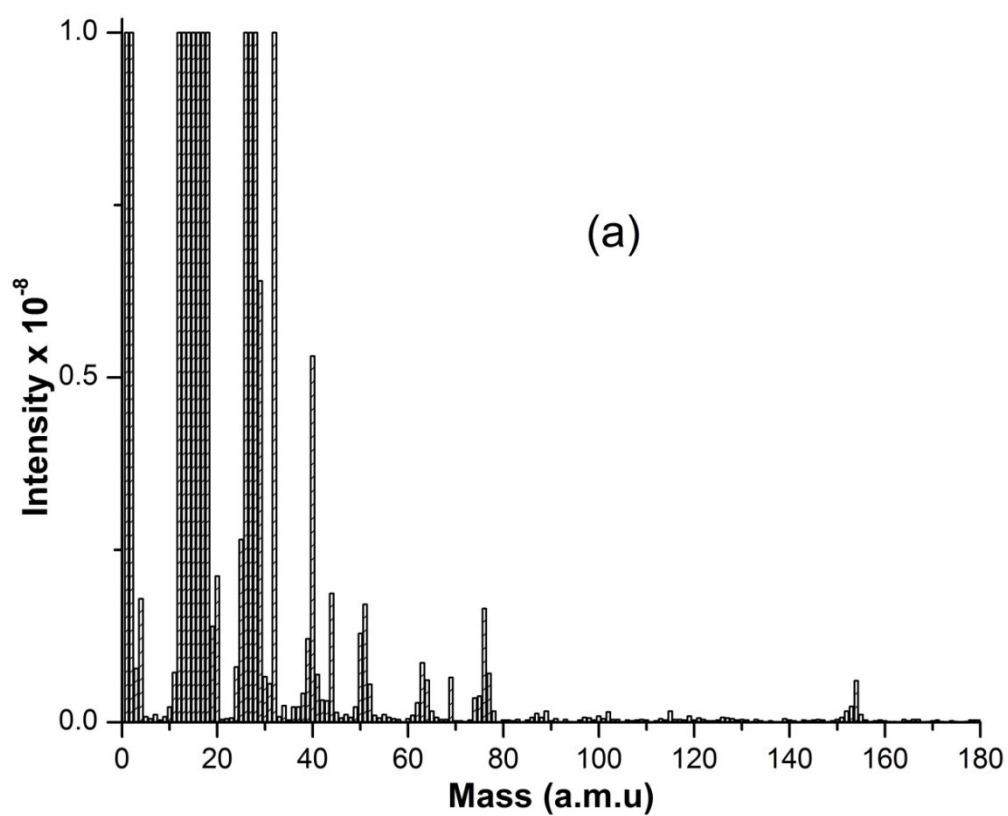
Figure 5.2 RGA mass spectra of volatile compounds (a) before and (b) during plasma discharge

Consequently, during methane / biphenyl plasma discharge it was expected to see an increase in the amount of $C_2H_4^+$ (*m/z* 28) and $C_2H_5^+$ (*m/z* 29) ions, and also $C_2H_2^+$, $C_3H_3^+$ from aromatic compounds. After the dissociation, the fragments continued to interact with electrons, ions and free radicals inside plasma, which made them activated. These active fragments started to recombine and formed new compounds and fragments in a short time. When the molecule of fluorene was generated from the mixture of biphenyl and methane, the Reaction 5.2 could be suggested. However, since energy density in the plasma was relatively high, besides this mechanism, various other chemical pathways were possible. Figure 5.2 showed the number of molecules before and during plasma discharge; possible compounds were listed on Table 5.1.
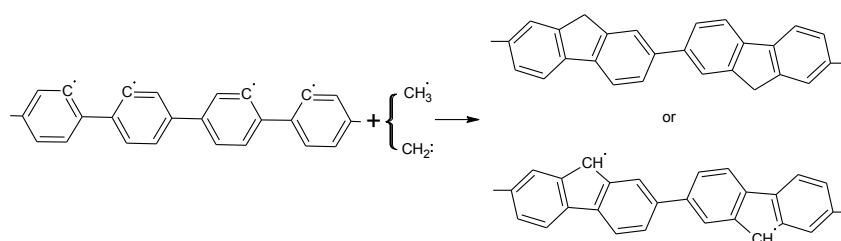
(Reaction 5.2)
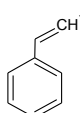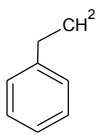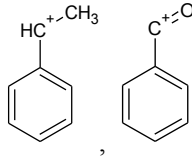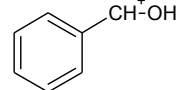
The generations of hydrocarbons from the RGA spectrometry, such as alkanes, alkenes and alkynes, could be clearly seen by the recombination. The mass 44 showed the formation of propane and its fragments were represented by the masses of 40(C_3H_4), 41($C_3H_5^+$), 42($C_3H_6^+$) and 43($C_3H_7^+$). The fragments of butane, C_4H_{10}, were indicated by the masses of 53($C_4H_5^+$), 54($C_4H_6^{++}$), 55($C_4H_7^+$), 56($C_4H_8^{++}$) and 57($C_4H_9^+$). We should emphasize that propyl ion $C_3H_7^+$ and butyl ion $C_4H_9^+$ showed important stabilities in the branched structures. There were also the fragments of pentane, C_5H_{12}, such as masses 65, 66, 67, 68, 69 and 70 with the formulas $C_5H_6^{++}$, $C_5H_5^+$, $C_5H_7^+$, C_5H_8, $C_5H_9^+$ and, respectively, C_5H_{10}. The ions of $C_6H_9^+$ and $C_6H_{10}^+$ at 81 and 82 mass were also present in mass spectra and showed the presence of hexane. Similar fragments could include double or triple bonds and also cyclic structures. In plasma depositions, the macromolecular compounds were generally prone to have crosslinking and branched structures [39]. Branched structures were significantly different from linear structures with their tendency of fragmentation at

the branches; the loss of a methyl group (-CH$_3$) was also common in branched compounds [37,38,40,41].

Table 5.1 The list of the compounds seen from RGA spectrometry

Mass	Chemical Structure	Formula	Ref.	Mass	Chemical Structure	Formula	Ref.
40	H$_2$C=CH^{2+}	C$_3$H$_4$	[38,42]	67	H$_3$C—...—CH$_2^+$; HC$^+$...—OH	C$_5$H$_7^+$, C$_4$H$_3$O$^+$	[38,42]
41	H$_2$C=CH$_2^+$	C$_3$H$_5$	[38,42]	68	H$_3$C—...—CH$_2$; HC^{2+}...—OH	C$_5$H$_8$, C$_4$H$_4$O^{++}	[38,42]
42	H$_3$C—CH^{2+}	C$_3$H$_6^+$	[38,42]	69	H$_2$C$^+$—...—CH$_3$; H$_2$C$^+$...—OH	C$_5$H$_9^+$, C$_4$H$_5$O$^+$	[38,42]
43	H$_3$C—CH$_2^+$	C$_3$H$_7^+$	[38,42]	70	H$_3$C—...—CH$_3$; H$_2$C—...—OH	C$_5$H$_{10}$, C$_4$H$_6$O	[38,42]
44	H$_3$C—CH$_3$; O=C=O	C$_3$H$_8$, CO$_2$	[38,42]	81	H$_2$C$^+$—...—CH$_3$; C$^+$≡...—OH	C$_6$H$_9^+$, C$_5$H$_5$O$^+$	[38,42]
53	H$_3$C—≡—CH$_2^+$	C$_4$H$_5^+$	[38,42]	82	H$_2$C$^+$—...=CH$_2$; HC≡...—OH	C$_6$H$_{10}^+$, C$_5$H$_6$O	[38,42]
54	H$_3$C—=—CH^{2+}	C$_4$H$_6$	[42]	91	CH$_2^+$ (benzyl ring)	C$_7$H$_7^+$	[38,42]

Table 5.1 (continued)

55		$C_4H_7^+$, $C_3H_3O^+$	[38,42]	92		C_7H_8	[38,42]
56		$C_4H_8^+$	[38,42]	103		$C_8H_7^+$	[38,41, 42]
57		$C_4H_9^+$	[38,42]	104		$C_8H_8^{++}$	[38,41, 42]
65		$C_5H_5^+$	[38,42]	105		$C_8H_9^+$, $C_7H_5O^+$	[38,41, 42]
66		$C_5H_6^+$	[42]	106		$C_7H_6O^+$	

Spectra showed at m/z 91 the stable tropylium ion, $C_7H_7^+$, and also the ion $C_7H_8^+$ at m/z 92 produced by rearrangements. These ions could be formed by the combination of benzene with methyl group and their abundance was important for the fluorene mechanism; the existence of these fragments with higher intensity was in a direct relation with the forming of fluorene thin film. Reaction 5.3 showed the possible mechanism of these fragments during the formation of the fluorene and derivatives. The presence of methyl benzyl (m/z 105, $C_8H_9^+$), as well as dehydrogenation products of m/z 104 and 103, $C_8H_8^{++}$ and $C_8H_7^+$ [38,41], could be corresponded to the generation of fluorene derivatives.
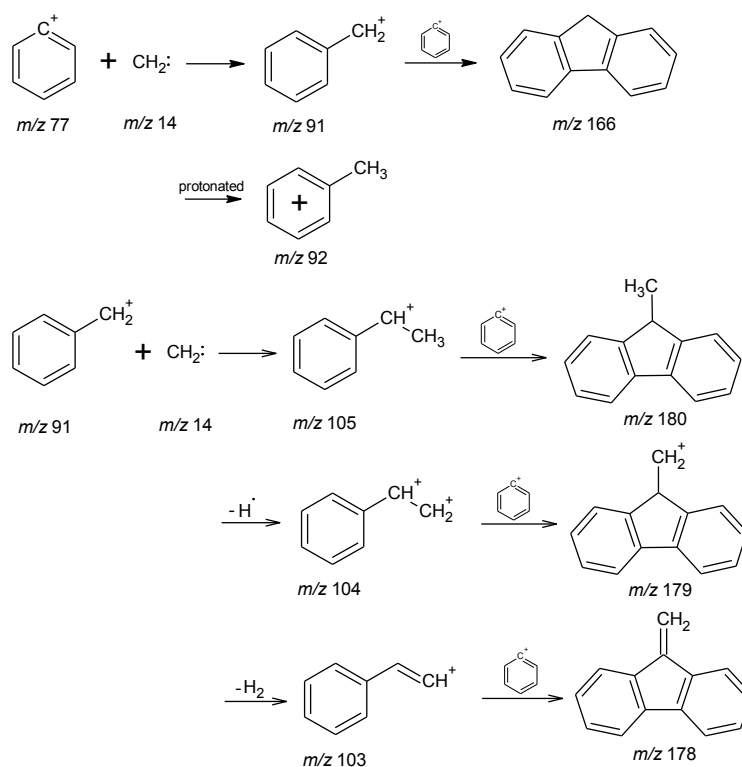
(Reaction 5.3)

When the plasma macromolecular compounds were exposed to the open air, they reacted with the oxygen and water vapor [43] due to trapped free radicals. Also contamination of plasma environment with air and moisture by leaks or absorbed / absorbed compounds could produce oxygen derivatives. Therefore, it was generally possible to see oxygen in the plasma polymers. These components could be occurred by directly combining the hydroxyl group to fragments of the biphenyl and the methane. The mass 44 corresponded to CO_2, but also referred to propane and, because of presence of its fragments in the spectra it could be considered that propane had higher probability. We could consider other masses such as 55, 67, 68, 69 and 70 belonging to $C_3H_3O^+$, $C_4H_3O^+$, $C_4H_4O^{++}$, $C_4H_5O^+$ and, respectively, C_4H_6O; the presence of fragments of butane and pentane suggested hydro carbonate structures. The other masses that could indicate presence of oxygen were $C_5H_5O^+$ and C_5H_6O with masses of 81 and, respectively, 82. In addition, although their intensities were low, there were some peaks showing derivatives of fluorene with carboxyl and hydroxyl group; these peaks were at m/z 105 and m/z 106 with structure of $C_7H_5O^+$ and $C_7H_6O^+$.
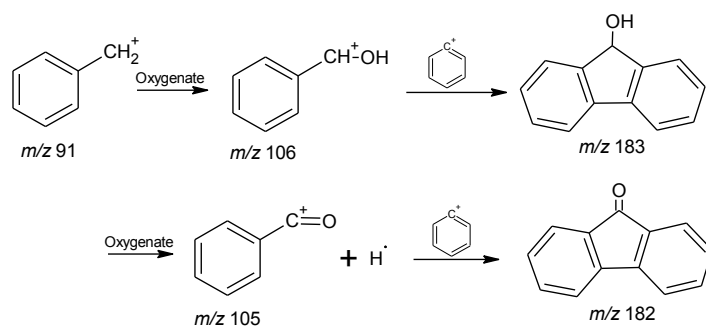
(Reaction 5.4)

We expected to obtain the fluorene-type thin films when corresponding fragments have higher intensities. Therefore, the ratios of the mass intensities during and before plasma discharge for all experiments were calculated and analyzed numerically using Design Expert software. The regressions were fitted to remove the hierarchically inferior terms by analysis of variance (ANOVA) and the equations are:

$$\textbf{\textit{ratio of }} \textbf{91} = 7.072 + 0.071003V + 6.9014f - 0.0257P$$
$$\textbf{\textit{ratio of }} \textbf{92} = 0.163 + 0.00075V - 0.0064f - 0.0014P - 0.000005VP + 0.000004P^2 \quad (5.1)$$

Where V is the bias voltage, f is the CH_4 flow rate and P is the power of the plasma discharge. Figure 5.3 showed that ions 91 and 92 give the highest intensities at higher plasma power, bias voltages and CH_4 flow rates.
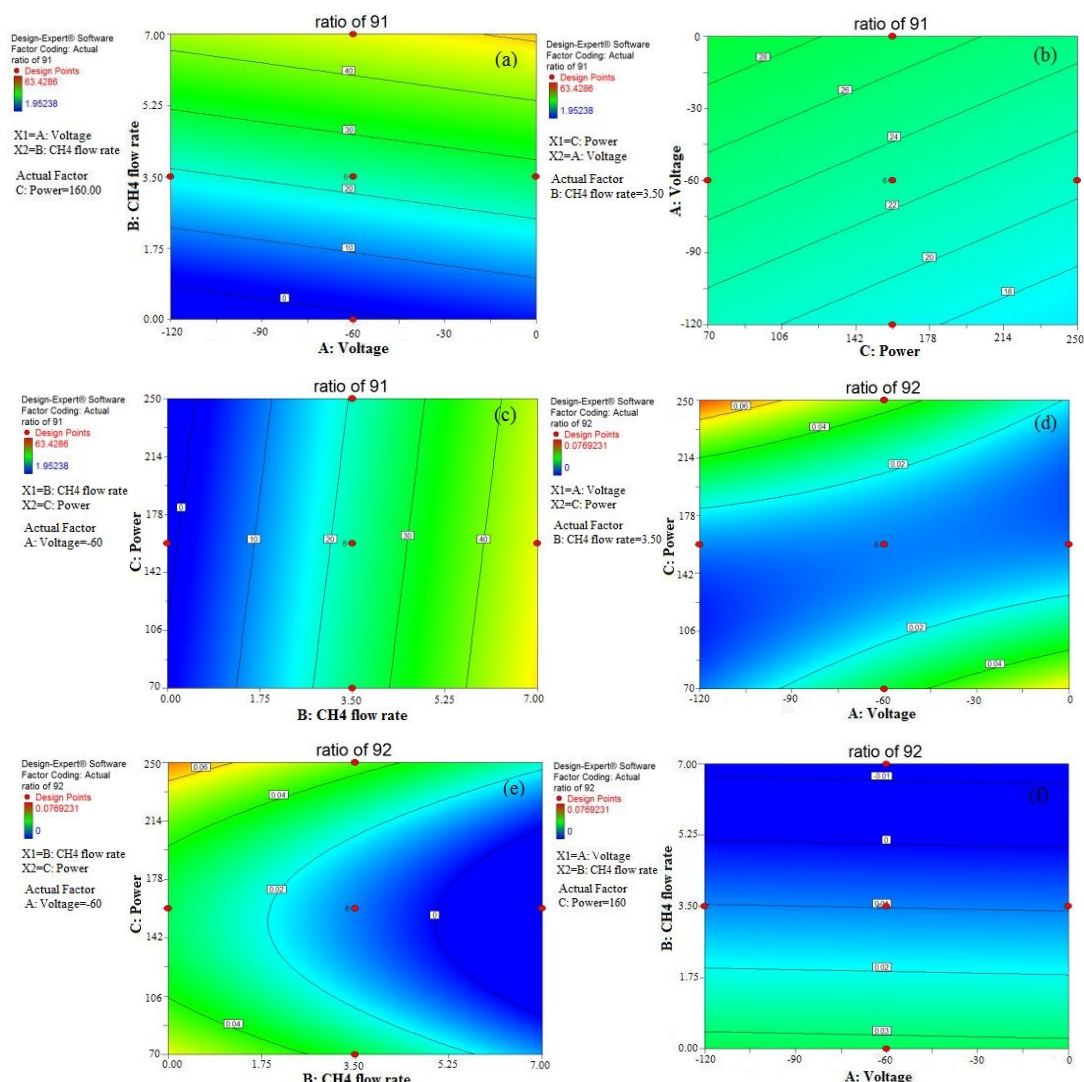
Figure 5.3 Design Expert diagrams for intensity ratios of $C_7H_7^+$ (91) and $C_7H_8^+$ (92) ions

5.3.1.2 UV-visible Spectroscopy

The optical properties of the thin films were investigated via UV spectroscopy and the results were indicated in Table 5.2. Since the energies, needed for transitions of the n or π electrons to the π^* excited state, are equivalent to the absorption bands into the ultraviolet-visible region (200 to 700 nm), the applications of absorption spectroscopy to organic compounds are generally based on these transitions. The absorbance peaks of our thin films are attributed to $\pi \rightarrow \pi^*$ excitation and the π orbitals play the most important role on the energy band gap for the most amorphous

C:H materials. The band transitions of fluorene are generally presented at peaks of 206, 260, 290, and 300 nm [44,45].

The light absorbed by thin film gives the peaks at different wavelengths due to material structures. In this work, it was investigated how the light absorption peak shifts according to plasma parameters. Increasing the ability of conjugation of the structure caused a shifting in the maximum absorption wavelength to higher values. The UV spectra of biphenyl and methane plasma deposited layers showed changes between 292.3 and 303.9 nm.
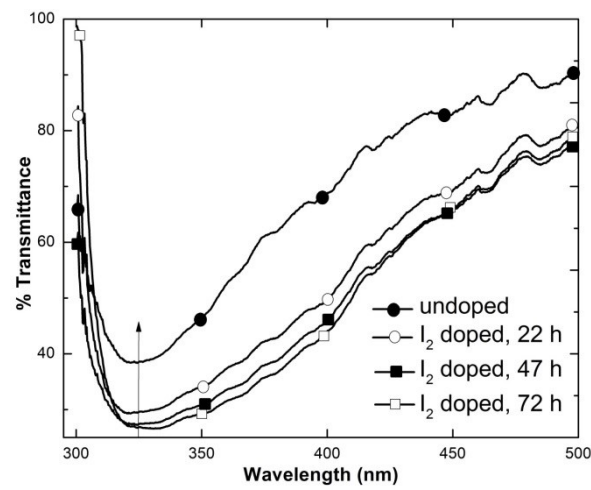
Figure 5.4 Transmittance of thin films undoped and doped with iodine for 22 hours, 47 hours, and 72 hours

When the absorption coefficient α refers to high absorption region, where is $\alpha \geq 10^4$ cm^{-1}, a relation about the optical energy band gap was defined by Tauc [46,47].

$$\alpha h\nu = B\left(h\nu - E_g\right)^n \tag{5.2}$$

Where $h\nu$ is the photon energy, B is an energy-independent constant, and E_g is the optical energy band gap and n is a variable depending on transition; 1/2 and 2 correspond to direct and, respectively, indirect allowed transition, 3/2 and 3 correspond to direct and, respectively, indirect forbidden transition. To find this

variable, we need to redefine the Equation (5.2) to obtain the Equation (5.3) and to plot dln($\alpha h v$) versus $h v$.

$$\frac{d\ln(\alpha h v)}{h v} = \frac{n}{(h v - E_g)} \tag{5.3}$$

From the graph of dln($\alpha h v$) versus $h v$ (Figure 5.5), the peak gave the approximate value of the energy band gap [48] and by using this value on the whole experiment data, we could plot a linear regression of $\ln(\alpha h v)$ and $\ln(h v - E_g)$; the slope gave the n value of 0.504 ± 0.002, supporting a direct allowed band transition. To obtain the energy band gap (E_g), extrapolation of the $(\alpha h v)^2$ vs $h v$ was taken for $(\alpha h v)^2 = 0$ and the value was read from the point of intersection. The E_g values of all experiments were found by this method and the results indicate values between 3.15 and 3.54 eV (Table 5.2).
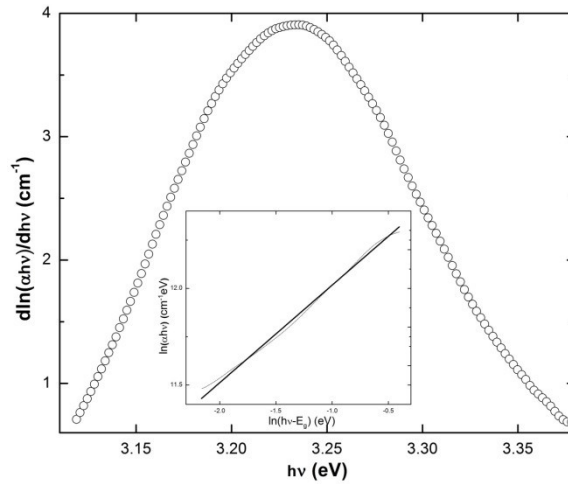
Figure 5.5 Plots of dln($\alpha h v$)/$dh v$ versus $h v$ and $\ln(\alpha h v)$ versus $\ln(h v - E_g)$ (inset figure)
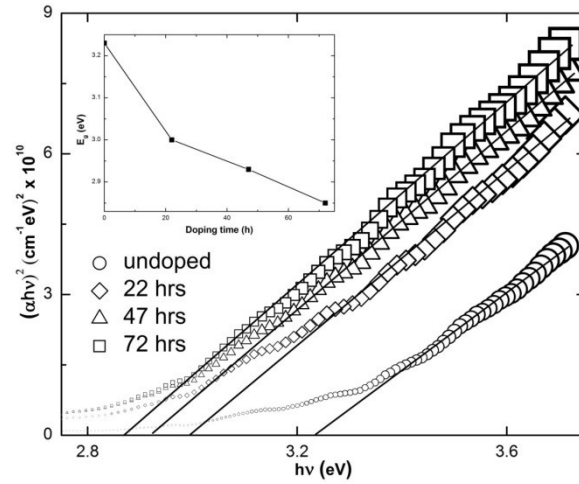
Figure 5.6 Plots of $(\alpha h\nu)^2$ versus photon energy $h\nu$ and E_g versus doping time (inset figure) of undoped and doped thin films

The light absorption wavelength exhibited the maximum shifting at the high power and bias voltage values and it could be asserted that the conjugation ability of the structure formed in plasma was more effective at these parameters. The result of the ANOVA analysis gave the Equation (5.4) and a result of the experiment done by using suggested optimal parameters, the peak wavelength was 323 nm and the energy band gap was 3.23 eV.

$$wavelength(\lambda) = 295.2704 - 0.01261V - 0.48054f + 0.02382P \qquad (5.4)$$

The films were exposed to iodine (I_2) for different time periods: 22, 47, and 72 hours. The samples were placed on a grid into a desiccator and the iodine was placed at the bottom of the desiccator; during the doping process, the desiccator was kept under vacuum. By this method, the light absorption wavelength was shifted as shown in Figure 5.4. The energy band gap of the thin films decreased by the iodine doping process and the values obtained from the graph of $(\alpha h\nu)^2$ and $h\nu$ are 2.99, 2.92 and 2.87 for 22, 47 and, respectively, 72 hours.

Table 5.2 List of the results according to independent parameters

No	V (Volt)	f (sccm)	P (W)	λ (nm)	E_g (eV)	t (a.u.)	T (Å)	R_q (Å)	R_a (Å)	R_z (nm)	d
1	-24	1.42	106	298.6	3.23	0.34718	1666.0	803.7	686.5	363.1	4.388
2	-120	3.50	160	296.0	3.23	0.27907	1545.3	1380.5	1183.9	711.8	0.666
3	-24	5.58	213	297.6	3.17	0.22645	1654.7	1173.3	1012.8	470.5	2.416
4	-60	7.00	160	296.0	3.42	0.44491	1685.4	1055.8	900.3	451.6	3.277
5	-60	3.50	160	297.6	3.42	0.36559	1669.1	862.6	738.5	364.9	2.805
6	-60	3.50	160	298.1	3.36	0.36634	1677.9	1118.2	956.8	467.9	1.416
7	0	3.50	160	293.9	3.39	0.38923	1650.4	1981.4	1700.4	785.0	3.833
8	-60	3.50	70	292.3	3.52	0.57135	1631.9	2051.7	1758.4	867.0	3.333
9	-60	3.50	250	298.6	3.25	0.24076	1422.9	1249.5	1068.4	518.0	2.694
10	-95	1.42	213	301.3	3.15	0.36688	1724.4	788.8	587.4	1116.2	0.972
11	-95	5.58	213	298.1	3.37	0.25937	1709.6	1093.7	944.4	422.5	0.555
12	-24	5.58	106	296.0	3.54	0.58563	1621.8	992.6	854.3	442.0	0.444
13	-24	1.42	213	303.9	3.16	0.35576	1725.3	966.7	834.4	378.8	1.166
14	-60	3.50	160	297.6	3.46	0.41157	1642.8	279.8	233.7	242.2	3.638
15	-60	0.60	160	297.6	3.27	0.47091	1627.5	1436.4	1241.4	543.4	0.194
16	-60	3.50	160	298.6	3.38	0.32866	1600.9	1253.6	1083.7	492.1	4.277
17	-95	1.42	106	299.2	3.34	0.49257	1575.8	1025.3	886.0	466.6	0.250
18	-60	3.50	160	301.3	3.38	0.33794	1640.2	963.6	829.8	404.4	5.333
19	-60	3.50	160	299.7	3.36	0.35813	1616.8	1146.3	987.2	462.0	2.861
20	-95	5.58	106	300.2	3.40	0.36359	1736.0	763.1	551.1	1524.6	0.472

5.3.1.3 Thickness and Transmittance Measurements

The ellipsometry was used for measurement of film thickness (T) and the results were correlated with the transmittance (t); if the thickness is increasing, the transmittance decreases. The thickness had a complex response surface increasing by either raising or reducing the CH_4 flow rate and the bias voltage (red areas) (Figure 5.7). When the power was kept at low values, the thickness increased at higher values of flow rate and if the power was increased, the high thickness values were measured at lower and higher negative bias voltage values. It could be suggested that the reason of this variability was the behavior of methane and complicated reactions in plasma. The values of power, CH_4 flow rate, and the negative bias voltage parameters should be higher to obtain the lower transmittance and higher thickness. The predicted optimum parameters, shown on Table 5.3,

91

produced the films with thickness of 1690.2±16.4 A with angle of 68.042±0.195 and the transmittance of 0.145358. The quadratic equation for thickness and the regression for transmittance were the following:

$$T = 1609.8 + 31.3V + 9.4f - 62.1P - 32.5Vf - 25.2fP + 16.5f^2 + 89V^2P - 41VP^2 + 50V^2f^2$$

$$t = 0.4106 - 0.0003V + 0.091f - 0.0007P + 0.0006Vf - 0.000007VP - 0.0004fP \qquad (5.5)$$

Table 5.3 The optimal parameters with respect to Design Expert analysis

V (V)	f (sccm)	P (W)			
-95	1.42	213		λ (nm)	
				323.95	
-95	5.58	213	T (Å)		t (a.u.)
			1690.2		0.145358
-24	3.46	106	R_q (Å)	R_a (Å)	R_z (nm)
			948.3	736.7	1158.7
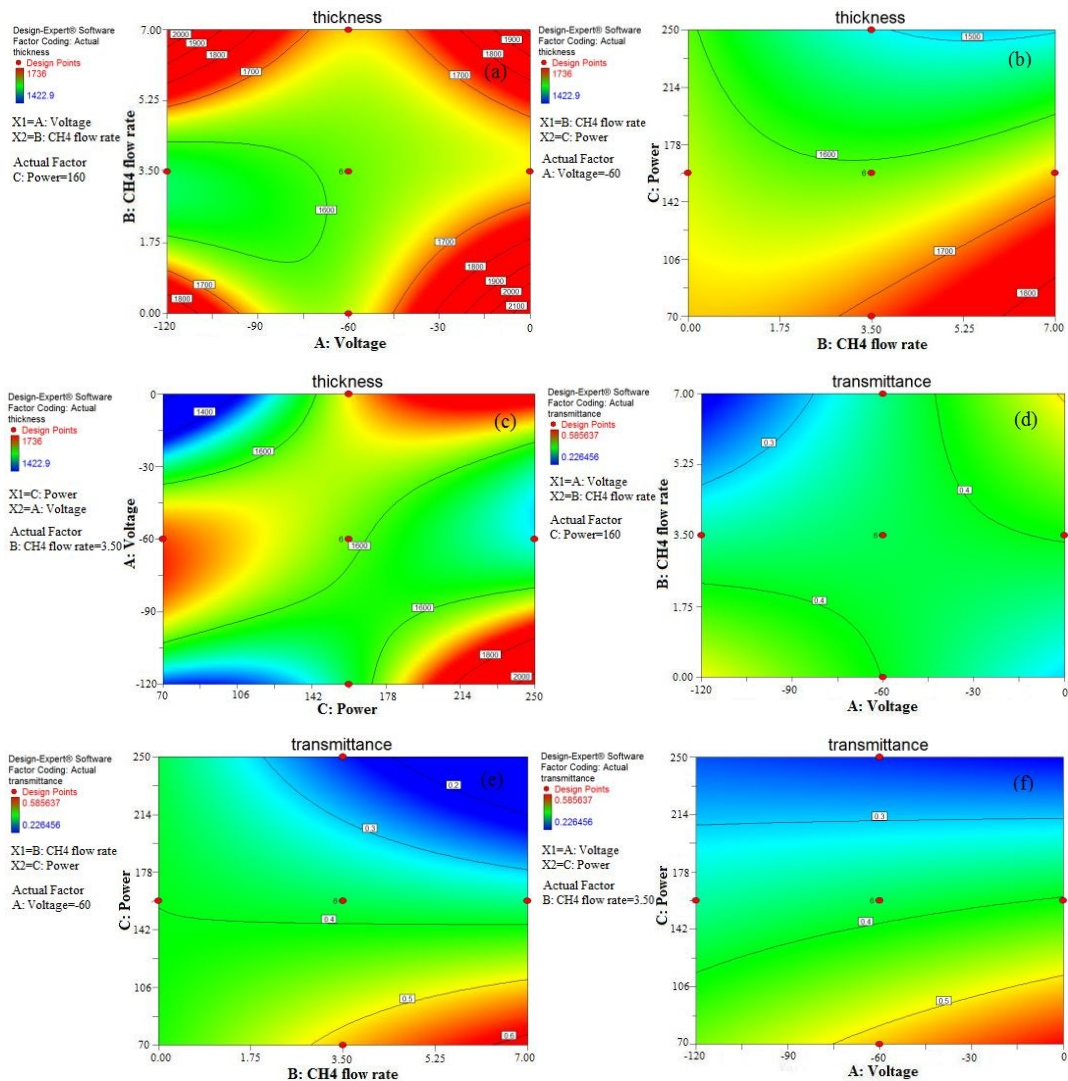
Figure 5.7 The diagrams for thickness and transmittance of the thin films

5.3.1.4 Atomic Force Microscope

The nanotopographical properties of the deposited films were analyzed by Atomic Force Microscope (AFM). The experimental findings of the standard deviation, R_q (rms roughness), the mean absolute deviation, R_a (ave roughness) and the maximum peak to valley, R_z (Rp-v) were presented in Table 5.2 with respect to the independent parameters. The average roughness R_a gives information about the relation between the surface and the center plane, and it is given by equating the volumes enclosed by the image of the surface above and below the plane, and it is determined as

$$R_a = \frac{1}{L_x L_y} \int_0^{L_x} \int_0^{L_y} |f(x,y)| dx dy \qquad (5.6)$$

Where *f(x, y)* is the surface relative to the center plane, and L_x and L_y are the dimensions of the surface. The root mean square roughness R_q is related with the standard deviation of the Z values, meaning the difference between the highest and lowest points within the sample area, and the R_q is calculated as

$$R_q = \sqrt{\frac{\sum(Z_i - Z_{avg})^2}{N}} \qquad (5.7)$$

Where Z_i is the current value, Z_{avg} is the average of the Z values, and N is the number of points within the given area. The maximum peak to valley R_z is the maximum observed range in the area of a substrate and describes the distance between the highest peak Z_{max} and lowest valley Z_{min}, and it is calculated as

$$R_z = Z_{min} - Z_{max} \qquad (5.8)$$

When the surface of the film is rather rough, peaks and valleys are clearly seen. The changes in average roughness and root mean square (rms) roughness give us information about the statistical variation of the height of points onto the film surfaces for all samples [49]. The surfaces can be compared in terms of these roughness parameters and when their values are close to each other the surface is found more uniform or points onto the surface has the same roughness for all area.
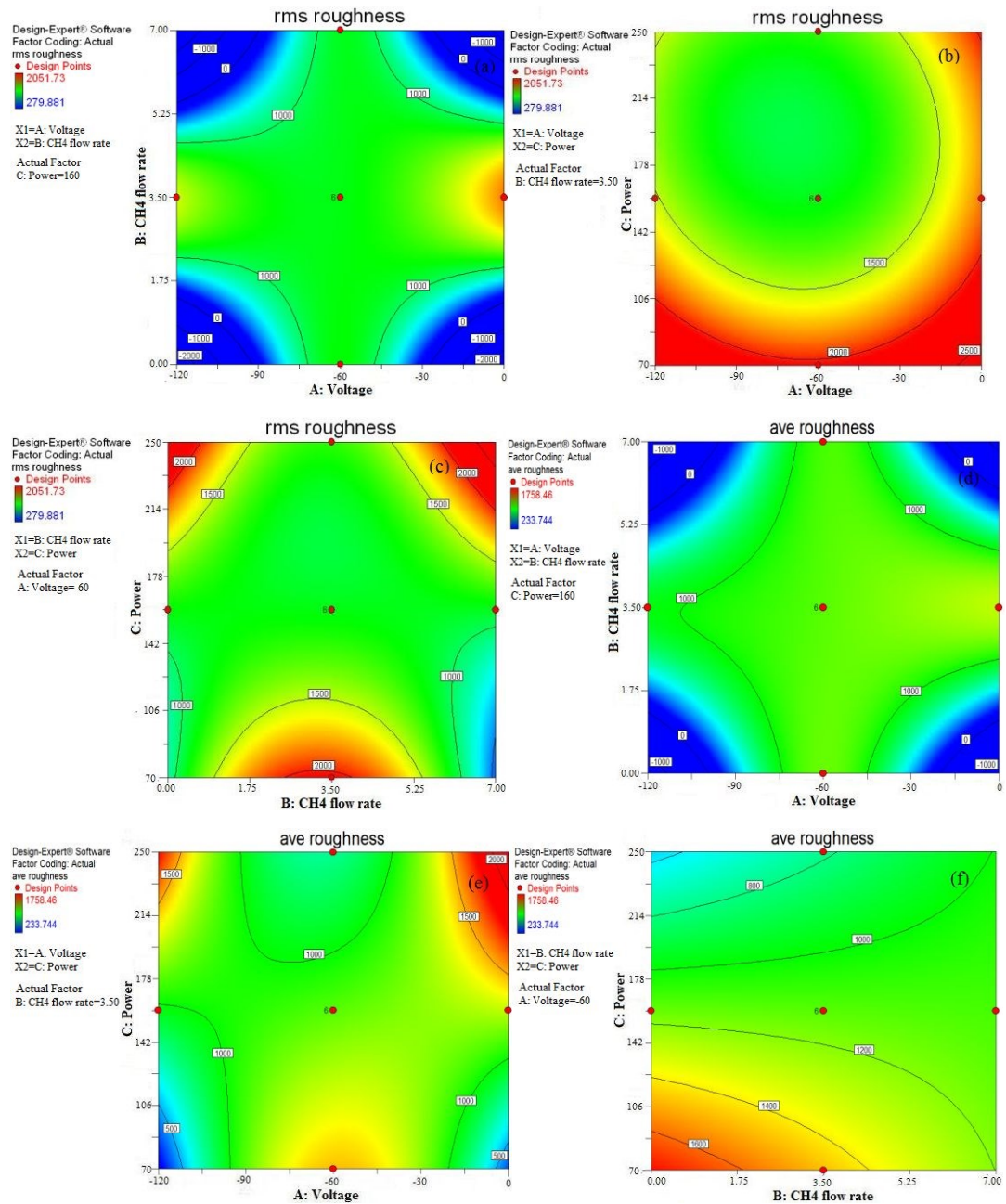
Figure 5.8 The images of ANOVA analysis for the rms roughness, the average roughness, the maximum peak to valley, and the density of nanostructures
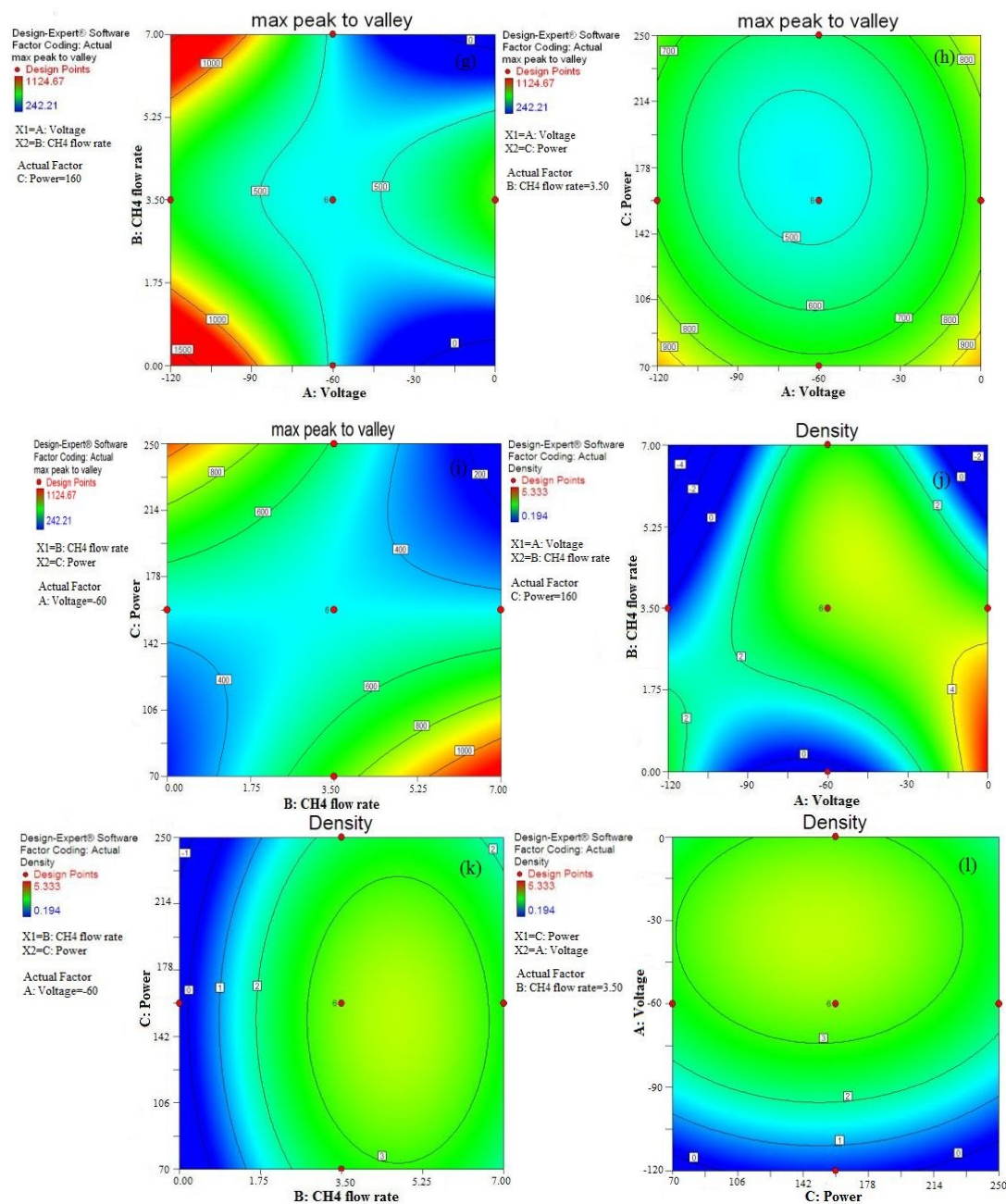
Figure 5.8 (continued)

According to images of the design expert (Figure 5.8), the rms roughness, ave roughness and max peak to valley showed high values at lower power (red areas) and the CH_4 flow rate in 1.50 - 5.50 range. Increasing the negative bias voltage caused the low rms and ave roughness values while high values were obtained for max peak to valley. The quadratic equations of the rms and ave roughness and of the max peak to valley were fitted by ANOVA to the equations presented below.

$$R_q = 1138 + 93V - 15f - 239P + 44Vf + 31VP + 73fP + 192V^2 + 181P^2 + 293f^2P - 560V^2f^2$$

$$R_a = 1599 + 1.2V - 145f - 1.4P - 1.4Vf + 0.1VP + 0.8fP + 0.001V^2P - 0.002V^2f^2 \quad (5.9)$$

$$R_z = 1775 + 27V - 152f - 12P - 6Vf - 0.1VP + fP + 0.1V^2 + 0.02P^2 + 0.04VfP - 0.1Vf^2$$

Maximizing these three terms of roughness, we got the parameters presented on the Table 5.3 (0.633 desirability). In AFM images, it was clear that the surfaces of thin films were not uniform and on the surface there were some peaks arisen from the structure of the films. The thin films were able to catch the light due to the presence of peaks and this property made the polymer thin films suitable for photo voltaic applications. The surface of thin film was exposed to various changes during the glow discharge because of impacts of the various ions, radicals, electrons, and molecules in plasma. The surface roughness of the thin films also depended on the nature of macromolecular compound and stability of the molecular structures. Therefore, reactivity of the fragments of the methane for reactions with biphenyl could be more effective on the surface.
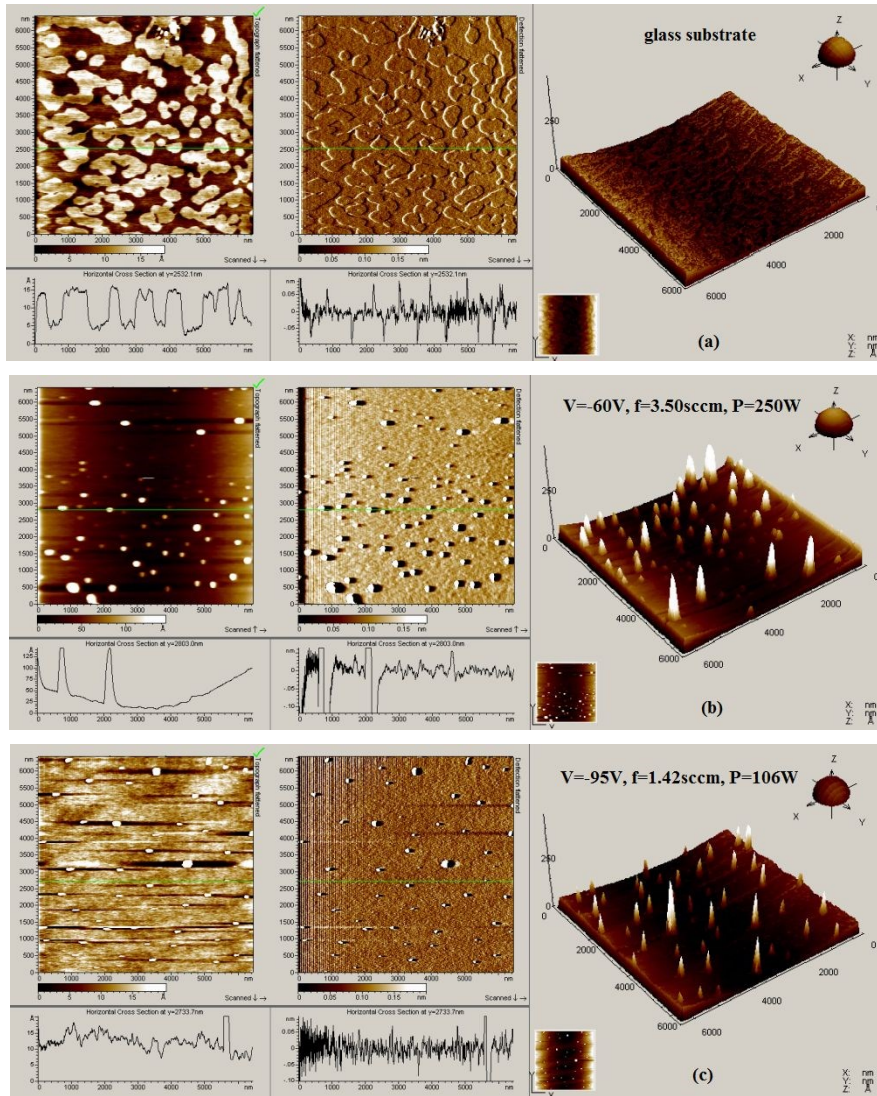
Figure 5.9 The AFM images of the glass substrate and the thin films with various plasma parameters
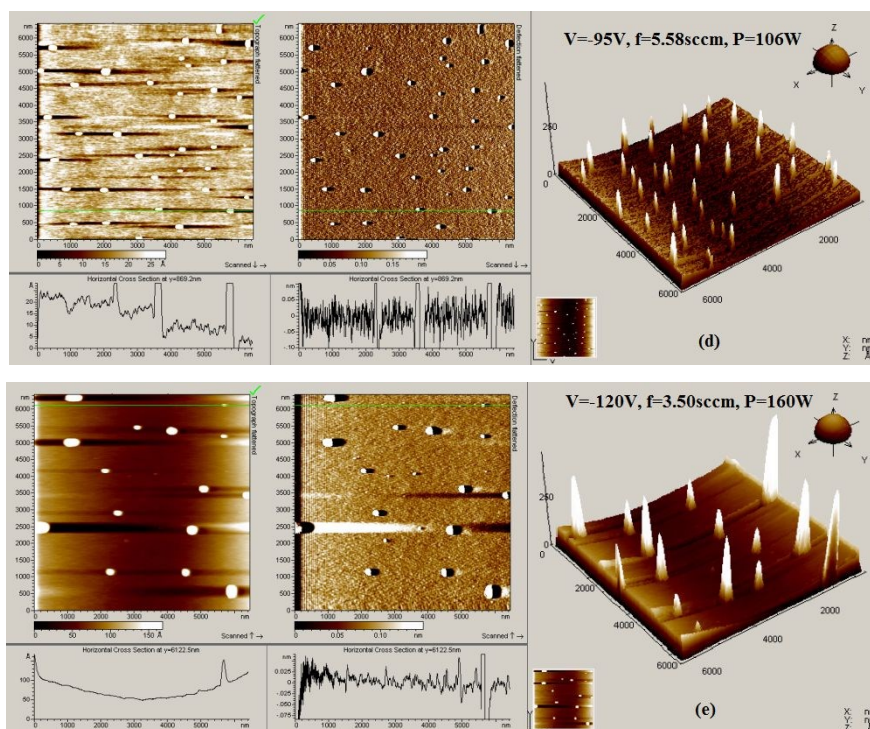
Figure 5.9 (continued)

The nanostructured film surfaces indicated significant differences with the variable applied negative bias voltage to substrate, as shown in Figure 5.9. It could be asserted that increasing the negative voltage led to an increase in the amount and sharpness of the peaks on the surface. In addition, the surface of deposited film was charged during the plasma discharge and this charging affected the formation of the peaks on the surface. The value of max peak to valley supported the assumption that negative bias voltage was raising the peaks on the surface. We reported the highest peaks at the negative voltage of -120 V and the surfaces exhibited higher peaks at lower power value and at higher flow rate value while we were increasing the voltage. The density (d), defined as a ratio of number of peaks to area of the surface, showed differences with respect to parameters. It gave the high values at lower power values and at high flow rate values; the max density was seen at lower voltage values, presented in Figure 5.8.

5.3.1.5 X-ray Diffraction Analysis
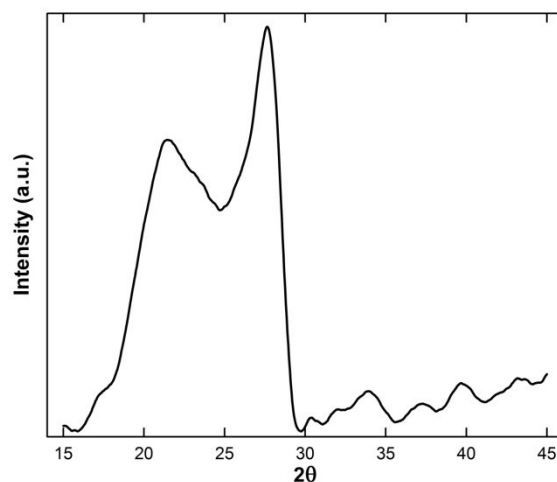
Figure 5.10 XRD pattern of the thin film

The XRD spectrum, recorded in the reflection mode at 30kV and 15mA with a scanning rate of 0.05° per 2s at room temperature (Figure 5.10). The crystallinity of the thin films was expected to decrease due to fragmentation generated inside the plasma. The ordering within the layer planes led to form a broad peak region starting at 2θ=16° and ending at 2θ=29°. This region included two nested peaks at 2θ=21.4° and at 2θ=27.7°. According to Yamamoto [50] a peak at about 2θ=23-25° was assigned to face-to-face distance in the π-π stacked molecular chains. Therefore, the peak of 21.4° could be caused by π-π stacking provided by the molecular chains of fluorene [51,52] or biphenyl [53]. The diffraction at 27.7° could come from the biphenyl substituents [53,54]. There were also two peaks with less intensity at 2θ=33.2° and 2θ=39.1°. These disordered and weak diffraction peaks showed that the thin film had a rather amorphous structure.

5.3.2 Fabrication Under Biphenyl/ Ethylene RF Plasma Environment

5.3.2.1 RGA Mass Spectrometer

Both of the excited biphenyl and ethylene dissociate their fragments after transferring sufficient energy from the inelastic collisions. Since the ethylene has two carbon atoms with double bond structure, it shows stability with the biphenyl inside the plasma and when it is fragmented, it is prone to form bigger molecules.

Since the aromatic hydrocarbons are more stable and they need high energies to cleavage the aromatic ring, the first break for molecule of biphenyl is expected at the C-C bond between two benzene rings and then, two carbon atoms are simultaneously separated from the rings [38] and dissociations of H-atoms follow this division. By the recombination of the fragments hydrocarbons were generated after plasma, such as alkanes, alkenes and alkynes. The compounds could have a structure including double or triple bonds and also it could be in cycle form. These compounds were explained in section 5.3.1.1 and they were listed in Table 5.1. The whole results of spectra for before and after plasma discharge were presented in Figure 5.11. In plasma polymerization, the polymers generally tend to have crosslinking and branched structures. Therefore, with more probability the generated compounds have branched structures instead of linear and branched structures are significantly different from linear structures with their tendency of rupturing the bond at the branches [37,38,40,41].
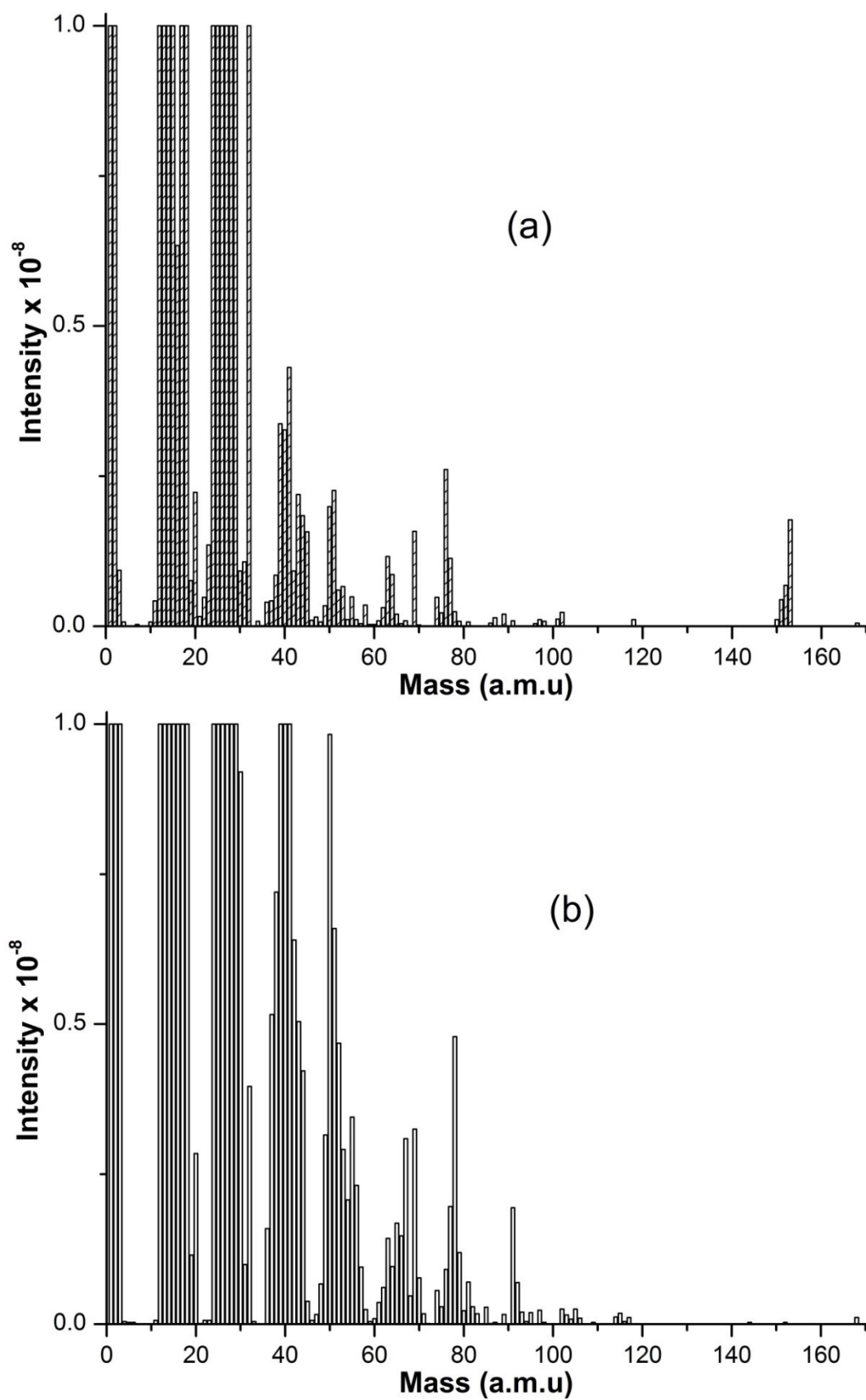
Figure 5.11 The result of RGA Spectrometry
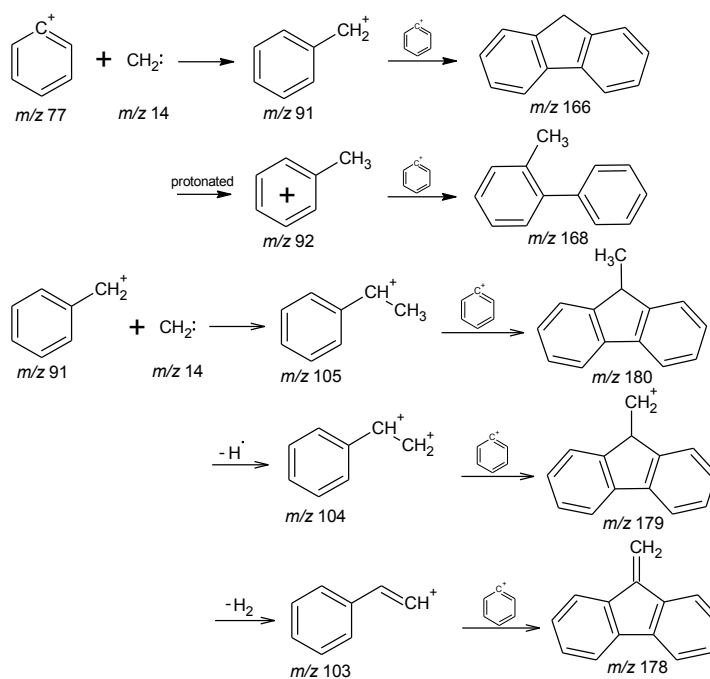
(Reaction 5.5)

In the reactions of biphenyl and ethylene, we focused on the ions of $C_7H_7^+$ and $C_7H_8^+$, at 91 and 92 respectively. They played more important role on synthesis molecule of fluorene and also the ion of $C_{13}H_{12}^+$ at mass of 168 represented the presence of derivatives. However, due the reactions in plasma were very complicated, we also obtained many compounds not related with the fluorene. The higher intensity of these points increased the probability of forming fluorene and its derivatives in these complicated reactions. From the Reaction 5.5, it could be seen that the role of these ions. It should be also emphasized that when the plasma polymers were exposed to the open air, they reacted with the oxygen and water vapor [43]. Therefore, it was possible to see the components occurred by directly combining the hydroxyl groups to the fragments. Since the oxygen atom was very reactive to connect with any ions or radicals in plasma, the intensities of these components should be kept at the lowest values. In addition, to raise the probability of formation bigger components, the small fragments of hydrocarbons should be also taken lowest values. Here, the most important role belonged to the ions of $C_7H_7^+$, $C_7H_8^+$ and $C_{13}H_{12}^+$, so the highest intensity of these ions should provide an atmosphere enhancing chance of forming the fluorene polymer thin film correctly. Therefore, the ratios of the mass intensities after to before plasma discharge for all experimental data were calculated and analyzed numerically by Design Expert

software. The images (Figure 5.12) showed the interaction between ratios of these three ions and independent plasma parameters. To obtain high intensity ratio for these ions, it should be chosen the lower values of power, negative voltage and C_2H_4 flow rate. The models of the results for the intensities were fitted by the analysis of variance (ANOVA) and the modified equations are presented below.

$ratio\ of\ 91 = 46.8 - 0.94V + 8.6f - 0.04P + 0.038fP - 0.014V^2 - 3.3f^2 - 0.0009VfP + 0.00002V^2P$

$ratio\ of\ 92 = -31.8 + 1.9V + 95.7f - 0.4P + 0.52Vf - 0.019VP - 0.33fP$

$ratio\ of\ 168 = (1.96E - 10) + (2.78E - 12)V - (2.5E - 11)f - (3E - 13)P - (3.7E - 13)Vf + (9.9E - 15)V^2$ (5.10)

Where V is the negative voltage, f is the C_2H_4 flow rate and P is the power of the plasma discharge. After the analysis, the suggested optimal parameters were found - 36 V for voltage, 1.96 sccm for flow rate and 106 W for power.
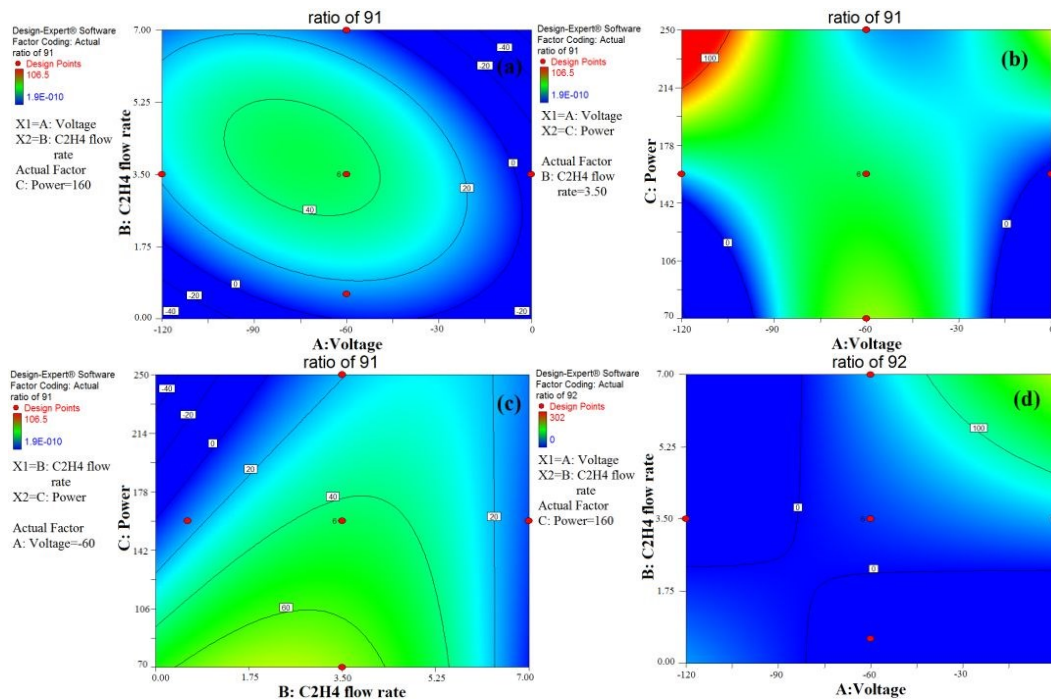
Figure 5.12 The images of Design Expert for intensity ratios of $C_7H_7^+$, $C_7H_8^+$ and $C_{13}H_{12}^+$ ions
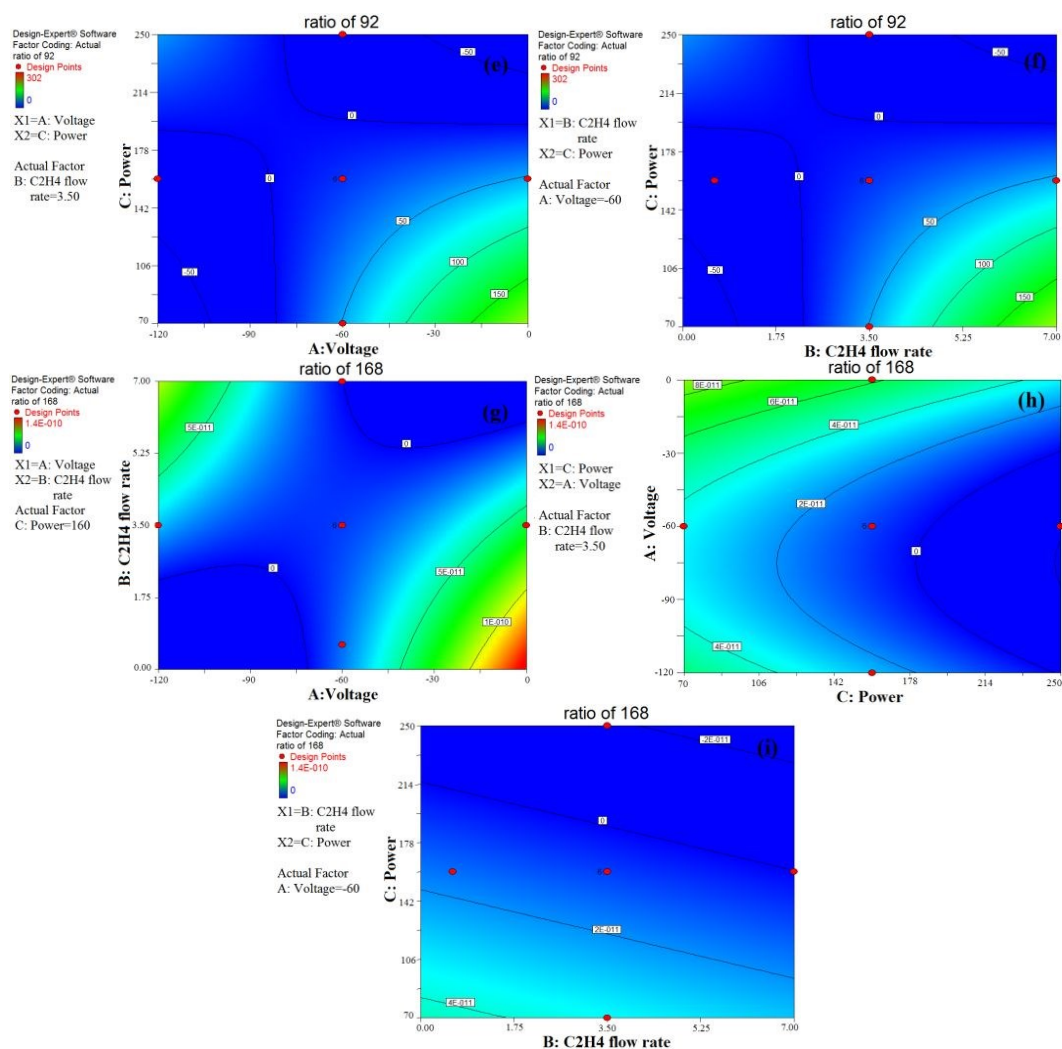
Figure 5.12 (continued)

5.3.2.2 UV-visible Spectroscopy

The absorption wavelength of the thin films was determined by UV spectroscopy and the results were listed in Table 5.4. The absorption wavelength for all experiments gave a change between 296.5 and 301.8 nm because of the structure of the compounds. The structure is determined by the fragments combining the main chain during the plasma discharge and this leads the maximum light wavelength to shift and increase the ability of conjugation. The π-π^{*} transition depends on the conjugation length and, thus, increasing the conjugation property is helpful to improve the optical and electronic properties of the thin film [9]. The optical energy band gap was determined by Tauc relation [46,47], which expressed in detail in

section 5.3.1.2. The generated polymer thin film exhibited a direct allowed transition and the E_g results indicated differences between 3.08 and 3.48 eV.
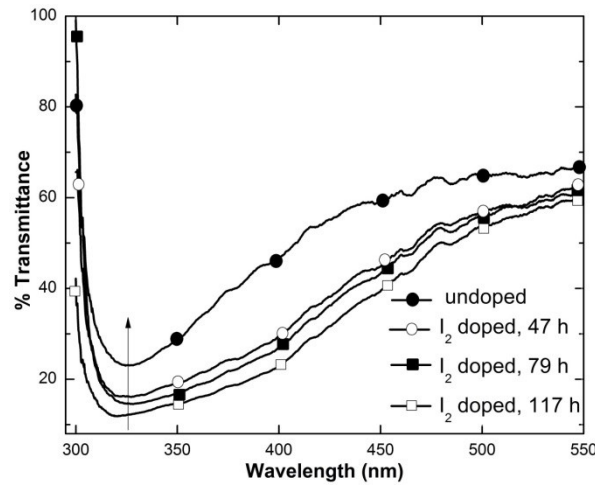
Figure 5.13 Transmittance % of thin films undoped and doped by iodine for 47 hours, 79 hours, and 117 hours
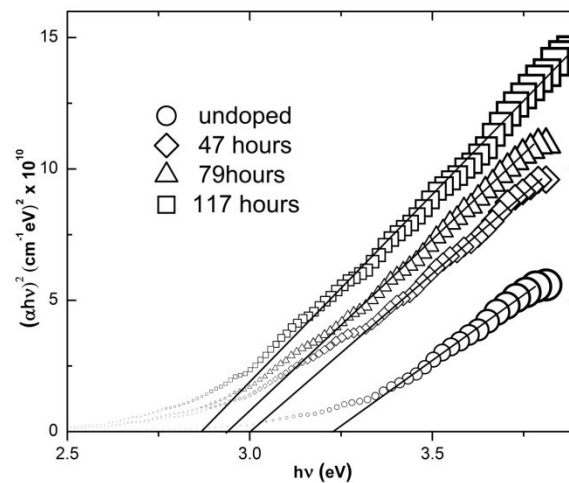
Figure 5.14 Plots of $(\alpha h\nu)^2$ versus photon energy hν of undoped and doped thin films

The surfaces of the films were doped by iodine (I_2) for different time periods of 47, 79, and 117 hours. After the doping process, the light absorption wavelength was shifted and this led to a broadened absorption shown in Figure 5.13, and the energy band gap of the thin films decreased, presented in Figure 5.14. The values were found 3.23, 3.00, 2.93 and 2.85 for undoped, 47, 79 and 117 hours, respectively. The

106

ANOVA analysis of results of the UV spectra was defined by the Equation 5.11. With respect to this equation, the suggested parameters corresponded to high values of power and negative bias voltage as well as low value of C_2H_4 flow rate.

$$wavelength(\lambda) = 294.54 - 0.02167V - 0.2166f + 0.02218P \tag{5.11}$$

Table 5.4 List of the results according to independent parameters

No	V (Volt)	f (sccm)	P (W)	λ (nm)	E_g (eV)	t (a.u.)	T (Å)	R_q (Å)	R_a (Å)	R_z (nm)	d
1	-24	1.42	106	297.1	3.28	0.32932	1850.9	772.1	561.1	1140.3	3.36
2	-120	3.50	160	301.3	3.27	0.17539	1766.7	905.0	648.4	1345.4	1.55
3	-24	5.58	213	298.1	3.33	0.14707	1798.6	810.6	607.0	1109.4	1.58
4	-60	7.00	160	296.5	3.43	0.17877	1804.6	864.5	555.1	1349.4	2.22
5	-60	3.50	160	297.1	3.38	0.26436	1756.7	801.8	597.7	1099.1	2.25
6	-60	3.50	160	298.6	3.32	0.24399	1770.4	837.8	642.9	1087.8	3.5
7	0	3.50	160	296.5	3.37	0.29881	1774.6	731.8	513.6	1126.2	4.41
8	-60	3.50	70	296.5	3.40	0.39991	1778.8	738.1	530.1	1101.7	4.08
9	-60	3.50	250	298.4	3.24	0.13786	1869.9	812.3	612.6	1098.8	4.38
10	-95	1.42	213	301.8	3.08	0.26284	1684.9	701.8	489.7	1100.3	0.19
11	-95	5.58	213	301.8	3.29	0.09849	1760.2	739.5	529.2	1114.3	2.69
12	-24	5.58	106	298.6	3.43	0.30352	1771.1	858.0	458.6	1584.6	2.25
13	-24	1.42	213	301.3	3.13	0.23807	1793.2	786.8	580.9	1106.0	1.94
14	-60	3.50	160	301.8	3.29	0.16534	1821.4	604.7	289.5	1206.7	2.25
15	-60	0.60	160	298.6	3.17	0.20145	1750.2	731.0	521.8	1107.9	3.52
16	-60	3.50	160	297.3	3.30	0.15472	1822.7	672.0	443.6	1125.1	0.44
17	-95	1.42	106	297.6	3.31	0.37856	1796.5	747.4	547.8	1082.0	2.66
18	-60	3.50	160	298.1	3.27	0.26647	1825.6	785.3	588.2	1090.6	0.66
19	-60	3.50	160	298.1	3.27	0.16664	1797.7	696.4	356.1	1317.1	3.41
20	-95	5.58	106	296.5	3.48	0.46663	1751.4	666.6	453.6	1088.8	0.83

5.3.2.3 Thickness and Transmittance Measurements

The thickness (T) of the thin films was measured by ellipsometry and all results were listed in Table 5.4. Due to the presence of the double bond in its structure, the molecule of ethylene chemically behaved more stable and tended to form bigger molecules during the plasma discharge. Therefore, this property played an important role on reactions with biphenyl for diffusing the thin film. Additionally, the transmittance (t) results were listed with thickness values and the correlation between the thickness and the transmittance showed that if the value of the thickness was increasing, the intensity of the transmittance decreased.
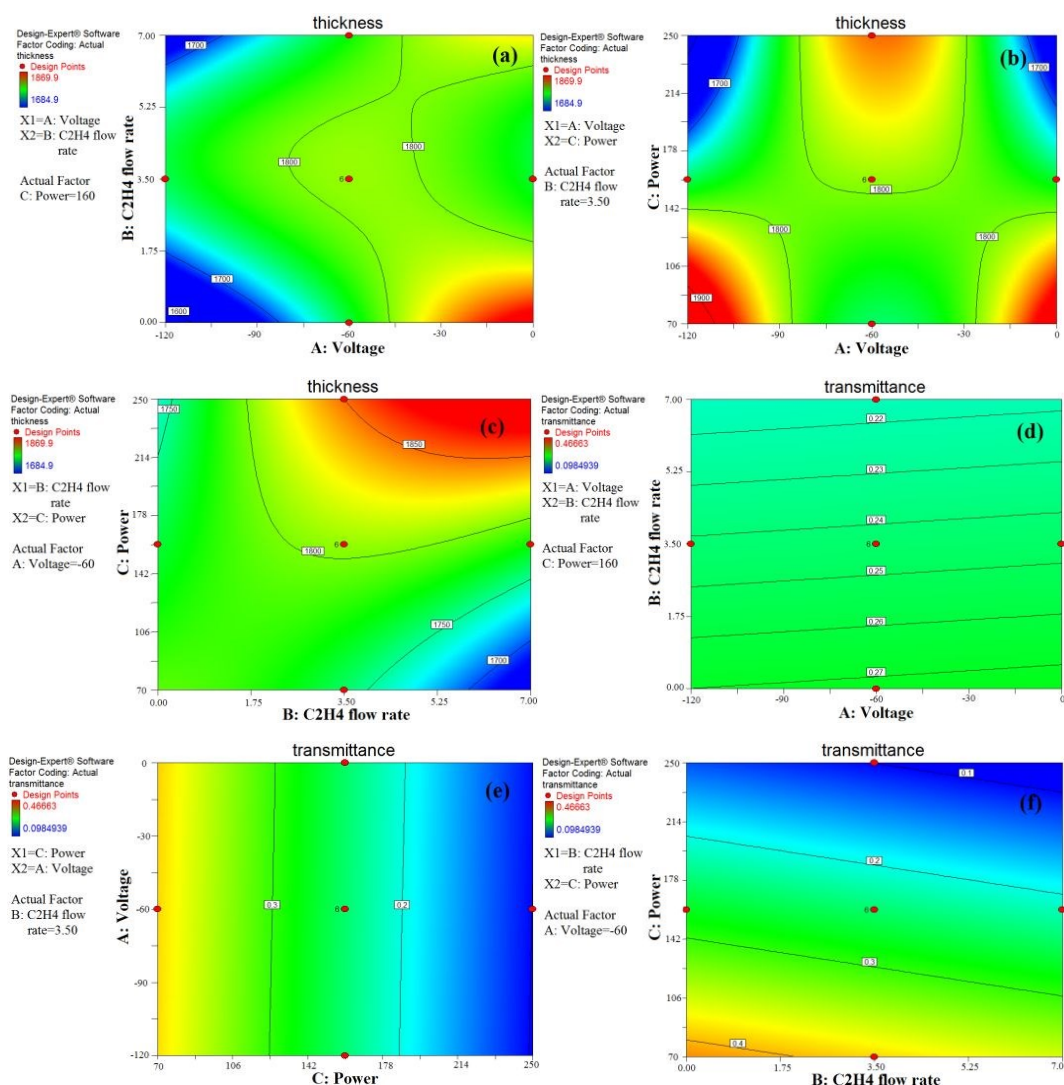
Figure 5.15 The images of ANOVA analysis for thickness and transmittance of the thin films

It could be seen how change the thickness and transmittance of the films according to independent plasma parameters from images of ANOVA analysis (Figure 5.15). When both values of power and C_2H_4 increased at constant negative voltage, the thickness was increasing (red area). At constant power value, the thickness gave high values at lower negative voltage values and C_2H_4 flow rate. When the flow rate was kept constant, the red areas were obtained at lower power with either the lower or higher negative voltage values, and if the power was raised, the negative voltage should be kept at intermediate values. It could be defined from the variable thickness results, the reactions in plasma was very complicated. On the other hand, because of the correlation, the parameters giving the lowest intensity of the transmittance (blue

areas) should give the highest thickness values. Therefore, to obtain the lower transmittance and higher thickness, according to images if transmittance, the values for the parameters of power and C_2H_4 flow rate should be higher while the negative voltage was at intermediate values. Results of the analysis showed that the new parameters of -52.86 V for negative voltage, 5.58 sccm for gas flow rate and 213.51 W for power, and the thickness was found 1895.1±28.5 Å with an angle of 67.872±0.248 and the transmittance was observed at intensity value of 0.088171. Cubic model for the findings of the thickness and linear model of the transmittance were reduced to the data without undesirable coefficients by the Design-Expert software and ANOVA analysis gave the Equation 5.12.

$$T = 2261.3 + 12.95V - 96.27f - 2.33P - 1.32Vf - 0.072VP + 0.23fP + 0.09V^2 + 7.2f^2 - (6.4E - 04)V^2P + 0.16Vf^2$$

$$t = 0.531 + (3.91E - 05)V - (8.14E - 03)f - (1.6E - 03)P \tag{5.12}$$

5.3.2.4 Atomic Force Microscope

The nanostructual and nanomechanical properties of the surface of the deposited films were investigated by Atomic Force Microscope (AFM). The results of the standard deviation (rms roughness), the mean absolute deviation (ave roughness) and the maximum peak to valley (Rp-v) were listed in Table 5.4 with the independent parameters.
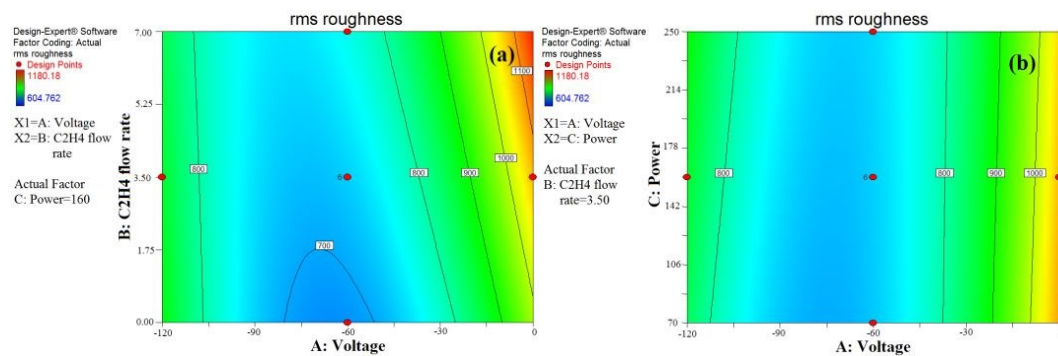
Figure 5.16 The images of ANOVA analysis for the rms roughness, the average roughness, the maximum peak to valley

109
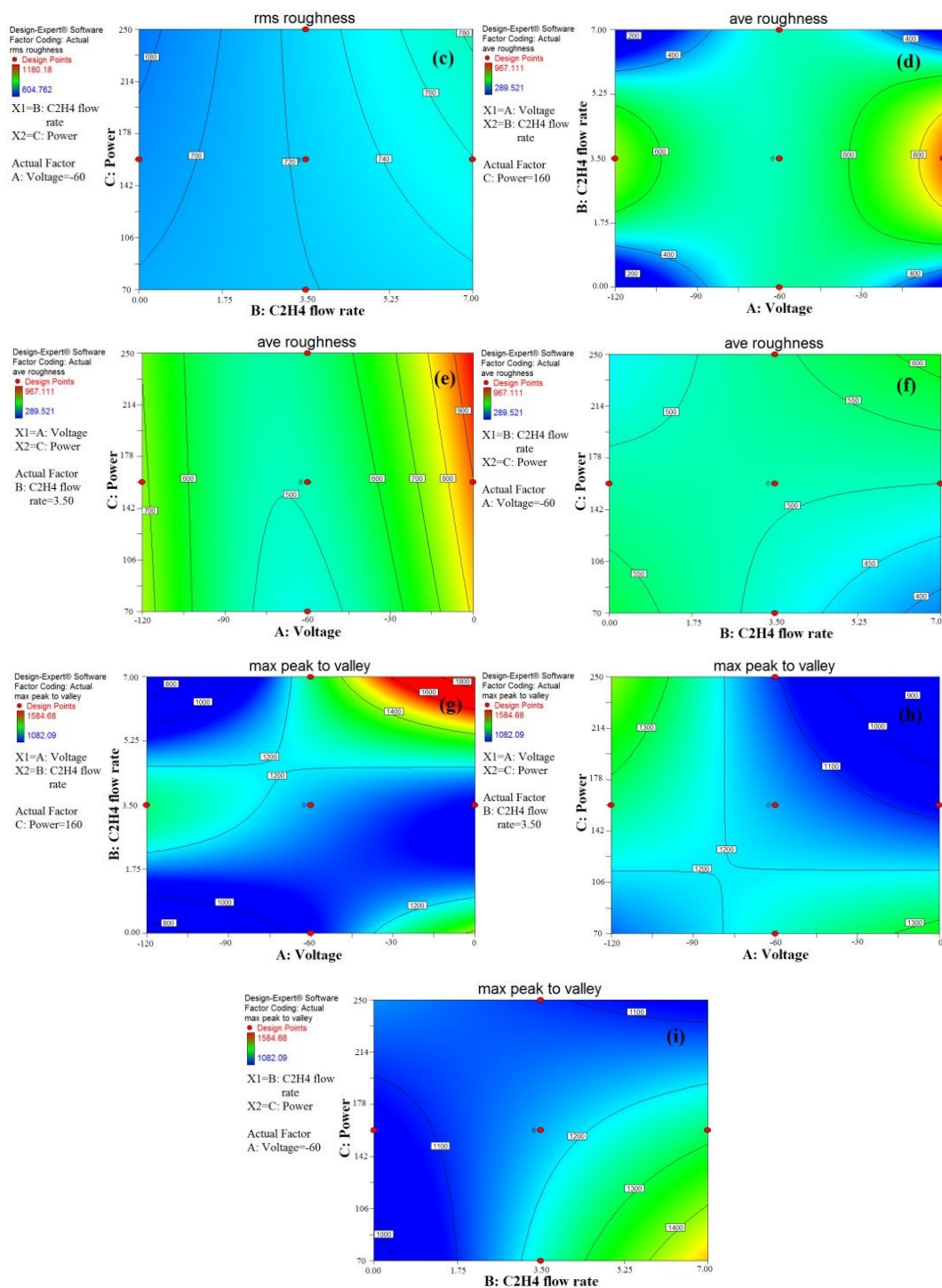
Figure 5.16 (continued)

Images of the design expert showed that all the roughness parameters gave high values at higher C_2H_4 flow rate (red areas) (Figure 5.16). While all roughness parameters had high values at lower negative voltages, only the ave roughness and max peak to valley values had high values at higher voltages. Analysis of software

gave the new parameters of -24 V for negative voltage, 5.58 sccm for flow rate and 106 W for power. The quadratic, quartic and cubic equations of the rms, ave roughness and max peak to valley, respectively, were simplified by ANOVA the solutions of the equations are presented below.

$$R_q = 1048.5 + 9.69V - 15.5f - 0.4P + 0.26Vf - 0.003VP + 0.06fP + 0.068V^2$$

$$R_a = 868.4 + 8.76V - 53.3f - 0.11P - 0.09Vf + 0.009VP + 0.3fP + 0.07V^2 - (6.5E - 05)V^2f^2$$

$$R_z = 647.5 - 4.29V + 2887.3f + 1.81P + 3.068Vf + 0.013VP - 1.3fP - 0.014VfP - 0.013Vf^2 \tag{5.13}$$

The plasma species, such as ions, radicals, electrons, and et al., caused various changes on the surfaces of thin films during the glow discharge. The plasma polymer thin films have occurred from cross-linked chemical structures and their surfaces exhibited cross-linking functionalities generated by radicals [39]. Thus, the cross-linking could be a reason of the differences at surface roughness parameters. In addition to this, given the stable structure of ethylene, concentration of the formed polymer thin films influenced the roughness parameters. AFM results showed that the film surfaces were not uniform and had features which give an opportunity to catch light, and this property made the polymer thin films appropriate for photo voltaic applications while it was not for the electrical industry.
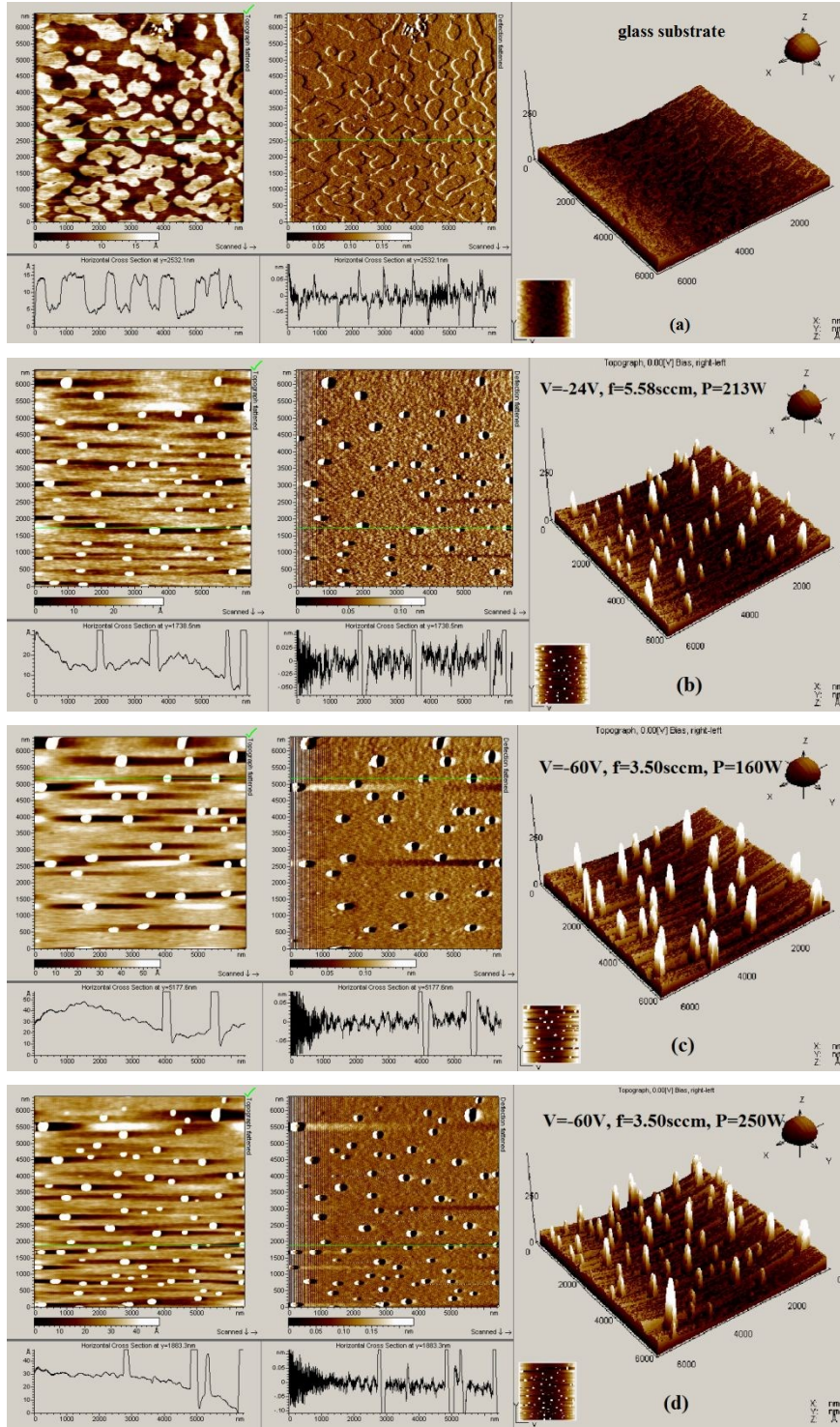
Figure 5.17 The AFM images of the glass substrate and the thin films with various plasma parameters
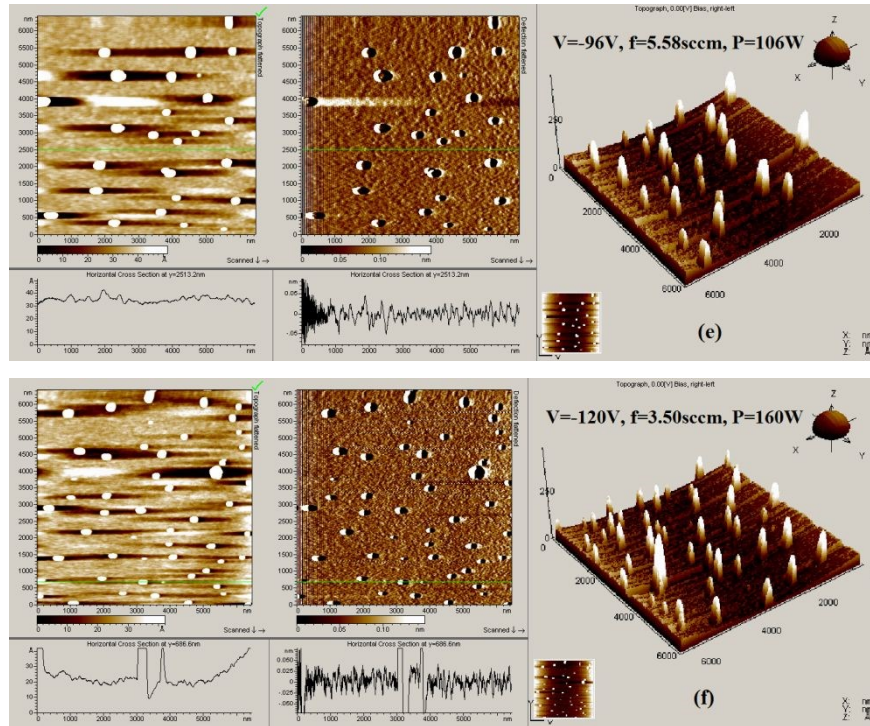
Figure 5.17 (continued)

There were remarkable differences, we can see from Figure 5.17, on surface roughness terms by changing the applied negative bias voltage to the substrate. According to Tagaki [25], the ion bombardment produced by applying voltage parallel or perpendicular to the substrate, the morphological properties of the surface of deposited film were significantly improved. It could be asserted from the AFM images that increasing the negative voltage led to increase the amount of the peaks on the surface and also sharpness and height of the peaks increased with higher voltages. In addition, since increasing the power caused more fragmentations in reactions, it was raising the amount of peaks having different sizes. The surfaces of thin film showed differences in density (d) with independent parameters (Table 5.4). When all the parameters of power, flow rate and negative voltage was at high values, high density was observed. Also, the high density was obtained as all the parameters were at low values. Thus, it could be concluded that to provide the surface with high density the parameters should be changed (increased or decreased) parallel to each other.

113

5.3.2.5 X-ray Diffraction Analysis
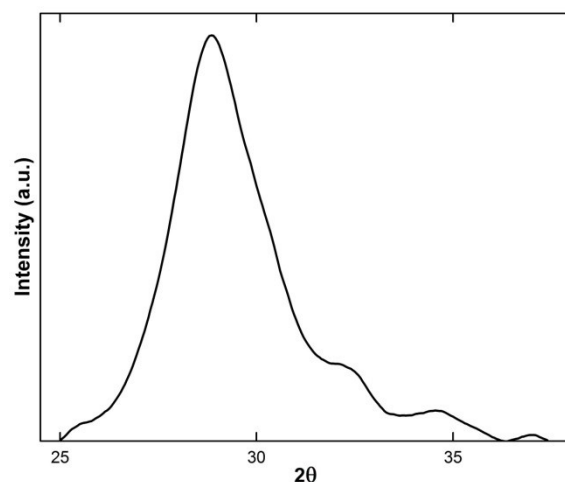
Figure 5.18 XRD pattern of the thin film

The XRD spectrum, recorded in the reflection mode at 30kV and 15mA with a scanning rate of 0.05˚ per 2s at room temperature (Figure 5.18). The crystallinity of the thin films was expected to decrease due to fragmentation generated inside the plasma. The thin film synthesized under biphenyl and ethylene plasma exhibited a broad peak centered at 28.8˚, which provided by the biphenyl substituents [53,54]. These disordered diffraction peak showed that the structure of the thin film was quite amorphous.

5.4 Conclusion

Fluorene-type thin films were produced under the mixtures of biphenyl/ methane and biphenyl/ ethylene plasma by using a single capacitively coupled rf plasma system. The plasma environment was analyzed via RGA mass spectrometry. Controlling the plasma chemistry during the plasma deposition was a difficult and very complicated work. Applying negative bias voltage led to positive ion bombardment on the substrate and this increased intensities of the corresponding fragments for the fluorene-type thin films. Therefore, this process can be considered as an effective way in controlling the reactions in the plasma depositions. In addition, due to the stability of the molecule of ethylene, it was more attractive than the molecule of methane to obtain the fluorene-type thin films. The optical properties of films were revealed by using UV-visible spectroscopy and thin films

were doped by iodine. The thin films indicated direct band energies and they changed in the region between 3.15 and 3.54 eV for the mixture with methane, and between 3.08 and 3.48 eV for the mixture with ethylene, which verified that the chains in the film structure were generated in different order with respect to the independent plasma parameters. I_2 doping improved the electro and optical properties of the thin films by decreasing the energy band gap up to 2.85 eV, which may result from the increase in the conjugation length of the structure. The energy band gap values of the films indicated almost same results for two mixtures after the doping process. Thicknesses of films were measured by ellipsometry and they showed a linear relation with the plasma parameters of power, CH_4 or C_2H_4 flow rate. The applied negative bias voltage should be at high values for deposited films obtained by using the methane gas while it should be at intermediate values for the ethylene gas. Since the molecule of the ethylene tended to form heavier compounds during the deposition, which caused increase in the deposition rate, thickness values corresponding to the mixture of biphenyl/ ethylene were found higher than the corresponding to the mixture with methane. Moreover, an AFM was employed to characterize the nanostructural properties of the film surfaces. The surfaces of thin films formed in both mixtures had remarkable nanostructured characteristics generated by the various bias voltages. Additionally, peaks on the surfaces of thin films provide the availability required for photovoltaic applications. As a result, it may be suggested that applying a negative bias voltage is an effective way to increase the height of these peaks. The surfaces of the thin films deposited with ethylene exhibited higher density than the ones obtained with the methane. The XRD spectrometry exhibited that all deposited films had amorphous structures and we are going to improve the crystallinity by annealing the thin films in the future. Finally, it could be suggested that the mixture of biphenyl/ ethylene plasma environment was more suitable to obtain the fluorene-type thin films.

5.5 References

[1]   A.C. Grimsdale, K. Müllen, Adv. Polym. Sci. 199 (2006) 1.

[2]   J. Pei, W.-L. Yu, W. Huang, A.J. Heeger, Chem. Commun. (2000) 1631.

[3]   W. Yu, J. Pei, Y. Cao, A.J. Heeger, R. Columbia, A. August, Chem. Commun. (1999) 1837.

[4]   Q. Pei, Y. Yang, J. Am. Chem. Soc. 118 (1996) 7416.

[5]   N.S. Cho, J.-H. Park, S.-K. Lee, J. Lee, H.-K. Shim, M.-J. Park, D.-H. Hwang, B.-J. Jung, Macromolecules 39 (2006) 177.

[6]   M. Bernius, M. Inbasekaran, E. Woo, W. Wu, L. Wujkowski, Thin Solid Films 363 (2000) 55.

[7]   M. Inbasekaran, E. Woo, W. Wu, M. Bernius, L. Wujkowski, Synth. Met. 111-112 (2000) 397.

[8]   H. Cho, D. Kim, Y. Kim, Adv. Mater. 9 (1997) 326.

[9]   B.U. Scherf, E.J.W. List, Adv. Mater. 14 (2002) 477.

[10]   M. Kreyenschmidt, G. Klaerner, T. Fuhrer, J. Ashenhurst, S. Karg, W.D. Chen, V.Y. Lee, J.C. Scott, R.D. Miller, Macromolecules 31 (1998) 1099.

[11]   A. Babel, S.A. Jenekhe, Macromolecules 36 (2003) 7759.

[12]   D. Neher, Macromol. Rapid Commun. 22 (2001) 1365.

[13]   E. Bundgaard, F. Krebs, Sol. Energy Mater. Sol. Cells 91 (2007) 954.

[14]   F. Zhang, K. Jespersen, C. Bjostrom, M. Svensson, M. Andersson, V. Sundstrom, Adv. Funct. Mater. 16 (2006) 667.

[15]   M. Leclerc, J. Polym. Sci. Part A Polym. Chem. 39 (2001) 2867.

[16]   B.S. Beauprø, M. Leclerc, Adv. Funct. Mater. 12 (2002) 192.

[17]   N.S. Cho, D.-H. Hwang, J.-I. Lee, B.-J. Jung, H.-K. Shim, Macromolecules 35 (2002) 1224.

[18]   F.F. Shi, Surf. Coatings Technol. 82 (1996) 1.

[19]   L. Martinu, D. Poitras, J. Vac. Sci. Technol. A 18 (2000) 2619.

[20]   H. Biederman, D. Slavínská, Surf. Coatings Technol. 125 (2000) 371.

[21]   A. Hiratsuka, I. Karube, Electroanalysis 12 (2000) 695.

[22]   M.V. Jacob, C.D. Easton, G.S. Woods, C.C. Berndt, Thin Solid Films 516 (2008) 3884.

[23]   J. Friedrich, Plasma Process. Polym. 8 (2011) 783.

[24]   F.F. Shi, J. Macromol. Sci. Part C Polym. 36 (1996) 795.

[25]   T. Tagaki, Thin Solid Films 92 (1982) 1.

[26]   J.H. Lee, D.S. Kim, Y.H. Lee, J. Electrochem. Soc. 143 (1996) 1443.

[27]   J. Coburn, E. Kay, J. Appl. Phys. 43 (1972) 4965.

[28]   M.L. Tarng, J. Appl. Phys. 42 (1971) 2449.

[29]   R. Jones, C. Standley, L. Maissel, J. Appl. Phys. 38 (1967) 4656.

[30]   L. Martinu, M.R. Wertheimer, Appl. Phys. Lett. 54 (1989) 2645.

[31]   M. Chen, T. Yang, Z. Ma, J. Polym. Sci. Part A Polym. Chem. 36 (1998) 1265.

[32]   S. Eufinger, W.J. van Ooij, T.H. Ridgway, J. Appl. Polym. Sci. 61 (1996) 1503.

[33]   A. Streitwieser, H. Ward, J. Am. Chem. Soc. 85 (1963) 539.

[34]   J. Stille, R. Sung, J. Kooi, J. Org. Chem. 30 (1965) 3116.

[35]   M. Vasile, G. Smolinsky, Int. J. Mass Spectrom. Ion Phys. 18 (1975) 179.

[36]   G. Smolinsky, M. Vasile, Int. J. Mass Spectrom. Ion Phys. 16 (1975) 137.

[37] T. Lee, A Beginner's Guide to Mass Spectral Interpretation, John Wiley & Sons, Ltd, 1998.

[38] B.D. Mistry, A Handbook of Spectroscopic Data Chemistry, Oxford Book Company, 2009.

[39] K.C. Khulbe, C.Y. Feng, T. Matsuura, Synthetic Polymeric Membranes, Springer, 2008.

[40] F.G. Kitson, B.S. Larsen, C.N. McEwen, Gas Chromatography and Mass Spectrometry, Academic Press, 1996.

[41] E. Pretsch, P. Buhlmann, M. Badertscher, Structure Determination of Organic Compounds, Springer, 2009.

[42] R.M. Silverstein, F.X. Webster, D.J. Kiemle, Spectrometric Identification of Organic Compounds, John Wiley & Sons, Ltd, 2005.

[43] H. Biederman, Plasma Polymer Films, Imperial College Press, London, 2004.

[44] H. Kenzo, Handbook of Ultraviolet and Visible Absorption Spectra of Organic Compounds, Plenum Press Data Division, New York, 1967.

[45] J.W. Robinson, Practical Handbook of Spectroscopy, CRC Press, Boca Raton, FL, 1991.

[46] J. Tauc, R. Grigorovici, A. Vancu, Phys. Status Solidi 15 (1966) 627.

[47] J. Tauc, in:, J. Tauc (Ed.), Amorph. Liq. Semicond., Plenum Press, London, New York, 1974.

[48] F.F. Muhammad, A.I. Abdul Hapip, K. Sulaiman, J. Organomet. Chem. 695 (2010) 2526.

[49] W. Bowen, N. Hilal, Atomic Force Microscopy in Process Engineering, Elsevier Ltd, 2009.

[50] T. Yamamoto, D. Komarudin, M. Arai, B. Lee, H. Suganuma, N. Asakawa, Y. Inoue, K. Kubota, S. Sasaki, J. Am. Chem. Soc. 120 (1998) 2047.

[51] L. Kinder, J. Kanicki, J. Swensen, P. Petroff, in:, C.D. Dimitrakopoulos (Ed.), Proc. SPIE Vol. 5217, 2003, pp. 35–42.

[52] Y.M. Kim, E. Lim, I.-N. Kang, B.-J. Jung, J. Lee, B.W. Koo, L.-M. Do, H.-K. Shim, Macromolecules 39 (2006) 4081.

[53] J. Simitzis, D. Triantou, S. Soulis, J. Appl. Polym. Sci. 110 (2008) 356.

[54] M. Granström, M. Havimo, M. Heikkilä, I. Kilpeläinen, J. Mater. Chem. 19 (2009) 639.

CHAPTER 6

SYNTHESIS AND CHARACTERIZATION OF AMORPHOUS HYDROGENATED CARBON (a-C:H) THIN FILM BY SINGLE RF PLASMA METHOD AND AN APPLICATION FOR c-SI SOLAR CELL

6.1 Introduction

Producing thin films by plasma deposition method is a very effective way to improve the properties of the films with the various plasma species, such as electrons, ions, and radicals, etc [1–6]. Among the thin films produced by plasma deposition, amorphous hydrogenated carbon (a-C:H) films are very promising materials, since they provide extraordinary physical and chemical properties such as high density, strength, thermal stability, chemical inertness for both acids and alkalis, effective infrared (IR) transparency and high electrical resistivity [7–14]. In recent studies, it has been demonstrated that the anti-reflective properties of infrared (IR) optical elements and solar cells could be enhanced by coating the surface with the a-C:H film, and it has also contributed to the protection for magnetic storage disks and tool materials [12–19]. Moreover, the a-C:H film has improved the performance of electronic devices [18,20] due to the property of having a wide band gap, and it has been used for flat-panel displays as a cathode emitter, and for biomedical applications [12–15,21–26].

The radio frequency (rf) plasma deposition has been used as the most common process to synthesize the a-C:H films [7,27]. The a-C:H thin film was usually produced from CH_4 or C_2H_2 plasma during the last decade, since the ions and radicals of carbon are well known [28]. The variable parameters of plasma such as the gas flow rate, the plasma pressure, the power and frequency of power supply, etc., determine the chemical structure and properties of the thin film by controlling the reactions of the species in a plasma. Several studies have been employed to reveal the properties of both plasma and thin films [29–31]. However, due to the complexity of the reactions in the plasma, there are still many details which are

121

difficult to understand and remain to be investigated. To our knowledge, there is no systematic investigation of properties of plasma deposited a-C:H thin films with a wide range of parameters and literature lacks a complete framework.

In this study, the properties of the a-C:H film were explored under the variable plasma parameters of input rf power (100 – 300 W), CH$_4$ flow rate (2 – 5 sccm), and deposition time (15, 30 min) at a constant pressure value of 0.2 torr. The changes of plasma chemistry during the deposition were investigated by optical emission spectroscopy (OES). The chemical structural properties were examined by fourier transform infrared (FTIR) spectroscopy and the optical properties of the films were explored by UV-visible spectroscopy. The morphology of the films was analyzed by X-ray diffraction (XRD) and the thicknesses were measured by a profilometer. Also, the a-C:H thin films were applied to a crystalline silicon (c-Si) solar cell and the efficiency of the solar cell was improved. This chapter was published in the journal of Plasma Science and Technology [32].

6.2 Experimental Details

The experimental setup is shown in Figure 6.1 and consists of two parallel cylindrical electrodes inside the chamber on top of each other; upper one has rf power with 13.56 MHz frequency and the lower one is connected to the ground. The diagnostics of the system were studied in section 3.5. The thin films were deposited on glass slides and on silicon wafers. The glass slides were used with two different sizes; thicker (1 mm) and thinner (0.2 mm). Since the best coating is obtained at the center of the bottom electrode, all samples were placed at the center of the electrode, and the distance between the electrodes was kept at 3 cm. After the pressure dropped below 10^{-2} torr, generally the base pressure of 5.0×10^{-3} torr, the MKS multi gas controller 647C was activated. When the pressure was increased to 0.2 torr by flowing CH$_4$ gas, it was kept constant at this value, and the discharge was generated. Cleaning of all the samples and the parts of the system was done with the ethanol and acetone. All the changes of plasma species were monitored during the deposition with the OES which collects all data with a fiber optic cable connected to the window of the chamber. For the optical emission measurements, a HR2000 high resolution miniature fiber optic spectrometer (Ocean Optics) was used. The chemical bonding of the thin films were determined by using Bruker IFS 66/s FTIR

spectrometer with 4 cm^{-1} spectral resolution and noise less than 10^{-5} AU within a minute. To measure the thickness of the samples masked by Cu tape, the Dektak profilometer with a measurement length of 500 μm and force of 3 mg for 7 second duration was used. For the optical transmission measurements, a PG Instruments T70+ UV/VIS spectrometer with a spectral bandwith of 0.5 nm was used. The XRD analysis was employed by a Rigaku Miniflex standard X-ray diffractometer (Cu K$_\alpha$, λ=1.54 Å) with the resolution of 0.05˚.
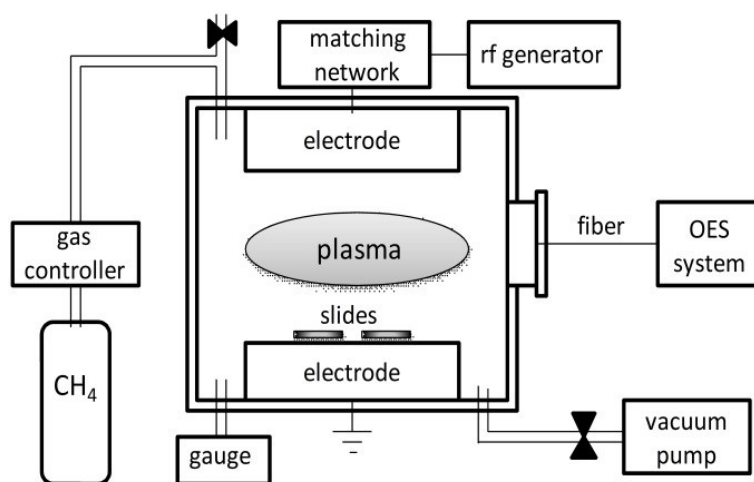
Figure 6.1 Experimental set up

6.3 Results and Discussion

6.3.1 Optical Emission Spectroscopy

The emissions of plasma species were measured by OES, in the wavelength region from 200 to 900 nm. Although the OES is a non-intrusive way to define the diagnostic plasma properties, it can only show the lines of compounds with lower masses such as the atomic and diatomic species H, H_2, CH and C_2. Despite the components with heavier masses such as CH_2, CH_3 and other polyatomic species cannot be seen in the spectra, measurements obtained from the spectroscopy are enough to analyze the chemical species in the plasma [33]. All dissociation steps of CH_4 molecule were seen in the reactions below with threshold energies [27]. The Reaction 6.1 refers to formation of CH(A$^2\Delta$) radical from CH_4 dissociation by direct electron impact. The H_2 (G$^1\Sigma_g^+$) emission can be produced from both the excitation

of CH$_4$ dissociation by electron impact (Reaction 6.3) and direct vibrational excitation of hydrogen atoms [27]. Additionally, the H atomic hydrogen is generated almost entirely from the H$_2$ molecules [34].

$$CH_4 + e \rightarrow CH(A^2\Delta) + H_2 + H + e \quad (E_{th}=12.2 \text{ eV}) \qquad \text{(Reaction 6.1)}$$

$$CH_4 + e \rightarrow CH_3 + H(n=4) + e \quad (E_{th}=17.1 \text{ eV}) \qquad \text{(Reaction 6.2)}$$

$$CH_4 + e \rightarrow CH_2 + H_2(G^1\Sigma_g^+) + e \quad (E_{th}=19 \text{ eV}) \qquad \text{(Reaction 6.3)}$$

$$H_2 + e \rightarrow H(n=4) + H + e \quad (E_{th}=17 \text{ eV}) \qquad \text{(Reaction 6.4)}$$

$$H + e \rightarrow H(n=4) + e \quad (E_{th}=12.75 \text{ eV}) \qquad \text{(Reaction 6.5)}$$
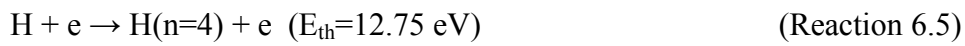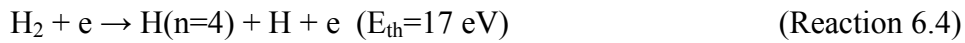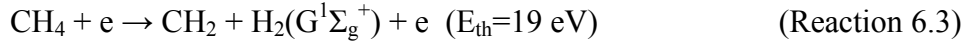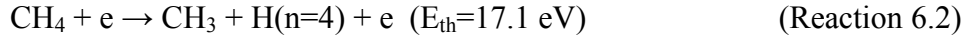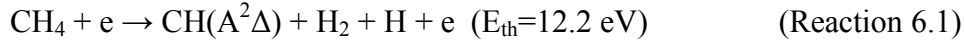
The OES of methane plasma at 200 W – 5 sccm – 15 min is shown in Figure 6.2. The intensities of the emissions were presented in Table 6.1. The CH Q(0,0) band head of the A$^2\Delta \rightarrow$X$^2\Pi$ system, which results from transition of direct electron impact on CH$_4$ molecule [27,35], was observed at 431.2 nm and the CH radical referring to system of B$^2\Sigma^- \rightarrow$X$^2\Pi$ transition was recorded at 387.1 nm [34]. The 486.1 nm line referred to H$_\beta$ (H(n=4→n=2)) transition and the 463.4 nm line belonged to H$_2$ G$^1\Sigma$g$^+$ [27,36]. The H$_\gamma$ (H(n=5→n=2)) and H$_\delta$ (H(n=6→n=2)) lines were at 434 and 410.1 nm, respectively, and the H$_\alpha$ (H(n=3→n=2)) line was seen at 656.2 nm with the H line at 397 nm [37]. In the spectra, the degradation of the CH R branch was seen from violet to the red colors at the lines from 421 to 425 nm and at the lines from 434 to 442 nm [37], respectively. The lines at 387.1 nm and 422.5 nm were referred to the CH R(0.0) band head of the B$^2\Sigma^- \rightarrow$X$^2\Pi$ system and the CH$^+$ R(0.0) band head of the A$^1\Pi \rightarrow$XΣ system, respectively [38]. At 601.8 nm, numerous molecular hydrogen lines attributed to the Fulcher band system of I$^{u3}\Pi_u$ was observed [39]. Carbon dimer (C$_2$) d$^3\Pi \rightarrow$a$^3\Pi$ Swan band emission line was represented around 516 nm [35,40].
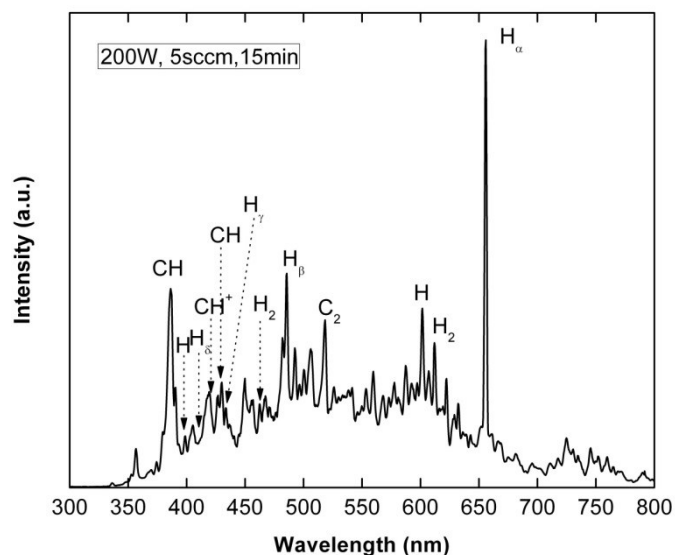
Figure 6.2 The OES spectra of selected a-C:H thin film

Table 6.1 The emission intensities of OES spectra

f	P	t	CH (387)	H_δ	CH^+	CH (431)	H_γ	H_2	H_β	C_2	H_α
2	100	15	421	248	375	564	475	509	1173	649	2149
2	150	15	486	307	463	670	631	626	1748	845	3268
2	200	15	486	377	576	795	812	793	2269	1281	4003
3	100	15	211	159	261	492	343	356	825	457	1553
3	150	15	252	215	334	611	465	510	1389	584	2919
3	200	15	301	263	397	715	572	648	1968	680	4002
3	150	30	528	178	297	502	401	372	1162	541	2744
3	200	30	256	288	465	778	576	752	2239	994	5727
3	250	30	227	259	415	670	634	741	2346	996	5706
3	300	30	207	261	432	710	692	781	2800	1251	6693
4	100	15	787	199	330	596	392	415	417	932	1940
4	150	15	2465	390	600	823	644	649	1595	984	3317
4	200	15	2363	472	725	1017	877	839	2257	1228	4001
5	100	15	201	128	211	505	269	305	672	299	1406
5	150	15	277	240	396	834	545	635	1607	603	3967
5	200	15	1649	376	527	722	667	655	1667	1063	3769
5	150	30	401	206	345	677	451	503	1177	633	2476
5	200	30	218	237	380	831	542	745	2037	640	4074
5	250	30	358	272	437	800	612	744	2075	884	4982
5	300	30	991	333	522	778	707	784	2296	1270	6093

f: CH_4 flow rate (sccm), P: Power (W), t: Deposition time (min)

The emission intensities of the thin films with various plasma parameters showed significant differences from each other. There was a decrease in the emission intensity of the CH (431.2) line at higher power values, so this could be defined by

the existence of chemical Reactions 6.1 and 6.2, Reaction 6.2 should become significant as the power increased. Therefore, it may be supposed that the dissociative excitation in the Reaction 6.1 should be accepted for the major route for the generated radicals. The H_β emission strongly depends on excitation in the Reactions 6.4 and 6.5. It can be seen from the Table 6.1 that the intensities of the hydrogen atom species (H_δ, H_γ, H_2, H_β, H_α) showed similar changes to each other by increasing the CH_4 flow rate. By increasing the power, the amount of species increased, except only H_α and H_2 showed stability at some power values. In this case, it can be suggested that increasing the rf input power led to an increase of secondary electrons which have large effect on the dissociative excitation of H_β and CH (431.4 nm) [27]. Changing the deposition time also caused some differences in the intensities of carbon atom species. As the gas flow rate was raised, the amount of all carbon species indicated an increase at 15 min deposition time while they decreased at 30 min, except CH(431.2). Increasing the power in both deposition times resulted in an increase of the amounts of all carbon species. The intensity of CH^+ ion increased linearly by the raised rf power and since the quality of the film could be symbolized with quantity of the CH^+, it can be suggested that higher power values are more effective in producing thin films with good quality and uniformity.

To understand the relation of species with each other, the ratios of intensities were investigated and presented in Table 6.2. The $I(CH)/I(H_\beta)$ ratio is important for determining the excitation of CH (431.2nm). From Figure 6.3, it was seen that this ratio increased for lower gas flow rate while it showed a decrease for higher gas flow rate. Increasing the power led to a decrease in this ratio. It could be suggested that more excitation of CH was occurred at low power and low gas flow rate. The ratio of $I(H_\beta)/I(H_\alpha)$ indicated a decrease with increased gas flow rate, except at 4 sccm. By increasing the power with the flow rate, the ratio first decreased and then exhibited small increase. The $I(H_2)/I(H_\beta)$ ratio is related with the dissociation and recombination of hydrogen components. Therefore, for higher levels of this ratio, it could be supposed that the producing of H_2 ($G^1\Sigma g^+$) in Reaction 6.3 is dominant way for excitation of the CH_4 molecules [34]. It indicated a decrease at high values of input power and low CH_4 flow rate, and this showed that the recombination of hydrogen species in plasma with these parameters was at low level.

126

Table 6.2 The ratio of OES emission intensities and measurements of thicknesses and band gap energy

f	P	t	$I(CH)/I(H_\beta)$	$I(CH)/I(C_2)$	$I(H_2)/I(H_\beta)$	$I(H_\beta)/I(H_\alpha)$	T_1	T_2	E_g
2	100	15	0.48	0.87	0.43	0.55	584	446	1.45
2	150	15	0.38	0.79	0.36	0.53	654	557	0.85
2	200	15	0.35	0.62	0.35	0.57	796	634	0.85
3	100	15	0.59	1.08	0.43	0.53	612	504	1.55
3	150	15	0.43	1.05	0.37	0.48	757	580	1.55
3	200	15	0.36	1.05	0.33	0.49	917	758	1.55
3	150	30	0.43	0.93	0.32	0.42	1017	852	1.60
3	200	30	0.34	0.78	0.34	0.39	1139	972	1.35
3	250	30	0.28	0.67	0.32	0.41	1160	1035	1.40
3	300	30	0.25	0.57	0.28	0.42	478	127	0.65
4	100	15	1.42	0.64	1.00	0.21	684	551	1.55
4	150	15	0.51	0.84	0.41	0.48	798	601	1.35
4	200	15	0.45	0.83	0.37	0.56	933	808	1.25
5	100	15	0.75	1.69	0.45	0.48	797	674	1.50
5	150	15	0.51	1.38	0.40	0.41	850	767	1.50
5	200	15	0.43	0.68	0.39	0.44	945	863	1.45
5	150	30	0.57	1.07	0.43	0.48	1664	1365	1.40
5	200	30	0.41	1.30	0.37	0.50	1757	1554	1.40
5	250	30	0.38	0.90	0.36	0.42	2200	1850	1.40
5	300	30	0.33	0.61	0.34	0.38	583	332	1.40

T_1: Thickness of 1mm sample (Å), T_2: Thickness of 0,2 mm sample (Å), E_g: Indirect Band Gap Energy (eV)
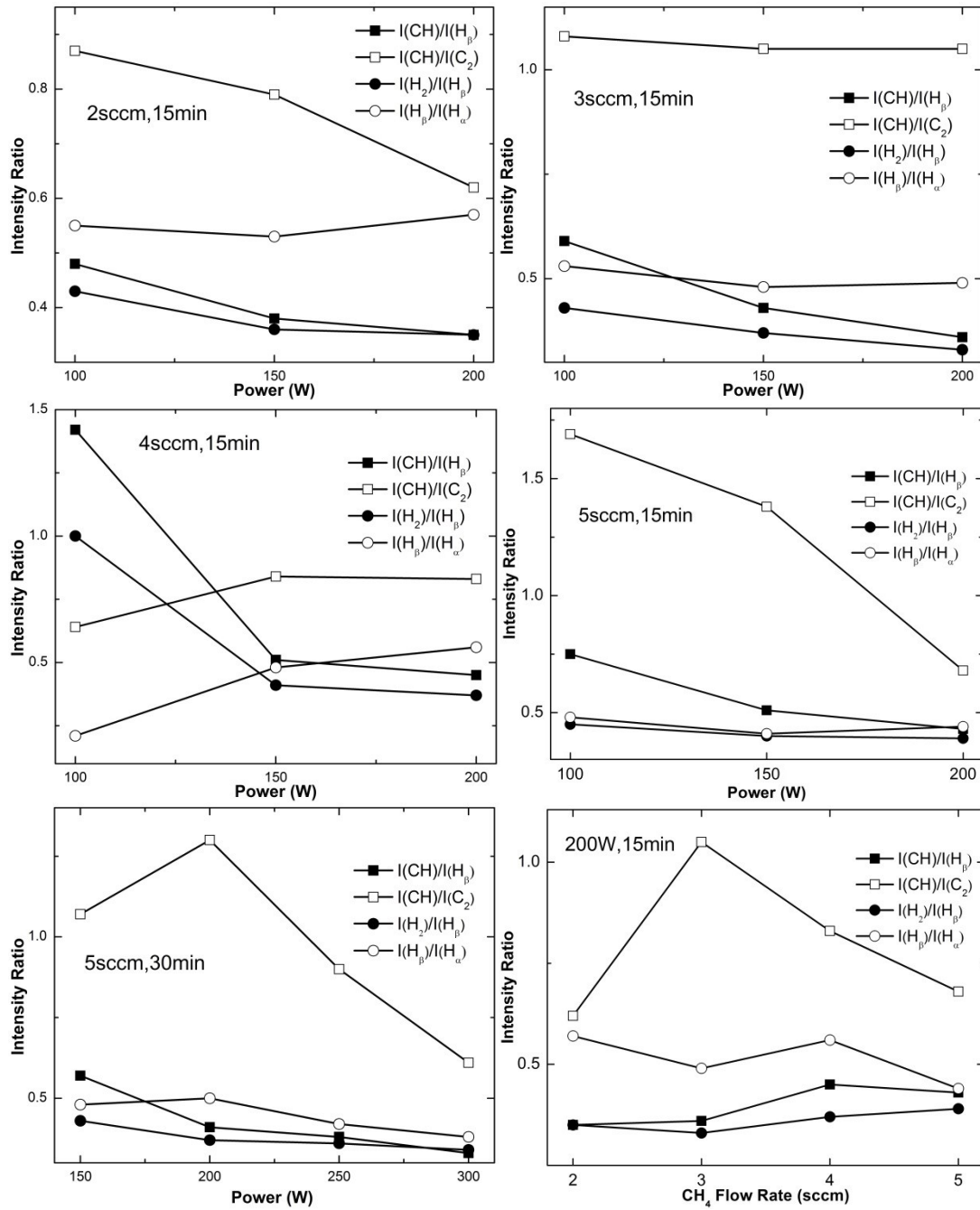
Figure 6.3 The ratios of $I(CH)/I(H_\beta)$, $I(CH)/I(C_2)$, $I(H_2)/I(H_\beta)$, and $I(H_\beta)/I(H_\alpha)$ with respect to parameters of rf power, CH_4 flow rate, and deposition time

The $I(CH)/I(C_2)$ ratio is directly related with the population of the excited species [41] and the variations of this ratio shows changes in the density or temperature of the electron. According to H. Song et al. [42], the C_2 radical is generated by the reactions caused by the collisions of carbon-containing radicals in gas phase. The results showed the intensity of C_2 radical increased at high power values and high

gas flow rate. Therefore, it could also be expected that the CH_4 dissociation by the electron impact increased with raised input power and gas flow rate. In addition, Kim and Lee [43] suggested that the increase of C_2 components in plasma leads to the deposition of sp^2 carbon during discharge. In this case, it may be suggested that the content of C_2 components is more useful for determination of the type of thin film [44].

6.3.2 Thickness Measurements

All thickness measurements were listed on the Table 6.2 with respect to variable plasma parameters. The flow rate plays an important role in determination of deposition rate. It leads to a change of plasma properties such as the density of ions and electrons, the electron temperature, and the chemical effect of ion energies. In addition, it controls the amount of and the presence time of gas inside the chamber, therefore, it determines the degree of dissociation [28]. From the table, it was seen that the increase in the CH_4 flow rate led to an increase in thickness of the thin film. However, at low flow rates (for 1sccm), a film couldn't be obtained, since the H content is higher than the C-containing compounds, and this results in decreasing the ion density while increasing the electron temperature. When the amount of the CH_4 gas diffusing through the chamber was increased, the ionization rate was raised by increased input power. However, this increase was not continuous and the thickness value started to decrease after it reached to its maximum value at 250 W input power. This can be due to the saturation of the electron temperature and density which leads to a loss in collision and diffusion [42]. At low power values, a deformation on the surface was observed when the deposition time was increased. It can be due to charging of the surface or insufficient ionization rate and much more the presence of electrons inside the plasma because of higher H content which results in etching the surface of the thin film. In contrast, as the input power was increased parallel to deposition time, this problem was solved and the thin films were obtained with a better quality and uniformity. Thickness of the thicker sample was measured higher than that of thinner sample for all experiments and both showed the same variations by changing the parameters. When the deposition time was increased from 15 min to 30 min, the thickness showed a significant increase (Figure 6.4).
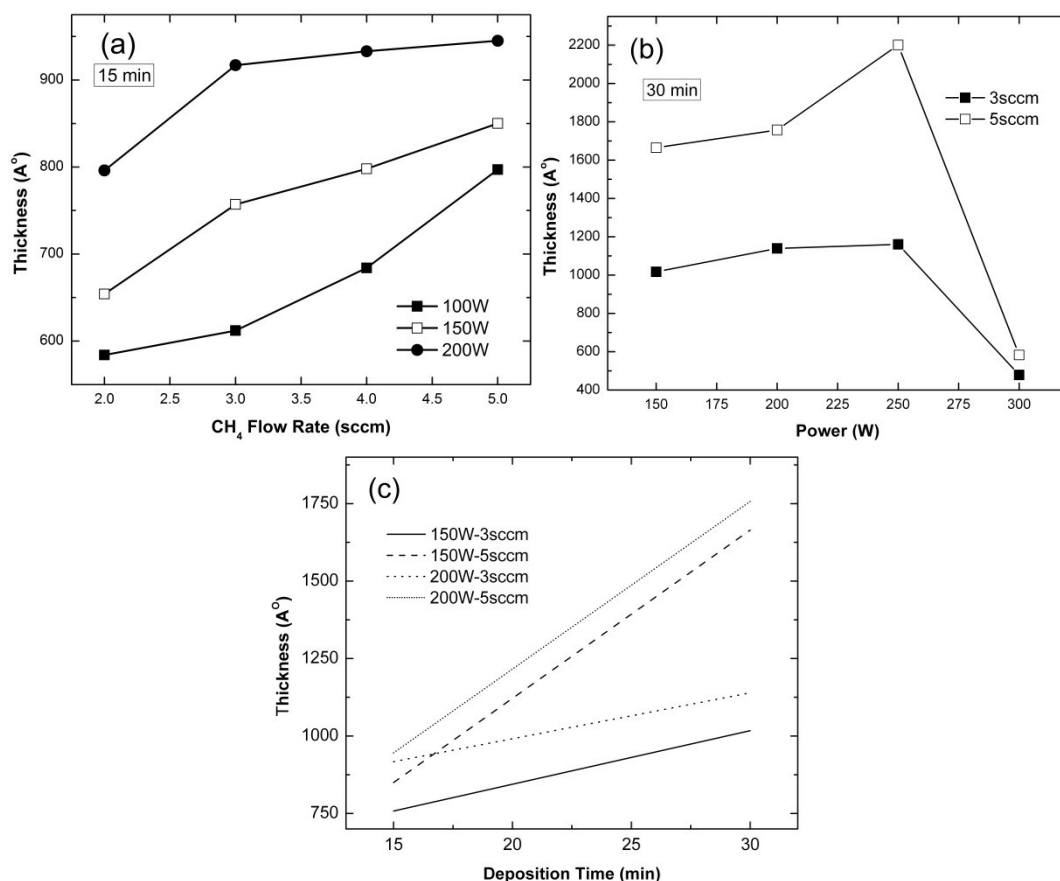
Figure 6.4 Variation of the thickness (thicker sample) with respect to plasma parameters: (a) CH4 flow rate, (b) input power, and (c) deposition time

6.3.3 Fourier Transform Infrared Spectroscopy

The infrared spectra of the thin films were collected in the region of 3100-600 cm^{-1}. In the spectra, a broad peak in the region from 2800 to 3100 cm^{-1} was assigned to the C-H stretching vibration band [18,34,42,45–47]. The peak at 1630 cm^{-1} was associated with the olefinic sp^2 C=C stretching vibration [18,46,48,49] and 1580 cm^{-1} was assigned to aromatic sp^2 C=C stretching vibration [18,49]. In addition, at 1450 and 1380 cm^{-1} the asymmetrical and symmetrical deformation modes (C-H bending) were observed in CH$_3$ groups, respectively [42,47,50]. The out of plane C-H bending was observed at the peaks seen in the range from 930 to 700 cm^{-1}, and the peaks of 1095 and 670 cm^{-1} corresponded to in-plane CH deformation and C=C out-of-plane ring deformation, respectively [51–53]. The presence of carbon double bond decreased with the increased power as shown in Figure 6.5. This case was

130

supported by the results of OES. The sharp peaks observed around 2360 and 2330 cm^{-1} were assigned to CO_2 vibration. The bands around 1750 cm^{-1} exhibited the presence of the carbonyl containing groups [48,50–53].
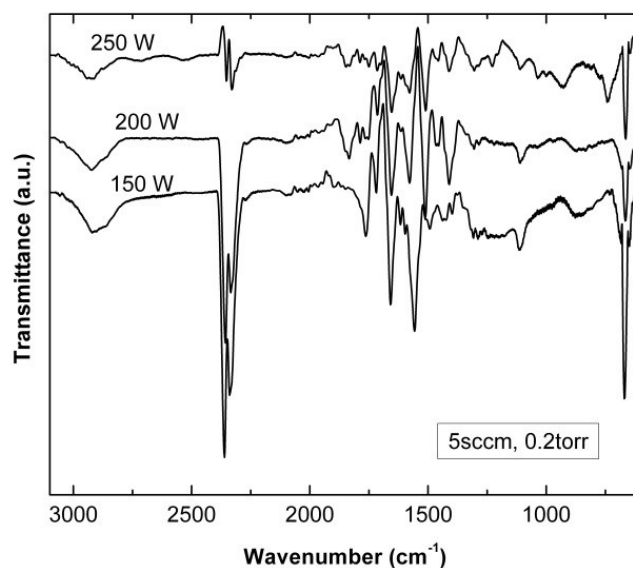
Figure 6.5 The FTIR spectra of selected a-C:H thin films

The structure of a-C:H film includes both diamond like (sp^3 bonding) and graphitic (sp^2 bonding) structures. In general, the structure of the a-C:H film is characterized with the sp^3/sp^2 bonding ratio and the H content. The sp^3/sp^2 ratio can be determined in four types of structures with percentage: diamond – 100% sp^3 bonding, amorphous carbon film (a-C) – up to 90% sp^3 bonding, amorphous hydrogenated carbon film (a-C:H) – up to 60% sp^3 bonding, and graphite – 100% sp^2 bonding [54]. Determining the levels of these bonds is possible by exploration of the broad band centered at 2920 cm^{-1}. The deconvolution of broad peak was analyzed with peak fit software (seasolve, version 4.12) as shown in Figure 6.6. After the fitting process, the configuration included the centered peak at 2920 cm^{-1} referring to monohydrogen radicals (-CH) [34] or sp^3 CH_2 asymmetric mode, and the peaks of 2960 and 2870 cm^{-1} attributed to sp^3 CH_3 asymmetric mode and sp^3 CH_3 symmetric mode [42,45–47,55–57], respectively. The other peaks contributing to broad band were at 2855, 2950, 3000, 3020, and 3050 cm^{-1} and attributed to sp^3 CH_2 symmetrical, sp^2 CH_2 olefinic, sp^2 CH olefinic, sp^2 CH_2 olefinic, and sp^2 CH aromatic, respectively [29,45–47,55–57]. The sp^3/sp^2 ratio could be calculated from

131

the areas of these non-overlapping peaks [45,46]. The ratio increased with increasing CH_4 diffusion. The higher flow level caused an increase in the H content, and since the sp^3 bond is directly related to hydrogen, this could be suggested as a reason of the increase in the ratio. Increasing the input power led to a decrease of the sp^3/sp^2 ratio. This could be explained by influence of the power to the degree of ionization. By increasing the power, the degree of ionization was also increased, and this caused the sp^3 bond to fragment and C bonds to become more unhydrogenated in the deposition [57]. Therefore, the ratio showed the H content was low at a higher power. These results were consistent with results of OES. Additionally, the structures of generated thin films were closer to graphitic structures at high power and CH_4 flow rate.
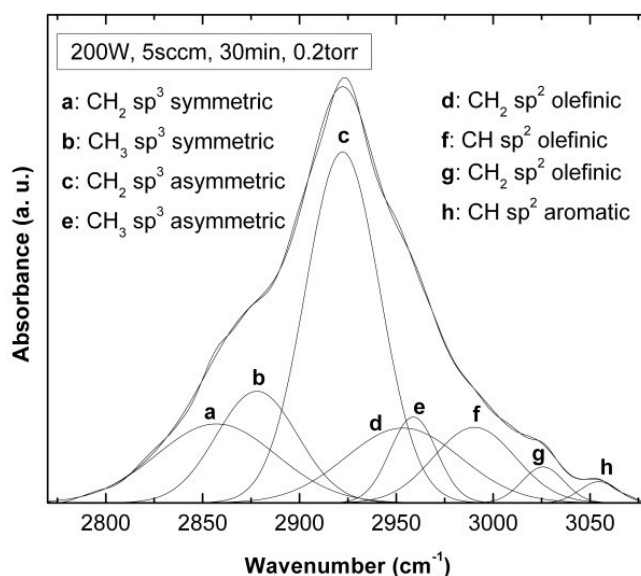
Figure 6.6 Deconvolution of the 2920 cm^{-1} peak of FTIR
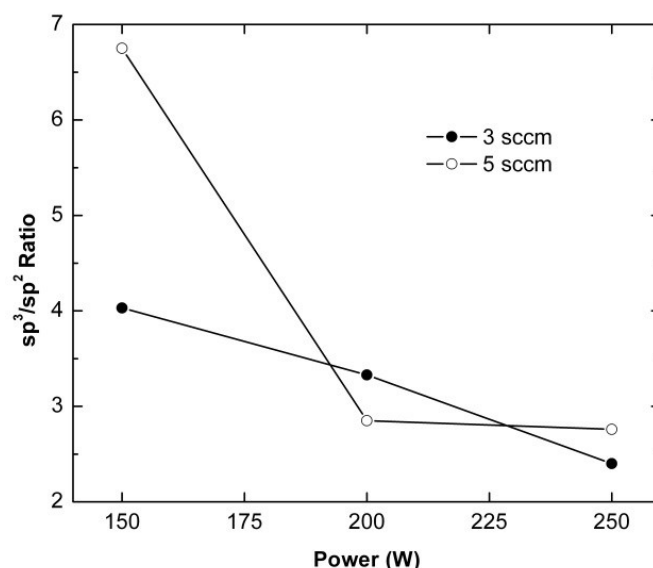
Figure 6.7 The variation of sp^3/sp^2 ratio with respect to power

In plasma deposition, a thin film with cross-linking structure is an expected result. The degree of cross-linking decreases, while deposition rate increases by the increased gas flow rate. It was stated before that the low excitation and dissociation of the monomer in the plasma chamber causes to obtain the thin film with higher cross-linking degree [58]. As the degree of cross-linking increases, this leads to the removal of sp^2 bonding and increase of the sp^3/sp^2 ratio [45]. Therefore, it could be suggested that the structure of thin films indicated higher degree of cross-linking at the low power and flow rate.

6.3.4 X-ray Diffraction

X-ray diffraction analysis were employed to reveal the structural properties of a-C:H films. The X-ray diffractograms of only two selected films are presented in Figure 6.8, for clarity. It is seen from the figure that a diffused broad peak is present in both diffractograms showing amorphous nature of the film structure. It is a general knowledge that the property of crystallization could be improved by annealing.
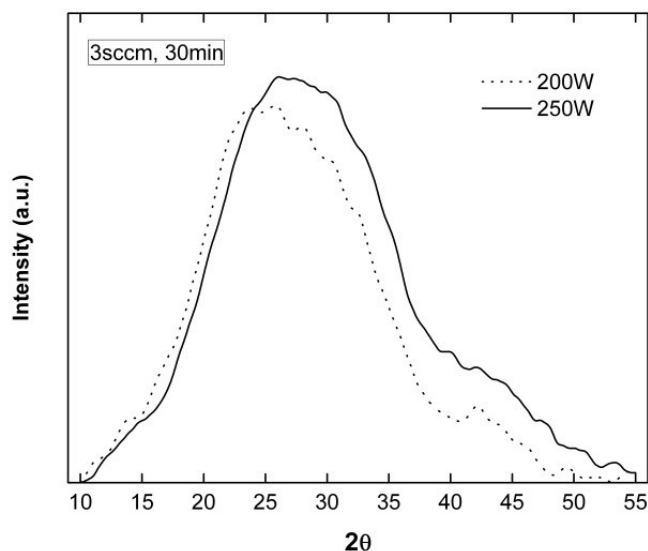
Figure 6.8 X-ray diffraction patterns of a-C:H films produced at 200 and 250W rf power with 3sccm flow rate under exposure time of 30 minutes

6.3.5 UV-visible Spectroscopy

The evaluation the optical performance of a-C:H thin films can be done by using the information about their optical transmittance. The result of the optical transmission measurements for the samples produced with the applied rf power of 150W in the wavelength range of 275 to 1100 nm were given in Figure 6.9 as an example. The ripples seen in some of the spectra are thought to originate from the interference of light due to their wave form. The results show that a wide wavelength range of absorption is present in all of the samples suggesting formation of amorphous film structure which was also confirmed by X-ray analysis previously.
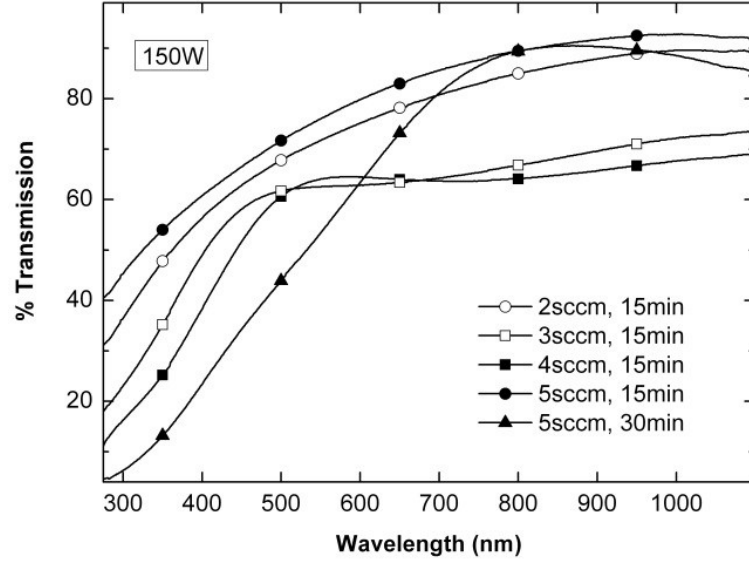
Figure 6.9 The spectral dependence of transmittance of a-C:H thin films produced with the applied rf power of 150W (Symbols were added to the figure for clarity)

The analysis of transmission data for all the samples can be done by using the absorption coefficient calculated by Beer Lambert's formula [59]

$$\alpha = -\frac{1}{d} ln\left(\frac{I}{I_0}\right) \qquad (6.1)$$

where d is the thickness of the film, I and I_0 are the transmitted and incident light intensities, respectively. The dependence of the absorption coefficient on photon energy can be used to obtain detailed information about the optical band gap energies of films. The calculation of α can yield information about the nature of the band gap by the help of Tauc's relation of the form [59]

$$(\alpha h v) = B\left(h v - E_g\right)^p \qquad (6.2)$$

where B is a constant that is related with the probability of transition and p is an index that defines the optical absorption process. The value of p is theoretically equal to 2 and 0.5 which refers to allowed transitions of indirect and direct origin, respectively. Figure 6.10 shows the dependence of α on light energy for a selected sample grown at a flow rate of 3 sccm, with the applied rf power of 300W and deposition time of 30 min. as an example. Analysis showed the dependence of absorption coefficient α to $(h v - E_g)^2$ for all samples, which suggests the presence of

135

an indirect band gap structure, since the value of the parameter p is equal to 2. As a result, a linear dependence of $(\alpha h v)^{0.5}$ on photon energy hv is expected. Inset of Figure 6.10 was drawn to show this dependence. In the figure, the experimental data were shown as circles and fitted to a linear equation shown as a solid line for finding the band gap energies. Extrapolation of the straight line to $(\alpha h v)^{0.5}=0$ reveals the value of indirect band gap energy, as suggested by equation (6.2). The resulting band gap energies calculated for all the samples by this method are given in Table 6.2.
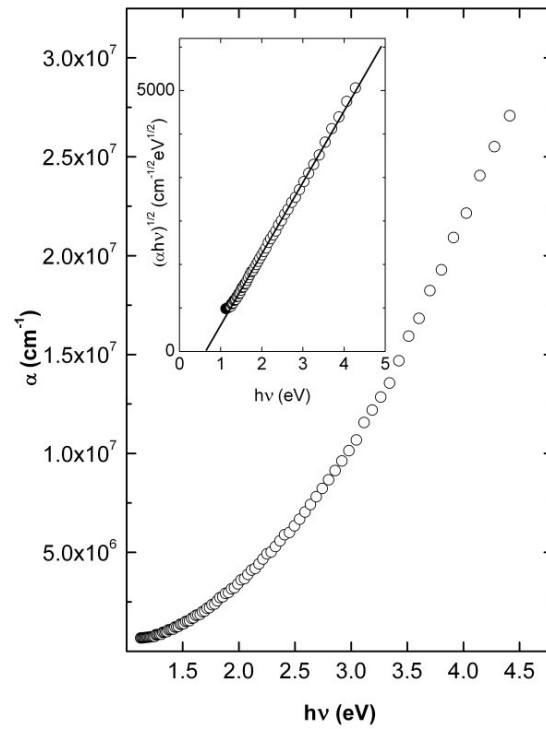
Figure 6.10 The dependence of α on hv. Inset: The linear dependence of $(\alpha h v)^{0.5}$ on photon energy hv

For the analysis of optical band gap data, Figure 6.11 is drawn. In the figure, the dependence of optical indirect band gap energy on rf power and flow rate is shown. The range of calculated optical band gap energy values is consistent with the ranges reported by Dischler [45], Couderc [46], Meyerson [60] and Bubenzer [49]. It is seen from the figure that band gap energy roughly increases as the flow rate increase except for the sample produced in 15 min. with 3 sccm flow rate. Such an increase in band gap energy with increasing flow rate can be related to the increase in H

content, and hence sp^3/sp^2 bond ratio [49,61,62]. It is also seen from the figure that band gap energy roughly decreases as the power increases except for the samples produced in 15 min. with 3 sccm flow rate and in 30 min. with 5 sccm flow rate. Similarly, such a decrease in band gap energy with increasing power can be related to the decrease in H content, as reported previously. It has been also reported that besides an increase in the optical gap, an increase in the hydrogen content also results in a decrease in the film density, volume stresses, hardness and an increase of the polymeric content of the film [46].
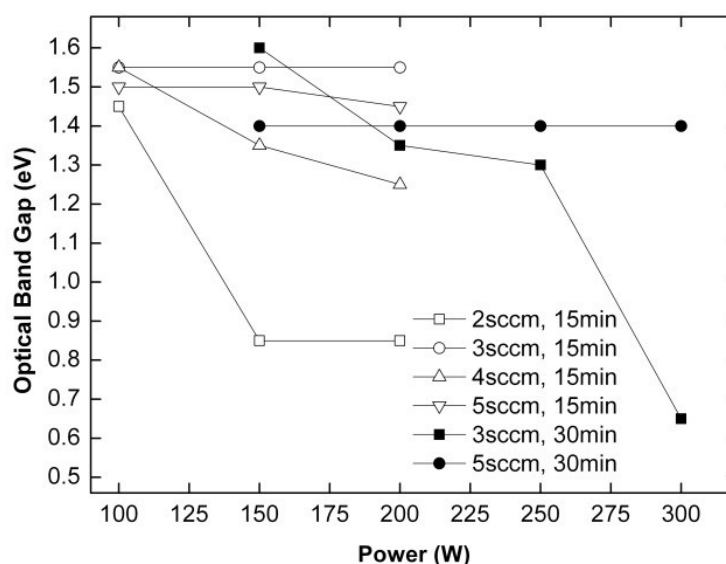
Figure 6.11 The dependence of optical band gap energy of produced films on power

6.3.6 Contact Angle Analysis

To define the characteristics of wettability, we measured the contact angle between a liquid (water for our measurements) and the surface of the films. Before the deposition, the contact angle of the sample was 70.3°, and this value increased after the deposition (Figure 6.12). It is known that if the contact angles are smaller than 90°, this refers to hydrophilic characteristics, and if larger, this refers to hydrophobic characteristics. The generated thin films exhibited more hydrophobic properties at low gas flow rate. Increasing the rf power led to an increase in the contact angle up to 200 W, and then a small decrease occurred at higher rf power. There was no

important difference as the deposition time was changed. As shown in the Figure 6.13, the contact angle represented a variable behavior with the sp^3/sp^2 ratio.
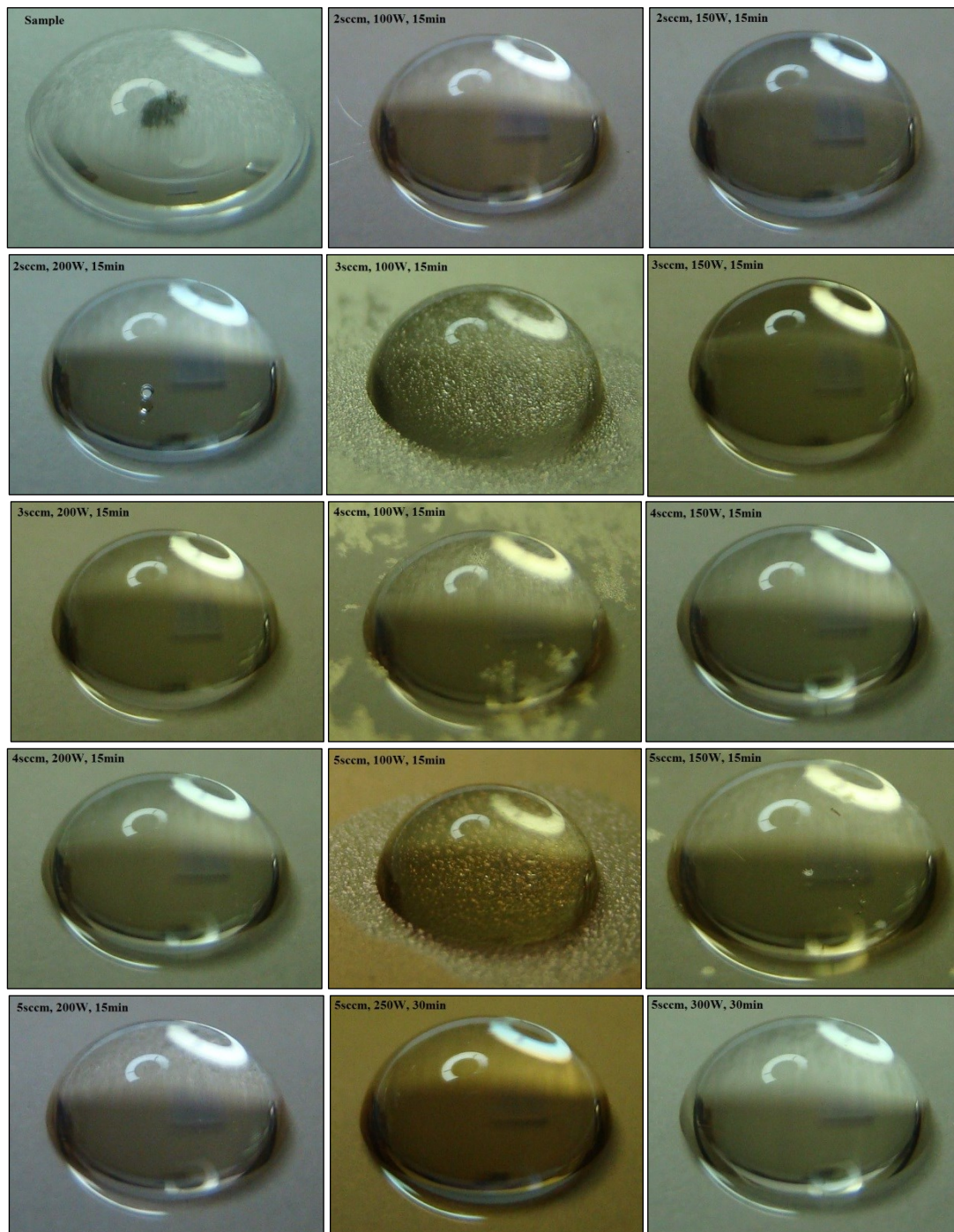
Figure 6.12 The contact angle images of thin films
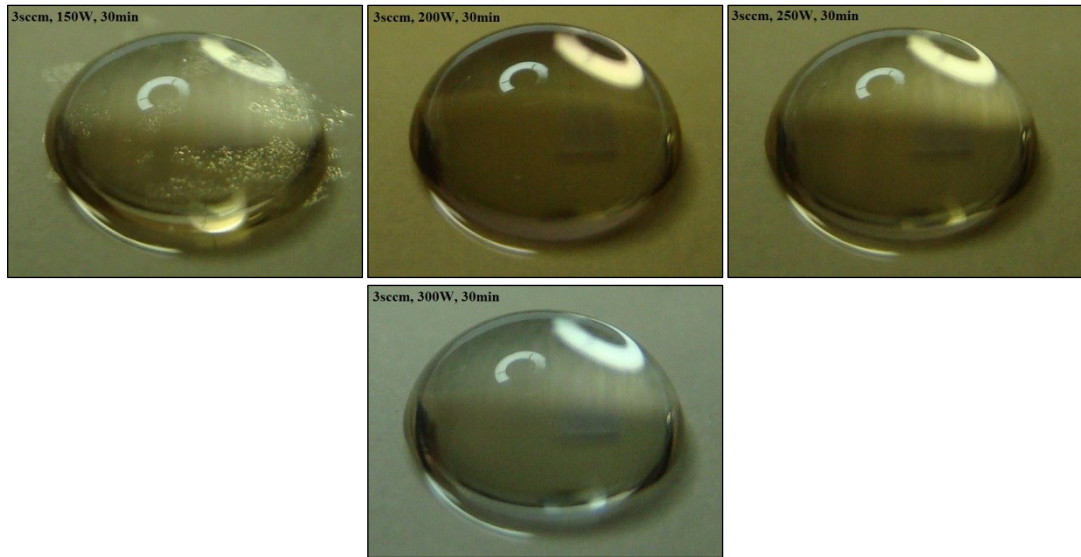
Figure 6.12 (continued)
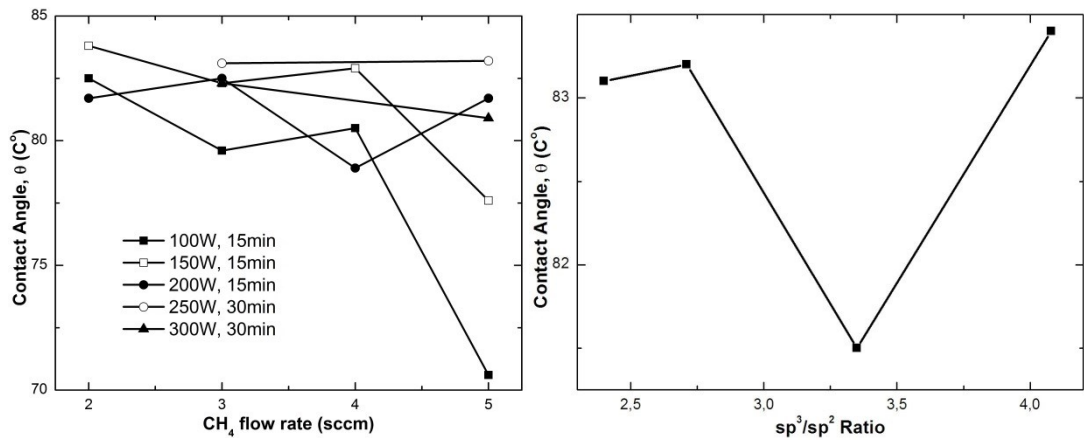
Figure 6.13 The change in contact angle with respect to flow rate and sp^3/sp^2 ratio

6.4 An Application for Crystalline Silicon (c-Si) Solar Cell

The efficiency of photovoltaic devices such as solar cells is limited due to the reflection of incoming radiation. To minimize the reflection and improve the efficiency of the solar cell, a suitable antireflection coating is used as an effective way. The antireflection coating should cover a wide range of wavelengths of solar radiation with low reflectance [63]. A good antireflection coating requires the cases of the sensitive control of coating, the high durability, the good response to ultraviolet radiation, and the effective combination with the surface. Although there

139

are many materials which have been used as antireflection coating for solar cells such as indium-tin-oxide (ITO), tin dioxide (SnO_2), silicon dioxide (SiO_2), magnesium fluoride (MgF_2), and zinc sulfide (ZnS), these materials are not practical due to the shortage problem and it increases the product cost. However, carbon based compounds such as amorphous carbon (a-C) and amorphous hydrogenated carbon (a-C:H) separated from these materials with their good environmental behavior and low cost opportunity [64,65].

The a-C:H (diamond-like) film was used in several studies as the antireflection coating material for silicon solar cells [65–73]. The diamond-like (sp^3 bonded) carbon film has been used as antireflecting coating due to its suitable transmission range, chemical and thermal stability, tunable optical properties, environmental behavior, internal stress, homogeneity, reproducibility, etc [74]. It can be obtained with various methods, such as plasma enhanced chemical vapor deposition (PECVD) [75–78], sputtering [79], ion beam deposition [80,81], microwave deposition [82], pulsed laser deposition [83,84], and filtered vacuum arc [85]. Among these methods, the radio frequency PECVD method is commonly used due to the opportunity of deposition to a large area under low temperature with low cost and providing the uniform coating for different sizes and shapes [86].

In our work, we investigated the effect of the a-C:H thin film by coating on a crystalline silicon (c-Si) solar cell. The c-Si wafer solar cells were produced in GUNAM laboratory at Middle East Technical University. The a-C:H thin film was formed under methane plasma with single radio frequency system. All measurements were shown in Table 6.3. The effect of the thin films was discussed with respect to the efficiency of the solar cell η which is defined as

$$\eta = \frac{V_{oc}I_{sc}FF}{EA_c} \tag{6.3}$$

where V_{oc} is the open-circuit voltage, I_{sc} is the short-circuit current, FF is the fill factor, E is the incident radiation flux, and A_c is the area of the solar cell. The change in the efficiency was investigated under the rf power, CH_4 flow rate, and the deposition time. As seen in Figure 6.14, deposition of the thin film on top of a moderate-efficiency solar cell resulted in improved efficiencies for a-C:H thin films. Also, thin film deposition caused higher fill factor (FF) values. The most effective

changes were seen for the samples deposited at 5, 10, and 15 min deposition time, at 200 W power, and 5 sccm flow rate. The efficiency showed small increases as the deposition time was decreased below 5 min. Also, decreasing the power value caused insignificant increases in the efficiency as the deposition time and the flow rate was hold at low values. It could be suggested that the interesting results were obtained at high values of the power, CH_4 flow rate and deposition time.
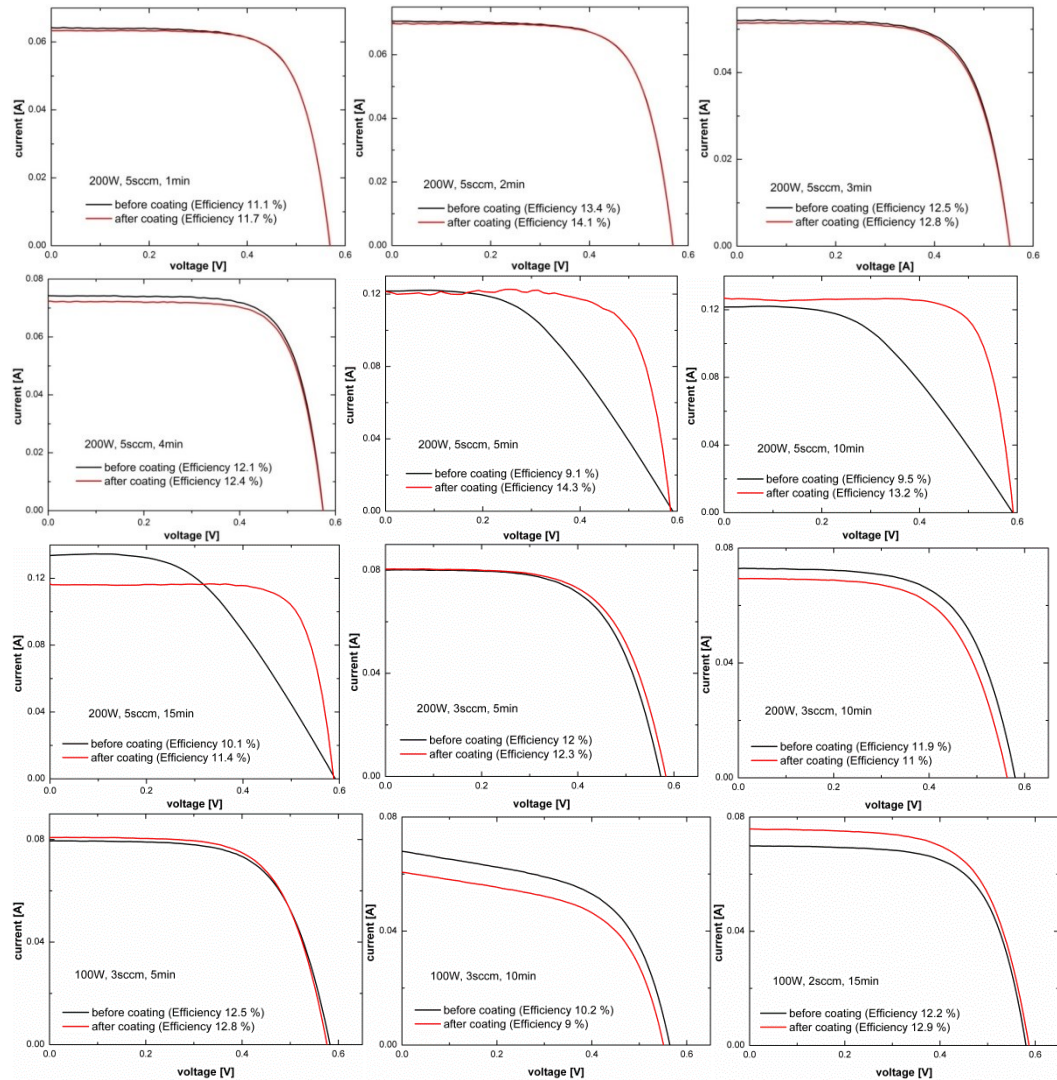
Figure 6.14 The I-V graphs of solar cells before and after the a-C:H film deposition
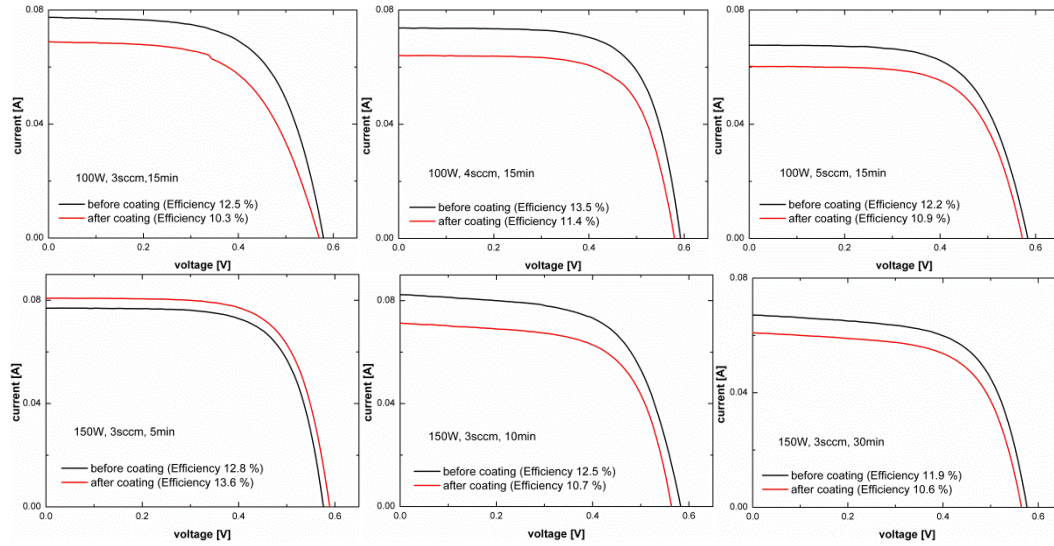
Figure 6.14 (continued)

It is known that, in order to use the a-C:H thin film as window (absorber) layer, it should exhibit a high absorption (especially in the visible region) to be able to form the sufficient electron-hole pairs, which help to trap the photons and prevent them from escaping from the absorber layers of solar cells. To obtain an effective absorber layer, the most crucial step is forming a layer with physical thickness as thin as possible and with maximizing the optical thickness. If the thickness is larger than the desired one, it leads to prevent the photons reaching the interlayers [69,87]. Therefore, it could be said that the efficiency of the solar cell depends on the thickness of the coating film [74] and the effective coating thickness for our parameters was obtained at high power and high flow rate.

In amorphous hydrogenated carbon film, the structure could occur in the form of the sp^3 bonding or the sp^2 bonding. The sp^3 bonding corresponding to a diamond-like structure has higher chemical inertness, optical transparency, mechanical hardness, thermal conductivity, and wider band gap than the sp^2 bonded structure [11]. To provide the photons penetrate into the silicon solar cells, the antireflection coating materials should have a large band gap. Because of that, it can be said that the sp^2 bonded films (graphite-like) which have small band gap are not recommended for antireflection coating [65]. In other words, the sp^3 bonded structures are more appropriate for the antireflection coating. The utility of band gap in an a-C:H-based solar cell was investigated by Tinchev et al [88]. We studied the optical properties of

142

a-C:H thin film in section 6.3.5. It was shown that the deposited thin film had a good transmission and a wide range of band gap which is changeable with respect to the variable plasma parameters.

Table 6.3 Measurements of I-V graph for a-C:H films

Power (W)	Flow rate (sccm)	Dep. Time (min)		Voc (V)	Isc (A)	Jsc (mA/cm^2)	Fill Factor (%)	Efficiency (%)
100	2	15	before	0.58	0.07	31.2	66.9	12.2
			after	0.586	0.075	33.8	65.4	12.9
100	3	5	before	0.582	0.079	33.1	65	12.5
			after	0.576	0.081	33.7	65.8	12.8
100	3	10	before	0.564	0.068	32.7	55.8	10.2
			after	0.55	0.061	29.2	55.7	9
100	3	15	before	0.584	0.077	34.5	62.9	12.5
			after	0.571	0.069	30.7	58.6	10.3
100	4	15	before	0.592	0.073	32.8	69.3	13.5
			after	0.579	0.064	28.6	68.8	11.4
100	5	15	before	0.583	0.067	32.5	64.8	12.2
			after	0.572	0.06	28.9	65.7	10.9
150	3	5	before	0.575	0.077	32.1	69.3	12.8
			after	0.589	0.081	33.7	69.1	13.6
150	3	10	before	0.582	0.082	34.2	63	12.5
			after	0.563	0.071	29.7	64	10.7
150	3	30	before	0.576	0.067	32.3	64.2	11.9
			after	0.565	0.061	29.3	63.8	10.6
200	3	5	before	0.572	0.08	29.7	62.8	12
			after	0.583	0.08	33.5	63.4	12.3
200	3	10	before	0.579	0.073	32.5	63.2	11.9
			after	0.563	0.069	31	62.5	11
200	5	1	before	0.568	0.064	22.9	71.2	11.1
			after	0.573	0.063	22.6	72.2	11.7
200	5	2	before	0.568	0.070	27.6	70.9	13.4
			after	0.573	0.069	27.3	71.7	14.1
200	5	3	before	0.552	0.052	27.1	69.1	12.5
			after	0.554	0.051	26.8	69.0	12.8
200	5	4	before	0.574	0.074	24.2	72.4	12.1
			after	0.577	0.072	23.6	72.9	12.4
200	5	5	before	0.591	0.121	25.3	47.3	9.1
			after	0.600	0.125	26.1	74.3	14.3
200	5	10	before	0.593	0.134	30.7	48.4	9.5
			after	0.599	0.120	25.1	73.5	13.2
200	5	15	before	0.591	0.134	27.9	47.7	10.1
			after	0.599	0.125	26.1	74.4	11.4

Besides the antireflection effect, the hydrogen passivation effect on the solar cell was also investigated for a-C:H films [89–91]. The improvement of the efficiency of

c-Si solar cells can be supplied with both of the appropriate antireflection coating on the solar cell and passivation of recombination active centers on the solar cell surface during the film deposition [74]. In the passivation process, the properties of cells are improved via the interaction of H with impurities and defects in the bulk of Si. The H passivation also provides to obtain devices with high quality and low surface recombination [92].

The electrical activities of deep impurities and shallow of acceptors in silicon solar cells are neutralized by hydrogen interaction [93]. It is expected that the formation of a pair of neutral and hydrogen vacancy with the formation of a bridged Si-H bond. Firstly, in the case of absence of hydrogen, a Si atom moves toward the vacancy. While the Si atom is following into a straight path toward the vacancy, it changes along the curved path by the existence of hydrogen atom. Secondly, as a result of this interaction, the hydrogen atom breaks one S-H bond and then generates a new bond with Si atom. Finally, this new Si-H bond occurs with rotated position, and to get back to its initial position a rotation is required. After this rotation, the total energy decreases [92]. In other words, the passivation can be explained by the deep penetration of hydrogen into the out of layer of the solar cell and connecting with dangling bonds in the deflected multicrystalline material [91].
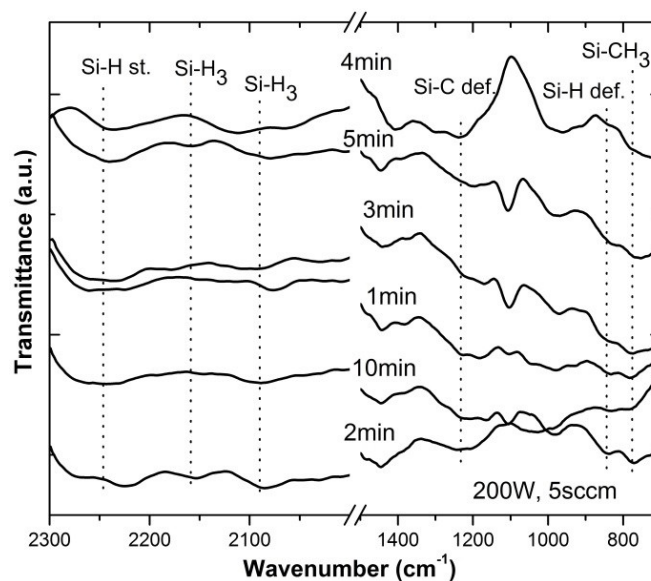
Figure 6.15 The FTIR spectra results for a-C:H films

In the FTIR measurements, the 2246 cm^{-1} band corresponded to Si-H stretching vibration [52,94,95], which is the main band giving information about H-bonding to the silicon surface. The band around 740 cm^{-1} was assigned to Si-CH$_3$ rocking/wagging mode or to Si-C stretching mode [96,97]. For a-C:H films, two bands observed at 2160 and 2090 cm^{-1} assigned to Si-H$_3$ bonding. The bands at 1240 and 846 cm^{-1} corresponded to deformation of Si-C and Si-H, respectively [94,95]. There is a shifting in wavenumbers for some bands which can be due to the difference in the optical thickness or the carbon content in thin films. We can discuss the H passivation effect from the H-bonding with silicon surface. The existence of H-bonding was clearly seen for each result, but more distinctive result was observed for the solar cell coated at 5 min deposition time, which is in good agreement with the effect of antireflective coating.

6.5 Conclusion

The a-C:H thin films were synthesized by using a single capacitively coupled rf powered CH$_4$ plasma system under variable plasma parameters in a wide range. The amorphous structure of the thin film was revealed by XRD spectroscopy. The diagnostic properties of plasma species during the deposition were investigated by using OES and the structural properties of thin films were analyzed via FTIR spectroscopy. As a result of the measurements and analysis, it was found that the sp^3/sp^2 ratio and H content in the plasma are the most significant factors in determination of the type of the thin films, which was generally closer to graphitic structure. A profilometer was employed to measure thicknesses of the films, which were found to be in a linear relation with the sufficient ionization rate and deposition time. Moreover, the values of the optical band gap energies of films were revealed by using UV-visible spectroscopy. It was found that the indirect band gap energies changed in the region from 0.65 to 1.60 eV, which may result from different order of chains in the film structure generated with respect to the parameters. As a result of all analysis, it was found that the plasma reactor should contain enough C compounds and this content should be higher than the level of the H content to be able to obtain a thin film with good quality. The H content can be controlled with changing the plasma parameters. The a-C:H films generally exhibited good characteristics at higher input power and higher CH$_4$ flow rate, at 30 min deposition time. The produced a-C:H thin films were coated on the surfaces of c-Si solar cells

and it led to the improvement of the solar cell efficiency at high values of the deposition time, rf power, and CH_4 flow rate. This improvement can be due to the antireflective property or the hydrogen passivation effect of the deposited films.

6.6 References

[1]   F.F. Shi, Surf. Coatings Technol. 82 (1996) 1.

[2]   L. Martinu, D. Poitras, J. Vac. Sci. Technol. A 18 (2000) 2619.

[3]   H. Biederman, D. Slavínská, Surf. Coatings Technol. 125 (2000) 371.

[4]   A. Hiratsuka, I. Karube, Electroanalysis 12 (2000) 695.

[5]   M.V. Jacob, C.D. Easton, G.S. Woods, C.C. Berndt, Thin Solid Films 516 (2008) 3884.

[6]   J. Friedrich, Plasma Process. Polym. 8 (2011) 783.

[7]   J. Angus, P. Koidl, S. Domitz, in:, J. Mort, F. Jansen (Eds.), Plasma Depos. Thin Film., CRC Press, Boca Raton, FL, 1986, p. 89.

[8]   D. Green, D. McKenzie, P. Lukins, Mater. Sci. Forum 52-53 (1990) 103.

[9]   H. Tsai, Mater. Sci. Forum 52-53 (1990) 71.

[10]   J. Robertson, Mater. Sci. Eng. R Reports 37 (2002) 129.

[11]   J. Robertson, Surf. Coatings Technol. 50 (1992) 185.

[12]   M. Geis, M. Tamor, Encyclopedia of Applied Physics, VCH, New York, 1993.

[13]   H.T. Kim, S.H. Sohn, Vacuum 86 (2012) 2148.

[14]   H. Vora, J. Appl. Phys. 52 (1981) 6151.

[15]   G. Dearnaley, J.H. Arps, Surf. Coatings Technol. 200 (2005) 2518.

[16]   C. Casiraghi, A.C. Ferrari, R. Ohr, D. Chu, J. Robertson, Diam. Relat. Mater. 13 (2004) 1416.

[17]   C. Casiraghi, A.C. Ferrari, J. Robertson, R. Ohr, M. V Gradowski, D. Schneider, H. Hilgers, Diam. Relat. Mater. 13 (2004) 1480.

[18]   B.N. Jariwala, C. V. Ciobanu, S. Agarwal, J. Appl. Phys. 106 (2009) 073305.

[19]   J. Robertson, Thin Solid Films 383 (2001) 81.

[20]   G.A.J. Amaratunga, Science 297 (2002) 1657.

[21]   R.J. Narayan, Mater. Sci. Eng. C 25 (2005) 405.

[22]   S.E. Rodil, R. Olivares, H. Arzate, S. Muhl, Diam. Relat. Mater. 12 (2003) 931.

[23]   S.R.P. Silva, R.D. Forrest, D.A. Munindradasa, G.A.J. Amaratunga, 7 (1998) 645.

[24]   J. Xu, X. Huang, W. Li, L. Wang, X. Huang, K. Chen, J. Xu, I.H. Wilson, Appl. Phys. Lett. 79 (2001) 141.

[25]   J. Robertson, Thin Solid Films 296 (1997) 61.

[26]   M.W. Geis, N.N. Efremow, K.E. Krohn, J.C. Twichell, T.M. Lyszczarz, 393 (1998) 431.

[27]   A. Pastol, Y. Catherine, J. Phys. D. Appl. Phys. 799 (1990).

[28]   M. Weiler, R. Kleber, K. Jung, H. Ehrhardt, Diam. Relat. Mater. 1 (1992) 121.

[29]   J.W. Zou, K. Schmidt, K. Reichelt, B. Dischler, J. Appl. Phys. 67 (1990) 487.

[30]   J.W. Zou, K. Reichelt, K. Schmidt, B. Dischler, J. Appl. Phys. 65 (1989) 3914.

[31] J.W. Zou, K. Schmidt, K. Reichelt, B. Dischler, J. Appl. Phys. 68 (1990) 1558.

[32] D. Mansuroglu, K. Goksen, S. Bilikmen, Plasma Sci. Technol. 17 (2015) 488.

[33] K. Tsuji, K. Hirokawa, Appl. Surf. Sci. 59 (1992) 31.

[34] C. Gómez-Aleixandre, J. Vac. Sci. Technol. A Vacuum, Surfaces, Film. 11 (1993) 143.

[35] R.L. Vander Wal, J.H. Fujiyama-Novak, C.K. Gaddam, D. Das, A. Hariharan, B. Ward, Appl. Spectrosc. 65 (2011) 1073.

[36] C.B. Hansena, M.D. Bentzona, M.E. Vigild, E. Findeise, R. Feidenhans, J. Bindslev, 69 (1994) 702.

[37] R.C. Weast, Handbook of Chemistry and Physics 64th Edition, CRC Press, Boca Raton, FL, 1983.

[38] R. Pearse, A. Gaydon, The Identification of Molecular Spectra, 4th Editio, Chapman and Hall, London, New York, 1984.

[39] K.P. and G.H. Huber, Molecular Spectra and Molecular Structure Vol 4. Constants of Diatomic Molecules, New York, 1978.

[40] A.N. Goyette, J.E. Lawler, L.W. Anderson, D.M. Gruen, T.G. McCauley, D. Zhou, A.R. Krauss, Plasma Sources Sci. Technol. 7 (1998) 149.

[41] A. Yanguas-Gil, K. Focke, J. Benedikt, A. von Keudell, J. Appl. Phys. 101 (2007) 103307.

[42] H. Song, X. Yu, N. Zhaoyuan, Plasma Sci. Technol. 7 (2005) 2669.

[43] Y.-K. Kim, J.-Y. Lee, J. Appl. Phys. 81 (1997) 3660.

[44] D.M. Gruen, J. Vac. Sci. Technol. A Vacuum, Surfaces, Film. 13 (1995) 1628.

[45]   B. Dischler, A. Bubenzer, P. Koidl, Solid State Commun. 65 (1983) 105.

[46]   P. Couderc, Y. Catherine, Thin Solid Films 146 (1987) 93.

[47]   T. Heitz, B. Drevillon, C. Godet, J.E. Bouree, 37 (1999) 771.

[48]   S.C. Cho, Y.C. Hong, H.S. Uhm, J. Mater. Chem. 17 (2007) 232.

[49]   A. Bubenzer, B. Dischler, G. Brandt, P. Koidl, J. Appl. Phys. 54 (1983) 4590.

[50]   R. Mota, I. Perrenoud, R. Honda, Ep.liu.se (2012) 368.

[51]   H. Goktas, D. Mansuroglu, B. Atalay, S. Bilikmen, I. Kaya, Plasma Chem. Plasma Process. 32 (2011) 35.

[52]   B.H. Stuart, Infrared Spectroscopy: Fundamentals and Applications, John Wiley & Sons, Ltd, New York, 2004.

[53]   D. Pavia, G. Lampman, G. Kriz, J. Vyvan, Introduction to Spectroscopy, 4th ed., Brooks Cole, Fort Worth, 2001.

[54]   L. Ostrovskaya, V. Perevertailo, V. Ralchenko, A. Dementjev, O. Loginova, Diam. Relat. Mater. 11 (2002) 845.

[55]   L. Valentini, J.M. Kenny, 6 (2001) 5295.

[56]   N. Mutsukura, S. Inoue, Y. Machi, J. Appl. Phys. 72 (1992) 43.

[57]   J.W.A.M. Gielen, P.R.M. Kleuskens, M.C.M. van de Sanden, L.J. van Ijzendoorn, D.C. Schram, E.H.A. Dekempeneer, J. Meneve, J. Appl. Phys. 80 (1996) 5986.

[58]   J. Park, J. Kim, D. Lee, 2002 Annu. Rep. Conf. Electr. Insul. Dielectr. Phenom. (2002) 64.

[59]   J. Pankove, Optical Processes in Semiconductors, Prencite-Hall, Englewood Cliffs, NJ, 1971.

[60] B. Meyerson, F. Smith, J. Non. Cryst. Solids 35-36 (1980) 435.

[61] E. Freeman, W. Paul, Phys. Rev. B 20 (1979) 716.

[62] G. Cody, T. Tiedje, B. Abeles, B. Brooks, Y. Goldstein, Phys. Rev. Lett. 47 (1981) 1480.

[63] V.M. Aroutiounian, K.S. Martirosyan, P.G. Soukiassian, Phys. Status Solidi 4 (2007) 2107.

[64] P.A. Iles, J. Vac. Sci. Technol. 14 (1977) 1100.

[65] M.H. Oliveira, D.S. Silva, A.D.S. Côrtes, M.A.B. Namani, F.C. Marques, Diam. Relat. Mater. 18 (2009) 1028.

[66] T.J. Moravec, J. Vac. Sci. Technol. 20 (1982) 338.

[67] M. Allon-Alaluf, J. Appelbaum, M. Maharizi, Thin Solid Films 303 (1997) 273.

[68] M. Alaluf, J. Appelbaum, L. Klibanov, Thin Solid Films 256 (1995) 1.

[69] N. Dwivedi, S. Kumar, H.K. Malik, J. Appl. Phys. 111 (2012) 014908.

[70] V. Litovchenko, N. Klyui, Sol. Energy Mater. Sol. Cells 68 (2001) 55.

[71] A. Tamulevičienė, Š. Meškinis, V. Kopustinskas, S. Tamulevičienė, Mater. Sci. 16 (2010).

[72] W.S. Choi, K. Kim, J. Yi, B. Hong, Mater. Lett. 62 (2008) 577.

[73] D.S. da Silva, A.D.S. Cortes, M.H. Oliveira, E.F. Motta, G.A. Viana, P.R. Mei, F.C. Marques, J. Appl. Phys. 110 (2011) 043510.

[74] V. Buršíková, P. Sládek, P. St'ahel, L. Zajíčková, J. Non. Cryst. Solids 299-302 (2002) 1147.

[75] S. Meskinis, R. Gudaitis, S. Tamulevičius, V. Kopustinskas, M. Andrulevicius, Mater. Sci. 15 (2009) 3.

[76] G. Lazar, Mater. Lett. 57 (2006) 586.

[77] J. Suzuki, S. Okada, Jpn. J. Appl. Phys. 34 (1995) L1218.

[78] M. Tamor, C. Wu, R. Carter, N. Lindsay, Appl. Phys. Lett. 55 (1989) 1388.

[79] N. Savvides, J. Appl. Phys. 59 (1986) 4133.

[80] S. Meskinis, V. Kopustinskas, K. Slapikas, R. Gudaitis, S. Tamulevičius, G. Niaura, V. Rinnerbauer, K. Hingerl, in:, Proc. SPIE 6596, 2007, p. 65961L−1.

[81] T. Kim, S. Han, B. Bae, Met. Mater. 5 (1999) 33.

[82] M. Stoikou, P. John, J. Wilson, Diam. Relat. Mater. 17 (2008) 1164.

[83] S. Kassavetis, P. Patsalas, S. Logothetidis, J. Robertson, S. Kennou, Diam. Relat. Mater. 16 (2007) 1813.

[84] Y. Lu, S. Huang, C. Huan, X. Luo, Appl. Phys. A 68 (1999) 647.

[85] J.W. Chung, C. Lee, D. Ko, J. Han, K. Eun, K. Lee, Diam. Relat. Mater. 10 (2001) 2069.

[86] T. Michler, M. Grischke, I. Traus, K. Bewilogua, H. Dimigen, Diam. Relat. Mater. 7 (1998) 459.

[87] M. Zeman, J. Electr. Eng. 61 (2010) 271.

[88] S. Tinchev, P. Nikolova, J. Dyulgerska, G. Danev, T. Babeva, Sol. Energy Mater. Sol. Cells 86 (2005) 421.

[89] P. Sana, A. Rohatgi, J. Kalejs, R. Bell, Appl. Phys. Lett. 64 (1994) 97.

[90] L. Verhoef, P. Michiels, W. Sinke, Appl. Phys. Lett. 57 (1990) 2704.

[91] F. Duerinckx, J. Szlufcik, Sol. Energy Mater. Sol. Cells 72 (2002) 231.

[92] B. Sopori, X. Deng, J. Benner, A. Rohatgi, P. Sana, S. Estreicher, Y. Park, M. Roberson, Sol. Energy Mater. Sol. Cells 41-42 (1996) 159.

[93] D. Mathiot, Phys. Rev. B 40 (1989) 5867.

[94] B.D. Mistry, A Handbook of Spectroscopic Data Chemistry, Oxford Book Company, 2009.

[95] E. Pretsch, P. Buhlmann, M. Badertscher, Structure Determination of Organic Compounds, Springer, 2009.

[96] B. Mitu, G. Dinescu, M. Dinescu, A. Ferrari, M. Balucani, G. Lamedica, A.P. Dementjev, K.I. Maslakov, Thin Solid Films 383 (2001) 230.

[97] T. Stapinski, G. Ambrosone, U. Coscia, F. Giorgis, C.F. Pirri, Phys. B Condens. Matter 254 (1998) 99.

CHAPTER 7

ANNNEALING EFFECT ON FLUORENE-TYPE THIN FILM SYNTHESIZED BY BIPHENYL/METHANE RF PLASMA SYSTEM AND AN APPLICATION FOR c-SI SOLAR CELL

7.1 Introduction

As mentioned in section 5.1 the fluorene and its derivatives have stood out from the conjugated polymers by their excellent chemical and thermal stability and large photoluminescence quantum efficiency [1–5]. They are generally used as stable and highly blue light-emitting materials [6–10] for organic light emitting diodes (OLEDs). The fluorene derivatives can provide almost the entire visible colors range with high efficiency by the adjustable property of the backbone structure of fluorene [11–13]. In addition, their high carrier mobility [14] and the ability of construction ultrathin layers [15] make them suitable for photovoltaic applications [16,17].

In this chapter, we investigated the annealing effect on the fluorene-type thin films produced under the biphenyl and methane plasma. The annealing is an effective process to change and improve the optical, electrical, mechanical, and chemical properties of the plasma polymerized thin films [18–21]. The effect of the annealing can be determined by the annealing temperature and time, the degree of crystallinity and branching in the structure [22] and it has been investigated in several publications [18,19,23–26]. Improvement in the thermal and hydrophobic stability, and an increase in the extent of crosslinking in film structures can be obtained under the annealing temperature [18,19,23,25–27]. In addition, the annealing technique has used to improve the morphology and the electrical mobility of conjugated polymer films for photovoltaic devices and other applications [28–35].

The variable parameters of plasma such as the gas flow rate, the plasma pressure, the power and frequency of power supply, determine the chemical structures and properties of the thin film by controlling the reactions of the species in plasma. The

properties of the fluorene thin films were explored under the variable plasma parameters of input rf power (150, 200, 250 W), CH_4 flow rate (3, 5 sccm), negative bias voltage (-66 V), and deposition time (10, 20, 30 min) at a constant pressure value of 0.3 mbar. The thin films were annealed under 200, 300, 400 and 500 C temperatures. During the deposition the changes of plasma chemistry were investigated by optical emission spectroscopy (OES). The chemical structural properties were examined by the fourier transform infrared (FTIR) spectroscopy. The morphology of the films was analyzed by X-ray diffraction (XRD) and nanotopographic properties of the surfaces were revealed by Atomic Force Microscope (AFM). The thickness was measured by the ellipsometer. The water contact angle was measured by taking a photo of the water drop on the surface of the films. The generated thin films were also coated on a crystalline silicon (c-Si) solar cell and the changes in the efficiency of the solar cell were studied.

7.2 Experimental Details

7.2.1 Experimental Set up

The experimental set up constructed with the combination of two parallel cylindrical electrodes, which was explained in detail in section 6.2 and its diagnostics were mentioned in section 3.5. As shown in Figure 7.1, a negative bias voltage was applied between the substrate holder and the wall of the chamber. The distance between the electrodes was kept at 4 cm. Solid biphenyl (purchased from Sigma-Aldrich Company), melting at 69°C, was introduced into a heated reservoir and degassed down to base pressure of the installation before heating the device. When biphenyl became volatile enough (reservoir thermostated at 120°C), vapors were mixed with methane and introduced into the chamber; the total pressure was controlled at 0.3 mbar. For gas controller, the MKS multi gas controller 647C was used. Plasma discharge was activated and the negative potential, between the holder and the ground, was applied simultaneously.

The plasma parameters used in the experiments were listed in Table 7.1 with respect to the sample names. To measure the optical emission a HR2000 high resolution miniature fiber optic spectrometer (Ocean Optics) was used. The chemical bonding of the thin films were determined by using a Bruker IFS 66/s FTIR spectrometer with 4 cm^{-1} spectral resolution and noise less than 10^{-5} AU within a minute. The

XRD analysis was employed by a Rigaku Miniflex standard X-ray diffractometer (Cu K$_\alpha$, λ=1.54 Å) with a scan step of 0.05˚. To measure the thickness of the samples a VASE Instruments (J.A. Woollam Co., Inc.) ellipsometry was used. The nanostructual properties of the surface of the deposited films were investigated by an Atomic Force Microscope (AFM) (Pico Scan, Molecular Imaging Inc. Tempe, AZ) in contact mode with silicon nitride nanoprobe for scanning area of 6×6 μm^2.
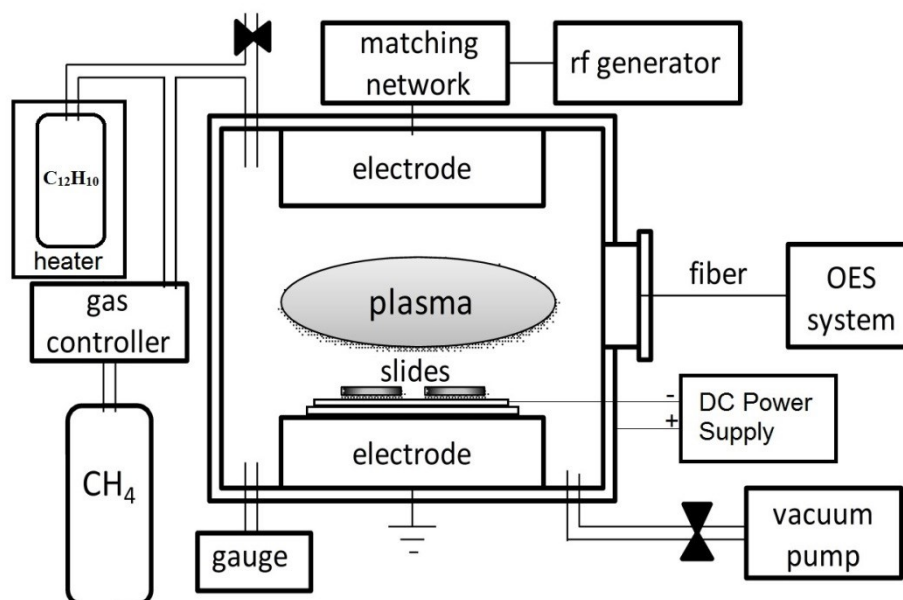
Figure 7.1 The experimental set up

Table 7.1 Sample names with experimental parameters

BM refers to mixture of biphenyl and methane plasma					
Sample Name	Power (W)	Flow rate (sccm)	Dep. Time (min)	Pressure (mbar)	Bias Voltage (V)
BM1	150	3	20	0.3	-66
BM2	150	5	20	0.3	-66
BM3	200	3	20	0.3	-66
BM4	200	5	20	0.3	-66
BM5	150	3	30	0.3	-66
BM6	150	5	30	0.3	-66
BM7	150	3	10	0.3	-66
BM8	200	3	10	0.3	-66
BM9	250	3	10	0.3	-66
BM10	150	5	10	0.3	-66
BM11	200	5	10	0.3	-66
BM12	250	5	10	0.3	-66

7.2.2 Applying Negative Bias Voltage

The kinetic energy of the ions plays an important role in determining chemical and physical properties in the film formation [36,37]. At low deposition temperature and low substrate temperature, the positive ion bombardment is very effective way to improve the film quality, topography, stoichiometry, re-emission coefficient, and deposition rate [38–43]. When a negative voltage is applied between the substrate holder and the grounded reactor, the surface of the substrate is exposed to the positive ion bombardment and it causes an energy exchange between the ions and the atoms on the surface and as a result, the average energy of these atoms increases [36]. The fluency of the ions provides an easier electrical controllability of chemical pathway.
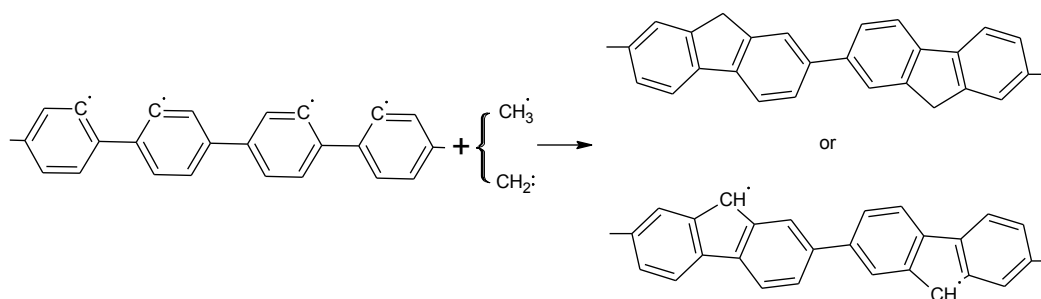
(Reaction 7.1)

Here is a diagram, shown in Reaction 7.1, representing the expected reactions during the formation of fluorene and its derivatives by the mixture of biphenyl and methane. The excited biphenyl and methane in plasma dissociate into their fragments after transferring sufficient energy from the inelastic collisions. After the dissociation, the fragments continue to interact with electrons, ions and free radicals inside the plasma, and this causes to activate them. These active fragments, in a short time, start to recombine between each other and form new compounds and fragments. The fragmentation and recombination in the plasma can be controlled by applying a negative bias voltage. As shown in Figure 7.2, after the negative voltage was applied, the intensities of the selected species increased for both cases of biphenyl plasma and the mixture of biphenyl and methane plasma. In other words,

156

the amount of the fragments, especially positive ions, around the substrate holder increased so that the quality of deposited film was improved.
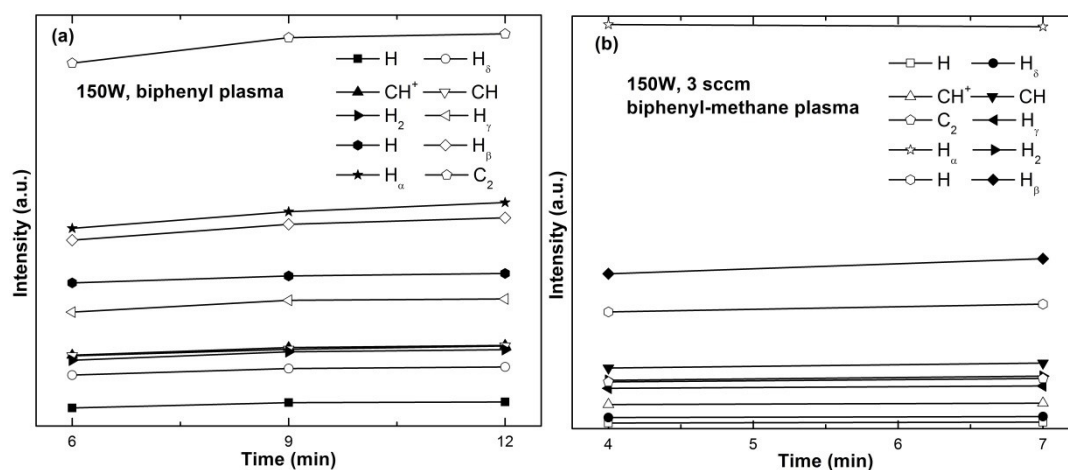
Figure 7.2 Change in the OES intensities of the selected species under negative bias voltage applied a) after 6 min, b) after 5 min

7.3 Results and Discussion

7.3.1 Optical Emission Spectroscopy

The emissions of the plasma species were measured by optical emission spectroscopy in the wavelength region from 200 to 900 nm. The intensities of the emissions and assignment list of emissions were presented in Table 7.2 and 7.3. The CH Q(0,0) band head of the $A^2\Delta \rightarrow X^2\Pi$ system, which results from transition of direct electron impact on CH_4 molecule [44][45], was observed at 431.2 nm and the CH radical referring to system of $B^2\Sigma^- \rightarrow X^2\Pi$ transition was recorded at 387.1 nm [46]. The 486.1 nm line referred to H_β (H(n=4→n=2)) transition and the 463.4 nm line belonged to H_2 $G^1\Sigma g^+$ [44][47]. The H_γ (H(n=5→n=2)) and H_δ (H(n=6→n=2)) lines were at 434 and 410.1 nm, respectively, and the H_α (H(n=3→n=2)) line was seen at 656.2 nm with the H line at 397 nm [48]. In the spectra, the degradation of the CH R branch was seen to the violet and to the red colors at the lines from 421 to 425 nm and at the lines from 434 to 442 nm [48], respectively. The lines at 387.1 nm and 422.5 nm were referred to the CH R(0.0) band head of the $B^2\Sigma^- \rightarrow X^2\Pi$ system and the CH^+ R(0.0) band head of the $A^1\Pi \rightarrow X\Sigma$ system, respectively [49]. At 601.8

nm, numerous molecular hydrogen line attributed to the Fulcher band system of $I^{u3}\Pi_u$ was observed [50]. Carbon dimer (C_2) $d^3\Pi\rightarrow a^3\Pi$ Swan band emission line was represented around 516 nm [45][51].

Table 7.2 Assignment list of emissions of OES spectra

Species	System	Transition	Wavelength (nm)
CH	3900 A	$B^2\Sigma^-\rightarrow X^2\Pi$, ground state	387.1(390)
H			397.0
H_δ	Balmer	n=6→n=2	410.1
CH^+		$A^1\Pi\rightarrow X\Sigma$	422.5
CH		$A^2\Delta\rightarrow X^2\Pi$	431.2
H_γ	Balmer	n=5→n=2	434.0
H_2		$G^1\Sigma g^+$	463.4
H_β	Balmer	n=4→n=2	486.1
C_2	Swan band	$d^3\Pi\rightarrow a^3\Pi$	516.5
H	Fulcher band	$I^{u3}\Pi_u$	601.8
H_2		$d^3\Pi_u\rightarrow a^3\Sigma_g^+$	612.2
H_α	Balmer	n=3→n=2	656.2
O			725

Table 7.3 Results of OES Spectra

Sample Name	CH (387.1)	H	H_δ	CH^+	CH (431.2)	H_γ	H_2	H_β	C_2	H	H_2	H_α	O
BM1	181.6	125.5	163.3	252.0	484.1	355.7	410	1093	413.2	782	745	2625	259.9
BM2	131.7	113.6	136.5	214.4	535.1	295.4	376	948	314.6	832	777	2341	245.5
BM3	200.6	169.7	221.1	331.3	601.5	494.0	548	1710	578.2	1027	957	3978	348.7
BM4	99.2	85.0	110.7	168.0	414.5	242.3	318	911	247.9	623	596	2464	212.2
BM5	136.6	110.0	147.3	222.0	486.7	334.0	346	1195	330.5	814	786	3102	261.4
BM6	65.2	61.2	78.5	126.7	326.6	172.3	244	541	239.8	650	608	1406	189.1
BM7	328.2	141.2	178.8	281.9	474.78	366.3	417	940	503.9	942	840	2137	305.2
BM8	335.2	144.9	186.9	302.8	499.66	409.1	473	1232	540.7	1063	949	2929	326.9
BM9	173.8	144.3	189	275.5	540.93	419.9	531	1611	594.1	1086	1021	3004	360.4
BM10	173.8	116.7	147.9	227.6	557.25	312.3	370	906	325.2	743	684	2090	231.6
BM11	152.5	119.5	156.5	237.3	571.22	324.8	391	1030	354	749.1	679	2111	231.5
BM12	183.4	136.1	170.1	258.1	557.53	338	436	1125	371	772	699	2058	245.8
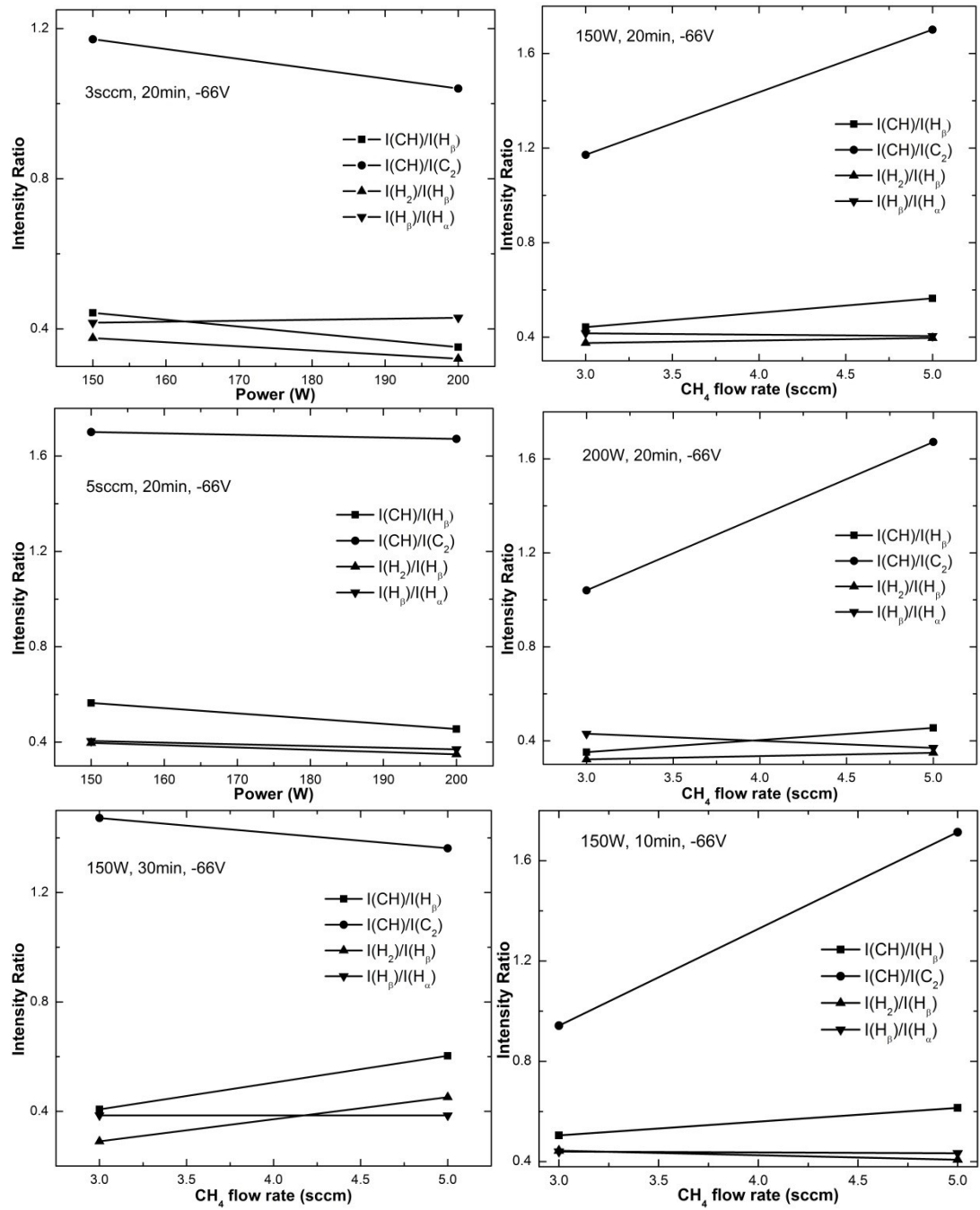
Figure 7.3 The ratios of $I(CH)/I(H_\beta)$, $I(CH)/I(C_2)$, $I(H_2)/I(H_\beta)$, and $I(H_\beta)/I(H_\alpha)$ with respect to plasma parameters
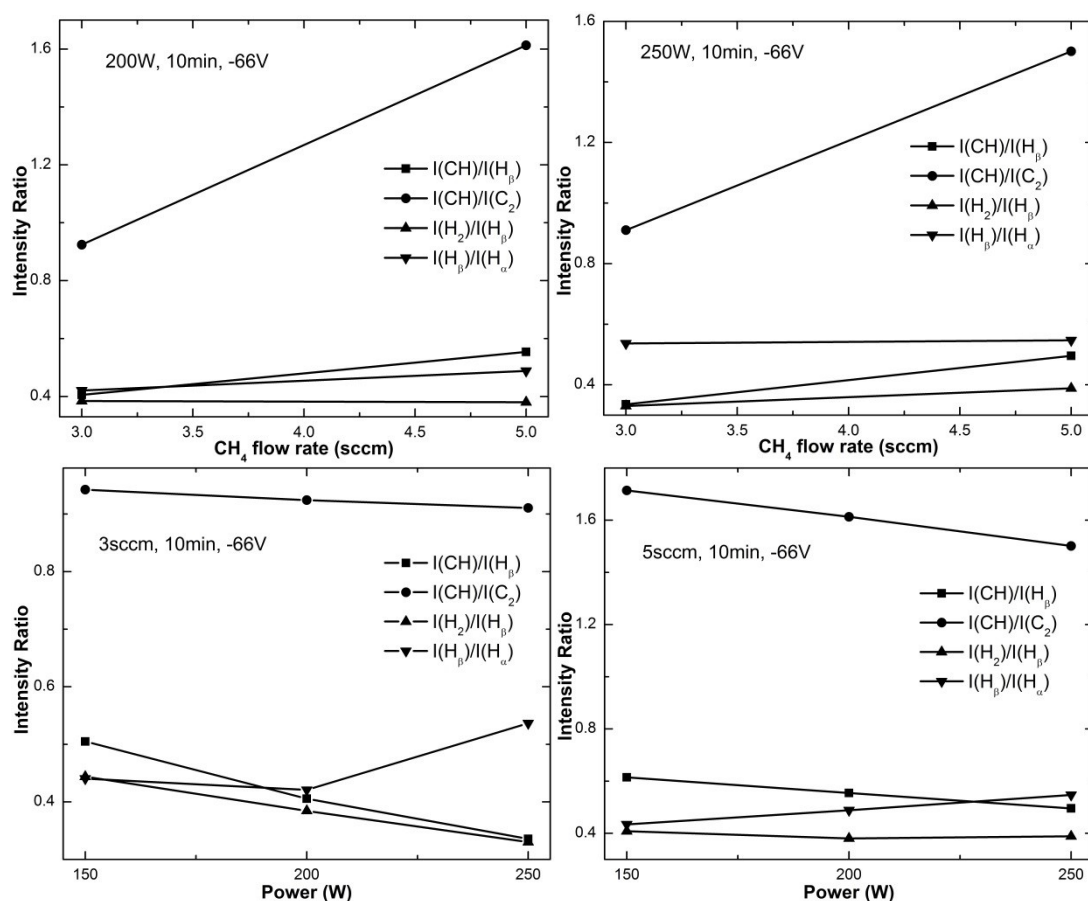
Figure 7.3 (continued)

From the results of OES spectra, it was observed that the intensities of emissions decreased with the increased the deposition time which can be due to the existence of more heavy components than weak fragments in the chamber. At 3 sccm CH_4 flow rate, almost all the intensities increased with increasing rf power, except the components of CH(387.1) and CH^+ indicated a decrease that is maybe due to the insufficient gas diffusion. At 5 sccm flow rate, all the intensities indicated an increase with increasing rf power at low deposition time whereas they decreased with the increased rf power when the deposition time increased. Increasing the gas flow rate resulted in a decrease in the intensities of emissions.

To understand the relation of species with each other, the ratios of intensities were investigated. The $I(CH)/I(H_\beta)$ ratio is important for determining the excitation of CH (431.2nm). From Figure 7.3, it was seen that this ratio increased with higher gas flow rate at constant power values. When the deposition time was increased, it

160

didn't cause an important change, whereas increased power led to decrease this ratio. The ratio of $I(H_\beta)/I(H_\alpha)$ showed a decrease at the higher flow rate. At lower deposition time, the increased rf power created an unstable change in the ratio at low gas flow rate, while it caused a linear decrease at high gas flow rate and high deposition time. The $I(H_2)/I(H_\beta)$ ratio is related with the dissociation and recombination of hydrogen components. Therefore, for higher levels of this ratio, it could be supposed that the producing of H_2 ($G^1\Sigma g^+$) is a dominant way for excitation of the CH_4 molecules [46]. It indicated a decrease at high values of input rf power, therefore, it can be said that the recombination of the hydrogen species in the plasma was at low level in high rf power. While increasing the flow rate increased the ratio at high deposition time, it led to a small decrease at low deposition time. We could say that the deposition time is effective on determining this ratio.

The $I(CH)/I(C_2)$ ratio is directly related to the population of the excited species [52] and the differences in this ratio show some changes in the density or the temperature of the electron. According to H. Song et al. [53], the C_2 radical is generated by the reactions caused from the collisions of carbon-containing radicals in gas phase. The results showed that the intensity of C_2 radical increased linearly by raised input rf power. However, the C_2 radical decreased by increasing the flow rate at constant power. Increasing the deposition time increased the amount of this radical at higher flow rate. In addition, Kim and Lee [54] suggested that the increase of C_2 components in the plasma leads to the deposition of sp^2 carbon during discharge. In this case, it may be suggested that the content of C_2 components is more useful for determination of the type of thin film [55][56].

7.3.2 Fourier Transform Infrared Spectroscopy

The infrared spectra of the thin films were collected in the region of 4000-600 cm^{-1}. In the spectra, the broad peaks in the region from 2700 to 3300 cm^{-1} were assigned to the C-H stretching vibration band [57,46,53,58–60]. The peak at 1630 cm^{-1} was associated with the O-H bending [61] or the olefinic sp^2 C=C stretching vibration [57–59,62] and 1560 cm^{-1} was assigned to aromatic sp^2 C=C stretching vibration [57,58]. In addition, at 1450 the asymmetrical deformation mode (C-H bending) was observed in CH_3 groups [53,60,61]. The out of plane C-H bending in alkenes and aromatics was observed at the peaks seen from 1095 to 600 cm^{-1}; the peak of

1095 corresponded to in-plane aromatic CH deformation and the peak of 670 cm^{-1} showed out-of-plane aromatic C=C ring deformation, and the peaks between 930 and 700 cm^{-1} corresponded to C-H bending in alkenes [63–65]. The peak observed around 2330 cm^{-1} was assigned to CO_2 vibration. The band around 1700 cm^{-1} exhibited the presence of the carbonyl containing groups [62,61,63–65]. The broad band around 3600 cm^{-1}, especially observed in annealed samples, assigned to O-H stretching vibration.
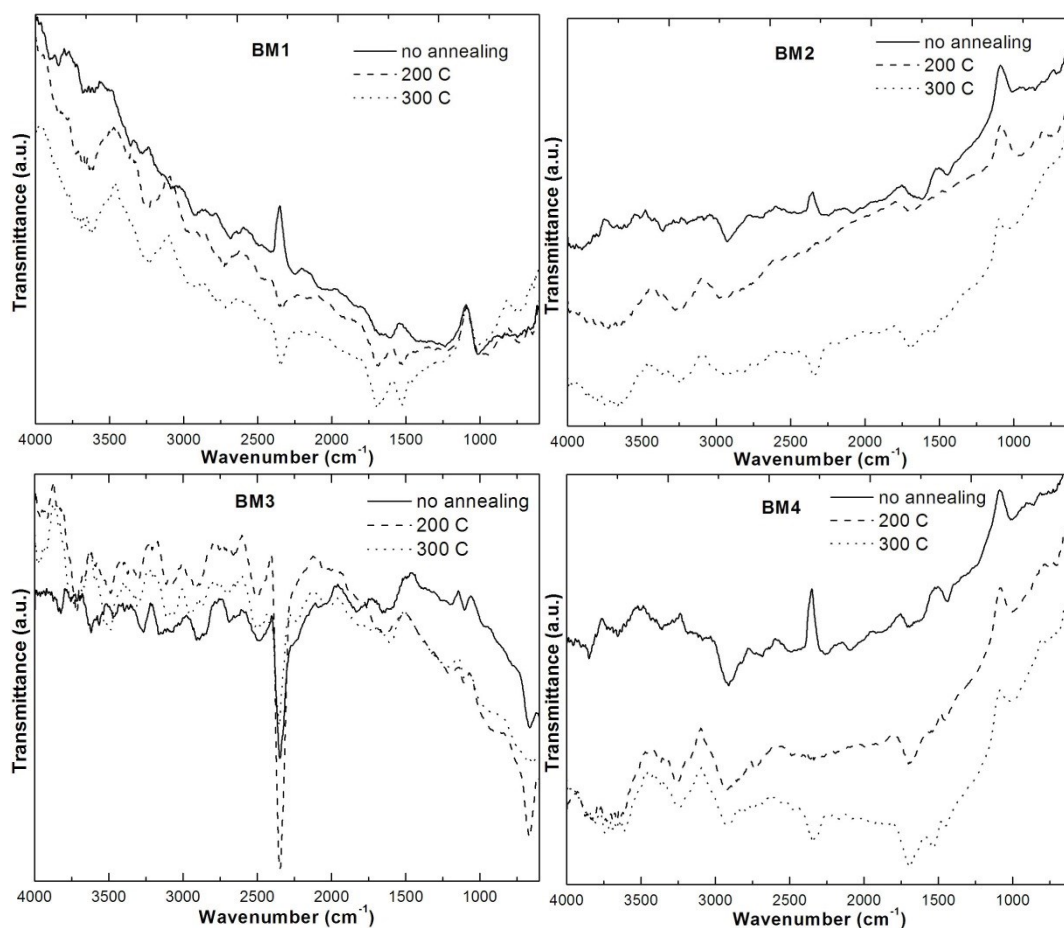

Figure 7.4 Graphs of FTIR spectra for BM1, BM2, BM3, BM4, BM5, BM6, BM7, BM8, BM9, BM10, BM11, and BM12
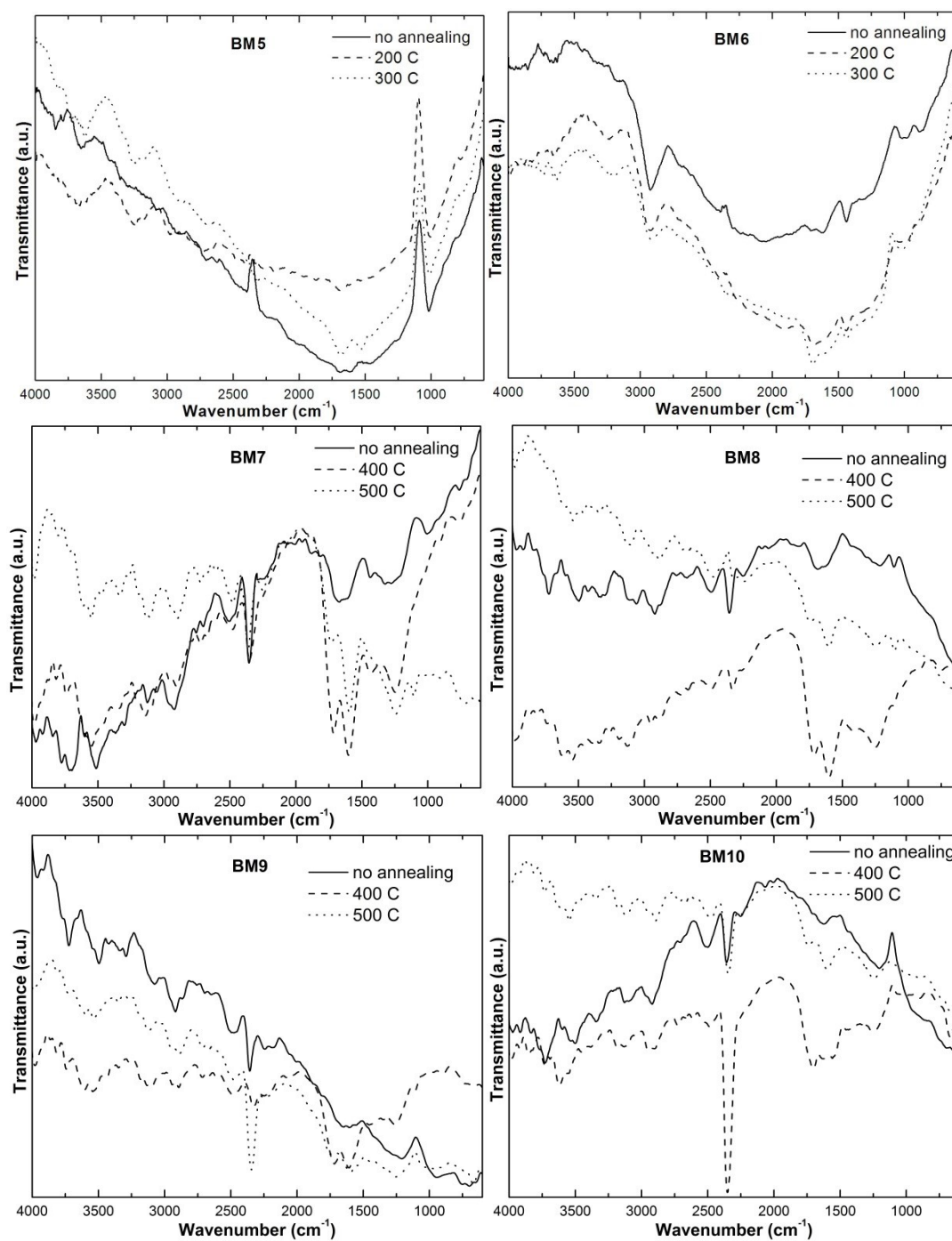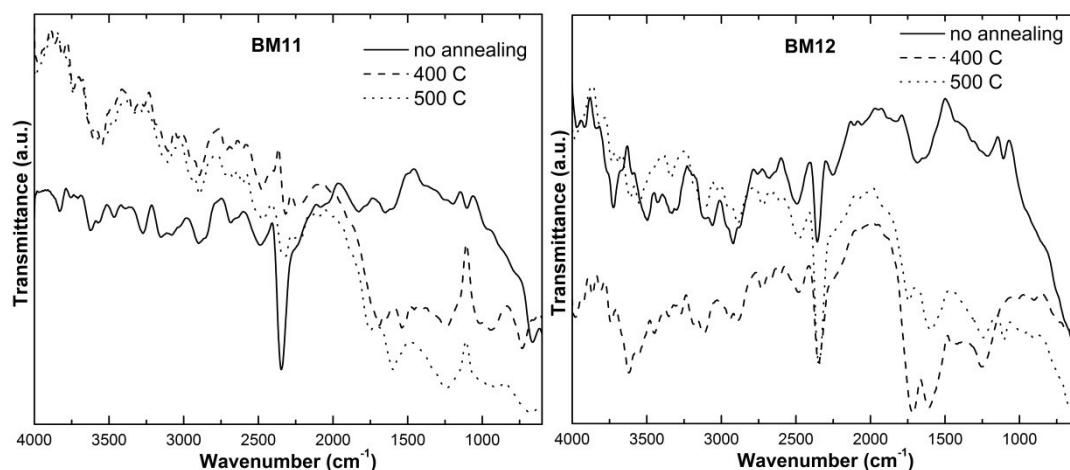
Figure 7.4 (continued)

Figure 7.4 (continued)

We could see from the FTIR results that the level of C-C and C=C bonding in the film structure showed an increase when the rf power increased, which is in agreement with the OES results. The carbon contents in the structure directly related to the degree of film quality. Therefore, we could suggest that the high quality thin film is generated with high rf power. The intensities of peaks between 1095 and 680 cm^{-1} assigning to aromatic sp^2 C-H bending or C-H bending in alkenes were increasing with increased both rf power and CH_4 flow rate. Since the contents of the aromatic structures play important role in the film formation, it can be said that this case supported the formation of desired film structure. The intensity of CH_x peaks indicated a small decrease as increasing rf power whereas no changes with increasing gas flow rate. This decrease could be explained by that many radicals and ions occurred as increased rf power which increase the fragmentation and it led to decrease in formation of the micro-voids or nano-pores in the film.

The samples were annealed for 1 hour at different temperatures; 200, 300, 400, and 500 C°. After annealing, the broad peak seen from 1800 to 1100 cm^{-1} generated sharper peaks with higher intensity at 1690, 1600, 1560, 1440, and 1250 cm^{-1} corresponding to C=C or C=O stretching vibration, C-C or C=C stretching vibration, aromatic sp^2 C=C stretching vibration, sp^3 C-H bending in CH_x (x=1, 2, 3), and C-C or aromatic C-O stretching vibration, respectively [66]. By increasing the annealing temperature, the peak intensities were also increased as seen in references [18,19]. Therefore, it can be suggested that the high temperature resulted in the dissociation

164

of the C-H components and methyl groups (-CH$_3$). The reconfiguration of chemical bonds in the film structure caused the changes in the intensity of band peaks [67]. According to results, the oxygen content more increased for samples annealed which may refer to the increase in the extent of crosslinking in the structure of thin films after the annealing [25,26].

The structure of the thin film includes the types of carbon bonding like sp^3 bonding (diamond), sp^2 bonding (graphite), and sp^1 bonding (carbyne) structures. Determining the levels of sp^3 and sp^2 bonds is possible by exploration of the broad band centered at 2920 cm^{-1}. The deconvolution of broad peak was analyzed with peak fit software (seasolve, version 4.12) as shown in Figure 7.5, selected sample. After the fitting process, the configuration included the centered peak at 2920 cm^{-1} referring to monohydrogen radicals (-CH) [46] or sp^3 CH$_2$ asymmetric mode, and the peaks of 2960 and 2870 cm^{-1} attributed to sp^3 CH$_3$ asymmetric mode and sp^3 CH$_3$ symmetric mode [53,58–60,68–71], respectively. The other peaks contributing to broad band were at 2855, 2950, 3000, 3020, and 3050 cm^{-1} attributed to sp^3 CH$_2$ symmetrical, sp^2 CH$_2$ olefinic, sp^2 CH olefinic, sp^2 CH$_2$ olefinic, and sp^2 CH aromatic, respectively [71,58–60,68–70]. The sp^3/sp^2 ratio could be calculated from the areas of these non-overlapping peaks [58,59]. The ratio was an increase with increasing the CH$_4$ diffusion at lower input power. The higher flow level caused an increase in the H content, and since the sp^3 bond is directly related with hydrogen, this could be suggested as a reason of the increase in the ratio. Increasing the input power led to an increase of the sp^3/sp^2 ratio. This could be explained with influence of the power on the degree of the ionization, which increased as the power increased. This caused to fragment the sp^3 bond and transfer to sp^2 bond [70]. Therefore, there were not enough unhydrogenated C bonds in the deposition and this increased H level. When the deposition time was increased, the sp^3/sp^2 ratio decreased.
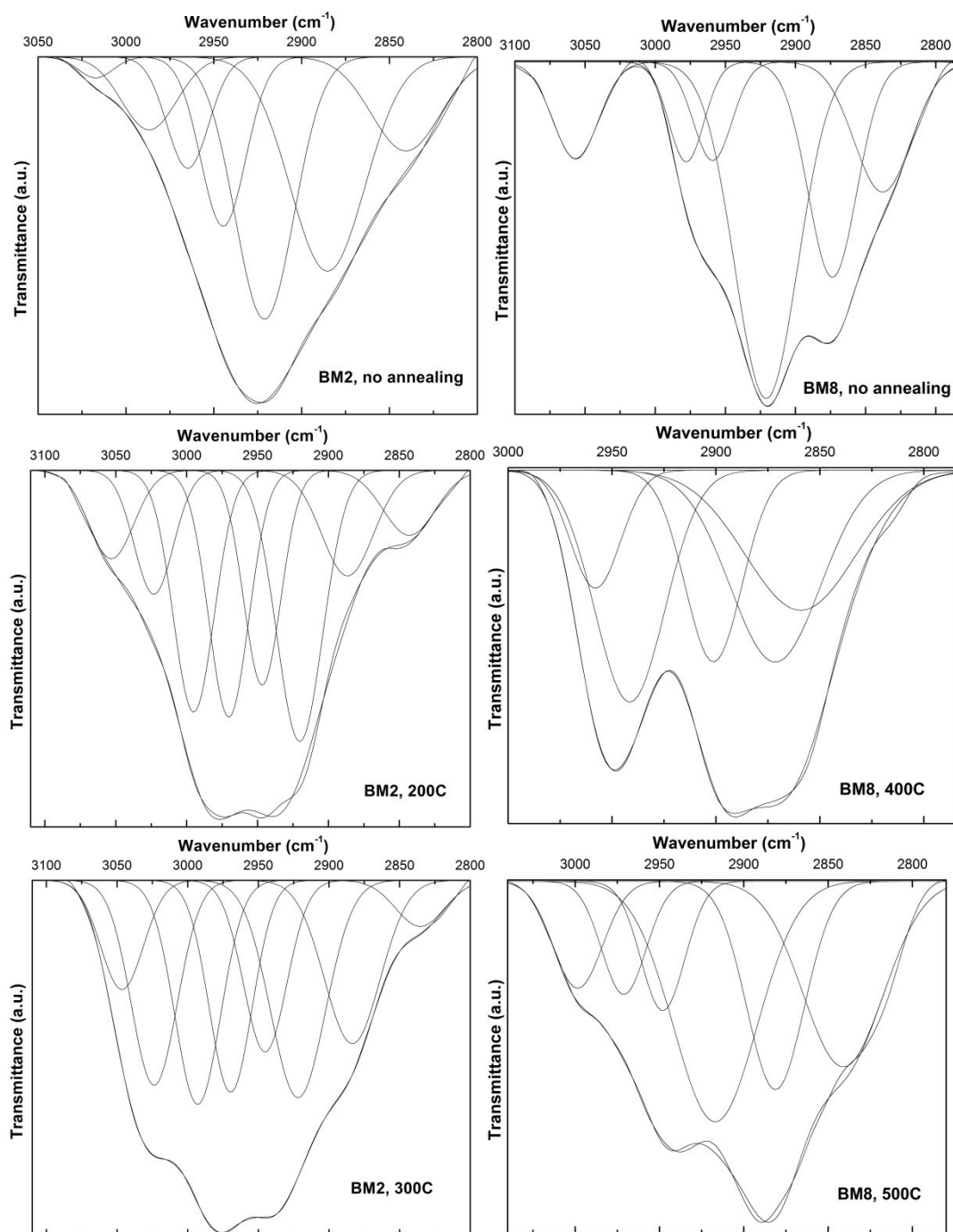
Figure 7.5 The deconvolution of peak centered at 2910 cm^{-1} selected samples before and after annealing, and results of sp^3/sp^2 ratio with respect to temperature
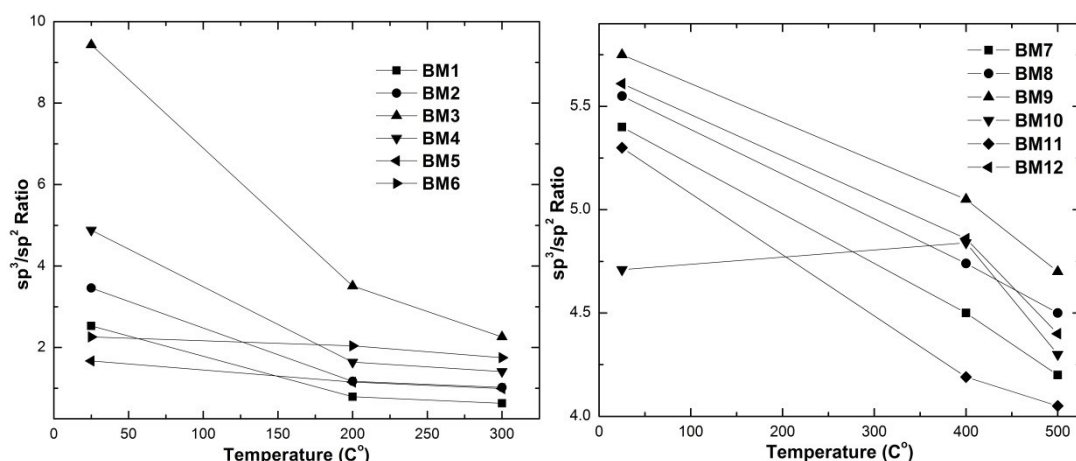
Figure 7.5 (continued)

After annealing the sp^3/sp^2 ratio decreased with increasing temperature for almost all samples; only sample of BM10 showed an increase at 400 C [72], that is the plasma bombardment should be more dominant than heat effect here. This decrease can be explained by degassing of CH_x from the surface and hydrogen release with temperature. The existence of a large number of CH_2 and CH_3 groups as well as C=C double bonds can be suggested as a proof of the polymeric nature of films. Moreover, decrease of the ratio provides the existence of the aromatic sp^2 hybridization.

The annealing increased the amount sp^1 carbon bonding (carbyne) in the deposited film. The carbyne is defined by the formula of $R-C^3$ and assigned to broad band observed around 3300 cm^{-1}. The existence of this structure was more distinctive at annealed samples, as shown in Figure 7.4. Additionally, in plasma deposition, a thin film with cross-linking structure is an expected result. As the degree of cross-linking increases, this leads to the removal of sp^2 bonding and increase of the sp^3/sp^2 ratio [58]. Therefore, it could be suggested that the structure of the thin films indicated higher degree of cross-linking at the high power and flow rate [18,19].

7.3.3 Contact Angle Measurement

The wettability of the thin films was investigated by measurement of contact angles which the degree of wetting from the interaction of a liquid (water for our measurements) and the surface of the films. If the contact angles are smaller than 90°, they correspond to high wettability (hydrophilic), and if larger, they correspond

167

to low wettability (hydrophobic). If we make a comparison between surfaces of sample before and after the deposition, their property of wettability decreased after the deposition. In other words, the surfaces of the thin films indicated more hydrophobic properties. The contact angle had larger values at high power and low flow rate values, and but it decreased when the flow rate was increased at high power value. At high flow rate, it should be decreased the power value to able to raise the contact angle.
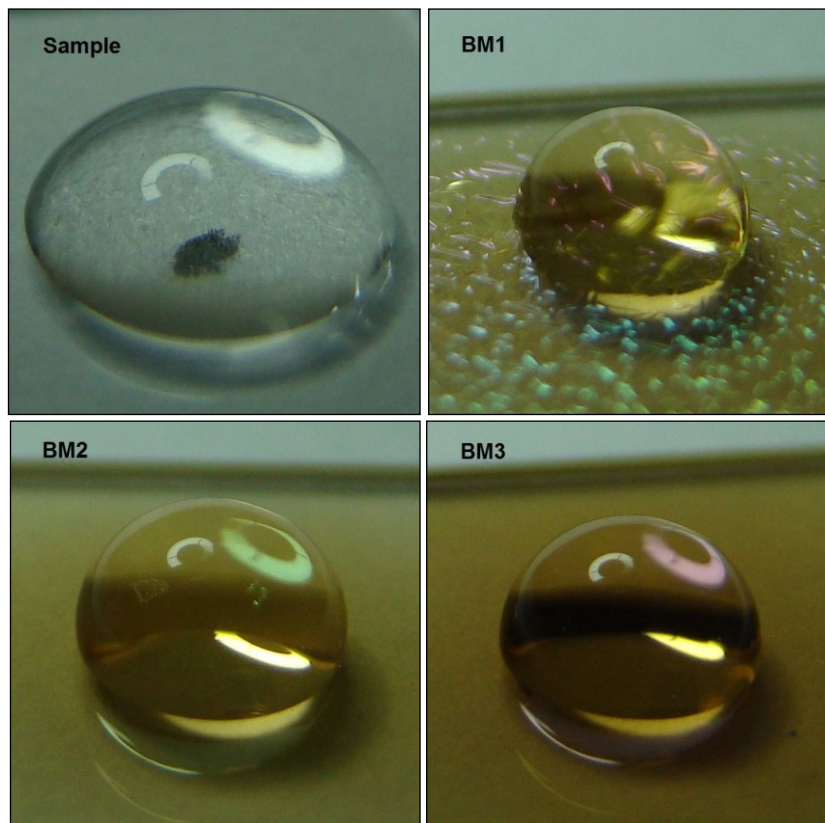

Figure 7.6 The images of contact angle
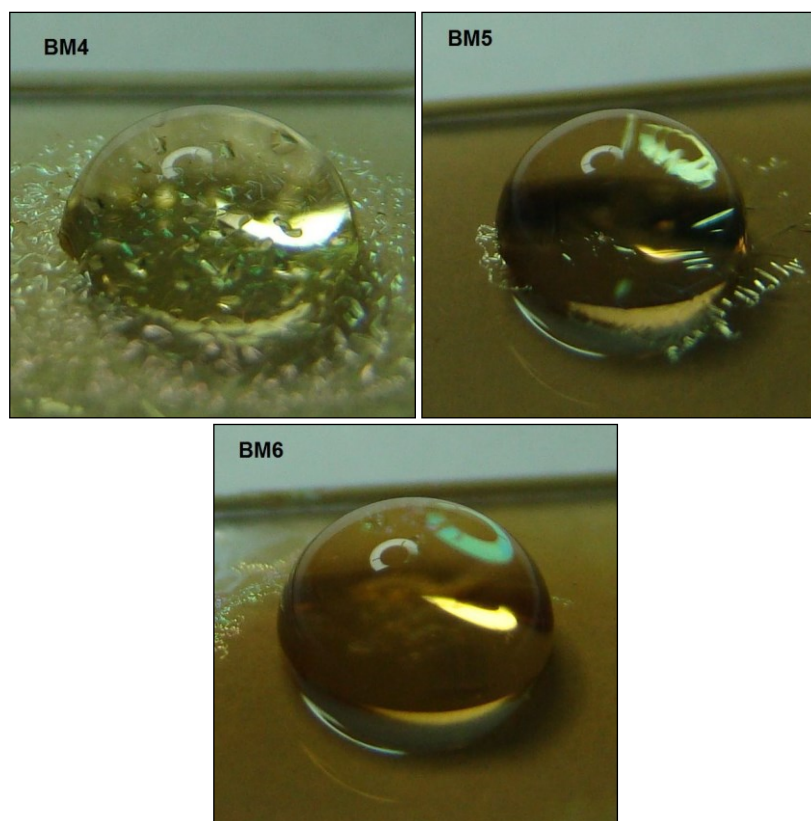
Figure 7.6 (continued)
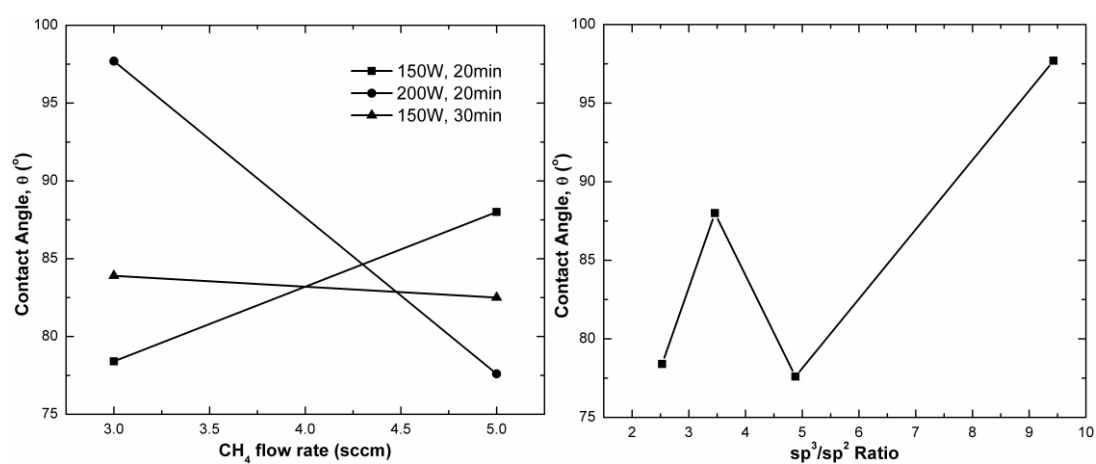
Figure 7. 7 The change in contact angle with respect to flow rate and sp^3/sp^2 ratio

7.3.4 X-ray Diffraction

X-ray diffraction analysis was employed to reveal the structural properties of the thin films. Polymers generally become in the amorphous phase which doesn't have

chains with order in parallel and closely packed situations like in the crystalline phase. It is possible to improve the property of the crystallization by heating the polymers above the glass transition temperature (T_g). The polymer chains were in rigid phase at the temperature below T_g. To be able to reach the sufficient chain segmental movement and crystallization, it is needed to have a required free volume. When it reaches T_g temperature, the polymer chains start to become more flexible and be able to open under stress, thus the sufficient free volume is able to be attained at T_g temperature. Above the T_g, stretching is accomplished and the randomly coiled and entangled chains begin to disentangle, unfold, and straighten. Therefore, the occurrence of the latter is dependent on the first order. A sharp change in the lattice structure can be a reason of critical change in free volume and an onset of segmental chain movement in the amorphous phase. It is expected that the degree of lattice parameter shift has a nominally linear relationship with respect to anneal temperature and annealing step causes a large change in lattice parameter and an increase in grain size. However, the providing 100% crystallinity for polymers is not possible because of the non-uniform molecular weight of the polymers [73–75].

Figure 7.8 X-ray diffraction patterns for all samples before and after annealing
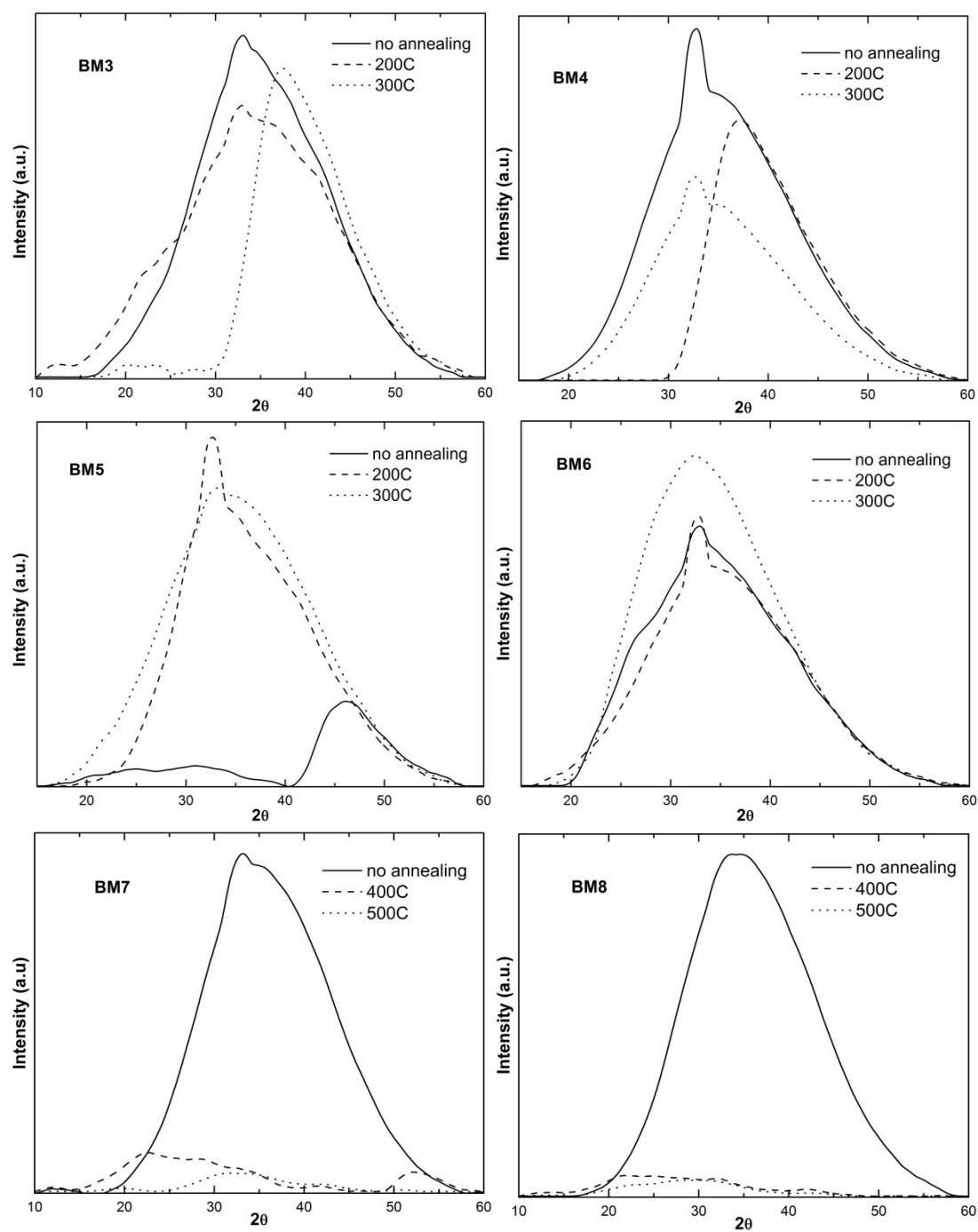
Figure 7.8 (continued)
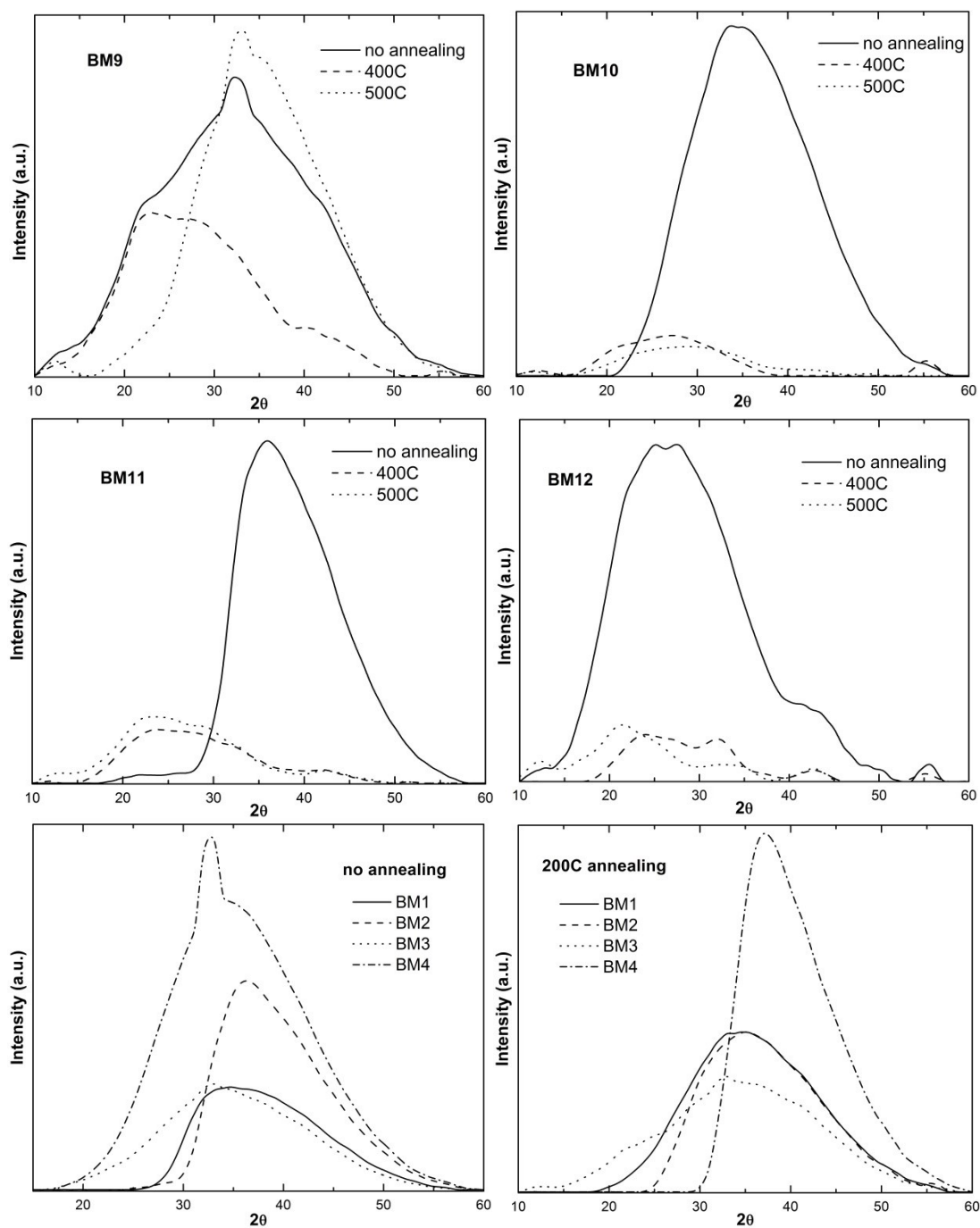
Figure 7.8 (continued)
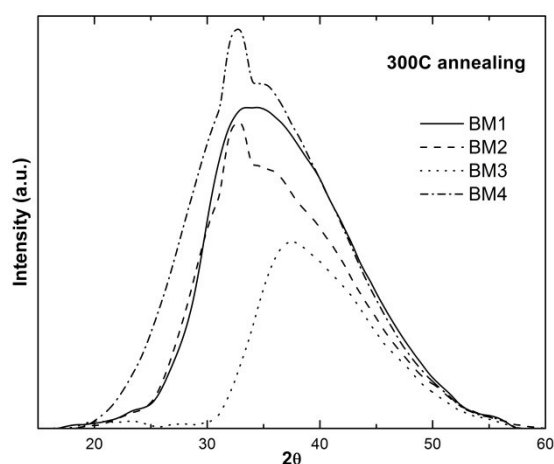
Figure 7.8 (continued)

It is seen from Figure 7.8 the generated thin films show amorphous nature of the film structure. Generally, the diffraction peaks locat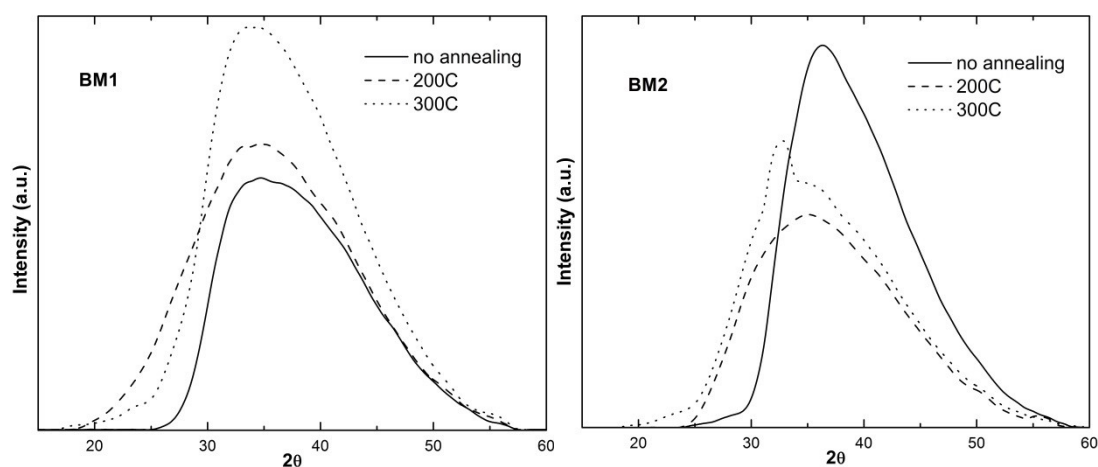e according to families of lattice planes and these peaks for our films almost centered at 35˚. The annealing caused some changes in the intensities of the diffraction peaks. These changes can give information about the ordering in the structure. An increase in the diffraction intensity may be assigned to increase in the crystallinity or long range crystallographic ordering. The highest intensity change by annealing was seen in sample of BM1, so it can be said that the most influence in the property of crystallization was seen at lower power and CH_4 flow rate values. The intensity for other samples of BM2, BM3, and BM4 showed a decrease with the annealing. When the deposition time was increased, the intensities of the diffraction peaks increased for both of BM5 and BM6 samples, but again higher change was observed at lower flow rate. The samples deposited at 10 min indicated a sharp decrease in the intensity after the annealing, except the BM9 sample. Here, the effective change obtained at 250 W rf power and 3 sccm gas flow rate. There was a shifting represented in the diffraction peaks after the annealing. While the peaks were shifting to the right side for samples of BM3 and BM4, it is left for samples of BM2, BM10, and BM11. This shifting could be due to the arrangement of atoms in the structure or strain which changes the lattice parameters. In addition, the shifting to lower 2Θ values in the diffraction could be due to the existence of small oxygen impurities or nitrogen vacancies within the crystal lattice [76]. The width of the diffraction peaks can be explained with the crystallite size. Even though it is small

173

for some, the diffraction peaks for all samples showed a decrease in width, as shown in Figure 7.8. The samples of BM4 and BM3 exhibited their effective decrease at 200C and 300C annealing temperatures, respectively. The diffraction peak of BM9 also decreased in width at 500 C. The sample of BM1 showed in a linear decrease with increased annealing temperature. Since the peak width varies inversely with crystalline size, a decrease in peak width can correspond to an increase in crystalline size.

7.3.5 Thickness Measurements

The thickness of the thin films increased with raised rf power up to 200 W, then decreased at 250 W which may be due to more fragmentation than recombination during the polymerization. Increasing the CH_4 flow rate resulted in an increase in thickness since it grows the reactions with fragments of biphenyl and provides a suitable case to easily generate new components that is increasing the deposition rate. Since the annealing temperature caused an effective thermal decay and a disruption of microvoids in the films [67], the thickness of the thin films had a decrease as the temperature increased. With the thermal decay, some weak components (C-H) and methyl groups (-CH_3) started to disconnect and this led to increase the porosity in the thin films. The decrease in thickness can be related with degassing of CH_x components from surface as a result of annealing [72,77].
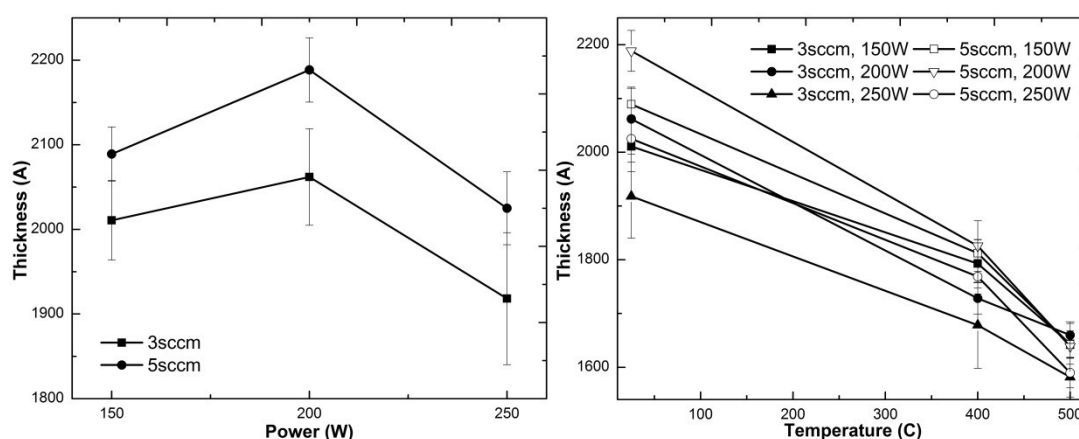
Figure 7.9 Thickness measurements and the change of thickness with respect to the annealing temperature

7.3.6 Atomic Force Microscope

The surface of the thin film has significant nanostructures as shown in the AFM images. The peaks on the surface increased by increasing the rf power, a result of more fragmentation and reconstruction during the film formation in the reaction chamber. The increase of CH_4 flow rate also created effective changes in morphology, which may become due to the higher gas level which is efficient in the reactions with the biphenyl. After annealing, the intensity of peaks showed a decrease at 400 and 500 C annealing temperatures, and also some deformation and peak loss were seen on the surfaces. Increasing the annealing temperature results in the degassing of film components and this causes to deformation on the surface of the film. Moreover, the high temperature leads to decomposition and compaction of the films, and reformation of the amorphous covalent network that is causing smoother surfaces [67,72].
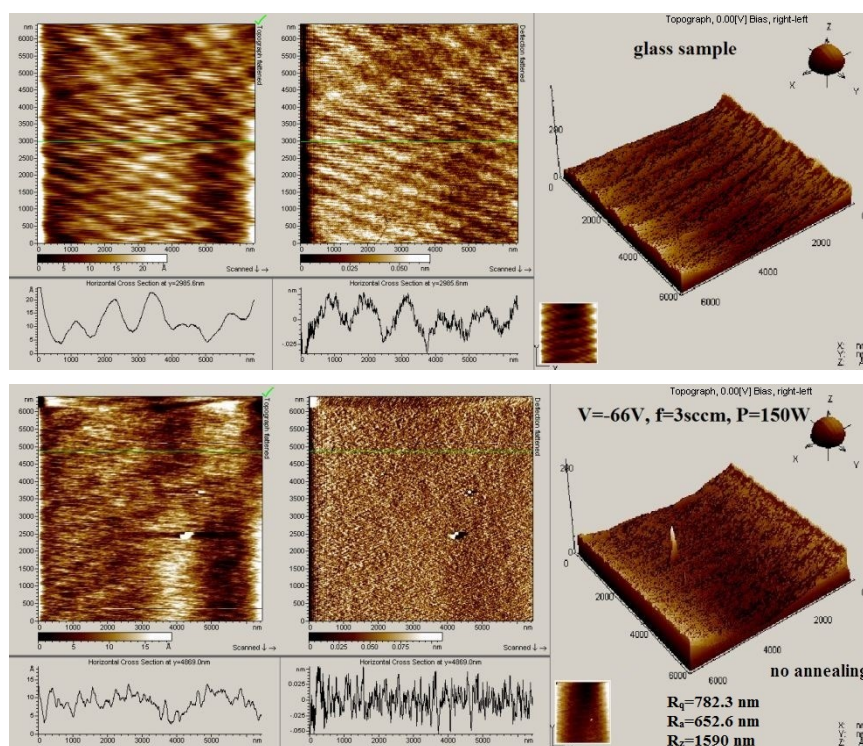
Figure 7. 10 The AFM images before and after annealing

Figure 7.10 (continued)

176
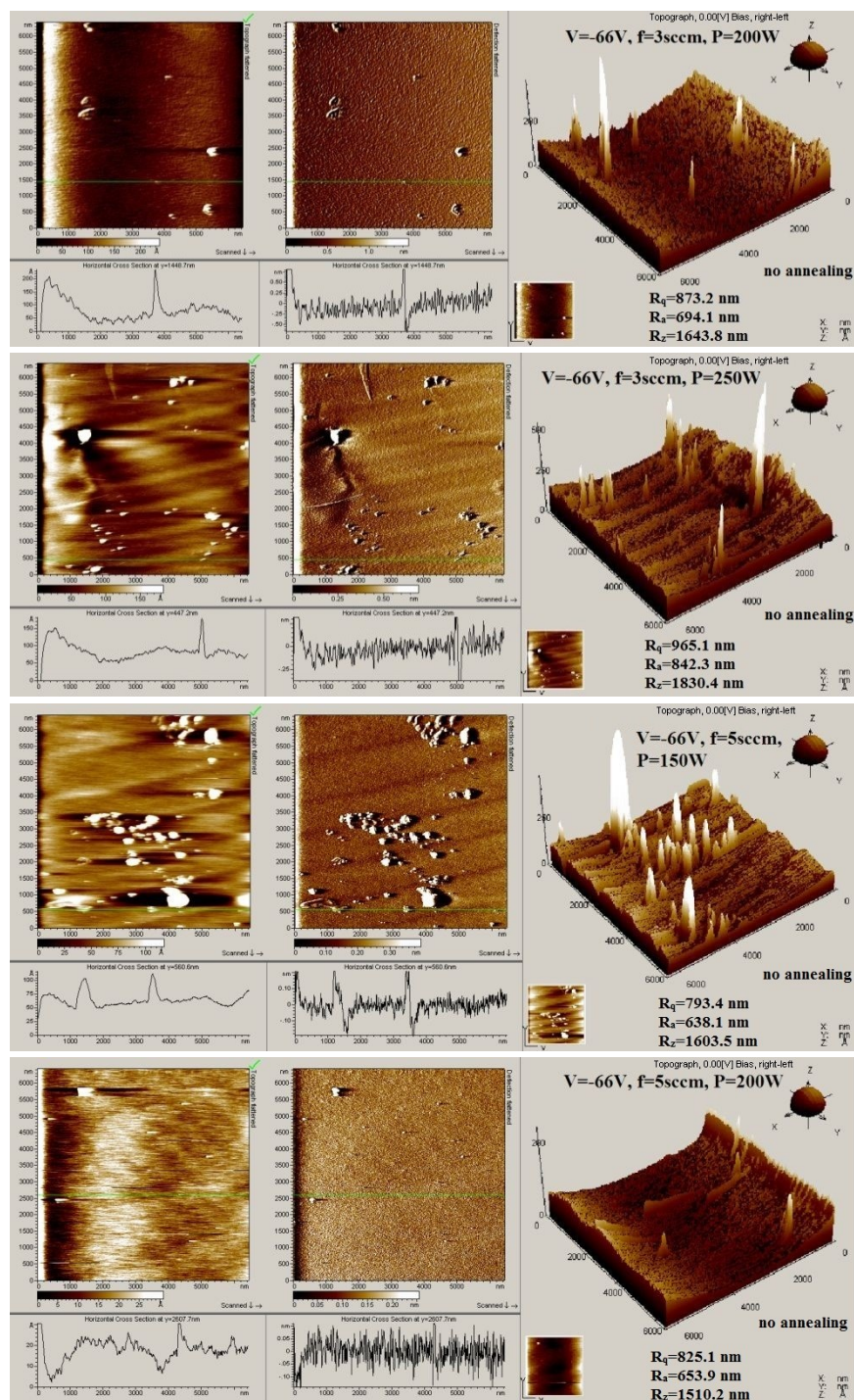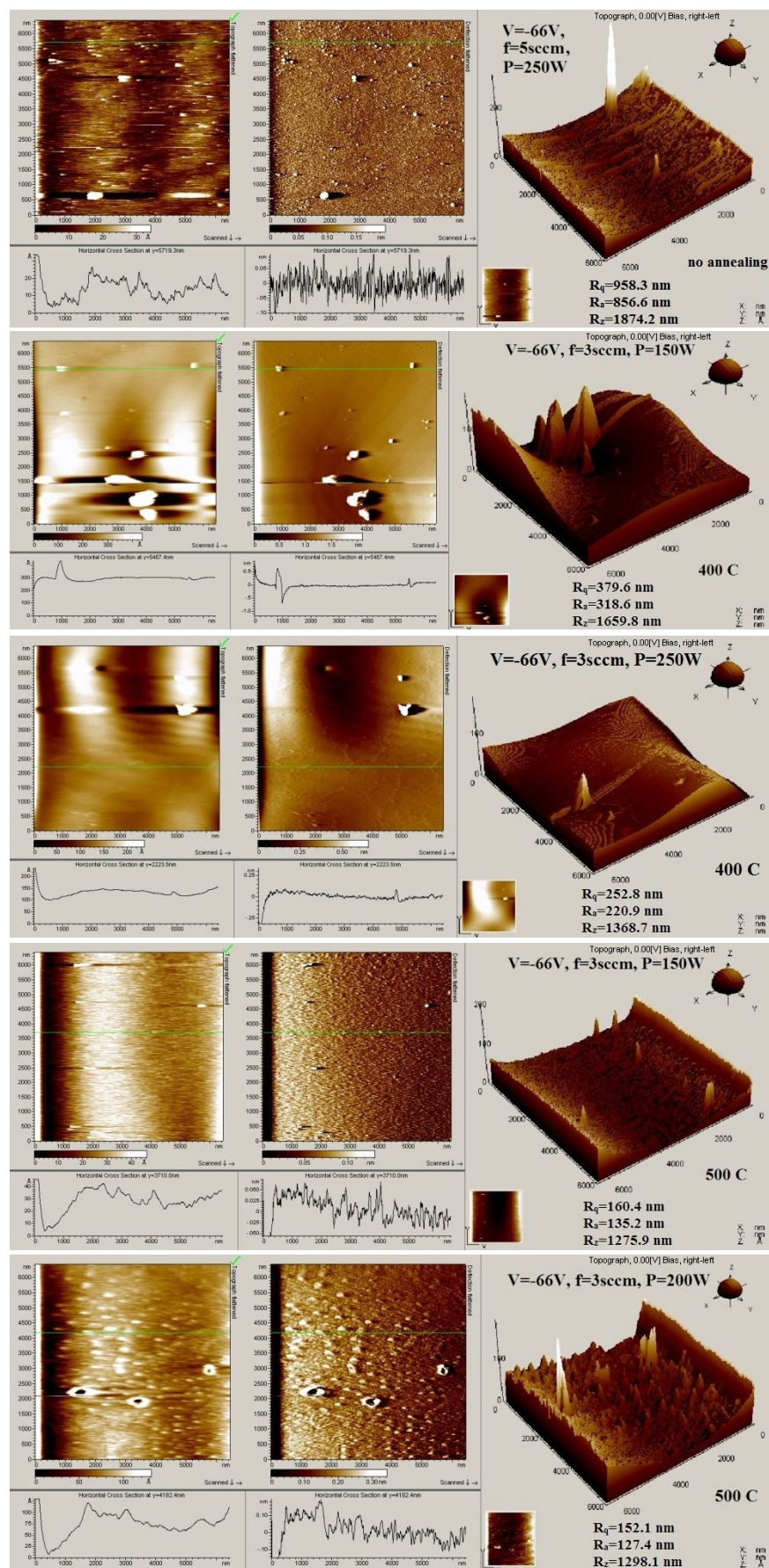
Figure 7.10 (continued)
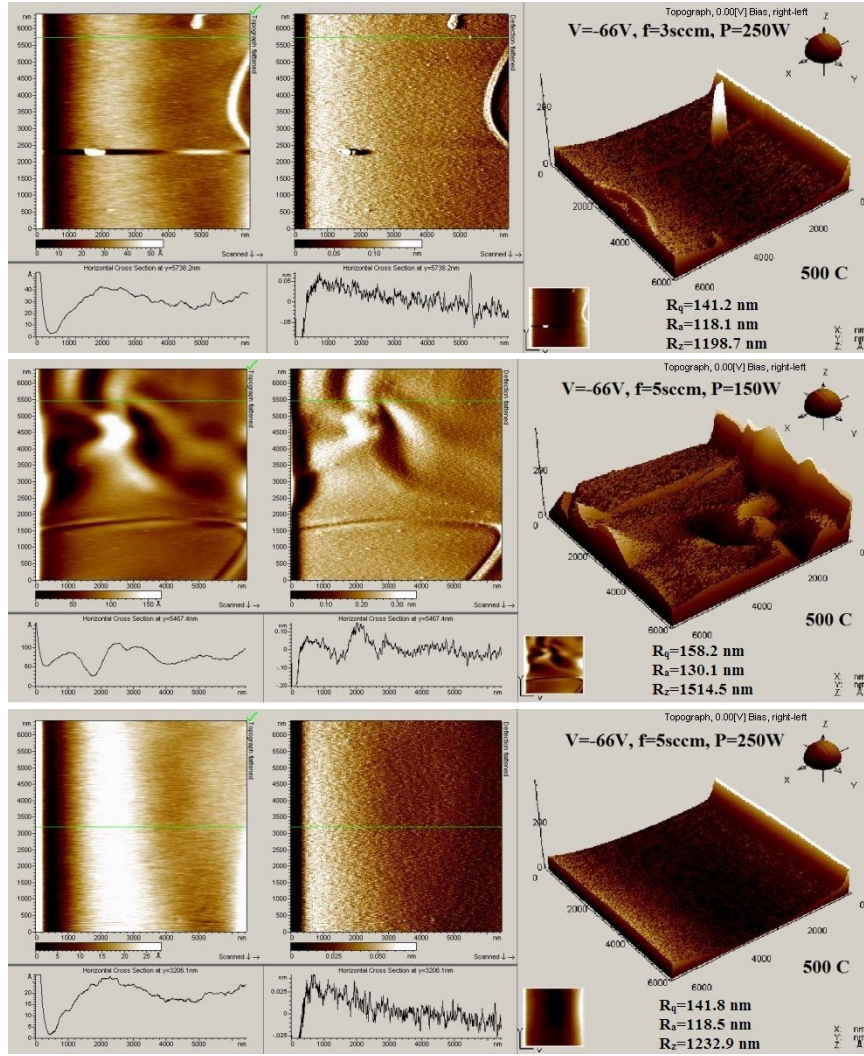
Figure 7.10 (continued)

The parameters of the standard deviation (rms roughness, R_q), the mean absolute deviation (ave roughness, R_a), and the maximum peak to valley (Rp-v, R_z) were measured from AFM images. It presented an increase for these parameters with raising rf power. Due to easy fragmentation to small and open components at high rf power, it can be said that the plasma bombardment plays an important role on the roughness parameters [72]. However, no any important changes were observed as the CH_4 flow rate increased. The annealing led to decrease in the roughness parameters at 400 and 500 C temperatures [23]. This can be explained by the important thermal decomposition and the collapse of microvoids in the films at these temperatures [67].

7.4 An Application for c-Si Solar Cell

The thin films generated from the mixture of biphenyl and methane plasma deposited on the c-Si solar cells. We characterized the optical properties of these films in chapter 5 and it was known that they showed an absorption in a wide range of wavelength and had wide optical band gaps which are suitable for antireflection coating. When the thin film deposited under the negative bias voltage, the efficiency showed a sharp decrease after deposition. Also, some deformations were observed on the surface of the solar cells which may be due to the high level of ion bombardment. Therefore, we tried to deposit the films without the bias voltage and the efficiency of the solar cell was improved in this case. However, the results was not attractive as ones obtained by the a-C:H thin films which was mentioned in section 6.4. As shown in the Figure 7.11, the efficiency showed only small increases at low deposition time as the flow rate was at high value. It could be suggested that the required thickness was achieved in a short time under the high gas concentration.
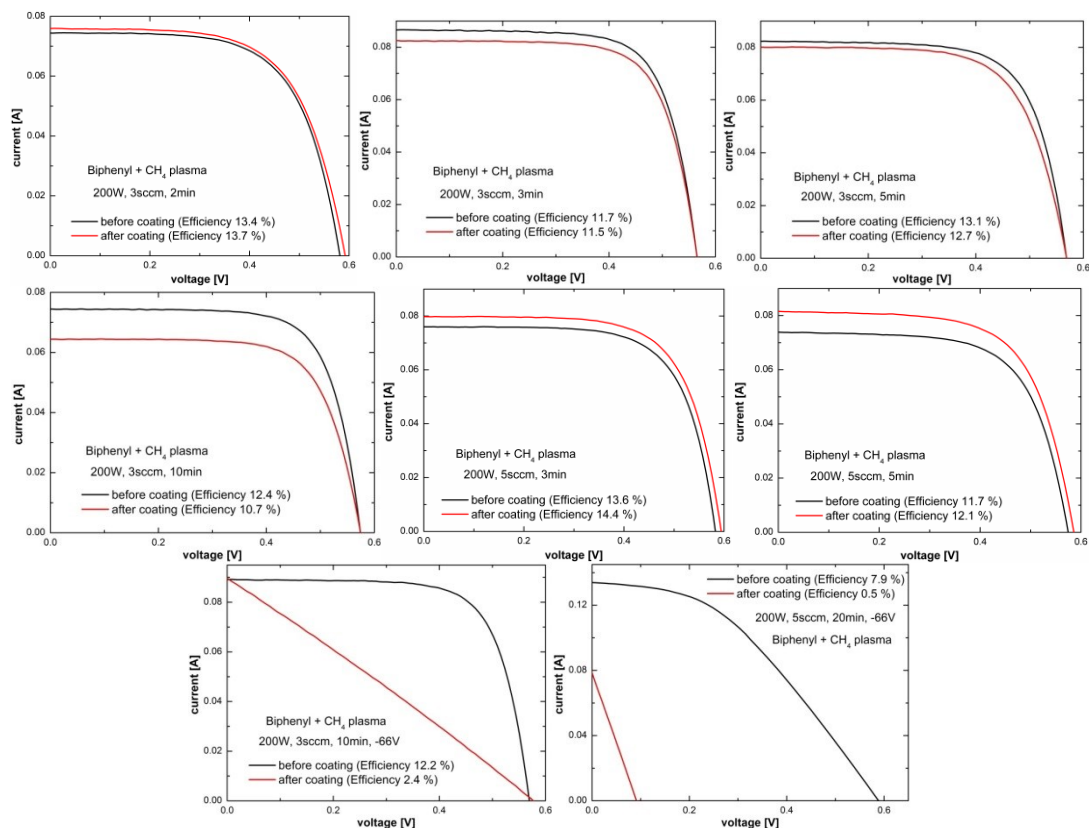
Figure 7.11 The I-V graphs of solar cells before and after the film deposition under the mixture of biphenyl and methane plasma

The hydrogen passivation effect was also analyzed for the deposited films. The improvement of the efficiency of c-Si solar cells can be supplied with the passivation of recombination active centers on the solar cell surface during the film deposition [78]. In the passivation process, the properties of cells are improved via the interaction of H with impurities and defects in the bulk of Si. The H passivation also provides to obtain devices with high quality and low surface recombination[79].

The hydrogen interacts in the silicon solar cells and neutralizes the electrical activities of deep impurities and shallowness of acceptors in cells [80]. It is expected that the formation of a pair of neutral and hydrogen vacancy with the formation of a bridged Si-H bond. Firstly, in the case of absence of hydrogen, a Si atom moves toward the vacancy. While the Si atom is following into a straight path toward the vacancy, it changes along the curved path by the existence of hydrogen atom. Secondly, as a result of this interaction, the hydrogen atom breaks one S-H bond and then generates a new bond with Si atom. Finally, this new Si-H bond occurs with rotated position, and to get back to the initial position a rotation is required. After this rotation, the total energy decreases [79]. In other words, the passivation can be explained by the deep penetration of hydrogen into the outer layer of the solar cell and connecting with dangling bonds in the deflected multicrystalline material [81]. The efficiency measurements of the solar cell have shown a higher response for which the improvement due to the hydrogen passivation in the bulk of solar cell [81].

Table 7.4 Measurements of I-V graph for the films of the mixture

Power (W)	Flow rate (sccm)	Voltage (V)	Dep. Time (min)		Voc (V)	Isc (A)	Jsc (mA/cm^2)	Fill Factor (%)	Efficiency (%)
200	3	-	2	before	0.581	0.074	35.4	65.2	13.4
				after	0.592	0.076	36.1	64.1	13.7
200	3	-	3	before	0.565	0.086	24.0	71.8	11.7
				after	0.563	0.082	22.8	71.3	11.5
200	3	-	5	before	0.568	0.082	27.4	69.9	13.1
				after	0.567	0.080	26.6	67.4	12.7
200	3	-	10	before	0.574	0.074	24.8	72.7	12.4
				after	0.568	0.064	21.4	70.6	10.7
200	5	-	3	before	0.582	0.075	33.7	69	13.6
				after	0.593	0.079	35.4	68.4	14.4
200	5	-	5	before	0.574	0.073	30.7	66.3	11.7
				after	0.585	0.081	31.4	65.7	12.1
200	3	-66	10	before	0.569	0.089	24.7	71.8	12.2
				after	0.320	0.081	22.5	26.4	2.4
200	5	-66	20	before	0.589	0.133	27.7	41.2	7.9
				after	0.091	0.078	16.4	25.3	0.5
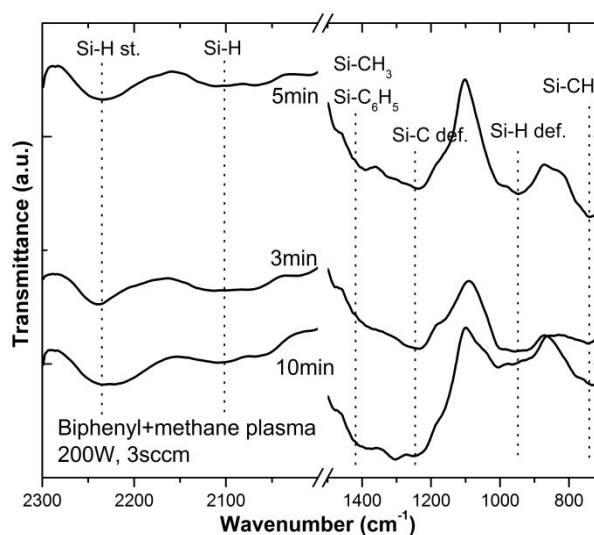
Figure 7.12 The FTIR spectra results for the films of mixture

In the FTIR measurements, the 2246 cm^{-1} band corresponded to Si-H stretching vibration [64,82,83], which is the main band giving information about H-bonding to the silicon surface. The band around 740 cm^{-1} was assigned to Si-CH$_3$ rocking/wagging mode or to Si-C stretching mode [84,85]. The bands at 1240 and 846 cm^{-1} corresponded to deformation of Si-C and Si-H, respectively [82,83]. The band observed at 1420 cm^{-1} referred to Si-CH$_3$ asymmetric stretching [83] or Si-

C_6H_5 (silicon attached to benzene ring) stretching vibration [64] and the band assigned to Si-H deformation was seen at 948 cm^{-1} [82]. There is a shifting in wavenumbers for some bands which can be due to the difference in the optical thickness or the carbon content in thin films. We can discuss the H passivation effect from the H-bonding with silicon surface. As seen in the spectra, the films represented H-bonding with narrower band as the deposition time.

7.5 Conclusion

The fluorene-type thin film was synthesized under a single capacitively coupled rf plasma system by using the biphenyl and methane plasma. The films were annealed under the different temperatures and the changes in the physical and chemical properties were discussed. The OES measurements were used to characterize the plasma during the deposition. The C atom content increased with the rf power whereas the H content decreased. At the high power, increasing the CH_4 flow rate led to increase the excitation of the CH component. From the FTIR spectra, it was seen that the level of C-C and C=C bonding in the film structure increased with the rf power. Therefore, we could suggest that the high quality thin film is generated with high rf power. The sp^3/sp^2 ratio also increased by the rf power. Increasing the deposition time decreased the sp^3/sp^2 ratio. After annealing the sp^3/sp^2 ratio decreased with increasing the temperature and the cross-linked structures increased in the films. The surfaces of the thin films indicated hydrophobic properties at high power and low flow rate values. At high flow rate, it should be kept the power at lower values to able to raise the contact angle. The deposited thin films had an amorphous structure and a small increase was obtained in crystalline size after the annealing. The thickness of the thin films increased with raised rf power and gas flow rate up to the state of saturation. The thickness of annealed samples declined with the increasing temperature. The AFM images showed that the surfaces of the films have nanostructured features. After the annealing, the height of the peaks on surface decreased and smoother surfaces was obtained. Also, the heating the films caused a decrease in the roughness parameters. The generated thin films were coated on the surfaces of c-Si solar cells and smaller increases in the solar cell efficiency were achieved as compared with the a-C:H films.

182

7.6 References

[1]   N.S. Cho, J.-H. Park, S.-K. Lee, J. Lee, H.-K. Shim, M.-J. Park, D.-H. Hwang, B.-J. Jung, Macromolecules 39 (2006) 177.

[2]   A.C. Grimsdale, K. Müllen, Adv. Polym. Sci. 199 (2006) 1.

[3]   J. Pei, W.-L. Yu, W. Huang, A.J. Heeger, Chem. Commun. (2000) 1631.

[4]   W. Yu, J. Pei, Y. Cao, A.J. Heeger, R. Columbia, A. August, Chem. Commun. (1999) 1837.

[5]   Q. Pei, Y. Yang, J. Am. Chem. Soc. 118 (1996) 7416.

[6]   M.T. Bernius, M. Inbasekaran, J. O'Brien, W. Wu, Adv. Mater. 12 (2000) 1737.

[7]   M. Inbasekaran, E. Woo, W. Wu, M. Bernius, L. Wujkowski, Synth. Met. 111-112 (2000) 397.

[8]   B.U. Scherf, E.J.W. List, Adv. Mater. 14 (2002) 477.

[9]   M. Kreyenschmidt, G. Klaerner, T. Fuhrer, J. Ashenhurst, S. Karg, W.D. Chen, V.Y. Lee, J.C. Scott, R.D. Miller, Macromolecules 31 (1998) 1099.

[10]   H. Cho, D. Kim, Y. Kim, Adv. Mater. 9 (1997) 326.

[11]   M. Leclerc, J. Polym. Sci. Part A Polym. Chem. 39 (2001) 2867.

[12]   B.S. Beauprø, M. Leclerc, Adv. Funct. Mater. 12 (2002) 192.

[13]   N.S. Cho, D.-H. Hwang, J.-I. Lee, B.-J. Jung, H.-K. Shim, Macromolecules 35 (2002) 1224.

[14]   A. Babel, S.A. Jenekhe, Macromolecules 36 (2003) 7759.

[15]   D. Neher, Macromol. Rapid Commun. 22 (2001) 1365.

[16]   E. Bundgaard, F. Krebs, Sol. Energy Mater. Sol. Cells 91 (2007) 954.

[17] F. Zhang, K. Jespersen, C. Bjostrom, M. Svensson, M. Andersson, V. Sundstrom, Adv. Funct. Mater. 16 (2006) 667.

[18] I.-S. Bae, S.-J. Cho, S.-H. Jeong, H.J. Cho, B. Hong, J.-H. Boo, Plasma Process. Polym. 4 (2007) S812.

[19] I.S. Bae, S.J. Cho, W.S. Choi, B.Y. Hong, Y.J. Kim, Y.M. Kim, J.H. Boo, Thin Solid Films 516 (2008) 3577.

[20] R. Matin, A.H. Bhuiyan, Thin Solid Films 520 (2012) 6463.

[21] S. Cho, I. Bae, J. Boo, J. Korean Phys. Soc. 53 (2008) 1634.

[22] G.S.Y. Yeh, R. Hosemann, J. Loboda-Čačković, H. Čačković, Polymer (Guildf). 17 (1976) 309.

[23] A.K. Gnanappa, C. O'Murchu, O. Slattery, F. Peters, B. Aszalós-Kiss, S. a. M. Tofail, Polym. Degrad. Stab. 93 (2008) 2119.

[24] B.D.D. Burkey, K.K. Gleason, Chem. Vap. Depos. 9 (2003) 65.

[25] L.M. Han, R.B. Timmons, W.W. Lee, J. Vac. Sci. Technol. B Microelectron. Nanom. Struct. 18 (2000) 799.

[26] V. Cech, P. Horvath, M. Trchova, J. Zemek, J. Matejkova, J. Appl. Polym. Sci. 82 (2001) 2106.

[27] S.C. Cha, E.K. Her, T.J. Ko, S.J. Kim, H. Roh, K.R. Lee, K.H. Oh, M.W. Moon, J. Colloid Interface Sci. 391 (2013) 152.

[28] J. Vogelsang, J. Brazard, T. Adachi, J.C. Bolinger, P.F. Barbara, Angew. Chemie - Int. Ed. 50 (2011) 2257.

[29] M. Granstrom, K. Petritsch, A.C. Arias, A. Lux, M.R. Andersson, R.H. Friend, Nature 395 (1998) 257.

[30] H. Sirringhaus, P.J. Brown, R.H. Friend, M.M. Nielsen, K. Bechgaard, B.M.W. Langeveld-Voss, A.J.H. Spiering, R.A.J. Janssen, E.W. Meijer, P. Herwig, D.M. de Leeuw, Nature 401 (1999) 685.

[31] T.-Q. Nguyen, I.B. Martini, J. Liu, B.J. Schwartz, J. Phys. Chem. B 104 (2000) 237.

[32] W. Ma, C. Yang, X. Gong, K. Lee, A.J. Heeger, Adv. Funct. Mater. 15 (2005) 1617.

[33] R.J. Kline, M.D. McGehee, E.N. Kadnikova, J. Liu, J.M.J. Fréchet, M.F. Toney, Macromolecules 38 (2005) 3312.

[34] M. Reyes-Reyes, K. Kim, D.L. Carroll, Appl. Phys. Lett. 87 (2005) 3.

[35] X. Yang, J. Loos, S.C. Veenstra, W.J.H. Verhees, M.M. Wienk, J.M. Kroon, M.A.J. Michels, R.A.J. Janssen, Nano Lett. 5 (2005) 579.

[36] J.H. Lee, D.S. Kim, Y.H. Lee, J. Electrochem. Soc. 143 (1996) 1443.

[37] T. Tagaki, Thin Solid Films 92 (1982) 1.

[38] J. Coburn, E. Kay, J. Appl. Phys. 43 (1972) 4965.

[39] M.L. Tarng, J. Appl. Phys. 42 (1971) 2449.

[40] R. Jones, C. Standley, L. Maissel, J. Appl. Phys. 38 (1967) 4656.

[41] L. Martinu, M.R. Wertheimer, Appl. Phys. Lett. 54 (1989) 2645.

[42] M. Chen, T. Yang, Z. Ma, J. Polym. Sci. Part A Polym. Chem. 36 (1998) 1265.

[43] S. Eufinger, W.J. van Ooij, T.H. Ridgway, J. Appl. Polym. Sci. 61 (1996) 1503.

[44] A. Pastol, Y. Catherine, J. Phys. D. Appl. Phys. 799 (1990).

[45]   R.L. Vander Wal, J.H. Fujiyama-Novak, C.K. Gaddam, D. Das, A. Hariharan, B. Ward, Appl. Spectrosc. 65 (2011) 1073.

[46]   C. Gómez-Aleixandre, J. Vac. Sci. Technol. A Vacuum, Surfaces, Film. 11 (1993) 143.

[47]   C. Barholm-Hansen, M.D. Bentzon, J.B. Hansen, Diam. Relat. Mater. 3 (1994) 564.

[48]   R.C. Weast, Handbook of Chemistry and Physics 64th Edition, CRC Press, Boca Raton, FL, 1983.

[49]   R. Pearse, A. Gaydon, The Identification of Molecular Spectra, 4th Editio, Chapman and Hall, London, New York, 1984.

[50]   K.P. and G.H. Huber, Molecular Spectra and Molecular Structure Vol 4. Constants of Diatomic Molecules, New York, 1978.

[51]   A.N. Goyette, J.E. Lawler, L.W. Anderson, D.M. Gruen, T.G. McCauley, D. Zhou, A.R. Krauss, Plasma Sources Sci. Technol. 7 (1998) 149.

[52]   A. Yanguas-Gil, K. Focke, J. Benedikt, A. von Keudell, J. Appl. Phys. 101 (2007) 103307.

[53]   H. Song, X. Yu, N. Zhaoyuan, Plasma Sci. Technol. 7 (2005) 2669.

[54]   Y.-K. Kim, J.-Y. Lee, J. Appl. Phys. 81 (1997) 3660.

[55]   D.M. Gruen, J. Vac. Sci. Technol. A Vacuum, Surfaces, Film. 13 (1995) 1628.

[56]   S.D. Lee, G.H. Hsiue, C.Y. Kao, P.C. Chang, Biomaterials 17 (1996) 587.

[57]   B.N. Jariwala, C. V. Ciobanu, S. Agarwal, J. Appl. Phys. 106 (2009) 073305.

[58]   B. Dischler, A. Bubenzer, P. Koidl, Solid State Commun. 65 (1983) 105.

[59]   P. Couderc, Y. Catherine, Thin Solid Films 146 (1987) 93.

[60] T. Heitz, B. Drevillon, C. Godet, J.E. Bouree, 37 (1999) 771.

[61] R. Mota, I. Perrenoud, R. Honda, Ep.liu.se (2012) 368.

[62] S.C. Cho, Y.C. Hong, H.S. Uhm, J. Mater. Chem. 17 (2007) 232.

[63] H. Goktas, D. Mansuroglu, B. Atalay, S. Bilikmen, I. Kaya, Plasma Chem. Plasma Process. 32 (2011) 35.

[64] B.H. Stuart, Infrared Spectroscopy: Fundamentals and Applications, John Wiley & Sons, Ltd, New York, 2004.

[65] D. Pavia, G. Lampman, G. Kriz, J. Vyvan, Introduction to Spectroscopy, 4th ed., Brooks Cole, Fort Worth, 2001.

[66] I.-S. Bae, S.-H. Cho, S.-B. Lee, Y. Kim, J.-H. Boo, Surf. Coatings Technol. 193 (2005) 142.

[67] E. Rusli, M.R. Wang, T.K.S. Wong, M.B. Yu, C.Y. Li, Diam. Relat. Mater. 15 (2006) 133.

[68] L. Valentini, J.M. Kenny, 6 (2001) 5295.

[69] N. Mutsukura, S. Inoue, Y. Machi, J. Appl. Phys. 72 (1992) 43.

[70] J.W.A.M. Gielen, P.R.M. Kleuskens, M.C.M. van de Sanden, L.J. van Ijzendoorn, D.C. Schram, E.H.A. Dekempeneer, J. Meneve, J. Appl. Phys. 80 (1996) 5986.

[71] J.W. Zou, K. Schmidt, K. Reichelt, B. Dischler, J. Appl. Phys. 67 (1990) 487.

[72] S.-J. Cho, I.-S. Bae, Y.S. Park, B. Hong, W. Park, S.C. Park, J.-H. Boo, Surf. Coatings Technol. 202 (2008) 5654.

[73] B. Demirel, A. Yaras, H. Elçiçek, BAU Fen Bil. Enst. Derg. 13 (2011) 26.

[74] Y. Wolanov, eXPRESS Polym. Lett. 3 (2009) 452.

[75] J.F. Whitacre, W.C. West, E. Brandon, B. V. Ratnakumar, J. Electrochem. Soc. 148 (2001) A1078.

[76] G. Rampelberg, K. Devloo-Casier, D. Deduytsche, M. Schaekers, N. Blasco, C. Detavernier, Appl. Phys. Lett. 102 (2013) 111910.

[77] S. Jangjian, C. Liu, Y. Wang, W. Hwang, W. Tseng, Thin Solid Films 469-470 (2004) 460.

[78] V. Buršíková, P. Sládek, P. St'ahel, L. Zajíčková, J. Non. Cryst. Solids 299-302 (2002) 1147.

[79] B. Sopori, X. Deng, J. Benner, A. Rohatgi, P. Sana, S. Estreicher, Y. Park, M. Roberson, Sol. Energy Mater. Sol. Cells 41-42 (1996) 159.

[80] D. Mathiot, Phys. Rev. B 40 (1989) 5867.

[81] F. Duerinckx, J. Szlufcik, Sol. Energy Mater. Sol. Cells 72 (2002) 231.

[82] B.D. Mistry, A Handbook of Spectroscopic Data Chemistry, Oxford Book Company, 2009.

[83] E. Pretsch, P. Buhlmann, M. Badertscher, Structure Determination of Organic Compounds, Springer, 2009.

[84] B. Mitu, G. Dinescu, M. Dinescu, A. Ferrari, M. Balucani, G. Lamedica, A.P. Dementjev, K.I. Maslakov, Thin Solid Films 383 (2001) 230.

[85] T. Stapinski, G. Ambrosone, U. Coscia, F. Giorgis, C.F. Pirri, Phys. B Condens. Matter 254 (1998) 99.

CHAPTER 8

SUMMARY AND FUTURE WORK

This thesis focused on fabrication and characterization of the fluorene-type and a-C:H thin films by plasma polymerization technique. Two different plasma systems were used for the film formation: the single capacitively coupled rf plasma system and the double discharge system which occurred from the combination of a low pressure dc glow discharge and a high current pulsed discharge. The plasma diagnostics of the rf plasma system were measured by using the double Langmuir probe under the N_2 and Ar plasmas. The results showed that the applied rf power caused an increase in both of the electron temperature and ion density. However, increasing the pressure led to a decrease in both of these features. As the electrode gap increased the electron temperature and the ion density decreased as a result of decrease in the plasma energy density.

We presented the plasma polymerized fluorene thin films synthesized by double discharge system and characterized by FTIR, UV-visible, XPS and XRD spectra, and SEM measurements. The produced thin films presented the substitution pattern formation and they had amorphous nature in structure. The optical energy band gap values of the produced and iodine doped samples would have potential applications at semiconductor devices.

Fluorene-type thin films were produced under the mixtures of biphenyl/ methane and biphenyl/ ethylene plasma by using a single capacitively coupled rf plasma system. The plasma environment was analyzed via RGA mass spectrometry. Controlling the plasma chemistry during the plasma deposition was a difficult and very complicated work. Applying negative bias voltage led to positive ion bombardment on the substrate and this increased intensities of the corresponding fragments for the fluorene-type thin films. Therefore, this process can be considered as an effective way in controlling the reactions in the plasma depositions. In addition, due to the stability of the molecule of ethylene, it was more attractive than

the molecule of methane to obtain the fluorene-type thin films. The optical properties of films were revealed by using UV-visible spectroscopy and thin films were doped by iodine. The thin films indicated direct band energies and they changed in the region between 3.15 and 3.54 eV for the mixture with methane, and between 3.08 and 3.48 eV for the mixture with ethylene, which verified that the chains in the film structure were generated in different order with respect to the independent plasma parameters. I_2 doping improved the electro and optical properties of the thin films by decreasing the energy band gap up to 2.85 eV, which may result from the increase in the conjugation length of the structure. The energy band gap values of the films indicated almost same results for two mixtures after the doping process. Thicknesses of films were measured by ellipsometry and they showed a linear relation with the plasma parameters of power, CH_4 or C_2H_4 flow rate. The applied negative bias voltage should be at high values for deposited films obtained by using the methane gas while it should be at intermediate values for the ethylene gas. Since the molecule of the ethylene tended to form heavier compounds during the deposition, which caused increase in the deposition rate, thickness values corresponding to the mixture of biphenyl/ ethylene were found higher than the corresponding to the mixture with methane. Moreover, an AFM was employed to characterize the nanostructural properties of the film surfaces. The surfaces of thin films formed in both mixtures had remarkable nanostructured characteristics generated by the various bias voltages. Additionally, peaks on the surfaces of thin films provide the availability required for photovoltaic applications. As a result, it may be suggested that applying a negative bias voltage is an effective way to increase the height of these peaks. The surfaces of the thin films deposited with ethylene exhibited higher density than the ones obtained with the methane. The XRD spectrometry exhibited that all deposited films had amorphous structures and we are going to improve the crystallinity by annealing the thin films in the future. It could be suggested that the mixture of biphenyl/ ethylene plasma environment was more suitable to obtain the fluorene-type thin films.

The a-C:H thin films were synthesized by using a single capacitively coupled rf powered CH_4 plasma system under variable plasma parameters in a wide range. The amorphous structure of the thin film was revealed by XRD spectroscopy. The diagnostic properties of plasma species during the deposition were investigated by

using OES and the structural properties of thin films were analyzed via FTIR spectroscopy. As a result of the measurements and analysis, it was found that the sp^3/sp^2 ratio and H content in the plasma are the most significant factors in determination of the type of the thin films, which was generally closer to graphitic structure. A profilometer was employed to measure thicknesses of the films, which were found to be in a linear relation with the sufficient ionization rate and deposition time. Moreover, the values of the optical band gap energies of films were revealed by using UV-visible spectroscopy. It was found that the indirect band gap energies changed in the region from 0.65 to 1.60 eV, which may result from different order of chains in the film structure generated with respect to the parameters. As a result of all analysis, it was found that the plasma reactor should contain enough C compounds and this content should be higher than the level of the H content to be able to obtain a thin film with good quality. The H content can be controlled with changing the plasma parameters. The a-C:H films generally exhibited good characteristics at higher input power and higher CH_4 flow rate, at 30 min deposition time. The produced a-C:H thin films were coated on the surfaces of c-Si solar cells and it led to the improvement of the solar cell efficiency at high values of the deposition time, rf power, and CH_4 flow rate. This improvement can be due to the antireflective property or the hydrogen passivation effect of the deposited films. From results, an increase around 5 % was achieved in the efficiency.

The annealing effect on the fluorene-type thin films synthesized by the single capacitively coupled rf plasma system by using the biphenyl and methane plasma was investigated under the different temperatures and the changes in the physical and chemical properties were discussed. The OES measurements were used to characterize the plasma during the deposition. The C atom content increased with the rf power whereas the H content decreased. At the high power increasing of the CH_4 flow rate led to increase the excitation of the CH component. From the FTIR spectra, it was seen that the level of C-C and C=C bonding in the film structure increased with the rf power. Therefore, we could suggest that the high quality thin film is generated with high rf power. The sp^3/sp^2 ratio also increased by the rf power. Increasing the deposition time decreased the sp^3/sp^2 ratio. After annealing the sp^3/sp^2 ratio decreased with increasing the temperature and the cross-linked structures increased in the films. The surfaces of the thin films indicated

hydrophobic properties at high power and low flow rate values. At high flow rate, it should be kept the power at lower values to able to raise the contact angle. The deposited thin films had an amorphous structure and a small increase was obtained in crystalline size after the annealing. The thickness of the thin films increased with raised rf power and gas flow rate up to the state of saturation. The thickness of annealed samples declined with the increasing temperature. The AFM images showed that the surfaces of the films have nanostructured features. After the annealing, the height of the peaks on surface decreased and smoother surfaces was obtained. Also, the heating the films caused a decrease in the roughness parameters. The generated thin films were coated on the surfaces of c-Si solar cells and smaller increases in the solar cell efficiency were achieved as compared with the a-C:H films.

It could be suggested that the thin films produced by the plasma polymerization were different than the ones produced by the conventional techniques in the physical and the chemical meaning. It is promising technique to generate thin films for several applications such as photovoltaic, organic and biomedical devices. In future, the application of the c-Si solar cells will be repeated for optimum parameters and different polymer materials will be tried for this application. We will also plan to use the produced polymer thin films for photovoltaic devices such as organic solar cell and organic light emitting diodes. Furthermore, we are going to synthesize plasma polymer thin films and discuss for the different polymer groups.

CURRICULUM VITAE

PERSONAL INFORMATION

Surname, Name: Mansuroğlu, Doğan
Nationality: Turkish (TC)
Date and Place of Birth: 4 March 1984, Antakya
Marital Status: Single
Phone: +90 312 210 43 30
Fax: +90 312 210 50 99
email: madogan@metu.edu.tr

EDUCATION

Degree	Institution	Year of Graduation
BS	Ankara University Physics	2005

WORK EXPERIENCE

Year	Place	Enrollment
2006 – Present	METU Department of Physics	Research Assistant
2010 – 2011	University of Wisconsin-Madison, Center For Plasma-Aided Manufacturing (CPAM) WI, USA	Visiting Researcher

PUBLICATIONS

1. **D. Mansuroglu** and S. Manolache, "Synthesis of Fluorene-type Thin Film under Biphenyl/Methane Plasma Environment", Plasma Processes and Polymers, 2015, doi: 10.1002/ppap.201400136
2. **D. Mansuroglu**, K. Goksen and S. Bilikmen, "Optical Characterization of Amorphous Hydrogenated Carbon (a-C:H) Thin Film Prepared by Single RF Plasma Method", Plasma Science and Technology, 2015, 17, 6, 488-495
3. H.Goktas, **D. Mansuroglu**, B. Atalay, S. Bilikmen, I. Kaya, "Polyfluorene Thin Films Synthesized by a Novel Plasma Polymerization Method" Plasma Chem. Plasma Process., 2012, 32, 35-44

PROCEEDINGS

1. **D. Mansuroglu** and S. Manolache, "Fluorene-type Thin Films Synthesized under Biphenyl and Ethylene Plasma", IEEE NANO 2012, 12th International Conference on Nanotechnology, August 20-23, 2012, Birmingham, UK, p. 510

2. H. Goktas, T. Gunes, Z. Demircioglu, **D. Mansuroglu**, I. Kaya, "Plasma Polymerized Polyaniline Thin Films by Double Discharge Technique", 20th International Symposium on Plasma Chemistry, June 24-29, 2011, Philadelphia, USA, p. 41

CONFERENCE PRESENTATIONS

Oral

1. **D. Mansuroglu** and S. Manolache, "Fluorene-type Thin Films Synthesized under Biphenyl and Ethylene Plasma", IEEE NANO 2012, 12th International Conference on Nanotechnology, August 20-23, 2012, Birmingham, UK

Poster

1. **D. Mansuroglu** and S. Bilikmen, "The Influence of Annealing on Fluorene-type Thin Film Produced by Biphenyl and Methane RF Plasma System", ICOPS-2015, The 42nd IEEE International Conference on Plasma Science, May 24-28, 2015, Antalya, TURKEY

2. **D. Mansuroglu** and S. Bilikmen, "Producing Polymer Thin Film with RF Plasma for Photovoltaic Applications", SolarTR-3, Third Turkish Solar Electricity Conference and Exhibition, April 27-29, 2015, Ankara, TURKEY

3. **D. Mansuroglu**, K. Goksen, S. Bilikmen, "Synthesis of Hydrogenated Amorphous Carbon (a-C:H) Thin Film by Single RF Plasma System", International Conference on Solar Energy for World Peace, August 17-19, 2013, Istanbul, TURKEY

4. **D. Mansuroglu**, D. Akbar, S. Bilikmen, "Surface Modification of Polypropylene by Single and Dual Radio Frequency Plasma", NANO-TR, 8th Nanoscience and Nanotechnology Conference, June 25-29, 2012, Ankara, TURKEY

5. H. Goktas, T. Gunes, Z. Demircioglu, **D. Mansuroglu**, I. Kaya, "Plasma Polymerized Polyaniline Thin Films by Double Discharge Technique", 20th International Symposium on Plasma Chemistry, June 24-29, 2011, Philadelphia, USA

6. **D. Mansuroglu**, F. G. Ince, H. Goktas, S. Bilikmen, R. Aydin, "The morphology and molecular structure of polyfluorene thin films synthesized by a

novel plasma polymerization method", 2nd İnternational conference on physics of optical materials and devices, ICOM 2009, p. 30, August 26 – September 1, 2009, Herceg Novi, Montenegro

7. **D. Mansuroglu**, F. G. Ince, H. Goktas, I. Kaya, R. Aydin, "A Novel Plasma Polymerization Method for Synthesizing Thin Films of Flourene" The International Conference on Nanotechnology: Science and Applications (Nanotech Insight '09), p. 264, Barcelona, SPAIN, March 29 - April 2, 2009

Attended

1. Photonic'09, 11th National Congress of Optic, Electro-optic and Photonic, Ankara, TURKEY, October 16, 200

2. Plasma in Nanomaterials and Nanocomposites, Antalya, TURKEY, October 8-9, 2009

3. NANO-TR, 5th Nanoscience and Nanotechnology Conference, Eskisehir, TURKEY, June 8-12, 2009

4. Photonic'09, 10th National Congress of Optic, Electro-optic and Photonic, Kocaeli, TURKEY, October 17, 2008

5. NANO-TR, 3th Nanoscience and Nanotechnology Conference, Ankara, TURKEY, June 11-14, 2007